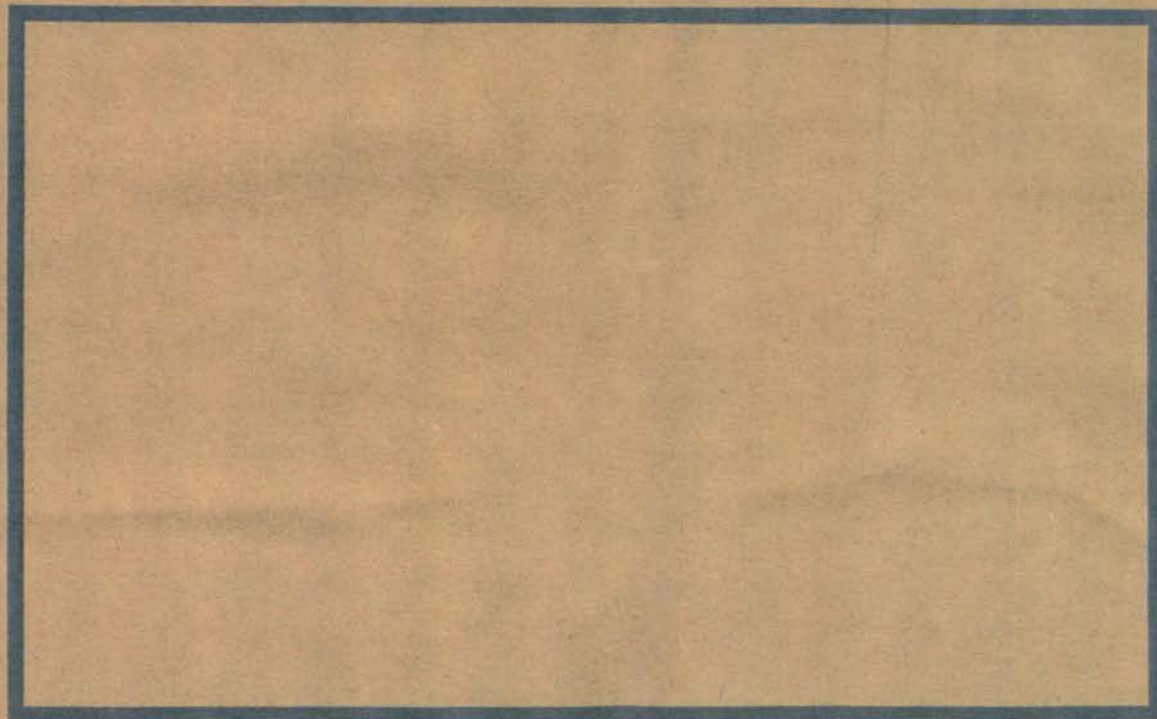
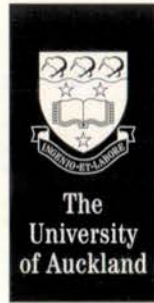


ENG 305-(EQC 1999/329)

**Influence of Loading History on Ultimate Displacement of  
Concrete Structures**

*Darrin Liddell, Jason M Ingham, Barry J Davidson, Dept of Civil &  
Resource Engineering, University of Auckland*





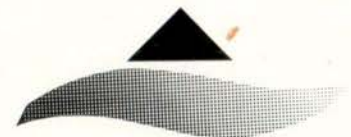
Department of  
Civil and  
Resource  
Engineering

**INFLUENCE OF LOADING HISTORY  
ON ULTIMATE DISPLACEMENT  
OF CONCRETE STRUCTURES**

By  
Darrin Liddell, Jason M. Ingham  
and Barry J. Davidson

School of Engineering  
Report No. 597

July 2000



*Civil and Resource Engineering*

**INFLUENCE OF LOADING HISTORY ON  
ULTIMATE DISPLACEMENT OF  
CONCRETE STRUCTURES**

**By Darrin Liddell, Jason M. Ingham,  
and Barry J. Davidson**

University of Auckland

Private Bag 92019

New Zealand

July 2000

## Technical Abstract

Currently there is considerable interest in displacement-based methods of structural design, with the expectation that these methods may lead to more rational, safer, and cost-effective designs. One of the key features of displacement-based design is the selection of a target ultimate displacement, with this decision based on the performance of laboratory subassemblies.

However, as laboratory loading regimes vary between research institutions throughout the world, it was necessary to establish the influence of the applied loading history on the ultimate displacement of the test subassemblage. Twelve tests, consisting of seven laboratory procedures and five acceleration histories, were conducted.

It was established that the ultimate displacement of the test subassemblage was dependent on the loading history and that previously published methods, such as energy dissipation and comparison of reinforcement strains, did not provide reliable comparisons of test results. It was established that the most accurate way to compare test results was through application of the Park and Ang damage index. Criteria for defining the individual damage states were also provided.

## Non-Technical Abstract

Current design methods for reinforced concrete buildings are based upon resisting forces that are calculated for each member from the loads applied to the building. However, it has been established that the ability of a building to withstand an earthquake is dependent on its ability to negotiate the deflections that arise during an earthquake. Therefore, new design methods have been proposed that are based on designing a building to negotiate certain displacements, with the expectation that these methods may lead to more rational, safer, and cost-effective designs. The displacements that buildings are designed for are established from testing of reinforced concrete beams, column, and beam-column joints in the laboratory.

However, there are numerous testing procedures that can be used to test reinforced concrete members. Therefore, it was necessary to determine whether the applied testing procedure influenced the test results. Twelve tests, consisting of seven different testing procedures used in laboratories around the world and five earthquake sequences, were conducted.

It was established that the maximum displacement of a reinforced concrete member was dependent on the applied testing procedure. It was also established that previously published methods, such as comparing the amount of energy transferred during testing or the increase in length of the reinforcing steel, did not provide reliable indicators of the differences between tests. It was established that the most accurate way to compare test results was through application of the damage index (a numerical indicator of the amount of damage suffered) proposed by Park and Ang. Criteria for relating the amount of physical damage to the numerical damage index were also provided.

## Acknowledgements

Several people and organisations were of immense help to me during the experimental investigations and the writing of this thesis. Firstly I would like to give the credit for this thesis to God—thanks for giving me the strength and the wisdom.

Secondly, I would like to thank Jason Ingham and Barry Davidson for supervising this thesis: for their ever-helpful advice and encouragement. Your efforts were greatly, greatly appreciated. I would like to thank Mark Abrahams for grammar checking a lot of my work and helping me to understand the joys of technical writing. I would also like to thank Hank Mooy and Mark Byrami for their assistance in building and testing of the test subassemblies. Thanks also to Athol Carr from the University of Canterbury for his advice regarding generation of the computer model in Ruaumoko, Shigeki Unjoh from the Public Works Research Institute in Japan for his help in implementing the Public Works Research Institute's loading history, and Sri Sriitharan from Iowa State University for his help in obtaining references from the United States.

The Earthquake Commission and the Cement and Concrete Association of New Zealand provided financial support for this project. Your support was greatly appreciated. I would like to thank Pacific Steel and Mike Findlay at Ready Mix Concrete for donating the necessary reinforcing steel and concrete for this project. Thanks also to Allan Hunter at Sika NZ Ltd for providing a place and means to build the test subassemblies and to Brett Beatson at Stevenson and Sons Ltd for transporting the test subassemblies to the laboratory.

Finally, I would like to thank all my friends and family for supporting me during the writing of this thesis. Your support—whether big or small—helped me to keep persevering and to finish the job with my sanity intact.

## Table of Contents

Technical Abstract.....	ii
Non-Technical Abstract .....	iii
Acknowledgements .....	iv
List of Figures .....	xiii
List of Tables.....	xxiii
List of Symbols.....	xxiv
<b>1.0 Introduction .....</b>	<b>1-1</b>
<b>2.0 Literature Review .....</b>	<b>2-1</b>
2.1 Loading Histories .....	2-1
2.1.1 Comparison of Loading Histories.....	2-2
2.1.2 Loading Rate.....	2-4
2.2 Effect of Loading History on Experimental Results .....	2-5
2.3 Energy Concepts.....	2-8
2.4 Constitutive Models.....	2-10
2.4.1 Concrete.....	2-10
2.4.1.1 Monotonic Behaviour .....	2-10
2.4.1.2 Cyclic Behaviour .....	2-11
2.4.2 Reinforcement Steel.....	2-13
2.4.2.1 Monotonic Behaviour .....	2-13
2.4.2.2 Cyclic Behaviour .....	2-14
2.5 Failure Mechanisms.....	2-15
2.5.1 Flexure.....	2-15
2.5.1.1 Tensile Failure .....	2-16
2.5.1.2 Compressive Failure .....	2-16
2.5.2 Shear .....	2-16
2.5.3 Low Cycle Fatigue.....	2-17
<b>3.0 Theory.....</b>	<b>3-1</b>
3.1 Nominal and Ideal Design Strengths .....	3-1
3.2 Sign Conventions.....	3-2
3.3 Cumulative Ductility .....	3-2
3.4 Hysteresis Behaviour of Concrete Under Cyclic Loading .....	3-3

3.4.1	Displacement Ductility .....	3-3
3.4.2	Elasto-Plastic Behaviour .....	3-3
3.4.3	Bilinear Behaviour .....	3-4
3.5	Damage Indices .....	3-5
3.5.1	Ductility Ratio .....	3-5
3.5.2	Cosenza et al. Index .....	3-5
3.5.3	Roufaiel and Meyer Index .....	3-6
3.5.4	Park and Ang Index .....	3-8
3.5.5	Banon and Veneziano Index .....	3-9
3.5.6	Bracci et al. Index .....	3-10
<b>4.0</b>	<b>Test Assembly Design, Construction, and Set-Up .....</b>	<b>4-1</b>
4.1	Prototype Design .....	4-2
4.2	Design Modifications .....	4-5
4.2.1	Scaling Techniques .....	4-5
4.2.2	Longitudinal Reinforcement .....	4-6
4.2.3	Transverse Reinforcement .....	4-8
4.3	Test Unit Details .....	4-11
4.3.1	Longitudinal and Transverse Reinforcement Details .....	4-11
4.3.2	Beam-Column Joint .....	4-12
4.4	Construction Procedure .....	4-13
4.4.1	Material Properties .....	4-13
4.4.1.1	Concrete .....	4-13
4.4.1.2	Reinforcing Steel .....	4-14
4.4.2	Construction of Test Assembly .....	4-15
4.5	Test Set-Up .....	4-17
4.6	Instrumentation .....	4-19
4.7	Calculation of Displacement Components .....	4-20
<b>5.0</b>	<b>Analytical Modelling .....</b>	<b>5-1</b>
5.1	Model of Ten-Storey Building .....	5-1
5.1.1	Structural Members .....	5-2
5.1.2	Material Strengths .....	5-4
5.1.3	Calibration of Model Parameters .....	5-5
5.1.4	Verification of Hysteresis Model .....	5-6

5.1.5	Mass and Damping Matrices .....	5-8
5.1.6	Time History Analysis .....	5-9
5.1.7	Model Output Data .....	5-9
5.2	Earthquake Excitations .....	5-10
5.2.1	Acceleration History A .....	5-12
5.2.2	Acceleration History B .....	5-16
5.2.3	Acceleration History C .....	5-20
5.2.4	Acceleration History D .....	5-23
5.2.5	Acceleration History E .....	5-25
<b>6.0</b>	<b>Applied Loading Histories .....</b>	<b>6-1</b>
6.1	Definition of Failure .....	6-1
6.2	New Zealand Loading History .....	6-2
6.3	Comparison with International Procedures .....	6-3
6.3.1	Conventional Approach from the University of California at Berkeley .....	6-4
6.3.2	Conventional Approach from the PRESSS Research Programme .....	6-5
6.3.3	Conventional approach from the Public Works Research Institute in Japan .....	6-6
6.4	Fabricated Loading Histories .....	6-7
6.4.1	Monotonic Loading .....	6-8
6.4.2	Bi-directional Cycling at Ductility 8 .....	6-8
6.4.3	Uni-Directional Cycling .....	6-9
6.5	Simulated Response of a Ten-Storey Building .....	6-9
6.5.1	Acceleration History A .....	6-10
6.5.2	Acceleration History B .....	6-11
6.5.3	Acceleration History C .....	6-11
6.5.4	Acceleration History D .....	6-12
6.5.5	Acceleration History E .....	6-13
<b>7.0</b>	<b>Analysis of Results .....</b>	<b>7-1</b>
7.1	Ultimate Displacement .....	7-2
7.1.1	Laboratory Procedures .....	7-3
7.1.2	Acceleration Histories .....	7-7
7.2	Comparison of Force-Displacement Hysteresis Loops .....	7-10
7.2.1	Laboratory Procedures .....	7-11

7.2.1.1	Comparison after Ductility 4 Cycles .....	7-11
7.2.1.2	Comparison after Ductility 6 Cycles .....	7-12
7.2.1.3	Comparison after Ductility 8 Cycles .....	7-13
7.2.2	Acceleration Histories .....	7-16
7.3	Energy Dissipation .....	7-17
7.3.1	Laboratory Procedures.....	7-17
7.3.2	Acceleration Histories .....	7-19
7.4	Reinforcement Steel Strain Behaviour .....	7-20
7.4.1	Laboratory Procedures.....	7-20
7.4.2	Acceleration Histories .....	7-21
7.5	Damage Indices .....	7-23
7.5.1	Comparison of Predicted Damage Indices with Actual Damage Indices .....	7-24
7.5.2	Comparison of Actual Damage Indices with Observed Damage .....	7-26
7.5.3	Relevance of Damage Indices .....	7-40
7.6	Comparison of Crack Behaviour .....	7-43
7.6.1	Comparison after Loading to Ductility 2.....	7-43
7.6.2	Comparison after Loading to Ductility 4.....	7-46
7.6.3	Comparisons after Loading to Ductility 6.....	7-48
<b>8.0</b>	<b>Conclusions.....</b>	<b>8-1</b>
8.1	Summary of Findings .....	8-1
8.1.1.	Literature Review .....	8-1
8.1.2.	Analytical Modelling.....	8-1
8.1.3.	Experimental Results.....	8-2
8.2	Recommendations for Future Research.....	8-4
<b>9.0</b>	<b>References.....</b>	<b>9-1</b>
<b>Appendix A —Ruaumoko Input File.....</b>		<b>A-1</b>
<b>Appendix B —Adaptability of Hysteresis Model.....</b>		<b>B-1</b>
<b>Appendix C – Experimental Results.....</b>		<b>C-1</b>
C.1	New Zealand Loading History .....	C-3
C.1.1	Test Observations.....	C-3
C.1.1.1	Force Control .....	C-4
C.1.1.2	Displacement Control .....	C-4

C.1.2	Displacement Components .....	C-7
C.1.3	Energy Components.....	C-9
C.1.4	Moment–Curvature Response.....	C-10
C.1.5	Reinforcement Strains.....	C-11
C.1.6	Beam Elongation.....	C-13
C.1.7	Summary of Results.....	C-14
C.2	University of California at Berkeley Loading History.....	C-15
C.2.1	Test Observations.....	C-15
C.2.1.1	Force Control .....	C-15
C.2.1.2	Displacement Control .....	C-16
C.2.2	Displacement Components .....	C-19
C.2.3	Energy Components.....	C-21
C.2.4	Moment–Curvature Response.....	C-22
C.2.5	Reinforcement Strains.....	C-23
C.2.6	Beam Elongation.....	C-25
C.2.7	Summary of Test Results .....	C-26
C.3	PRESSS Loading History .....	C-27
C.3.1	Test Observations.....	C-27
C.3.2	Displacement Components .....	C-31
C.3.3	Energy Components.....	C-32
C.3.4	Moment–Curvature Response.....	C-33
C.3.5	Reinforcement Strains .....	C-34
C.3.6	Beam Elongation.....	C-35
C.3.7	Summary of Test Results .....	C-36
C.4	Public Works Research Institute Loading History.....	C-38
C.4.1	Test Observations.....	C-38
C.4.1.1	Force Control .....	C-38
C.4.1.2	Displacement Control .....	C-39
C.4.2	Displacement Components .....	C-41
C.4.3	Energy Components.....	C-43
C.4.4	Moment–Curvature Response .....	C-44
C.4.5	Reinforcement Strains .....	C-45
C.4.6	Beam Elongation .....	C-47

C.4.7	Summary of Test Results .....	C-48
C.5	Monotonic Loading.....	C-49
C.5.1	Test Observations.....	C-49
C.5.2	Displacement Components .....	C-51
C.5.3	Energy Components.....	C-53
C.5.4	Moment–Curvature Response.....	C-54
C.5.5	Reinforcement Strains.....	C-55
C.5.6	Beam Elongation.....	C-56
C.5.7	Summary of Test Results .....	C-57
C.6	Bi-directional Cycling at Ductility 8.....	C-59
C.6.1	Test Observations.....	C-59
C.6.2	Displacement Components .....	C-61
C.6.3	Energy Components.....	C-63
C.6.4	Moment–Curvature Response.....	C-63
C.6.5	Reinforcement Strains.....	C-65
C.6.6	Beam Elongation.....	C-66
C.6.7	Summary of Test Results .....	C-67
C.7	Unidirectional Cycling.....	C-70
C.7.1	Test Observations.....	C-70
C.7.1.1	Force Control .....	C-70
C.7.1.2	Displacement Control .....	C-71
C.7.2	Displacement Components .....	C-72
C.7.3	Energy Components.....	C-74
C.7.4	Moment–Curvature Response .....	C-75
C.7.5	Reinforcement Strains.....	C-76
C.7.6	Beam Elongation .....	C-77
C.7.7	Summary of Test Results .....	C-78
C.8	Acceleration History A .....	C-80
C.8.1	Test Observations.....	C-80
C.8.2	Displacement Components .....	C-82
C.8.3	Energy Components.....	C-83
C.8.4	Moment–Curvature Response.....	C-84
C.8.5	Reinforcement Strains.....	C-85

C.8.6	Beam Elongation.....	C-86
C.8.7	Summary of Test Results .....	C-87
C.9	Acceleration History B.....	C-89
C.9.1	Test Observations.....	C-89
C.9.2	Displacement Components .....	C-91
C.9.3	Energy Components.....	C-91
C.9.4	Moment–Curvature Response.....	C-92
C.9.5	Reinforcement Strains.....	C-93
C.9.6	Beam Elongation .....	C-94
C.9.7	Summary of Test Results .....	C-95
C.10	Acceleration History C.....	C-98
C.10.1	Test Observations.....	C-98
C.10.2	Displacement Components .....	C-100
C.10.3	Energy Components.....	C-100
C.10.4	Moment Curvature .....	C-101
C.10.5	Reinforcement Strains.....	C-102
C.10.6	Beam Elongation .....	C-103
C.10.7	Summary of Test Results .....	C-104
C.11	Acceleration History D .....	C-107
C.11.1	Test Observations.....	C-107
C.11.2	Displacement Components .....	C-109
C.11.3	Energy Components.....	C-111
C.11.4	Moment–Curvature Response.....	C-112
C.11.5	Reinforcement Strains.....	C-112
C.11.6	Beam Elongation.....	C-114
C.11.7	Summary of Test Results .....	C-115
C.12	Acceleration History E.....	C-116
C.12.1	Test Observations.....	C-116
C.12.2	Displacement Components .....	C-118
C.12.3	Energy Components.....	C-119
C.12.4	Moment–Curvature Response.....	C-120
C.12.5	Reinforcement Strains.....	C-121
C.12.6	Beam Elongation.....	C-122

C.12.7 Summary of Test Results ..... C-123

## List of Figures

Figure 2-1 Loading History Applied by Park (1989) .....	2-1
Figure 2-2 PRESSSS Loading History .....	2-4
Figure 2-3 Stress-Strain Model for Monotonic Loading (Mander et al. 1988) .....	2-11
Figure 2-4 Concrete Stress-Strain Curve with Unloading and Reloading Branches (Mander et al. 1988) .....	2-12
Figure 2-5 Monotonic Tensile Curve for Mild Steel (Dodd & Restrepo 1995) .....	2-13
Figure 2-6 Features of Hysteretic Behaviour of Mild Steel (CEB 1996) .....	2-14
Figure 3-1(a) Sign Convention .....	3-2
Figure 3-1(b) Designation of Beam Sides .....	3-2
Figure 3-2 Elasto-Plastic Approximation .....	3-4
Figure 3-3 Bilinear Approximation .....	3-4
Figure 3-4 Definition of Modified Flexural Damage Ratio (Roufaiel and Meyer 1987) .....	3-7
Figure 3-5 Damage Index Terms (Bracci et al. 1989) .....	3-11
Figure 3-6 Bi-Linear Moment Curvature Relationship (Bracci et al. 1989) .....	3-12
Figure 4-1 Frame Building Plan (C&CA 1998) .....	4-2
Figure 4-2(a) Perimeter Frame Elevation (C&CA 1998) .....	4-3
Figure 4-2(b) Frame Design Actions (C&CA 1998) .....	4-3
Figure 4-3 Level Two Reinforcement Layout (C&CA 1998) .....	4-4
Figure 4-4 Location of Potential Plastic Hinge Zones (C&CA 1998) .....	4-4
Figure 4-5 Prototype Cross Section (C&CA 1998) .....	4-5
Figure 4-6 Reinforcement Layout in Test Sub-Assemblage .....	4-11
Figure 4-7(a) Cross Section at A-A .....	4-12
Figure 4-7(b) Cross Section at B-B .....	4-12
Figure 4-8 Beam Column Joint .....	4-12
Figure 4-9 History of Concrete Strength .....	4-14
Figure 4-10 Stress-Strain Curve for Longitudinal Reinforcement .....	4-15
Figure 4-11 Reinforcement Cage in Upright Position .....	4-15
Figure 4-12 Reinforcement Cage Rotated 90 Degrees .....	4-16
Figure 4-13 Reinforcement Cages Positioned in Boxing .....	4-16
Figure 4-14 Front Elevation of Test Set-Up .....	4-17

Figure 4-15 End Elevation of Test Set-Up .....	4-18
Figure 4-16 Instrumentation Layout .....	4-19
Figure 4-17(a) Flexural Displacement .....	4-20
Figure 4-17(b) Shear Displacement .....	4-20
Figure 4-18 Rocking Displacement .....	4-21
Figure 5-1 Model Dimensions .....	5-2
Figure 5-2 Giberson One Component Beam Model (Carr 1998) .....	5-3
Figure 5-3 Ten-Storey Model with Beam Elements Numbered and Joint Elements Shaded .....	5-4
Figure 5-4 Emori and Schnobrich Unloading Curve (Carr 1998) .....	5-8
Figure 5-5 Comparison of Experimental Data and Takeda Model .....	5-8
Figure 5-6 Components of Relative Vertical Deflection at Critical Node .....	5-10
Figure 5-7 Acceleration History A .....	5-13
Figure 5-8 Critical Beam Displacement-Time History (Acceleration History A) ..	5-14
Figure 5-9 Top Storey Displacement History (Acceleration History A) .....	5-14
Figure 5-10 Predicted Force-Displacement Response (Acceleration History A) ...	5-15
Figure 5-11(a) Pushover Analysis of Full-Scale Model .....	5-17
Figure 5-11(b) Pushover Analysis of Two-Thirds Model .....	5-17
Figure 5-12 Acceleration History B .....	5-18
Figure 5-13 Critical Beam Displacement Time History (Acceleration History B) .	5-18
Figure 5-14 Top Storey Displacement-Time History (Acceleration History B) .....	5-19
Figure 5-15 Predicted Force-Displacement Response (Acceleration History B) ....	5-19
Figure 5-16 Acceleration History C .....	5-20
Figure 5-17 Critical Beam Displacement Time History (Acceleration History C) 5-21	
Figure 5-18 Top Storey Displacement-Time History (Acceleration History C) .....	5-21
Figure 5-19 Predicted Force-Displacement Response (Acceleration History C) ....	5-22
Figure 5-20 Acceleration History D .....	5-23
Figure 5-21 Critical Beam Displacement Time History (Acceleration History D) 5-24	
Figure 5-22 Top Storey Displacement-Time History (Acceleration History D) .....	5-24
Figure 5-23 Predicted Force-Displacement Response (Acceleration History D) ....	5-25
Figure 5-24 Acceleration History E .....	5-26
Figure 5-25 Critical Beam Displacement Time History (Acceleration History E) .	5-26
Figure 5-26 Top Storey Displacement-Time History (Acceleration History E) .....	5-27

Figure 5-27 Predicted Force-Displacement Response (Acceleration History E) ....5-27

Figure 6-1 New Zealand Loading History .....6-2

Figure 6-2 Bilinear Approach .....6-3

Figure 6-3 Loading History Applied at the University of California at Berkeley .....6-5

Figure 6-4 Storey Drift .....6-6

Figure 6-5 PRESSSS Loading History .....6-6

Figure 6-6 Public Works Research Institute Loading History .....6-7

Figure 6-7 Monotonic Loading .....6-8

Figure 6-8 Direct Cycling at Ductility 8 .....6-9

Figure 6-9 Unidirectional Cycling .....6-9

Figure 6-10 Acceleration History A .....6-10

Figure 6-11 Earthquake History B .....6-11

Figure 6-12 Earthquake History C .....6-12

Figure 6-13 Acceleration History D .....6-12

Figure 6-14 Acceleration History E .....6-13

Figure 7-1 Force-Displacement Response (New Zealand Loading History) .....7-2

Figure 7-2 Force-Displacement Response (Berkeley Loading History) .....7-3

Figure 7-3 Force-Displacement Response (PRESSSS Loading History) .....7-3

Figure 7-4 Force-Displacement Response (Public Works Research Institute Loading History) .....7-4

Figure 7-5 Force-Displacement Response (Monotonic Loading) .....7-5

Figure 7-6 Force-Displacement Response (Cycling at Ductility 8) .....7-5

Figure 7-7 Force-Displacement Response (Unidirectional Loading) .....7-6

Figure 7-8 Force-Displacement Response (Acceleration History A) .....7-8

Figure 7-9 Force-Displacement Response (Acceleration History B) .....7-8

Figure 7-10 Force-Displacement Response (Acceleration History C) .....7-9

Figure 7-11 Force-Displacement Response (Acceleration History D) .....7-9

Figure 7-12 Force-Displacement Response (Acceleration History E) .....7-10

Figure 7-13 Comparison after Loading to Ductility 4 .....7-11

Figure 7-14 Comparison after Loading to Ductility 6 .....7-13

Figure 7-15 Comparison after Loading to Ductility 8 .....7-14

Figure 7-16 Comparison of Acceleration Histories' Envelope with Monotonic Response .....7-16

Figure 7-17 Comparison of Energy Dissipated during Laboratory Procedures .....	7-18
Figure 7-18 Comparison of Energy Dissipated from Acceleration Histories .....	7-19
Figure 7-19 Comparison of Reinforcement Strain Envelopes for Laboratory Procedures .....	7-21
Figure 7-20 Comparison of Reinforcement Strain Envelopes for Acceleration Histories .....	7-22
Figure 7-21 Damage Indices (New Zealand Loading History) .....	7-28
Figure 7-22 Damage Indices (Berkeley Loading History) .....	7-29
Figure 7-23 Damage Indices (PRESSSS Loading History) .....	7-30
Figure 7-24 Damage Indices (Public Works Research Institute) .....	7-32
Figure 7-25 Damage Indices (Monotonic Loading) .....	7-33
Figure 7-26 Damage Indices (Bi-directional Cycling at Ductility 8) .....	7-33
Figure 7-27 Damage Indices (Unidirectional Loading) .....	7-34
Figure 7-28 Damage Indices (Acceleration History A) .....	7-35
Figure 7-29 Damage Indices (Acceleration History B) .....	7-36
Figure 7-30 Damage Indices (Acceleration History C) .....	7-37
Figure 7-31 Damage Indices (Acceleration History D) .....	7-38
Figure 7-32 Damage Indices (Acceleration History E) .....	7-39
Figure 7-33 Comparison of Park and Ang Damage Index for Tests where Failure Occurred .....	7-41
Figure 7-34 Crack Patterns after Loading to Ductility 2.....	
(a) New Zealand .....	7-44
(b) University of California at Berkeley .....	7-44
(c) PRESSSS .....	7-44
(d) Public Works Research Institute .....	7-44
(e) Monotonic Loading .....	7-44
(f) Bi-directional Cycling at Ductility 8 .....	7-45
(g) Unidirectional Loading .....	7-45
Figure 7-35 Crack Patterns after Loading to Ductility 4.....	
(a) New Zealand .....	7-46
(b) University of California at Berkeley .....	7-46
(c) PRESSSS .....	7-46
(d) Public Works Research Institute .....	7-46

(e) Monotonic Loading .....	7-47
(f) Bi-directional Cycling at Ductility 8 .....	7-47
(g) Unidirectional Loading .....	7-47
Figure 7-36 Comparison of Crack Patterns after Loading to Ductility 6 .....	
(a) New Zealand .....	7-48
(b) University of California at Berkeley .....	7-48
(c) PRESSS .....	7-49
(d) Public Works Research Institute .....	7-49
(e) Monotonic Loading .....	7-49
(f) Bi-directional Cycling at Ductility 8 .....	7-49
(g) Unidirectional Loading .....	7-49
Figure B-1 Comparison of Experimental Data and Modified Takeda Model (Berkeley Loading History) .....	B-1
<b>New Zealand Loading History</b>	
Figure C-1 Test Subassemblage Condition at Ductility 6 (Cycle 2) .....	C-5
Figure C-2 Test Subassemblage Condition at Ductility 10 (Cycle 2) .....	C-5
Figure C-3 Components of Displacement .....	C-6
Figure C-4(a) Flexural Displacement Component .....	C-7
Figure C-4(b) Shear Displacement Component .....	C-7
Figure C-4(c) Rocking Displacement Component .....	C-8
Figure C-5 Components of Energy Dissipation .....	C-8
Figure C-6(a) Moment–Curvature Response (Panel 1) .....	C-9
Figure C-6(b) Moment–Curvature Response (Panel 2) .....	C-10
Figure C-6(c) Moment–Curvature Response (Panel 3) .....	C-10
Figure C-7(a) Reinforcement Strains (Panel 1) .....	C-11
Figure C-7(b) Reinforcement Strains (Panel 2) .....	C-11
Figure C-7(c) Reinforcement Strains (Panel 3) .....	C-12
Figure C-8 Horizontal Beam Elongation .....	C-13
<b>University of California at Berkeley</b>	
Figure C-9 Rupture of Longitudinal Bar .....	C-18
Figure C-10 Components of Displacement .....	C-19
Figure C-11(a) Flexural Displacement Component .....	C-19
Figure C-11(b) Shear Displacement Component .....	C-20

Figure C-11(c) Rocking Displacement Component .....	C-20
Figure C-12 Components of Energy Dissipation .....	C-21
Figure C-13(a) Moment–Curvature Response (Panel 1) .....	C-21
Figure C-13(b) Moment–Curvature Response (Panel 2) .....	C-22
Figure C-13(c) Moment–Curvature Response (Panel 3) .....	C-22
Figure C-14(a) Reinforcement Strains (Panel 1) .....	C-23
Figure C-14(b) Reinforcement Strains (Panel 2) .....	C-23
Figure C-14(c) Reinforcement Strains (Panel 3) .....	C-24
Figure C-15 Horizontal Beam Elongation .....	C-24

### **PRESSS**

Figure C-16 Test Subassemblage Condition at Ductility 6.14 (Cycle 3) .....	C-29
Figure C-17 Components of Displacement .....	C-30
Figure C-18(a) Flexural Displacement Component .....	C-31
Figure C-18(b) Shear Displacement Component .....	C-31
Figure C-18(c) Rocking Displacement Component .....	C-32
Figure C-19 Components of Energy Dissipation .....	C-32
Figure C-20(a) Moment–Curvature Response (Panel 1) .....	C-33
Figure C-20(b) Moment–Curvature Response (Panel 2) .....	C-33
Figure C-20(c) Moment–Curvature Response (Panel 3) .....	C-34
Figure C-21(a) Reinforcement Strains (Panel 1) .....	C-34
Figure C-21(b) Reinforcement Strains (Panel 2) .....	C-35
Figure C-21(c) Reinforcement Strains (Panel 3) .....	C-35
Figure C-22 Horizontal Beam Elongation .....	C-36

### **Public Works Research Institute**

Figure C-23 Test Subassemblage Condition at Ductility 4 (Cycle 10) .....	C-39
Figure C-24 Components of Displacement .....	C-41
Figure C-25(a) Flexural Displacement Component .....	C-41
Figure C-25(b) Shear Displacement Component .....	C-42
Figure C-25(c) Rocking Displacement Component .....	C-42
Figure C-26 Components of Energy Dissipation .....	C-43
Figure C-27(a) Moment–Curvature Response (Panel 1) .....	C-43
Figure C-27(b) Moment–Curvature Response (Panel 2) .....	C-44
Figure C-27(c) Moment–Curvature Response (Panel 3) .....	C-44

Figure C-28(a) Reinforcement Strains (Panel 1) .....	C-45
Figure C-28(b) Reinforcement Strains (Panel 2) .....	C-45
Figure C-28(c) Reinforcement Strains (Panel 3) .....	C-46
Figure C-29 Horizontal Beam Elongation .....	C-46
<b>Monotonic Loading</b>	
Figure C-30 Test Subassembly Condition at Ductility 20 .....	C-50
Figure C-31 Components of Displacement .....	C-51
Figure C-32(a) Flexural Displacement Component .....	C-51
Figure C-32(b) Shear Displacement Component .....	C-52
Figure C-32(c) Rocking Displacement Component .....	C-52
Figure C-33 Components of Energy Dissipation .....	C-53
Figure C-34(a) Moment–Curvature Response (Panel 1) .....	C-53
Figure C-34(b) Moment–Curvature Response (Panel 2) .....	C-54
Figure C-34(c) Moment–Curvature Response (Panel 3) .....	C-54
Figure C-35(a) Reinforcement Strains (Panel 1) .....	C-55
Figure C-35(b) Reinforcement Strains (Panel 2) .....	C-55
Figure C-35(c) Reinforcement Strains (Panel 3) .....	C-56
Figure C-36 Horizontal Beam Elongation .....	C-56
<b>Bi-directional Cycling at Ductility 8</b>	
Figure C-37 Test Subassembly Condition at Ductility 8 (Cycle 6) .....	C-60
Figure C-38 Components of Displacement .....	C-61
Figure C-39(a) Flexural Displacement Component .....	C-61
Figure C-39(b) Shear Displacement Component .....	C-62
Figure C-39(c) Rocking Displacement Component .....	C-62
Figure C-40 Components of Energy Dissipation .....	C-63
Figure C-41(a) Moment–Curvature Response (Panel 1) .....	C-63
Figure C-41(b) Moment–Curvature Response (Panel 2) .....	C-64
Figure C-41(c) Moment–Curvature Response (Panel 3) .....	C-64
Figure C-42(a) Reinforcement Strains (Panel 1) .....	C-65
Figure C-42(b) Reinforcement Strains (Panel 2) .....	C-65
Figure C-42(c) Reinforcement Strains (Panel 3) .....	C-66
Figure C-43 Horizontal Beam Elongation .....	C-66
<b>Unidirectional Loading</b>	

Figure C-44 Spalling of Cover Concrete (Ductility 22) .....	C-70
Figure C-45 Components of Displacement .....	C-71
Figure C-46(a) Flexural Displacement Component .....	C-71
Figure C-46(b) Shear Displacement Component .....	C-72
Figure C-46(c) Rocking Displacement Component .....	C-72
Figure C-47 Components of Energy Dissipation .....	C-73
Figure C-48(a) Moment–Curvature Response (Panel 1) .....	C-73
Figure C-48(b) Moment–Curvature Response (Panel 2) .....	C-74
Figure C-48(c) Moment–Curvature Response (Panel 3) .....	C-74
Figure C-49(a) Reinforcement Strains (Panel 1) .....	C-75
Figure C-49(b) Reinforcement Strains (Panel 2) .....	C-75
Figure C-49(c) Reinforcement Strains (Panel 3) .....	C-76
Figure C-50 Horizontal Beam Elongation .....	C-76
<b>Acceleration History A</b>	
Figure C-51 Test Subassemblage Condition at Conclusion of Acceleration History A .....	C-79
Figure C-52 Components of Displacement .....	C-80
Figure C-53(a) Flexural Displacement Component .....	C-81
Figure C-53(b) Shear Displacement Component .....	C-81
Figure C-53(c) Rocking Displacement Component .....	C-82
Figure C-54 Components of Energy Dissipation .....	C-82
Figure C-55(a) Moment–Curvature Response (Panel 1) .....	C-83
Figure C-55(b) Moment–Curvature Response (Panel 2) .....	C-83
Figure C-55(c) Moment–Curvature Response (Panel 3) .....	C-84
Figure C-55(a) Reinforcement Strains (Panel 1) .....	C-84
Figure C-56(b) Reinforcement Strains (Panel 2) .....	C-85
Figure C-56(c) Reinforcement Strains (Panel 3) .....	C-85
Figure C-57 Horizontal Beam Elongation .....	C-86
<b>Acceleration History B</b>	
Figure C-58 Test Subassemblage Condition at Conclusion of Acceleration History B .....	C-88
Figure C-59 Components of Displacement .....	C-89
Figure C-60(a) Flexural Displacement Component .....	C-90

Figure C-60(b) Shear Displacement Component .....	C-90
Figure C-60(c) Rocking Displacement Component .....	C-91
Figure C-61 Components of Energy Dissipation .....	C-91
Figure C-62(a) Moment–Curvature Response (Panel 1) .....	C-92
Figure C-62(b) Moment–Curvature Response (Panel 2) .....	C-92
Figure C-62(c) Moment–Curvature Response (Panel 3) .....	C-93
Figure C-63(a) Reinforcement Strains (Panel 1) .....	C-93
Figure C-63(b) Reinforcement Strains (Panel 2) .....	C-94
Figure C-63(c) Reinforcement Strains (Panel 3) .....	C-94
Figure C-64 Horizontal Beam Elongation .....	C-95
<b>Acceleration History C</b>	
Figure C-65 Test Subassemblage Condition at Conclusion of Acceleration History C .....	C-98
Figure C-66 Components of Displacement .....	C-99
Figure C-67(a) Flexural Displacement Component .....	C-99
Figure C-67(b) Shear Displacement Component .....	C-100
Figure C-67(c) Rocking Displacement Component .....	C-100
Figure C-68 Components of Energy Dissipation .....	C-101
Figure C-69(a) Moment–Curvature Response (Panel 1) .....	C-101
Figure C-69(b) Moment–Curvature Response (Panel 2) .....	C-102
Figure C-69(c) Moment–Curvature Response (Panel 3) .....	C-102
Figure C-70(a) Reinforcement Strains (Panel 1) .....	C-103
Figure C-70(b) Reinforcement Strains (Panel 2) .....	C-103
Figure C-70(c) Reinforcement Strains (Panel 3) .....	C-104
Figure C-71 Horizontal Beam Elongation .....	C-104
<b>Acceleration History D</b>	
Figure C-72 Test Subassemblage Condition After Application of Maximum Displacement .....	C-107
Figure C-73 Components of Displacement .....	C-107
Figure C-74(a) Flexural Displacement Component .....	C-108
Figure C-74(b) Shear Displacement Component .....	C-108
Figure C-74(c) Rocking Displacement Component .....	C-109
Figure C-75 Components of Energy Dissipation .....	C-109

Figure C-76(a) Moment–Curvature Response (Panel 1) .....	C-110
Figure C-76(b) Moment–Curvature Response (Panel 2) .....	C-110
Figure C-76(c) Moment–Curvature Response (Panel 3) .....	C-111
Figure C-77(a) Reinforcement Strains (Panel 1) .....	C-111
Figure C-77(b) Reinforcement Strains (Panel 2) .....	C-112
Figure C-77(c) Reinforcement Strains (Panel 3) .....	C-112
Figure C-78 Horizontal Beam Elongation .....	C-113
<b>Acceleration History E</b>	
Figure C-79 Test Subassemblage Condition at Conclusion of Acceleration History E .....	C-116
Figure C-80 Components of Displacement .....	C-116
Figure C-81(a) Flexural Displacement Component .....	C-117
Figure C-81(b) Shear Displacement Component .....	C-117
Figure C-81(c) Rocking Displacement Component .....	C-118
Figure C-82 Components of Energy Dissipation .....	C-118
Figure C-83(a) Moment–Curvature Response (Panel 1) .....	C-119
Figure C-83(b) Moment–Curvature Response (Panel 2) .....	C-119
Figure C-83(c) Moment–Curvature Response (Panel 3) .....	C-120
Figure C-84(a) Reinforcement Strains (Panel 1) .....	C-120
Figure C-84(b) Reinforcement Strains (Panel 2) .....	C-121
Figure C-84(c) Reinforcement Strains (Panel 3) .....	C-121
Figure C-85 Horizontal Beam Elongation .....	C-122

## List of Tables

Table 3-1 Nominal and Ideal Material Properties .....	3-1
Table 3-2 Park and Ang Damage Classification Levels .....	3-9
Table 3-3 Bracci et al. Damage Classification Levels .....	3-12
Table 4-1 Scaling Factors .....	4-6
Table 4-2 Change in Confinement Safety Factor due to Scaling Constraints .....	4-9
Table 4-3 Concrete Mix Design .....	4-13
Table 4-4 Chemical Analysis of Longitudinal Reinforcement .....	4-14
Table 5-1 Summary of Frame Properties .....	5-3
Table 5-2 Earthquakes Records Selected for Generating Acceleration Histories ...	5-11
Table 5-3 Summary of Five Earthquake Histories .....	5-12
Table 5-4 Predicted Damage Indices (Acceleration History A) .....	5-15
Table 5-5 Predicted Damage Indices (Acceleration History B) .....	5-20
Table 5-6 Predicted Damage Indices (Acceleration History C) .....	5-22
Table 5-7 Predicted Damage Indices (Acceleration History D) .....	5-25
Table 5-8 Predicted Damage Indices (Earthquake History E) .....	5-27
Table 6-1 Summary of Earthquake Records' Scale Factors .....	6-10
Table 7-1 Comparison of Predicted and Actual Damage Indices (At Conclusion of Test) .....	7-25
Table 7-2 Criteria for Damage Levels .....	7-27
Table 7-3 Collation of Intermediate Index Values with Observed Damage Levels	7-27
Table 7-4 Criteria for Damage Levels (Based on Testing Reported Herein) .....	7-42
Table 7-5 Comparison of Crack Widths after Loading to Ductility 2 .....	7-45
Table 7-6 Comparison of Crack Widths after Loading to Ductility 4 .....	7-48
Table 7-7 Comparison of Crack Widths after Loading to Ductility 6 .....	7-50

## List of Symbols

$A_b$	Area of individual bar
$A_g$	Area of gross section
$A_p$	Area associated with prototype
$A_s$	Area of non-prestressed tension reinforcement
$A_T$	Area associated with test unit
$A_{te}$	Area of one leg of stirrup-tie
$A_v$	Area of shear reinforcement
$a$	Depth of equivalent rectangular stress block
	Calibration factor (Banon and Veneziano damage index)
$b$	Width of compression face of member
	Calibration factor (Banon and Veneziano damage index)
$b_w$	Web width
$C$	Compression Force
$D$	Damage index
$D_d$	Deformation damage (Bracci et al. damage index)
$D_p$	Damage potential (Bracci et al. damage index)
$D_s$	Strength damage (Bracci et al. damage index)
$D_1$	Damage parameter (Bracci et al. damage index)
$D_2$	Damage parameter (Bracci et al. damage index)
$d$	Distance from extreme compression fibre to centroid of tension reinforcement
$d_b$	Nominal diameter of bar
$d_{b_p}$	Nominal diameter of bar in prototype unit
$d_{b_T}$	Nominal diameter of bar in test unit
$d_1$	Damage parameter (Banon and Veneziano damage index)
$d_2$	Damage parameter (Banon and Veneziano damage index)
$d_1^*$	Modified damage parameter (Banon and Veneziano damage index)
$d_2^*$	Modified damage parameter (Banon and Veneziano damage index)

$dE$	Incremental dissipated hysteresis energy
$d_m$	Maximum displacement (Modified Takeda hysteresis rule)
$d_p$	Strain hardening displacement (Modified Takeda hysteresis rule)
$d_y$	Yield displacement (Modified Takeda Hysteresis rule)
$E_c$	Modulus of elasticity of concrete
$E_h$	Dissipated Energy
$E_s$	Modulus of elasticity of steel
$E_{sec}$	Secant modulus of confined concrete at peak stress
$F_i$	Force associated with the nominal ideal moment
$F_{max}$	Maximum force measured during testing
$F_n$	Force associated with the nominal design moment
$F_p$	Force associated with prototype unit
$F_T$	Force associated with test unit
$F_y$	Force associated with the yield moment
$f$	Scale factor
$f_c$	Compressive strength of concrete
$f'_c$	Specified compressive strength of concrete
$f'_{cc}$	Compressive strength (peak stress) of confined concrete
$f'_{co}$	Compressive strength of unconfined concrete
$f_{new}$	New concrete stress on reloading at strain of $\epsilon_{un}$
$f_{re}$	Return point stress on monotonic stress-strain curve
$f_{ro}$	Concrete stress at reloading reversal
$f_{sh,1}$	Engineering stress at strain $\epsilon_{sh,1}$
$f_{su}$	Ultimate stress in engineering co-ordinate system
$f'_t$	Tensile strength of concrete
$f_{un}$	Reversal (unloading) stress in concrete model
$f_y$	Lower characteristic yield strength of longitudinal reinforcement

---

$f_{yt}$	Lower characteristic yield strength of transverse reinforcement
$H$	Height of single bay portal frame
$h$	Total depth of beam
$I$	Moment of inertia
$k_{max}$	Stiffness at maximum measured moment from testing
$k_o$	Initial stiffness
$k_u$	Unloading stiffness
$k_{ult}$	Stiffness at maximum moment recorded under monotonic loading
$k_y$	Stiffness at yield displacement
$L_p$	Length associated with prototype unit
$L_T$	Length associated with test unit
$l$	Distance from face of concrete pedestal to actuator
$l_p$	Length of plastic hinge zone
$M_{max}$	Maximum moment recorded during testing
$M_n$	Nominal design moment
$M_{np}$	Nominal flexural strength of prototype section
$M_{nT}$	Nominal flexural strength of test unit section
$M_p$	Moment associated with prototype
$M_T$	Moment associated with test unit
$M_u$	Maximum moment recorded under monotonic loading
$M_y$	Yield moment
$m$	Power function (Cosenza et al. damage index)
$n$	Ductility level
$n_o$	Normalised axial stress
$P_e$	Axial load
$r$	Flexural bilinear factor
$S_{sd}$	Strength deterioration factor
$s$	Spacing of stirrups (measured centre-to-centre)
$T$	Tension force

$V_c$	Shear strength associated with concrete
$V_n$	Nominal shear force
$V_P$	Shear strength of prototype unit
$V_T$	Shear strength of test unit
$v_c$	Nominal shear stress provided by concrete mechanisms
$v_{jo\ int}$	Vertical displacement at midpoint of critical beam in Ruaumoko analysis due to vertical displacement of beam-column joint
$v_{node}$	Vertical displacement at midpoint of critical beam in Ruaumoko analysis due to vertical displacement of midpoint
$v_{rot}$	Vertical displacement at midpoint of critical beam in Ruaumoko analysis due to rotation of beam-column joint
$v_{total}$	Total vertical displacement at midpoint of critical beam in Ruaumoko analysis
$\alpha$	Coefficient associated with mass (Rayleigh damping) Unloading stiffness factor (Modified Takeda hysteresis rule)
$\beta$	Non-dimensional parameter (Park and Ang damage index) Coefficient associated with stiffness (Rayleigh damping) Reloading stiffness factor (Modified Takeda hysteresis rule)
$\Delta$	Horizontal deflection of portal frame
$\Delta M$	Loss of strength due to load cycle
$\delta$	Damage parameter (Cosenza et al. damage index)
$\delta_{max}$	Maximum recorded displacement
$\delta_p$	Plastic deformation
$\delta_r$	Deformation at actuator due to rocking of the beam on its base
$\delta_u$	Damage parameter relating to failure (Cosenza et al. damage index)
$\delta_{ult}$	Ultimate displacement established from monotonic loading
$\delta_y$	Yield displacement Damage parameter relating to undamaged state (Cosenza et al damage index)
$\delta'_y$	First yield displacement
$\varepsilon_c$	Longitudinal concrete strain

---

$\varepsilon_{cc}$	Strain at maximum concrete stress
$\varepsilon_{co}$	Strain at maximum stress of unconfined concrete
$\varepsilon_{cu}$	Ultimate concrete compressive strain, defined as strain at first hoop fracture
$\varepsilon_{pl}$	Plastic strain in concrete model
$\varepsilon_{re}$	Return point strain on monotonic stress-strain curve
$\varepsilon_{ro}$	Concrete strain at reloading reversal
$\varepsilon_{sh}$	Engineering strain at initiation of strain-hardening region
$\varepsilon_{sh,1}$	Arbitrary engineering strain in strain-hardening region of tension monotonic curve
$\varepsilon_{sp}$	Strain at which cover concrete is considered to have completely spalled and ceases to carry any stress.
$\varepsilon_{su}$	Ultimate strain in engineering co-ordinate system
$\varepsilon_t$	Tensile rupture strain on concrete
$\varepsilon_{un}$	Reversal (unloading) strain in concrete model
$\varepsilon_y$	Yield strain in engineering co-ordinate system
$\phi_{max}$	Curvature associated with the maximum-recorded moment from testing
$\phi_{ult}$	Curvature associated with the maximum moment measured during monotonic loading
$\phi_y$	Curvature associated with the yield moment
$\mu$	Displacement ductility
$\mu_u$	Ultimate displacement ductility
$\theta$	Storey drift
$\theta_p$	Plastic rotation
$\rho_t$	Longitudinal steel ratio
$\rho_s$	Confinement ratio
$\rho_w$	Ratio of tension reinforcement
$\sigma_y$	Yield Stress
$\sigma_p$	Stress associated with prototype unit

$\sigma_T$  Stress associated with test unit

## 1.0 Introduction

If a structure is subjected to an earthquake ground motion its response depends upon the attributes of the earthquake ground motion and the structure's dynamic and nonlinear characteristics, which includes the hysteresis form and strength degradation properties. However, it is not possible to predict in advance the equivalent force-time history that a building may be subjected to because of the randomness inherent in the earthquake ground motion.

To overcome this difficulty, researchers commonly adopt quasi-static cyclic loading histories of increasing amplitude and continue testing until the subassembly suffers significant strength loss. This enables the likely seismic performance of structures and their components to be determined. Parameters such as the curvature ductility capacity of plastic hinges and the influence of joint and member shear deformations are calculated from test data, from which the available structural capacity of subassemblies and structural forms is derived. To establish whether an acceptable response is achieved, these conclusions need to be compared with the predicted response corresponding to a design level earthquake.

Presently researchers are showing considerable interest in displacement-based methods of structural design, proposing that these methods lead to more rational, safer, and cost-effective designs. For these reasons it has been suggested that these methods be introduced in combination with the next release of the New Zealand Loadings Code. One of the key attributes of designing structures using displacement-based methods is the selection of a target ultimate displacement. This decision is based on the performance of laboratory subassemblies. However, the simulated loading history applied to subassemblies in the laboratory will be different from that arising when the structure is shaken during an earthquake. Hence the influence which the laboratory load history has on the resultant conclusions warrants careful consideration.

Compounding this issue is that the applied loading history often varies between experimental studies conducted at research institutions throughout the world. It is

desirable to be able to compare experimental results from testing using different loading histories, and also compare the demands placed on a structure or structural component from these different tests with the demands exerted on them by a design level earthquake.

This report attempts to address the aforementioned problems. A typical structural member from a ten-storey building (designed to the New Zealand Standard for the Design of Concrete Structures) was subjected to a range of standard tests and displacement sequences that could be expected if the structure was built. Performance was measured through several means, with the principal means of comparison through the calculation of five damage indices that were then compared to the observed damage during testing.

This report reviews common load histories used throughout the world in the testing of concrete subassemblies and previous studies that have attempted to compare experimental results derived from testing using different loading histories. This is presented in Chapter 2.0. Chapter 3.0 provides background information on concepts that enabled the performance of each test specimen to be established. Twelve nominally identical reinforced concrete beams were subjected to twelve different loading histories to establish their ultimate displacement capacity and the relationship between the adopted loading history and measured ultimate displacement. These twelve loading histories consisted of seven laboratory procedures and five displacement sequences simulating the seismic response of a ten-storey building. Chapter 4.0 details the design of the test subassemblage, the methods of construction, and the experimental procedures followed. Chapter 5.0 reports on the analytical modelling conducted to simulate the seismic response of a ten-storey building and Chapter 6.0 summarises the twelve loading histories that were applied in the experimental component of this project. Chapter 7.0 compares results derived from experimental data recorded while testing using the twelve loading histories and lastly, Chapter 8.0 presents the conclusions established from the literature review undertaken, the analytical modelling, and the derived experimental results.

## 2.0 Literature Review

A comprehensive literature review was conducted as part of this report. Section 2.1 summarises loading histories applied at various research institutions throughout the world. Section 2.2 reviews past experimental studies that have attempted to quantify the influence of the applied loading regime. Section 2.3 details previous attempts to compare experimental results derived from testing using different loading histories. Section 2.4 reviews various constitutive models for concrete and reinforcing steel under monotonic and cyclic loading. Finally, Section 2.5 summarises principal failure mechanisms associated with reinforced concrete members undergoing seismic excitation.

### 2.1 Loading Histories

In 1989, Park (1989) from the University of Canterbury, presented a paper on the evaluation of ductility of structures and structural assemblages from laboratory testing. New Zealand researchers, when establishing the available ductility of a structural subassemblage, have adopted the loading procedure presented in the aforementioned paper and shown in Figure 2-1. As Park's recommendations have been adopted in New Zealand, it follows that this work forms the benchmark for the current proposal. Consequently, in the remainder of this section these recommendations are correlated with recent procedures used internationally, with Park's recommendations hereafter referred to as the New Zealand loading history. Section 2.1.1 compares the New Zealand loading history with loading histories applied at research institutions throughout the world and Section 2.1.2 examines the

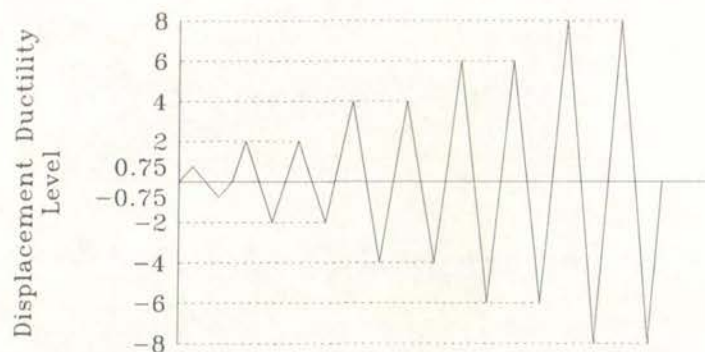


Figure 2-1 Loading History Applied by Park (1989)

affect of the applied loading rate.

### 2.1.1 Comparison of Loading Histories

A review of recently published literature from the United States reveals that the procedures adopted in New Zealand have not been widely employed elsewhere. There are numerous examples of projects published through the United States' 'National Centre for Earthquake Engineering Research' (NCEER) that apply loading histories different to the New Zealand loading history. These include projects by Mander et al. (1996a) and Mander et al. (1996b) from the State University of New York at Buffalo, Wehbe et al. (1996) from the University of Nevada at Reno, and Mosalam et al. (1997a) from Cornell University at Ithaca, New York. Also, a review of seismic structural research reports published recently by NCEER yields no reference to the New Zealand loading history.

One of the more prominent earthquake engineering journals in the United States is 'Earthquake Spectra – Professional Journal of the Earthquake Engineering Research Institute'. Again there are numerous examples of recent projects where the loading histories differ from the New Zealand loading history. Examples include Beres et al. (1996) from Cornell University and Lehigh University at Bethlehem, Pennsylvania, Masri and Geol (1996) from the University of Michigan at Ann Arbor, and Saadatmanesh et al. (1997) from the University of Arizona at Tucson.

Notably, the aforementioned projects come from a wide distribution of research institutions throughout the United States, and the absence of reference to the New Zealand loading history indicating that in general there is little awareness or regard for this method. Possibly most telling is that in February 1996, 'Earthquake Spectra' contained a theme issue on experimental methods. In this issue, Krawinkler (1996) from Stanford University, California published "Cyclic Loading Histories for Seismic Experimentation on Structural Components". Krawinkler discussed the selection of suitable loading histories for laboratory testing based on the number and magnitude of inelastic excursions. However, as with the aforementioned authors, Krawinkler made no reference to the New Zealand loading history.

Shepherd (1996) from the University of California at Irvine also contributed to the previously mentioned theme issue. Shepherd reported on the development of guidelines to ensure that experimental investigations are representative of the structural performance of mixed material systems under seismic action. Shepherd discussed the standardisation of testing procedures and as an example presented the "sequential phased displacement test procedure" developed in 1987 by the Joint Technical Coordinating Committee on Masonry Research (TCCMAR).

Many independent projects have applied sequential phased test histories to investigate strength degradation and loss of stiffness in connections of varying types. Durrani and Diaz (1992) from Rice University in Texas applied a loading routine that consisted of several cycles of increasing lateral displacements to determine the effect of fibre-reinforcement on the seismic performance of slab-column connections. Stiffness and strength degradation of the specimens were evaluated through small displacement cycles of 0.75% drift included between major displacement cycles. Emam et al. (1997) from Cairo University, Egypt also investigated slab-column connections by subjecting four interior slab-column connections to simulated seismic loading to determine the influence of high-strength concrete. Raffaele and Wight (1995) from the University of Michigan in Ann Arbor subjected four reinforced concrete eccentric beam-column connections to cyclic loading to investigate the effects of torsion. Dimitrijevic (1992) from Institute IMS in Belgrade applied cyclic loading to test sub-assemblages with prestress connections and concluded that such joints had the necessary ductility capacity under seismic loading. Soudki et al. (1995) from Queens University and the University of Manitoba applied cyclic loading to precast concrete shear wall panels and presented design recommendations for mild steel connections of precast concrete walls in seismic zones.

Other independent projects have applied sequential phased test histories to investigate various structural components. These include Saatcioglu and Ozcebe (1989) from the University of Toronto, who investigated the influence of axial loading, shear and confinement reinforcement, and the deformation path on the response of reinforced concrete columns. Also, Mosalam et al. (1997b) from the University of California at

Berkeley and Cornell University, Ithaca investigated the response of infilled frames so that a hysteresis model for infilled frames under seismic loading could be developed.

The aforementioned independent examples made use of loading histories that were different to the New Zealand loading history. Other researchers that have applied contrasting loading histories include Ghee et al. (1989) from the University of Canterbury, Chai et al. (1991) from the University of California at San Diego, and Tsonos et al. (1992) from Aristotle University in Thessaloniki, Greece.

Of particular note is the recent coordinated TCCMAR and PRESSS research studies, which have both involved a considerable number of institutions and employed a common sequentially phased loading history. As shown in Figure 2-2, the loading regime in the PRESSS programme is different to the New Zealand loading history. Hence, from the preceding review of loading histories applied in research institutions throughout the world, it has been established that the loading procedure adopted in New Zealand differs from that commonly used elsewhere.

### 2.1.2 Loading Rate

Several papers from the Earthquake Spectra theme issue on experimental methods discussed the issue of loading rate. Abrams (1996) from the University of Illinois at Urbana-Champaign observed that damage was much more prominent at a slower loading rate because of increased crack propagation. Abrams concluded, "gaps will continue to exist between data from laboratory experiments and real dynamic response of buildings because of differences in load application at static rates." Leon

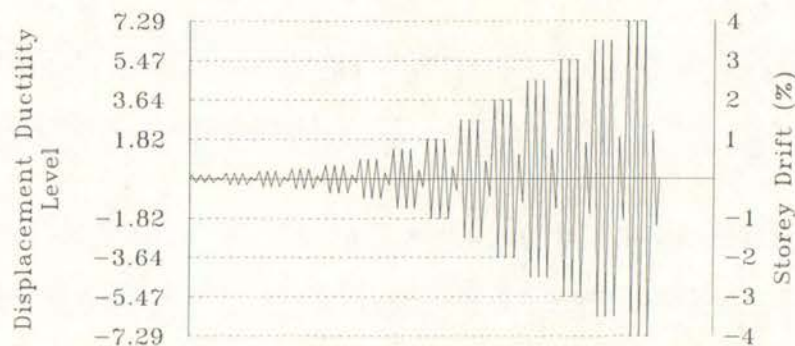


Figure 2-2 PRESSS Loading History

and Deierlein (1996) from Georgia Tech in Atlanta and Cornell University respectively discussed the evolution of quasi-static testing and noted that loading rates are not usually rigorously controlled during testing. Leon and Deierlein also noted that quasi-static testing could provide misleading results if strain-rate effects under seismic loadings are significant. Finally Shepherd from the University of California at Irvine made several recommendations regarding loading protocols for use when testing low-rise structures.

Chung and Shah (1989) subjected assemblages to a total of four different load histories to establish the influence of the loading rate on variables such as anchorage bond, stiffness degradation, energy dissipation, and failure modes. It was observed that diagonal shear cracks emerge at an earlier stage of loading under fast-rate loading but that the crack pattern was more widely distributed under slow-rate loading. It was established that while fast-rate specimens had larger ultimate loads than slow-rate specimens, fast-rate specimens lost strength at a lower ductility ratio. However, Chung and Shah established that stiffness degradation and energy dissipation of fast and slow-rate loading specimens were dependent on other variables such as the spacing of shear reinforcement.

The preceding papers clearly show that the rate of loading can influence experimental results. However this project focuses only on the influence of loading history and hence in-depth investigation of this variable will not be conducted.

## **2.2 Effect of Loading History on Experimental Results**

In their report on the evolution of quasi-static testing, Leon and Deierlein (1996) concluded that the selected load history could have a significant effect on experimental results. This was evident in the results from tests where a progressive increase in deformation levels was applied in contrast with large deformations being followed by smaller cycles. A progressive increase in deformation level led to stiffness degradation at large displacements that was inconsistent with results from testing using a loading history where large deformations were followed by smaller cycles.

Several researchers have considered the use of multiple loading histories. Lefas and Kotsovos (1990) from the Imperial College of Science and Technology, London conducted studies on reinforced concrete shear walls to determine the effect of using different loading histories and repair methods. Four identical wall specimens were subjected to various loading histories. Three walls were able to be repaired and were again subjected to various loading histories. Comparisons were made between shear walls tested using monotonic loading and those tested using cyclic loading. Lefas and Kotsovos concluded that the strength and deformational response of the original specimens were independent of the cyclic loading regime. Of the repaired walls, the wall subjected to monotonic loading had greater load capacity than the walls subjected to cyclic loading. However, it was found that there was very little difference between the results from different cyclic loading regimes. Lefas and Kotsovos established that under cyclic loading, increasing the maximum displacement of the loading cycle increased the stiffness deterioration and that the amount of energy dissipation increased considerably with the ductility level of the cyclic loading.

Hwang and Scribner (1984) from Sargent and Lundy Engineers and the University of Illinois conducted research on reinforced concrete beams to determine the effect of variations in loading histories. Hwang and Scribner concluded that while the size of the displacements was closely related to strength and stiffness degradation, the actual sequence in which large and small displacements were applied did not have a significant effect on the results. Hwang and Scribner also concluded that any estimation of the energy dissipation capacity of a member must take into account the displacement history.

Tomazevic and Lutman (1996) from the National Building and Civil Engineering Institution in Slovenia conducted 32 tests on identically reinforced masonry walls under four contrasting loading histories: monotonic loading, two different cyclic loading histories, and a simulated response of a masonry building during earthquake excitation. Experimental results aided in the development of correlation factors between the monotonic and cyclic hysteresis envelope curves, as well as stiffness and strength degradation parameters.

Tomazevic and Lutman referred to earlier work published by Tomazevic et al. (1996) regarding the influence of different loading histories on test results. Tomazevic et al. noted that higher resistance and larger ultimate displacements were measured in the case of monotonic loading than in the case of cyclic loading histories of any type. Tomazevic et al. observed that strength and stiffness degradation and deterioration took place when the walls were subjected to repeated cyclic lateral load reversals. Hence, a significantly lower resisting force was measured when cyclic loading was applied than for the corresponding displacement when testing using monotonic loading. It was also noted that the maximum lateral resistance attained in the case of monotonic loading was much greater than corresponding values obtained by cyclic loading. Therefore it can be stated that at the same lateral displacement amplitude, actual stiffness degradation was less severe in the case of monotonic loading than in the case of cyclic loading.

Studies on the influence of loading history have also been conducted in Japan. Kinugasa and Nomura (1992) from the Science University of Tokyo subjected five nominally identical beam units to five different cyclic load histories. Kinugasa and Nomura proposed a new failure mode based on the accumulation of strain in the hinge zone as the member dissipated energy. It was concluded that the strain accumulation behaviour of a hinge zone was closely related to the type of loading history. Shimazu and Mollick (1991) from Hiroshima University subjected frame structures to four different loading histories and noted that "the hysteretic response characteristics are different under different lateral loading programmes in respect of strength deterioration."

In 1994, Kawashima (1994), of the Public Works Research Institute in Japan, published a paper outlining the seismic design of bridges. In his paper Kawashima noted that in reinforced concrete piers, the rupture of main reinforcement due to inelastic load reversals was strongly related to low cycle fatigue of the reinforcement. Kawashima concluded that the number of load reversals at each ductility level was an important factor for controlling damage levels and that damage that developed in the shake table test was much smaller than that developed in the step-wise increasing loading test.

Kunnath et al. (1997) from the University of Central Florida and the National Institute of Standards and Technology in Maryland subjected twelve identical small-scale bridge columns to different pseudo-static displacement histories representing both benchmark tests and predicted earthquake displacement records. Among other objectives this testing was conducted to determine whether the energy capacity of a member was dependent or independent of the applied load history. However, conclusions made regarding damage models for bridge columns are of only limited relevance in the study of reinforced concrete buildings. Notably, there was a total absence of reference to typically adopted load histories worldwide, and while it was determined that the energy capacity of a member at failure is strongly path (history) dependent, no conclusions were made about the relevance of particular loading regimes.

### **2.3 Energy Concepts**

In his paper on the evaluation of ductility of structures and structural assemblages from laboratory testing, Park presented a thorough discussion of the issues associated with the determination of structural ductility demand and capacity. Park noted the need for agreement regarding definitions of yield and ultimate displacement so that performance obtained from analytical and experimental investigations can be properly assessed and compared. In the past, researchers have used a range of displacement histories as well as various definitions of yield and ultimate deformation. This has made the comparison of results from different investigations difficult. To overcome this difficulty researchers have proposed using energy concepts as a means of comparing experimental studies. For instance, Tomazevic and Lutman used the amount of input energy (defined as the actuator work done to deform the specimens during the test) applied during testing of masonry walls to correlate the response of monotonic loading with cyclic loading.

In the Earthquake Spectra theme issue on experimental methods discussed in Section 2.1.1, Krawinkler stated that cumulative damage concepts have to be utilised to assess performance and that loading histories in experiments must account for the history dependence of seismic performance. Krawinkler observed that the level of damage

depended not only on the maximum deformation, but also on the history of deformations that the component undergoes before and after the occurrence of the maximum deformation. The number of inelastic excursions and the magnitude of each excursion were found to be dependent on, among other variables, the period of the structure. In his paper Krawinkler made recommendations, taking into account the period of the structure, regarding the number of inelastic excursions in loading histories.

Exercises have also been conducted to correlate the performance of reinforced concrete beams with contrasting detailing and tested by different researchers using a diverse range of loading regimes. For instance, Gosain et al. (1977) compared a number of tests reported in the literature and established a 'work index'. The 'work index' was a measure of the energy absorbed at the hinging region during the loading history and accounted for the severity of the loading. Gosain et al. developed their 'work index' taking into account the member geometry and strength, but not the actual load history. As was reported earlier, Hwang and Scribner concluded that any estimation of the energy dissipation capacity of a member must take into account the displacement history. To obtain a more accurate measure of member response to cyclic loading, Darwin and Nmai (1986) extended Gosain's research by establishing an 'energy dissipation index' for different structural details that took into account the influence of different loading histories.

Fang et al. (1994) used the aforementioned reports and a study by Scribner and Wight (1980) as a basis for an investigation of the strength and ductility of short high-strength concrete ( $\geq 60$  MPa) beams with low flexural reinforcement ratios. Fang et al. considered a total of seven loading histories. It was concluded that the degradation in strength and stiffness varied with the type of loading history applied to the specimen and that the type of loading history influenced the energy dissipation characteristics of the subassemblies. By correlation with the works discussed previously it was concluded that "high-strength concrete short beams exhibited better displacement ductility and smaller strength degradation than those of normal strength concrete beams under cyclic loads."

## 2.4 Constitutive Models

In the design of reinforced concrete frames under seismic loading, correct detailing of the plastic hinge zones is critical in ensuring stability. Theoretical moment-curvature analysis for reinforced concrete frames provides an indication of the available flexural strength and ductility. However, before a moment-curvature analysis can be conducted, the stress-strain behaviour of concrete and steel under cyclic loading must be known. Section 2.4.1 and Section 2.4.2 detail models developed in New Zealand to predict the behaviour of concrete and reinforcing steel respectively under monotonic and cyclic loading. Models developed in other countries are also briefly reported on.

### 2.4.1 Concrete

In many cases the ultimate compression strain of unconfined concrete is inadequate to allow the structure to achieve the design level of ductility without extensive spalling of the cover concrete. Therefore, failure may occur unless adequate transverse reinforcement is provided to confine the compressed concrete within the core region, and to prevent buckling of the longitudinal compression reinforcement. Hence, this report only details models for confined concrete under monotonic or cyclic loading. These monotonic and cyclic models are presented in Section 2.4.1.1 and Section 2.4.1.2 respectively.

#### 2.4.1.1 Monotonic Behaviour

Behaviour of concrete under monotonic loading was investigated because it has been found that this forms the basis of cyclic models. For example, Karsan and Jirsa (1969), concluded that the monotonic loading stress-strain curve formed an envelope or skeleton curve to the cyclic loading stress-strain curve.

Figure 2-3 illustrates the stress-strain model proposed by Mander et al. (1988) to define the behaviour of confined concrete under monotonic compression loading. Mander et al. based their model on a unified stress-strain approach and the model was applicable to concrete confined by either circular or rectangular shaped transverse

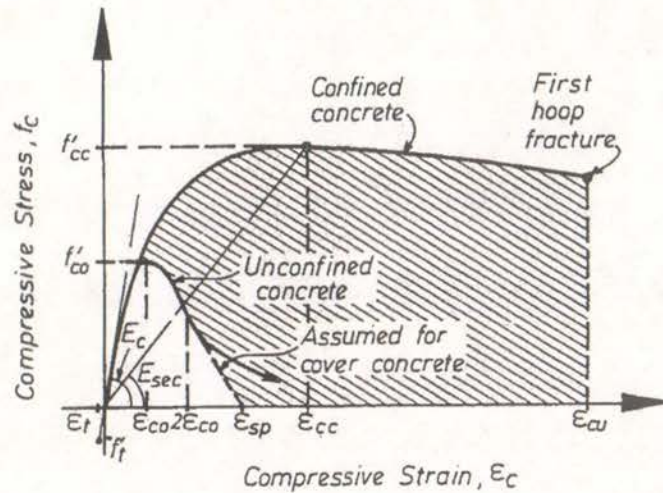


Figure 2-3 Stress-Strain Model for Monotonic Loading (Mander et al. 1988)

reinforcement. Under tensile loading, and as long as the tensile strength of the concrete was not exceeded, Mander et al. proposed that a linear stress-strain relation be assumed.

#### 2.4.1.2 Cyclic Behaviour

Mander et al. (1988) also presented a stress-strain model for concrete subjected to uniaxial compressive loadings and confined by transverse reinforcement. Features of the model included an ability to be applied to either rectangular or circular sections, as well as accounting for strain rate effects.

Mander et al. established rules for unloading from both the compressive or tensile section of the skeleton stress-strain curve. Experimental curves were used to calibrate the various coefficients. As demonstrated in Figure 2-4, reloading was assumed to follow a linear stress-strain relation between  $\epsilon_{ro}$  and  $\epsilon_{un}$  to a revised stress magnitude to account for cyclic degradation.

Numerous researchers have reported that the strength and stiffness of concrete increase with strain rate. Mander et al. established dynamic magnification factors that modified the strength, stiffness, and strain at peak stress found through quasi-static

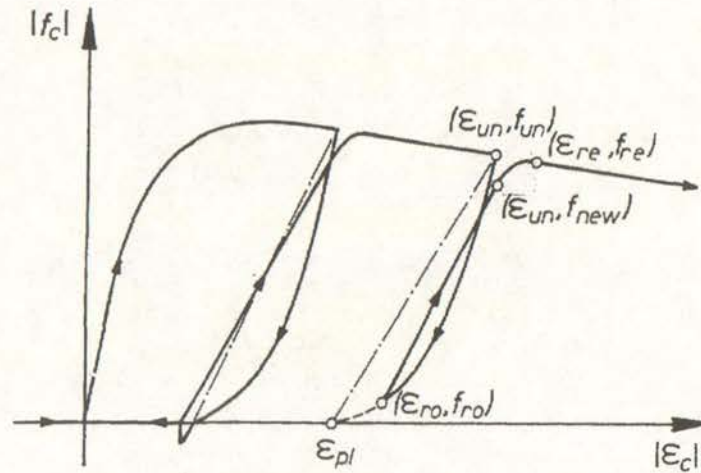


Figure 2-4 Concrete Stress-Strain Curve with Unloading and Reloading Branches  
(Mander et al. 1988)

testing. These relationships were based on experimental results from previous investigations.

Other models include those proposed by Otter and Naaman (1989), Martinez-Rueda and Elnashai (1997), and the Comité Euro-International Du Béton (1996). Otter and Naaman developed a model to predict the stress-strain behaviour of concrete composites under random cyclic compressive loadings and utilised the enveloped unloading strain as an index of load history. Importantly, this model could be applied to the prediction of energy dissipation and fatigue life as well as the nonlinear analysis of earthquake-resistant structures.

Martinez-Rueda and Elnashai developed a uniaxial cyclic model for confined and unconfined concrete. Martinez-Rueda and Elnashai based their model on that established by Mander et al. but proposed new rules for the cyclic degradation of strength, inelastic strain and the shape of the unloading branches.

The Comité Euro-International Du Béton (CEB) formed a group to study non-linear analysis of structures. As a result, a new non-local microplane model for concrete under three-dimensional cyclic conditions was postulated. The model also accounted for strain softening and the rate of deformation. The model represented a constitutive model where the material was characterised by a relation between stress and strain components on planes of various orientations. These planes represented the weak

planes in the microstructure; for example, contact layers between aggregate pieces in concrete. Numerical examples were then provided showing the affect of different deformation rates and comparing the model to experimental behaviour.

#### 2.4.2 Reinforcement Steel

As with concrete, the behaviour of reinforcing steel under monotonic loading forms the basis of cyclic models. Section 2.4.2.1 summarises a model of the behaviour of reinforcing steel under monotonic loading and Section 2.4.2.2 details models that predict the behaviour of reinforcing steel under cyclic loading.

##### 2.4.2.1 Monotonic Behaviour

As discussed in Section 2.4.2.2, Dodd and Restrepo (1995) have published a report detailing a model for predicting the behaviour of reinforcing steel under cyclic loading. Information on the monotonic stress-strain behaviour was used to establish the cyclic model.

The behaviour of mild steel under tensile loading presented in Figure 2-5 is well known. However, there are several methods available for modelling the behaviour of mild steel under compressive loading. The simplest method assumes that the skeleton curve from compressive loading is equal to and opposite to the skeleton curve from tensile loading. More complex methods modify the tensile behaviour by empirical

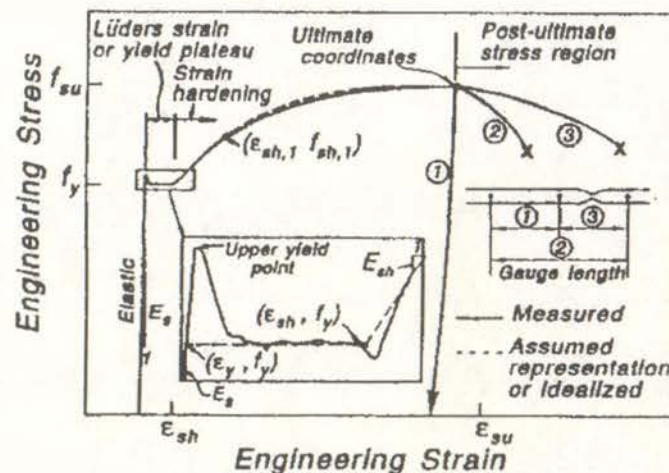


Figure 2-5 Monotonic Tensile Curve for Mild Steel (Dodd & Restrepo 1995)

relationships. Based on monotonic testing, Dodd and Restrepo proposed that the monotonic skeleton stress-strain curve of reinforcing steel in compression was identical to that in tension up to ultimate coordinates, if stress and strain were based on the instantaneous geometry of the specimen. This was defined, and hereafter referred to, as the natural coordinate system.

#### 2.4.2.2 Cyclic Behaviour

For accuracy to be maintained under cyclic loading, models need to account for the features presented in Figure 2-6. The first feature is the non-linear monotonic envelope, and especially the onset of strain hardening. The model also needs to allow for the Bauschinger effect and the isotropic strain hardening under plastic strain reversals.

In their paper, Dodd and Restrepo presented a model based on observed macroscopic behaviour that would predict the stress-strain behaviour of reinforcing steel under cyclic loading. As mentioned in Section 2.4.2.1, Dodd and Restrepo established their model using the natural coordinate system. The initial section of the unloading branch was assumed to follow a straight line of length  $1.0f_y$  with the slope equal to the unloading modulus. The unloading modulus was found to depend on the

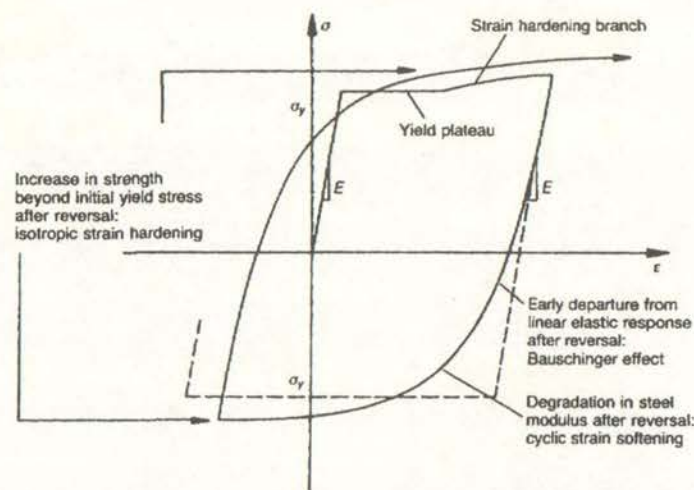


Figure 2-6 Features of Hysteretic Behaviour of Mild Steel (CEB 1996)

maximum plastic strain.

Dodd and Restrepo then proceeded to outline reversal behaviour from three regions: the yield plateau region, the strain-hardening region, and from the reversal curve itself. Apart from when the reversal occurred within the linear section of a preceding curve, the reversal curve was required to include the Bauschinger effect. Dodd and Restrepo defined a new approach that allowed the Bauschinger effect to be calculated. This required the curve to be modelled by a perfectly rigid – perfectly plastic coordinate system instead of the natural coordinate system defined previously. Finally, Dodd and Restrepo concluded that the shape of the Bauschinger effect was not dependent on the shape of the monotonic stress-strain curve, but instead was affected by the carbon content of the steel.

The CEB report previously mentioned also contained information on reinforcing steel models. A brief review of such models, ranging from the simple non-linear stress-strain model with a tri-linear monotonic envelope to a more complex model based on a model proposed by Giuffré et al. (1970), was provided.

## **2.5 Failure Mechanisms**

Researchers have shown that there are three principal failure mechanisms for reinforced concrete members undergoing seismic excitation. Sections 2.5.1 through 2.5.3 summarise the behaviour of the reinforced concrete member when failing in flexure, shear, and through low-cycle fatigue respectively.

### **2.5.1 Flexure**

Flexural failures can be classified as either a tensile failure or as a compressive failure. Section 2.5.1.1 summarises the characteristics of a reinforced concrete member failing in a tensile manner and Section 2.5.1.2 outlines the behaviour of reinforced member failing in a compressive manner.

#### 2.5.1.1 Tensile Failure

A tensile failure occurs when there is a low tensile reinforcement ratio. This allows the reinforcement steel to develop its yield strain before the concrete reaches its maximum strain capacity. A tensile failure mode is characterised by the reinforcement yielding and wide cracks developing before the concrete begins to crush. This allows large deformations to be sustained. Also it was found that the concrete strength has only a small influence on the flexural strength.

This type of failure mode was demonstrated by Shimazu and Mollick (1991) who applied seven different loading histories to single-bay multi-storey reinforced concrete interior plane frames. It was noted that in each case the failure mechanism was yielding of the column longitudinal reinforcement under reversed cyclic loading.

#### 2.5.1.2 Compressive Failure

When there is a large amount of longitudinal steel, force equilibrium of the section is reached before the reinforcement develops its yield strain. In this case, crushing of the concrete dictates the member's response. This failure mode is characterised by small crack widths and corresponding deflections due to the reinforcement remaining elastic. This type of failure is brittle and explosive with little warning. In contrast to tensile failures, the flexural strength of the reinforced concrete member depends on the compressive strength of the concrete.

Numerous researchers have investigated the flexural failure of members under seismic loading. For instance, Scribner and Wight (1980) conducted tests on eight half-scale and six full-scale T-shaped beam-column subassemblies and noted that all specimens failed through cracking and crushing of concrete in the hinge zone.

#### 2.5.2 Shear

In developing their work index Gosain et al. (1977) noted that a member's ductility was limited under repeated and reversed loads due to shear distress. Ghee et al. (1989) also noted the importance of eliminating shear failures in their study on the

seismic shear strength of circular columns. They stated that "shear failure, in conjunction with axial compression was non-ductile, and was associated with rapid strength, stiffness, and physical degradation under cyclic loading." Given that ductility is a desired characteristic in a structure, avoiding shear failures is critical in ensuring the stability of the structure during an earthquake.

A shear failure may occur in one of three ways. The first failure mode is due to there being insufficient web reinforcement. After the stirrups yield, the angle of the compression forces in the web reduces to approximately  $25^\circ$ . Wide cracks are observed prior to the beam failing. The second failure mode is due to diagonal compression stresses increasing until the concrete is crushed in compression. This occurs prior to the yielding of the stirrups. The third failure mode is due to the redistribution of forces following diagonal cracking. This leads to an increase in the flexural tension forces, which in some cases, leads to anchorage failure of the longitudinal reinforcement.

### 2.5.3 Low Cycle Fatigue

As was reported in Section 2.2, Kunnath et al. (1997) subjected twelve identical small-scale bridge columns to different pseudo-static displacement histories representing both benchmark tests and predicted earthquake displacement records. Kunnath observed two potential failure modes: low cycle fatigue of the longitudinal reinforcement or confinement failure due to rupture of the confining spirals. Low cycle fatigue of longitudinal reinforcement was associated with relatively large displacement amplitudes in excess of 5% drift whereas confinement failure was associated with a larger number of smaller amplitude cycles. Therefore if the bridge column is subjected to predominantly high amplitude inelastic cycles, it is more likely that the longitudinal bars will rupture before confinement failure occurs.

### 3.0 Theory

This chapter provides background information on concepts that formed the basis of this report. Section 3.1 defines the nominal and ideal design strengths that the maximum force measured during testing was compared against in Section 7.1. Section 3.2 specifies the sign conventions that were applied to the descriptions of the observed behaviour during testing. Section 3.3 establishes the definition of cumulative ductility that was used as the basis for comparison of the energy dissipation capacity and damage indices from each test. Section 3.4 provides general information on the hysteresis behaviour of reinforced concrete members under cyclic loading. This provided the foundation of the damage indices presented in Section 3.5.

#### 3.1 Nominal and Ideal Design Strengths

Force-displacement responses depicted in Section 7.1 compare the maximum force measured during testing with the nominal and ideal design strengths. The nominal and ideal design strengths are defined as follows and were based on the material properties presented in Table 3-1.

Nominal design strengths were based on the specified material properties. Therefore, the increase in concrete strength over time and higher than specified material strengths was ignored. The nominal design strengths were also calculated assuming an ultimate concrete compressive strain of 0.003 and an equivalent rectangular stress block. Strain hardening in the longitudinal reinforcement and the effect of confinement by transverse reinforcement was ignored. The nominal design strengths are denoted with a subscript 'n'.

In contrast to nominal design strengths, ideal design strengths accounted for the increase in concrete strength over time and the higher than specified material

Table 3-1 Nominal and Ideal Material Properties

	$f_y$ (MPa)	$f_c'$ (MPa)
Nominal	430	30
Ideal	466.9	45

strengths. Thus, the concrete strength measured at the time of testing and the average measured yield strength of longitudinal reinforcement were used. However, an ultimate concrete compressive strain of 0.003 and a rectangular stress block were still assumed. As for nominal design strength calculations, strain hardening in the longitudinal reinforcement and confinement effects from the transverse reinforcement was ignored. Section 4.4.1 details the testing undertaken to determine the material strengths of the raw materials. The ideal design strengths are denoted with a subscript 'i'.

### 3.2 Sign Conventions

So that the observed beam behaviour from the twelve tests could be described, the direction of loading was given the following sign convention: The positive direction of loading referred to the upper right quadrant of the measured hysteresis response, a push force in the actuator, and tension on the lower edge of the beam. It followed that the negative direction of loading corresponded to the lower left quadrant of the measured hysteresis response, a pull force in the actuator, and tension on the upper edge of the beam. This is depicted in Figure 3-1(a).

Similarly, so that the observed beam behaviour could be described, the sides of the beam were given the following designation: The two sides of the beam were defined as Side A and Side B with Side A corresponding to the beam side facing the laboratory strong wall. This is depicted in Figure 3-1(b).

### 3.3 Cumulative Ductility

The dissipated energy and damage indices in Section 7.3 and Section 7.5 respectively

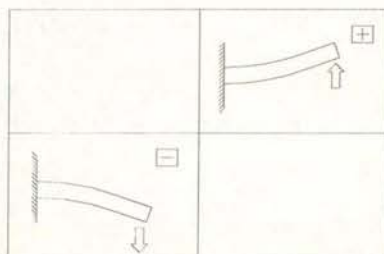


Figure 3-1(a) Sign Convention

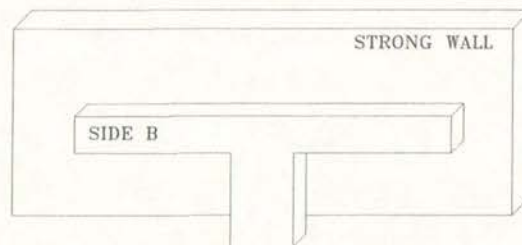


Figure 3-1(b) Designation of Beam Sides

are both plotted against the cumulative ductility from each test. The definition of cumulative ductility was taken to be that proposed by Park (1989) in his report on the evaluation of ductility of structures and structural assemblages from laboratory testing.

The cumulative ductility for each symmetric load step is defined as  $2n$  where  $n$  is the ductility level reached in both the positive and negative direction. The values are then summed for the duration of the test to determine the cumulative ductility for that particular test.

### 3.4 Hysteresis Behaviour of Concrete Under Cyclic Loading

There are several concepts that form the basis of damage indices discussed in the following section that are based on the hysteresis behaviour of reinforced concrete. These include the definition of displacement ductility, elasto-plastic behaviour, and bilinear behaviour. Sections 3.4.1 through 3.4.3 provide a brief explanation of these concepts.

#### 3.4.1 Displacement Ductility

Displacement ductility is defined as the ratio of maximum displacement achieved to the yield displacement—that is

$$\mu = \frac{\delta_{\max}}{\delta_y} \quad \dots \text{Equation 3.1}$$

There are a number of methods available that establish the yield displacement of a reinforced concrete member. This report applies the procedures established by Park (1989), which are outlined in Section 6.2.

#### 3.4.2 Elasto-Plastic Behaviour

In Section 3.5.5 the damage index of Banon and Veneziano (1982) with an elasto-plastic approximation to the force-displacement response is established. This elasto-plastic approximation is illustrated in Figure 3-2. The yield displacement is

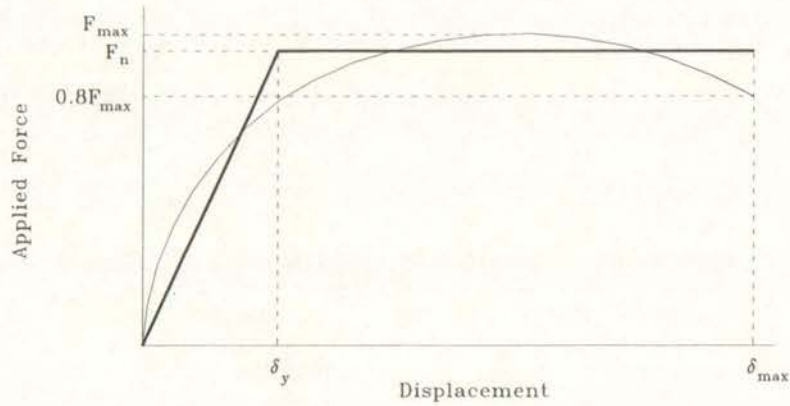


Figure 3-2 Elasto-Plastic Approximation

determined using the procedures summarised in Section 6.2 and a straight line is drawn from the origin to the co-ordinates  $(\delta_y, F_n)$ , where  $F_n$  is the force associated with the nominal design moment—that is,  $F_n = M_n/l$ . A horizontal line is then drawn from  $(\delta_y, F_n)$  to  $(\delta_{\max}, F_n)$ . This approximation ignores the effects of strain hardening after yielding has occurred.

### 3.4.3 Bilinear Behaviour

The damage index proposed by Roufaiel and Meyer and detailed in Section 3.5.3 is based upon the bilinear approximation to the force-displacement response illustrated in Figure 3-3. As for the elasto-plastic model, a straight line is drawn between the origin and  $(\delta_y, F_n)$ . A straight line of slope  $r$  is then drawn from  $(\delta_y, F_n)$  to the maximum displacement. This model is slightly more realistic than the elasto-plastic



Figure 3-3 Bilinear Approximation

model because it accounts for strain hardening after yielding has occurred.

### 3.5 Damage Indices

Damage indices attempt to quantify numerically the damage sustained in concrete structures due to seismic loading. Damage indices aid retrofit decisions, disaster planning, and post-earthquake assessment of affected structures.

The simplest damage indices are those that are ductility based. However such indices fail to consider the cumulative effect of repeated cycles. This led researchers to propose damage indices that accounted for cumulative loading; for example, Park and Ang who accounted for repeated loading by including the amount of energy dissipated during testing. Sections 3.5.1 through 3.5.6 summarise the damage indices that were applied in this report.

#### 3.5.1 Ductility Ratio

The most traditional and simple damage indicator is displacement ductility. As was reported in Section 3.4.1 and expressed mathematically in Equation 3.1, the maximum displacement ductility is defined as the ratio of the maximum displacement achieved to the yield displacement.

#### 3.5.2 Cosenza et al. Index

Powell and Allahabadi (1988) have reviewed concepts employed in the prediction of seismic damage. One concept reviewed was a demand versus capacity procedure, where an estimate is made of the demand on a structure and its capacity to resist this demand. A structural damage index provides a measure of the demand on a structural element. The damage index has minimum and maximum values relating to undamaged and failure conditions respectively. Between these two extremes, the damage index is related to the damage parameter by a damage function. Powell and Allahabadi proposed the following general damage function:

$$D = \left( \frac{\delta - \delta_y}{\delta_u - \delta_y} \right)^m, \quad \dots \text{Equation 3.2}$$

where  $\delta$  was defined as the damage parameter at a certain level,  $\delta_y$  was defined as the minimum value relating to an undamaged state, and  $\delta_u$  was defined as the ultimate value relating to failure. The variable  $m$  allowed more complex relationships between the damage parameter and the damage index to be assumed.

Cosenza et al. (1993) defined the displacement ductility value expressed in Equation 3.1 as a measure of the damage parameter defined in Equation 3.2. This was incorporated into Equation 3.2 by setting  $m$  equal to 1.0 and defining the ultimate value as the ductility obtained under monotonic testing to give the following expression:

$$D = \frac{\left( \left( \frac{\delta}{\delta_y} \right) - \left( \frac{\delta_y}{\delta_y} \right) \right)^{1.0}}{\left( \left( \frac{\delta_{ult}}{\delta_y} \right) - \left( \frac{\delta_y}{\delta_y} \right) \right)},$$

which was simplified to give

$$D = \frac{\mu - 1}{\mu_{ult} - 1}, \quad \dots \text{Equation 3.3}$$

A value less than zero indicates that yielding has not occurred and hence, the member is undamaged. In contrast a value equal to 1.0 represents failure of the member.

### 3.5.3 Roufaiel and Meyer Index

The damage indices reported in Sections 3.5.1 and 3.5.2 both rely on displacement ductility to define the level of damage. However these models do not include the effects of repeated cycling, which occur during earthquake excitation. The ability of a building to withstand an earthquake depends on the degradation of strength and stiffness suffered during previous earthquakes. Therefore, Roufaiel and Meyer (1987) proposed a model that was based on the reduction in secant stiffness. Although cumulative damage was not accounted for, the model was an improvement on

displacement ductility as it took some account of the stiffness and strength degradation that occurs under earthquake loading.

Roufaiel and Meyer proposed that the maximum modified flexural damage ratio (MFDR) from positive or negative loading should be established as an indicator of member damage. The modified flexural damage ratio was defined as

$$MFDR = \frac{\frac{\phi_{\max} - \phi_y}{M_{\max} - M_y}}{\frac{\phi_{ult} - \phi_y}{M_{ult} - M_y}} \quad \dots \text{Equation 3.4}$$

and is illustrated in Figure 3-4.

This damage ratio represents the increase in flexibility between the initial condition and the maximum moment divided by the increase in flexibility at failure. The flexibility at failure is typically found through monotonic testing. Equation 3.4 can also be expressed in terms of stiffness at the initial condition, the maximum deformation, and at failure to give

$$MFDR = \frac{k_{ult} (k_y - k_{\max})}{k_{\max} (k_y - k_{ult})} \quad \dots \text{Equation 3.5}$$

As with the damage index proposed by Cosenza et al., the member is undamaged when the MFDR is less than or equal to zero, and has failed when the MFDR is equal

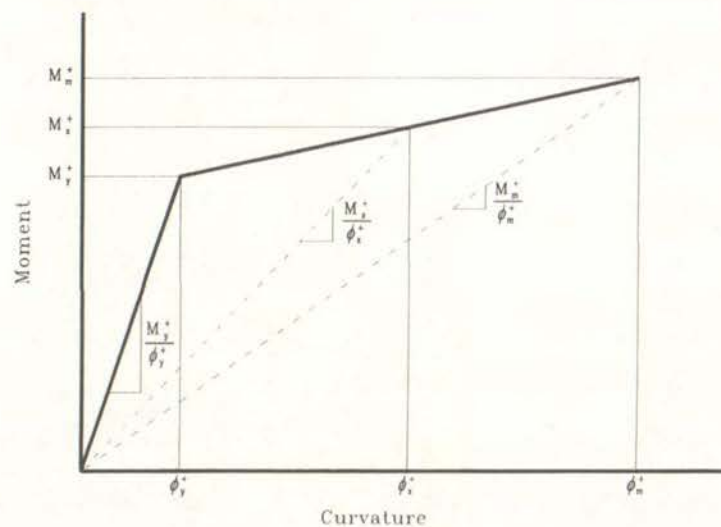


Figure 3-4 Definition of Modified Flexural Damage Ratio (Roufaiel and Meyer 1987)

to 1.0. An assumption inherent in this damage index is that premature failure modes are avoided through reinforcement details following conventional practice.

#### 3.5.4 Park and Ang Index

One of the more commonly applied damage indices is that proposed by Park and Ang (1985). Damage was defined as a linear combination of damage caused by deformation and that contributed by cyclic loading, and was expressed mathematically as

$$D = \frac{\delta_{\max}}{\delta_{ult}} + \frac{\beta}{F_y \delta_{ult}} \int dE. \quad \dots \text{Equation 3.6}$$

The second term in Equation 3.6 accounted for the cumulative damage that occurs due to repeated cyclic loading. In Equation 3.6  $\delta_{\max}$  was defined as the maximum deformation during an earthquake or test and  $\delta_{ult}$  was the ultimate deformation obtained from monotonic loading.  $F_y$  was the force associated with the calculated yield moment and  $dE$  was defined as the incremental dissipated hysteresis energy. Lastly,  $\beta$  was a non-dimensional parameter representing the effect of cyclic loading and is defined in Equation 3.7:

$$\beta = \left( 0.447 + 0.073 \frac{l}{d} + 0.24n_o + 0.314\rho_t \right) \times 0.7^{\rho_s}. \quad \dots \text{Equation 3.7}$$

Several terms represented in Equation 3.7 have lower bound values. These are the shear span ratio,  $l/d$ , which had a minimum value equal to 1.7, the normalised axial stress,  $n_o$ , which had a minimum value equal to 0.2, and the longitudinal steel ratio as a percentage,  $\rho_t$ , which had a minimum value of 0.75%. The confinement ratio,  $\rho_s$ , had no lower bound. Equation 3.7 was derived from a regression analysis on data from 402 reinforced concrete components of rectangular cross-section. Park and Ang then suggested the following classification levels based on the observed damage of nine reinforced concrete buildings from the 1971 San Fernando earthquake. Table 3-2 details the classification levels proposed by Park and Ang.

Table 3-2 Park and Ang Damage Classification Levels

$D < 0.1$	No damage or localised cracking
$0.1 \leq D < 0.25$	Minor damage
$0.25 \leq D < 0.4$	Moderate damage
$0.4 \leq D < 1.0$	Severe damage
$D \geq 1.0$	Collapse

Park and Ang defined minor damage as light cracking throughout, moderate damage as severe cracking and localised spalling, and severe damage as crushing of concrete and the exposure of reinforcement.

It should be noted that Equation 3.6 is not normalised and hence gives small values for  $D$  in the elastic range when the value of  $D$  should be zero. However these small values of  $D$  are negligible when compared to values of  $D$  once the structure passes through the elastic range.

### 3.5.5 Banon and Veneziano Index

Banon and Veneziano (1982) proposed another damage index based on a combination of ductility and dissipated energy. Banon and Veneziano developed a probabilistic damage index that gave the probability of survival at a certain time as a function of the flexural damage ratio and the dissipated energy up to that time.

The flexural damage ratio was defined as the ratio of stiffness at the yield point to the secant stiffness at failure. This was also found to be related to the ratio of the maximum displacement to the yield displacement with theoretical-experimental analysis showing a correlation coefficient between the two parameters of 0.95 (Cosenza et al. 1993). Thus the first damage parameter was defined as:

$$d_1 = \frac{\delta_{\max}}{\delta_y} = \mu. \quad \dots \text{Equation 3.8}$$

The second damage parameter was defined as the plastic dissipated energy normalised with respect to the absorbed energy at the elastic limit in the first quadrant. This was expressed as

$$d_2 = \frac{2E_h}{F_y \delta_y}. \quad \dots \text{Equation 3.9}$$

Equations 3.8 and 3.9 were then modified as demonstrated in Equations 3.10 and 3.11:

$$d_1^* = d_1 - 1 \text{ and} \quad \dots \text{Equation 3.10}$$

$$d_2^* = a d_2^b. \quad \dots \text{Equation 3.11}$$

The terms  $a$  and  $b$  in Equation 3.11 were calibrated using the results of 29 experimental studies, and were found to be 1.1 and 0.38 respectively.

The modified damage parameters were then combined to give a damage index function of

$$D = \sqrt{(d_1^*)^2 + (d_2^*)^2}. \quad \dots \text{Equation 3.12}$$

The damage index was then normalised by dividing the value given in Equation 3.12 by the value obtained under monotonic loading to give

$$D = \frac{\sqrt{\left(\frac{x_{\max}}{x_y} - 1\right)^2 + \left(1.1 \left(\frac{2E_h}{F_y x_y}\right)^{0.38}\right)^2}}{\text{Monotonic Value}}, \quad \dots \text{Equation 3.13}$$

which is the final form of the damage index.

As with the damage index proposed by Cosenza et al., the member is undamaged when the damage index is less than or equal to zero, and has failed when the damage index is equal to 1.0.

### 3.5.6 Bracci et al. Index

Bracci et al. (1989) proposed a damage index for the evaluation of structural damage of reinforced concrete based on the relation of demand and capacity. The damage potential, or total capacity of the component to sustain damage, was defined as the area between the monotonic load-deformation curve and the fatigue failure envelope. Damage demand consisted of two components. These were strength loss and deformation related damage. Strength loss was defined as the loss of a component's ability to sustain damage due to strength degradation and dissipated hysteric energy and accounted for the lowering of the monotonic curve as demonstrated in Figure 3-5.

Deformation damage corresponded to irrecoverable permanent deformations. The damage potential,  $D_p$ , the strength damage,  $D_s$ , and the deformation damage,  $D_d$ , are defined in Figure 3-5. The damage index was then defined as

$$D = \frac{D_s + D_d}{D_p} \quad \dots \text{Equation 3.14}$$

The above theory was applied using the origin-centred bilinear relationship shown in Figure 3-6 and assuming that initial and post-yielding stiffness was the same in both directions. This led to the following damage index equation:

$$D = \frac{\Delta M(\phi_{ult} - \phi_y) + (M_y - \Delta M)(\phi_{max} - \phi_y)}{M_y(\phi_{ult} - \phi_y)} = D_1 + D_2 - D_1 D_2 \quad \dots \text{Equation 3.15}$$

in which

$$D_1 = \frac{\phi_{max} - \phi_y}{\phi_{ult} - \phi_y} \quad \dots \text{Equation 3.16}$$

and

$$D_2 = \frac{\Delta M}{M_y} \quad \dots \text{Equation 3.17}$$

In Equation 3.16,  $\phi_{max}$  was defined as the curvature at the maximum recorded displacement,  $\phi_y$  was defined as the curvature at the force corresponding to the yield moment, and  $\phi_{ult}$  was the curvature at the ultimate displacement established from

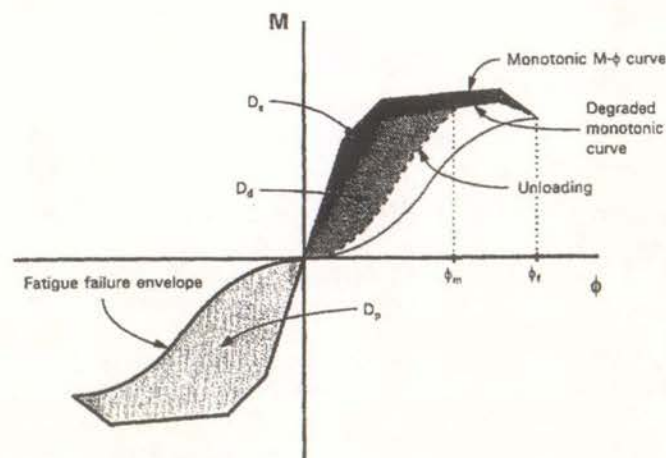


Figure 3-5 Damage Index Terms (Bracci et al. 1989)

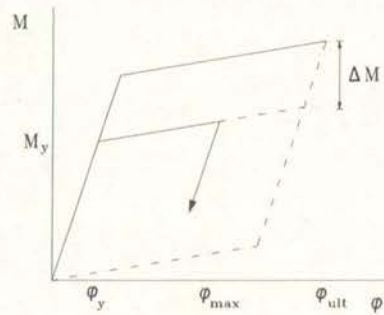


Figure 3-6 Bi-Linear Moment Curvature Relationship (Bracci et al. 1989)

monotonic loading. In Equation 3.17,  $\Delta M$  was found to be dependent on the dissipated energy of the member, the yield curvature, and a strength deterioration factor as detailed in Equation 3.18:

$$\Delta M = \frac{S_{sd} \int dE}{\phi_y} \quad \dots \text{Equation 3.18}$$

The strength deterioration factor in Equation 3.18 was dependent on the axial load, the longitudinal and transverse confinement ratios, and the material strengths of the component. A regression analysis on experimental results from 21 elements with the influencing parameters previously mentioned was conducted to give the following expression for the strength deterioration factor:

$$S_{sd} = 0.00857 \left( 1 + 12 \frac{P_e}{A_g f_c'} \right) \left( 1 - 0.5 \frac{\rho_s f_{yt}}{0.85 f_c'} \right) \left( 1 - \frac{\rho_t f_y}{0.85 f_c'} \right) \quad \dots \text{Equation 3.19}$$

Bracci et al. suggested four classification states based on experimental behaviour with Table 3-3 listing the four damage states.

Bracci et al. compared these classification levels with those proposed by Park and Ang, and concluded that although collapse occurred in both models when the damage index was equal to 1.0, the irreparable state varied between the two models. The

Table 3-3 Bracci et al. Damage Classification Levels

$D \leq 0.33$	Serviceable State
$0.33 < D \leq 0.66$	Repairable State
$0.66 < D \leq 1.0$	Irreparable State
$D > 1.0$	Collapse State

above model classified a structure as irreparable once the damage index is greater than 0.66 whereas the Park and Ang model classified a structure as irreparable once the damage index is greater than 0.4. The difference was due to damage in the model proposed by Bracci et al. being more linearly distributed between 0.0 and 1.0 than the model proposed by Park and Ang, where considerable damage was evident at small damage index values.

## 4.0 Test Assembly Design, Construction, and Set-Up

The assembly for testing reported herein consisted of a reinforced concrete beam mounted on a concrete pedestal. The test set-up and the method of loading simulate the response of the beam section of a reinforced concrete frame when subjected to seismic loading. A reinforced concrete frame was chosen because buildings are much more prevalent in New Zealand than other structural forms, such as bridges, and the majority of these buildings are concrete.

The Cement and Concrete Association (C&CA) of New Zealand has published a guide (C&CA 1998) demonstrating the design of a ten-storey office building to the requirements of the New Zealand Standard for the Design of Concrete Structures (Standards New Zealand 1995). This guide is commonly known, and hereafter referred to, as 'The Red Book'. The example presented in 'The Red Book' provided the assembly design for this project, and was chosen due to its high profile among New Zealand structural engineers. Section 4.1 presents the prototype design that the design of the test subassembly was based on. 'The Red Book' contains a thorough examination of the building's design actions and section design; hence such information was not included in this report.

However, even though the assembly design was taken from 'The Red Book', the testing reported herein was based on the development of a beam plastic hinge. This was instead of accounting for other potential sources of plastic deformation that may possibly develop in a frame—most notable that of inelastic joint deformations. All other parts of the assembly were therefore designed to minimise their influence on the beam and were not representative of conventional practice. Section 4.2 reports on the modifications made to the prototype due to scaling with the corresponding changes to the test subassembly detailed in Section 4.3.

Section 4.4 describes the procedures followed during construction of the test specimens. Section 4.5 presents the test set-up and Section 4.6 details the instrumentation layout, which enabled the relevant data to be collected. Lastly,

Section 4.7 describes how the instrumentation detailed in Section 4.6 enabled moment–curvature data and separate displacement components to be derived.

### 4.1 Prototype Design

As reported previously, the subassembly design was based on the design example presented in 'The Red Book'. Figure 4-1 illustrates the location of the internal and perimeter frames of the office building and Figure 4-2(a) presents an elevation of the perimeter frame.

The three-dimensional analysis programme ETABS (Version 5.0) was used to complete the seismic analysis of the building model. The ETABS analysis indicated

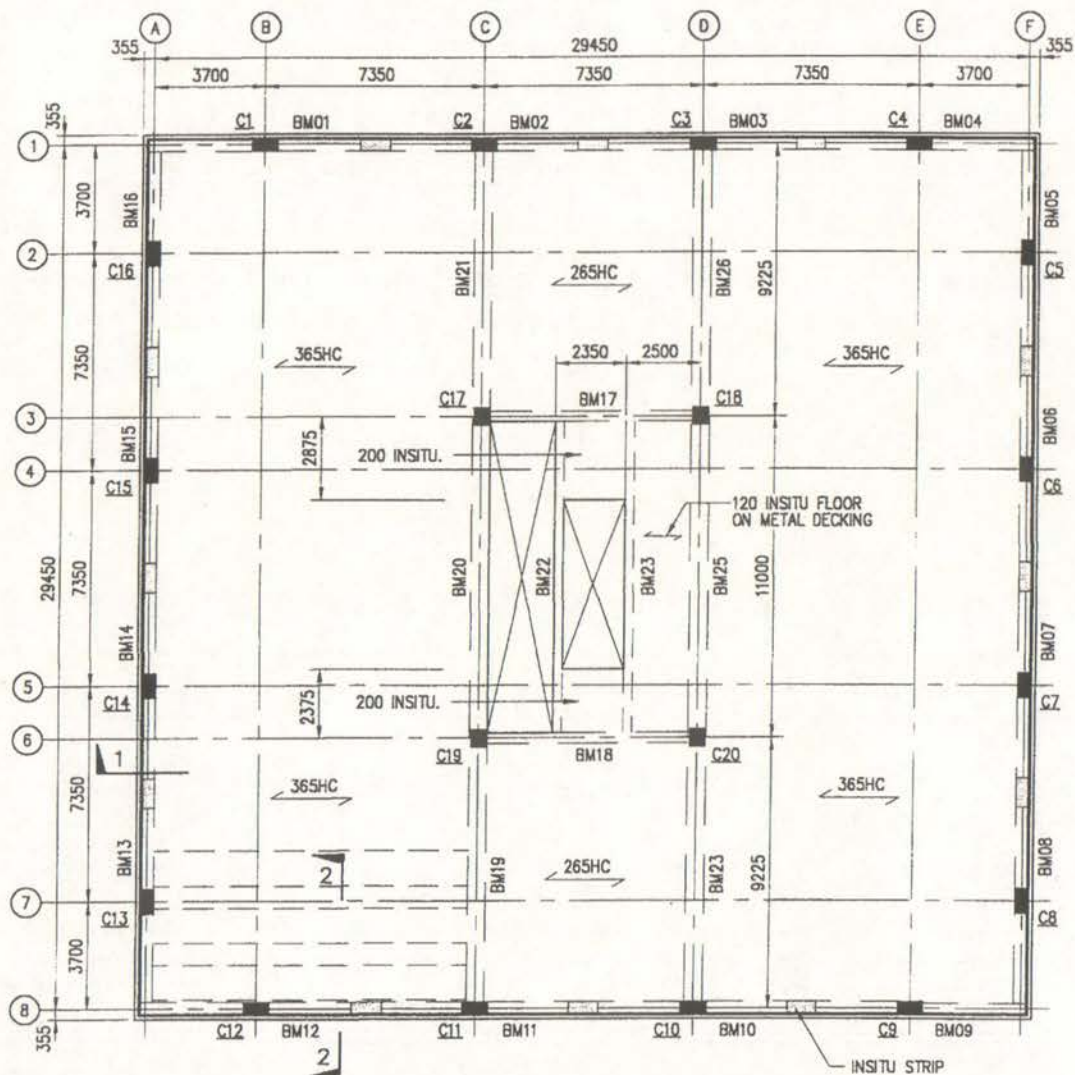


Figure 4-1 Frame Building Plan (C&CA 1998)

that the critical frame was located on Grid F. This was primarily caused by frames on the alphabetical grids having larger gravity loading than frames on the number grids due to the orientation of the precast hollow core flooring slab. Figure 4-2b displays the output from the combined modal analysis including P-Δ effects for the perimeter frame located on Grid F. Figure 4-2(b) indicates that Level 2 was the critical design level. Longitudinal and transverse reinforcement details were then established for the design actions at the critical position (Level 2 on Grid F). For simplicity this detail was extended to all perimeter frames, regardless of their position.

To simulate the response of a beam section under seismic loading it was necessary to base the design of the test assembly on a beam dominated by seismic loading. In 'The Red Book' example the perimeter frames were required to resist any lateral forces and, depending on the direction of the beam with respect to the orientation of the floor slab, varying amounts of gravity loads. The internal frames were designed as secondary elements because, while they resisted gravity loads, they played no part in resisting lateral forces. Therefore the beams where seismic loads were most dominant were those perimeter beams running parallel with the orientation of the floor slab.

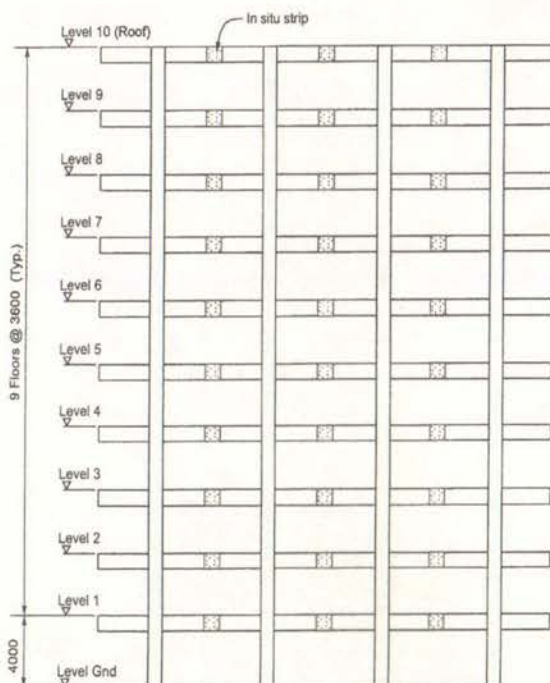


Figure 4-2(a) Perimeter Frame Elevation  
(C&CA 1998)

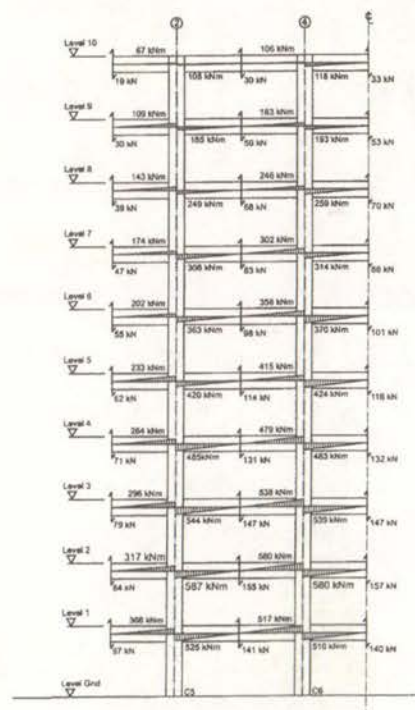


Figure 4-2(b) Frame Design Actions  
(C&CA 1998)

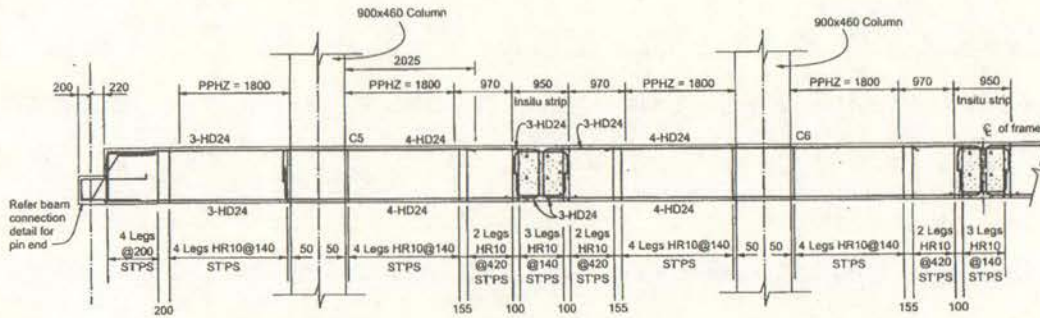


Figure 4-3 Level Two Reinforcement Layout (C&CA 1998)

Figure 4-1 demonstrates that beams along Grids 1 and 8 fulfilled this criterion. Hence, from Figure 4-1, the design of the test sub-assembly was based on beams BM 01-03 and BM 10-12.

Figure 4-3 presents the reinforcement layout for the reinforced concrete frame along Grid 8 at Level 2. Detailing of the test assembly was based on the central beam where the longitudinal reinforcement consisted of 4 HD 24 top and bottom. The transverse reinforcement in the central beam consisted of 4/HR 10 @ 140 c/c in the plastic hinge zone and 2/HR 10 @ 420 c/c outside the plastic hinge zone. Figure 4-4 demonstrates that the prototype's potential plastic hinge zone (PPHZ) was defined as a distance equal to 1800mm from the column face. Figure 4-5 details a cross section of the prototype beam taken through the plastic hinge zone.

Seismic analysis of the building model undertaken by the ETABS programme was based on a building located in Christchurch. It may be established from the New Zealand Loadings Standard (Standards New Zealand 1992) that Christchurch is located in a medium-risk seismic region. Hence the amount of longitudinal and transverse reinforcement detailed in 'The Red Book' example was less than

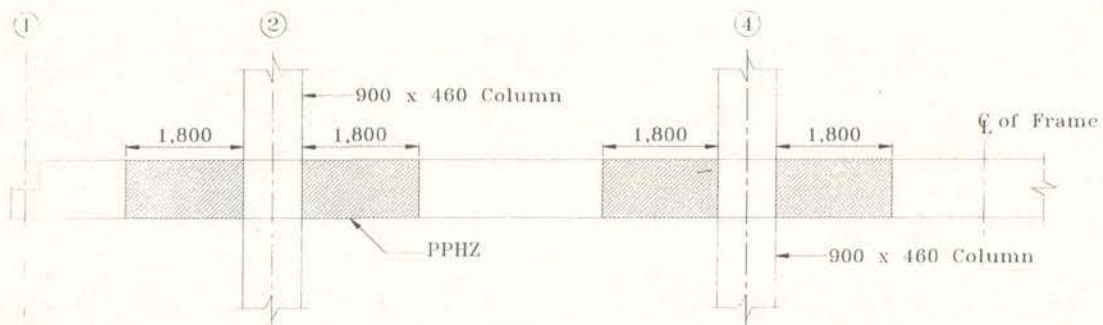


Figure 4-4 Location of Potential Plastic Hinge Zones (C&CA 1998)

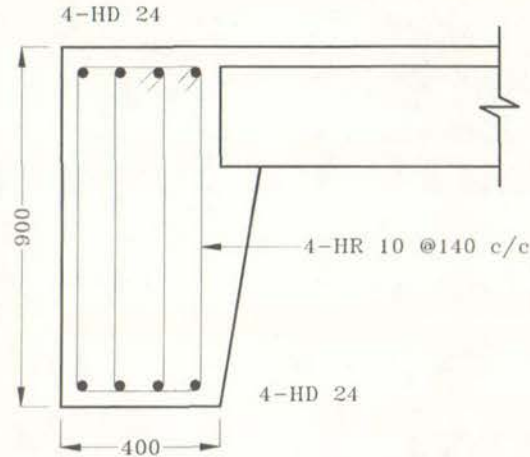


Figure 4-5 Prototype Cross Section (C&CA 1998)

conventional practice for a building located in a high-risk seismic region such as Wellington. However, based on seismic zone maps in the New Zealand Loadings Standard, the majority of the New Zealand population—and hence the majority of construction—are located in regions associated with either a medium or low seismic risk. Therefore the Red Book example is consistent with conventional practice for the majority of construction in New Zealand. It should also be noted that this project was based on establishing the influence of loading history and not the validity of ‘The Red Book’ example. Hence the adopted design of the test assembly, while attempting to be indicative of conventional practice, was not critical to this project.

## 4.2 Design Modifications

Laboratory restraints meant that the prototype design was constructed at two-thirds scale. Section 4.2.1 summarises the scaling techniques applied to the prototype with Section 4.2.2 and Section 4.2.3 detailing the modifications made to the longitudinal and transverse reinforcement respectively

### 4.2.1 Scaling Techniques

While the subassemblage design was taken from the aforementioned prototype design, the capacity of both the laboratory overhead crane and the available actuator resulted in the beam being built at two-thirds scale. Scaling was based on preserving stress levels between the prototype and the test unit. Table 4-1 summarises the scaling

Table 4-1 Scaling Factors

	Prototype	Test Unit
Length	$L_p$	$L_T = fL_p$
Force	$F_p$	$F_T = \sigma_T A_T = \sigma_p fL_p fL_p = f^2 F_p$
Moment	$M_p$	$M_T = f^2 F_p L_T = f^2 F_p fL_p = f^3 M_p$

techniques applied to the prototype design so that stress levels were preserved. In Table 4-1,  $f$  is the applied scale factor, which was two-thirds for this project.

Applying the dimensional scaling detailed in Table 4-1, it follows that the overall beam dimensions of the test assembly were 270mm wide and 600mm deep.

Use Equation 9-2 from NZS 3101:1995 to calculate the shear force of concrete,

$$V_c = v_c b_w d \quad \dots \text{Equation 4.1}$$

where

$$v_c = (0.07 + 10\rho_w) \sqrt{f'_c} \quad \dots \text{Equation 4.2}$$

demonstrates that stress levels were preserved between the prototype and the test unit.

The variables  $\rho_w$  and  $f'_c$  in Equation 4.2 remain constant under scaling, resulting in the value for  $v_c$  in the test unit being identical to the value in the prototype. This is also shown in Equation 4.1 where  $b_w$  and  $d$  in the test unit are two-thirds of the prototype values and  $v_c$  has the same value as the prototype value. Hence the value for  $V_c$  in the test unit was  $(4/9)$  of the prototype value, which was consistent with that indicated in Table 4-1.

#### 4.2.2 Longitudinal Reinforcement

From Table 4-1, the nominal flexural strength of the test unit should be  $(2/3)^3 = 8/27$  of the prototype beam. The following equations calculate the nominal flexural strength of the prototype beam, consistent with NZS 3101:1995:

$$T = A_s f_y \quad \dots \text{Equation 4.3}$$

$$T = \left( 4 \times \frac{\pi \times 24^2}{4} \right) \times 430$$

$$= 778.1 \text{ kN}$$

$$a = \frac{C}{0.85 f'_c b} \quad \dots \text{Equation 4.4}$$

$$a = \frac{778.1 \times 10^3}{0.85 \times 30 \times 400}$$

$$= 76.29 \text{ mm}$$

$$M_{nP} = T \left( d - \frac{a}{2} \right) \quad \dots \text{Equation 4.5}$$

$$M_{nP} = 778.1 \times \left( 850 - \frac{76.29}{2} \right)$$

$$= 631.7 \text{ kNm}$$

$$M_{nT} = f^3 M_{nP} \quad \dots \text{Equation 4.6}$$

$$M_{nT} = \left( \frac{2}{3} \right)^3 \times 631.7$$

$$= 187.2 \text{ kNm}$$

Equations 4.3 through 4.5 did not account for the presence of flexural compression reinforcement and assumed a specified reinforcement yield strength of 430MPa and a specified concrete strength of 30MPa. Cover to the transverse stirrups was 24mm, and the section was assumed to be prismatic, rather than have the flared geometry shown in Figure 4-5.

Given that the longitudinal reinforcement in the prototype beam consisted of 24mm diameter bars, the following bar size was required for the test unit:

$$d_T = f d_p \quad \dots \text{Equation 4.7}$$

$$d_T = \frac{2}{3} \times 24$$

$$= 16 \text{ mm}$$

Repeating Equations 4.3 through 4.5 confirmed that the actual flexural strength of the test unit was equal to 187.2 kNm:

$$\begin{aligned}
 T &= \left( 4 \times \frac{\pi \times 16^2}{4} \right) \times 430 \\
 &= 345.8 \text{ kN} \\
 a &= \frac{345.8 \times 10^3}{0.85 \times 30 \times 270} \\
 &= 50.23 \text{ mm} \\
 M_{nT} &= 345.8 \times \left( 560 - \frac{50.23}{2} \right) \\
 &= 185.0 \text{ kNm}
 \end{aligned}$$

The actual nominal flexural strength of the test unit was within 1.2% of the scaled prototype value, indicating that the test unit was scaled correctly.

#### 4.2.3 Transverse Reinforcement

Figure 4-3 reveals that the transverse reinforcement of the prototype beam in the plastic hinge zone was 4/HR10 @ 140 c/c. The shear strength provided by the transverse reinforcement of the prototype beam was calculated using Equation 9-14 of NZS 3101:1995:

$$V_p = A_v f_{yt} \frac{d}{s} \quad \dots \text{Equation 4.8}$$

$$\begin{aligned}
 V_p &= \left( 4 \times \pi \times \frac{10^2}{4} \right) \times 430 \times \frac{850}{140} \\
 &= 820.2 \text{ kN.}
 \end{aligned}$$

The required reinforcement shear strength of the test unit was

$$V_T = f^2 V_p \quad \dots \text{Equation 4.9}$$

$$\begin{aligned}
 V_T &= \left( \frac{2}{3} \right)^2 \times 820.2 \\
 &= 364.5 \text{ kN.}
 \end{aligned}$$

Given that the prototype beam contained 10 mm diameter bars, the following bar size was required for the test unit:

$$d_{bT} = f d_{bP}$$

$$d_{br} = \frac{2}{3} \times 10$$

$$= 6.7 \text{ mm}$$

Reinforcement steel is not manufactured with a diameter of 6.7mm and so 6mm bars were used instead. Also, reinforcement steel with a diameter of 6 mm was only available with a nominal yield strength of 300 MPa. The spacing of the transverse reinforcement (taking into account the change in yield strength and the small discrepancy in the scaled bar diameter) in the plastic hinge zone of the test unit was determined by rearranging Equation 4.8:

$$s = \frac{A_v f_{yt} d}{V_T} \quad \dots \text{Equation 4.10}$$

$$s = \frac{\left(4 \times \pi \times \frac{6^2}{4}\right) \times 300 \times 560}{364.5}$$

$$= 52 \text{ mm}$$

In conclusion, the transverse reinforcement in the plastic hinge zone of the test unit was 4/R6 @ 50 c/c.

It should be noted that decreasing the yield strength of transverse reinforcement in the test unit results in a more conservative design (with regard to preventing buckling of the longitudinal reinforcement) because the spacing of transverse reinforcement was less than the scaled prototype spacing. However because the bar size was decreased by a factor of 6/10 instead of 2/3, the test unit had approximately the same factor of safety against the longitudinal reinforcement buckling as the prototype. This is presented in Table 4-2 where comparisons are made between the scaled results given

Table 4-2 Change in Confinement Safety Factor due to Scaling Constraints

	$A_{te(\text{required})}$	$A_{te(\text{provided})}$	Factor of Safety
Theoretical Scaling	$A_{te} = \frac{201 \times 430 \times 93.3}{96 \times 430 \times 16}$ $= 12.2 \text{ mm}^2$	$A_{te} = \left(\frac{2}{3}\right)^2 \times 78.5$ $= 34.9 \text{ mm}^2$	$\frac{A_{te(\text{provided})}}{A_{te(\text{required})}} = 2.86$
Actual Scaling	$A_{te} = \frac{201 \times 430 \times 50}{96 \times 300 \times 16}$ $= 9.4 \text{ mm}^2$	$A_{te} = \left(\frac{6}{10}\right)^2 \times 78.5$ $= 28.3 \text{ mm}^2$	$\frac{A_{te(\text{provided})}}{A_{te(\text{required})}} = 3.0$

theoretical conditions and the scaled results allowing for practical constraints. The amount of transverse reinforcement required to prevent the longitudinal reinforcement buckling,  $A_{te(required)}$ , was based on

$$A_{te} = \frac{\sum A_b f_y}{96 f_{yt}} \frac{s}{d_b} \quad \dots \text{Equation 4.11}$$

(Equation 8.9 in the New Zealand Standard for the Design of Concrete Structures (Standards New Zealand 1995)) whereas the amount of transverse reinforcement provided to prevent buckling,  $A_{te(provided)}$ , was based on

$$A_T = f^2 A_P. \quad \text{Equation 4.12}$$

Figure 4-3 indicates that the transverse reinforcement of the prototype beam outside the plastic hinge zone was 2/HR10 @ 420 c/c. The prototype shear strength and the resulting test-unit shear strength were then calculated by repeating Equations 4.8 and 4.9:

$$\begin{aligned} V_p &= \left( 2 \times \pi \times \frac{10^2}{4} \right) \times 430 \times \frac{850}{420} \\ &= 136.7 \text{ kN} \\ V_T &= \left( \frac{2}{3} \right)^2 \times 136.7 = 60.8 \text{ kN} \end{aligned}$$

As before, it was necessary to use reinforcement steel with a diameter of 6 mm and yield strength of 300 MPa. The spacing of the transverse reinforcement taking into account these changes was then calculated to be:

$$\begin{aligned} s &= \frac{\left( 2 \times \pi \times \frac{6^2}{4} \right) \times 300 \times 560}{60.8} \\ &= 156 \text{ mm.} \end{aligned}$$

In conclusion, the transverse reinforcement outside the plastic hinge zone of the test unit was 2/R6 @ 155 c/c.

### 4.3 Test Unit Details

Section 4.3.1 summarises the modifications made to the prototype as a result of scaling. As was reported earlier, testing was based on the development of a beam plastic hinge along. Section 4.3.2 presents the modifications made to the joint region of the test assembly so that the influence of the joint behaviour on the beam plastic hinge was minimised.

#### 4.3.1 Longitudinal and Transverse Reinforcement Details

As detailed in Section 4-2, scaling of the prototype design resulted in changes to the longitudinal and transverse reinforcement details. The resultant reinforcement details are illustrated in Figure 4-6.

Figure 4-7(a) details the longitudinal and transverse reinforcement through the plastic hinge zone (Section A-A), whereas Figure 4-7(b) details the longitudinal and transverse reinforcement outside the plastic hinge zone (Section B-B).

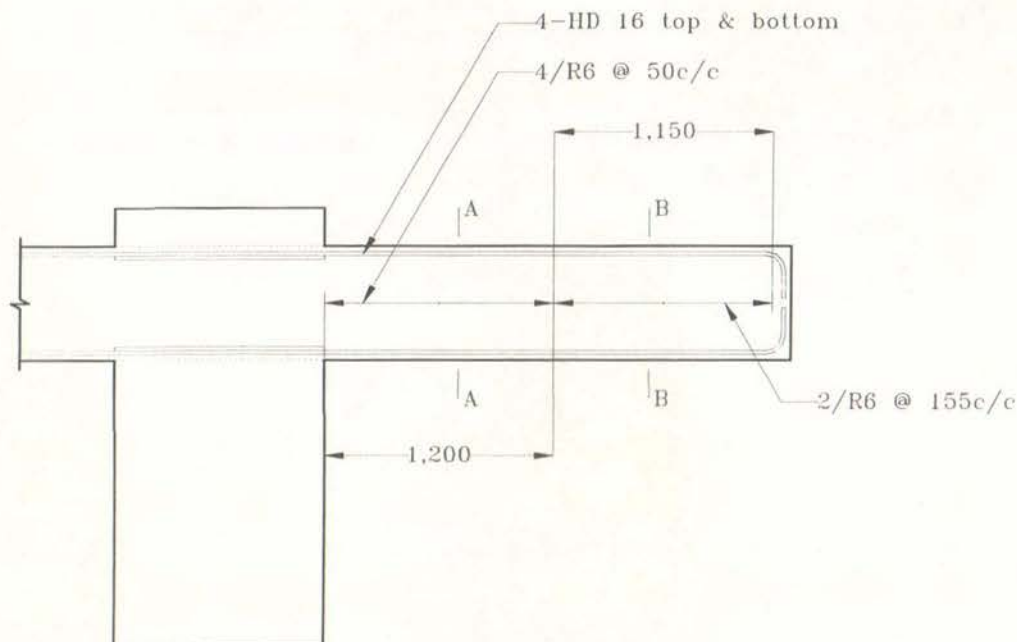


Figure 4-6 Reinforcement Layout in Test Sub-Assemblage

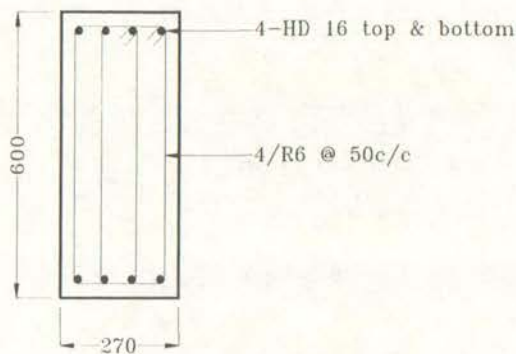


Figure 4-7(a) Cross Section at A-A

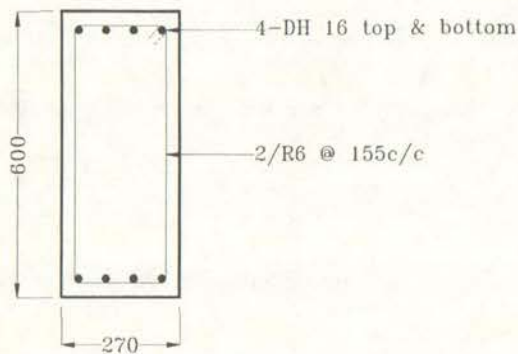


Figure 4-7(b) Cross Section at B-B

### 4.3.2 Beam-Column Joint

The joint design of the test unit was modified from the example presented in ‘The Red Book’ so that testing of the first beam did not affect the second beam of each assemblage. Firstly, an extra reinforcing bar was welded to each longitudinal bar in the joint region to ensure that strains in the longitudinal reinforcement within the joint region remained in the elastic range. Secondly, the length of the beam-column joint in the prototype design was 900 mm with a resulting scaled dimension of 600 mm. However the width of the concrete pedestal, on which the test sub-assemblage was mounted, was 1100 mm. This allowed a greater amount of vertical reinforcement in the joint region than the scaled amount from the prototype design. Figure 4-8 illustrates the modifications made to the joint region of the test unit.

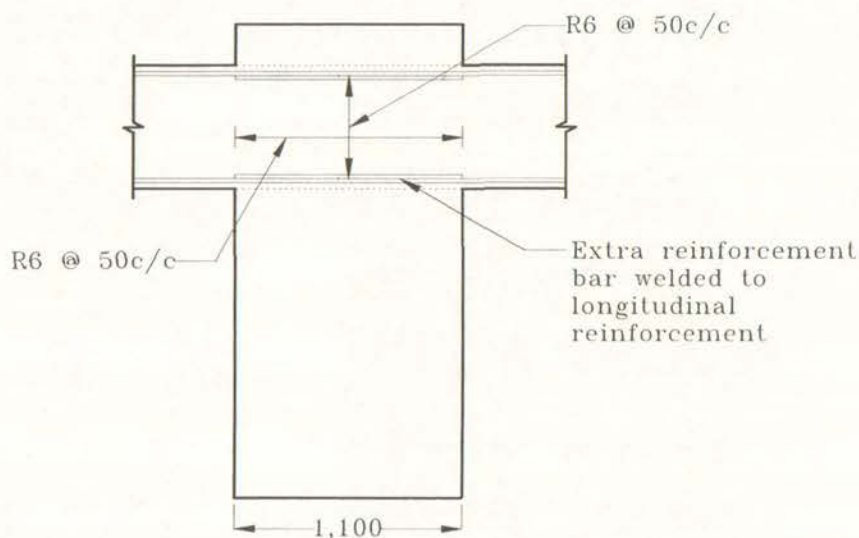


Figure 4-8 Beam Column Joint

#### 4.4 Construction Procedure

It was necessary to construct six nominally identical beams so that the influence of the applied loading history on the ultimate displacement of each test unit could be determined. Section 4.4.1 summarises how differences in the material properties of the construction materials were minimised and Section 4.4.2 describes the construction procedure of each test unit.

##### 4.4.1 Material Properties

Each test unit consisted of a reinforced concrete beam placed symmetrically on a concrete pedestal. Section 4.4.1.1 and Section 4.4.1.2 summarise the material properties of the concrete and reinforcement steel used for the construction of the test assembly respectively.

##### 4.4.1.1 Concrete

Table 4-3 summarises the concrete mix design that the beams were fabricated from. The mix had a specified slump of 100mm and an average strength of 37.5MPa after 28 days under standard conditions.

Differences in concrete strength between the six beams were minimised so that the influence of the applied loading history would be highlighted. Possible reasons for inconsistent concrete strengths were identified as the variability between different concrete batches and the age of the concrete at the time of testing. To eliminate

Table 4-3 Concrete Mix Design

Mix Type	30S
Mix Strength	30 MPa 20 mm
Cement Milburn GP	275 kg/m <sup>3</sup>
Free Water	168 Litres/m <sup>3</sup>
20 mm (SSD)	665 kg/m <sup>3</sup>
10 mm (SSD)	340 kg/m <sup>3</sup>
PAP6 (SSD)	665 kg/m <sup>3</sup>
Sand (SSD)	365 kg/m <sup>3</sup>
BV45 (Water Reducer)	250 mL/100 kg of cement

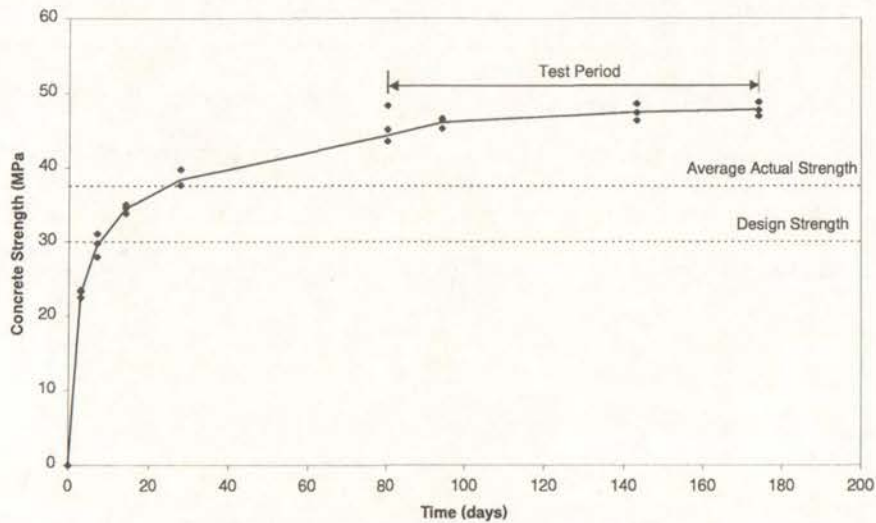


Figure 4-9 History of Concrete Strength

differences in concrete strength due to different production batches, the concrete for all six beams was placed in a single pour. To remove the change in concrete strength during the testing period, the concrete was cured for a period of 80 days instead of the standard 28 days. The history of the concrete strength over time illustrated in Figure 4-9 demonstrates that the concrete had gained the majority of its strength after 80 days. This meant the concrete strength was effectively constant during the test period.

#### 4.4.1.2 Reinforcing Steel

Table 4-4 summarises the chemical analysis of the longitudinal reinforcement. Manufacture of the reinforcement followed the New Zealand Standard for Steel Bars for the Reinforcement of Concrete (Standards New Zealand 1989). In Table 4-4, TCEQU is a measure of the carbon equivalent and the numbers in the second row are in percentages of the weight.

Differences in material properties of the reinforcing steel were minimised by obtaining the reinforcement steel for all six beams from the same production batch. Figure 4-10 presents stress-strain curves from four randomly selected longitudinal reinforcement samples. The stress-strain curves demonstrate that, while there were

Table 4-4 Chemical Analysis of Longitudinal Reinforcement

C	Mn	Si	S	P	TCEQU
0.21	1.23	0.34	0.027	0.008	0.449

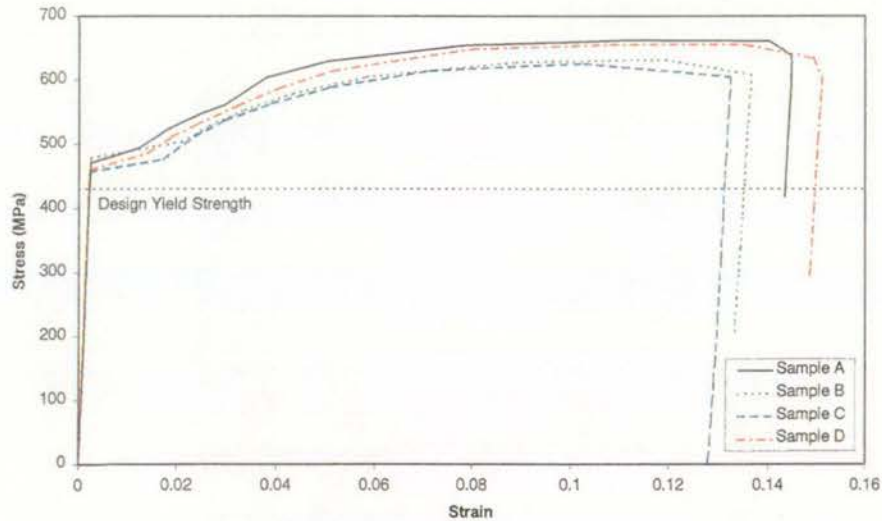


Figure 4-10 Stress-Strain Curve for Longitudinal Reinforcement

small differences in the strain hardening behaviour and ultimate strain value, the yield strength and Young's modulus were effectively constant. The average yield strength and Young's modulus was 466.9MPa and 196.5GPa respectively, with a maximum error of 2.9%.

#### 4.4.2 Construction of Test Assembly

The reinforced concrete beam section of the test assembly was constructed off-site to accommodate space constraints in the university laboratory. Figure 4-11 shows that the transverse reinforcement was positioned and tied while the reinforcement cage were situated in an upright position. The reinforcement cage was then rotated 90



Figure 4-11 Reinforcement Cage in Upright Position

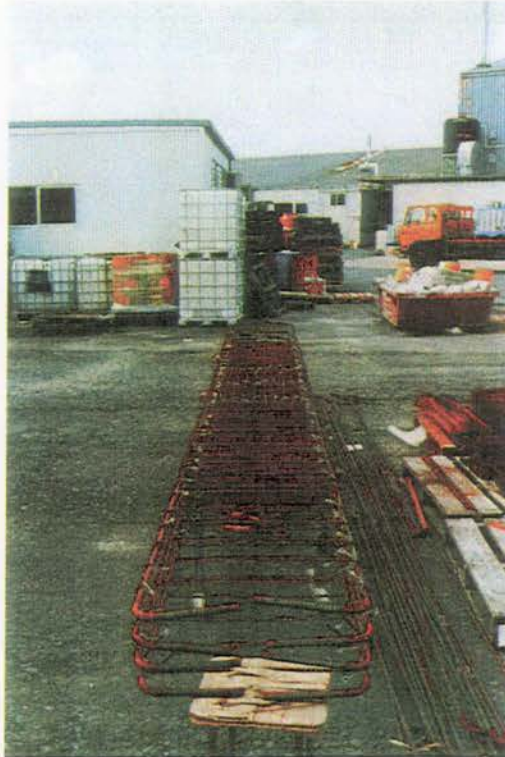


Figure 4-12 Reinforcement Cage Rotated 90 Degrees

degrees, as shown in Figure 4-12, to allow the horizontal joint steel to be positioned and tied.

Due to the lack of an overhead crane at the site, the boxing was constructed in its final upright position. The boxing consisted of a timber box beam placed either side of the reinforcement cage. The timber box beam was constructed from 75 x 50 timber and 20mm thick pinex floorboards, and was of sufficient strength to ensure that self-weight deflections were negligible. The beams were connected to bearers with M10-



Figure 4-13 Reinforcement Cages Positioned in Boxing

120 coach bolts at 960mm centres. This prevented lateral deflection of the timber box beam at its base. Once the reinforcement cages had been positioned, cross bracing, as illustrated in Figure 4-13, was placed on top of the boxing to ensure that there was no lateral spreading at the top of the beams during the pouring of the concrete.

#### 4.5 Test Set-Up

Testing of the 12 beams reported herein was conducted using the set-up presented in Figure 4-14 and Figure 4-15. Figure 4-14 reveals that the test set-up incorporated an assembly, consisting of two separate beams, placed symmetrically on a concrete pedestal. The test assembly was stressed to the strong floor with six stressing rods (loaded to 245kN each) that passed down the outside of the beam and the concrete pedestal as demonstrated in Figure 4-15. This ensured that structural deformations were not primarily attributable to rigid body rotation of the beam on its pedestal. Figure 4-15 indicates that the stressing rods were restrained at the top of the test assembly by a 100x100 RHS steel member.

Figure 4-14 illustrates that the beam on the opposite side of the pedestal to the actuator was left unsupported. This was to minimise the transfer of forces and strains from the first beam into the second beam due to testing of the first beam. A steel

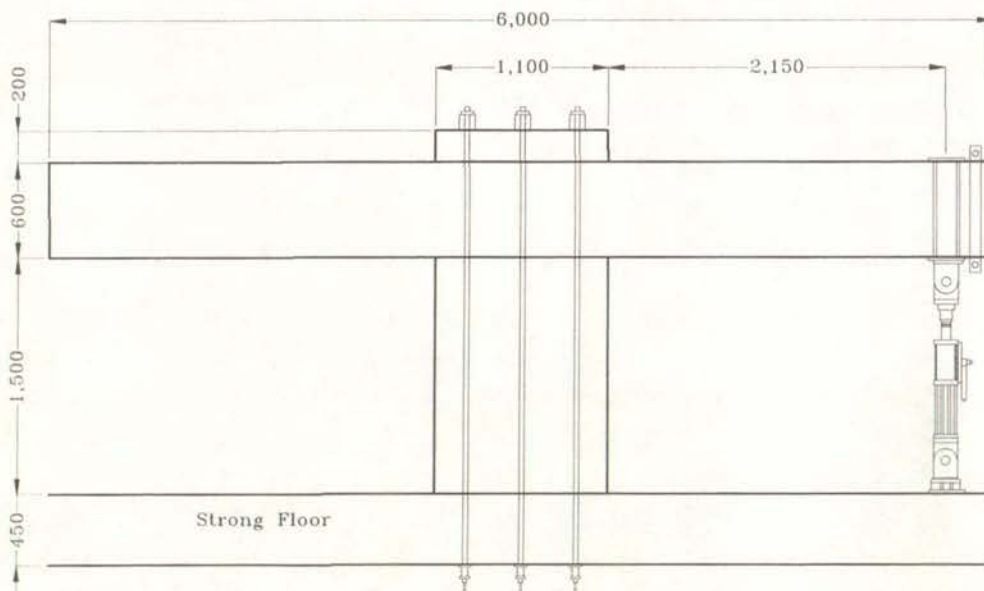


Figure 4-14 Front Elevation of Test Set-Up

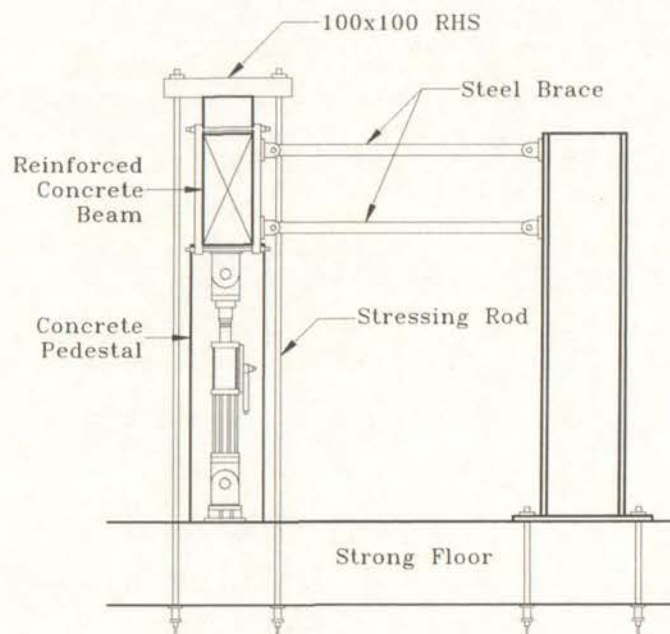


Figure 4-15 End Elevation of Test Set-Up

brace was placed on the end of the first beam to prevent any torsional response of the beam during testing. A 200mm high concrete appendage was placed on top of the beam in the joint region to ensure that a uniform stress was applied to the joint region from the stressing rods.

An actuator was placed 2.15m from the pedestal face to simulate the response of the prototype, discussed in Section 4.1, when subjected to seismic loading. This distance was based on half the clear distance between columns on Grids 1 and 8 in Figure 4-1, multiplied by the scale factor of two-thirds. The capacity of the actuator was 196kN in the push direction and 147kN in the pull direction. Recognising that symmetric loading was required for six of the twelve loading histories reported below, it followed that the lower of these two capacities limited the flexural strength of the beam. Using an overstrength factor of 1.3, an estimate of the probable maximum demand on the actuator was calculated to be  $\frac{1.3 \times 185}{2.15} = 111.9 \text{ kN}$ , ensuring that the actuator would be able to meet the maximum demand.

#### 4.6 Instrumentation

During fabrication of the reinforcement cage, steel studs were welded onto the longitudinal reinforcement at positions shown in Figure 4-16. Displacement transducers were connected to these studs and measured relative displacements between the studs during testing. The readings from the displacement transducers were collated using an HP data logger. This enabled the calculation of longitudinal reinforcement strains as well as flexural, shear, and rocking components of displacement for various loading stages.

The cantilever section of the test assembly was instrumented on both sides to allow for the possible failure of displacement transducers during testing. As was mentioned in Section 4.3.2, the joint region of the test assembly was modified to prevent damage from the first beam passing through the joint region into the second beam. It was assumed that these modifications eliminated relative displacements in the joint region. Instrumentation was placed on one side of the joint region to confirm the validity of this assumption.

Once the studs had been welded to the longitudinal reinforcement, grease tape was wrapped around the stud. A plastic tube was then placed over the grease tape and the stud. Once the concrete had cured, the grease tape and plastic tube were removed to leave a small gap around each stud. This eliminated the affects of cover concrete on

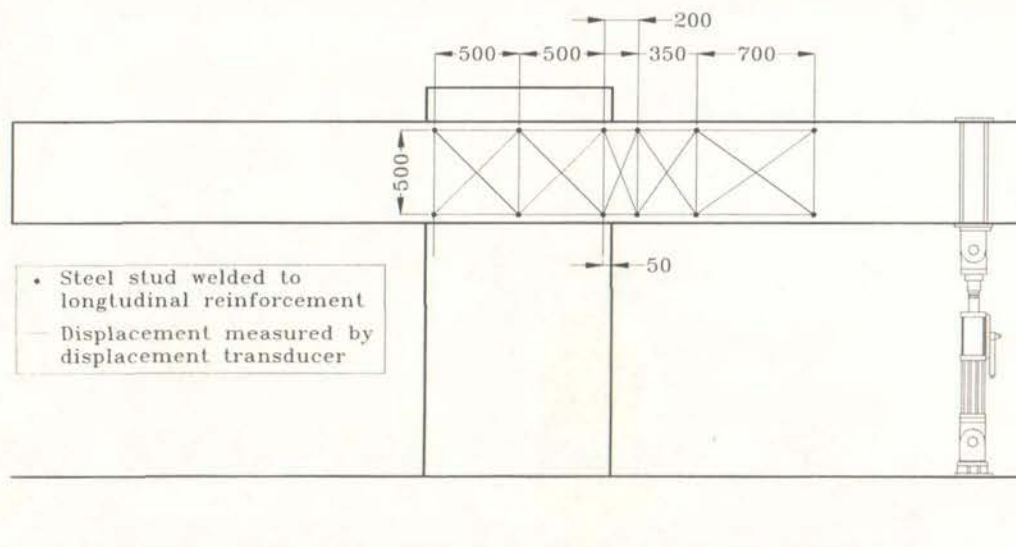


Figure 4-16 Instrumentation Layout

the transducer readings.

The displacement at the actuator was measured through two means. The first was through a linear variable deflection transformer (LVDT). The second measurement was obtained manually through a ruler attached to the beam. This provided confirmation of the LVDT reading.

#### 4.7 Calculation of Displacement Components

It was determined that the displacement at the actuator consisted of three components: flexural deformation, shear deformation, and rocking deformation. As covered in the previous section, steel studs were welded on to the longitudinal reinforcement at the positions shown in Figure 4-16. The displacement transducers that were connected to the studs allowed the three components to be isolated.

Flexural and shear displacement components as depicted in Figure 4-17(a) and Figure 4-17(b) respectively were calculated using procedures outlined by Ingham et al. (1994). These procedures also allowed moment-curvature data to be derived.

The rocking displacement component was calculated by extrapolating the rotation measured between points 1 and 2 to the end of the beam. This is demonstrated in Figure 4-18. Thus the deflection of the beam due to rocking on its base was calculated through the following equation:

$$\delta_r = \delta_2 + \frac{(l_1 + l_2)}{l_1} (\delta_1 - \delta_2). \quad \dots \text{Equation 4.13}$$

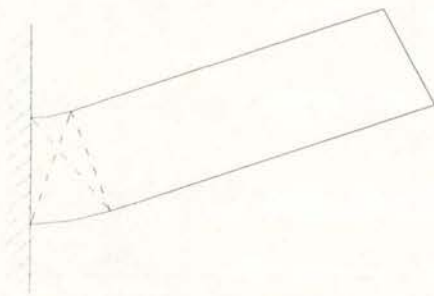


Figure 4-17(a) Flexural Displacement

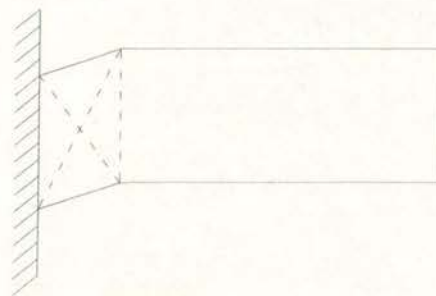


Figure 4-17(b) Shear Displacement

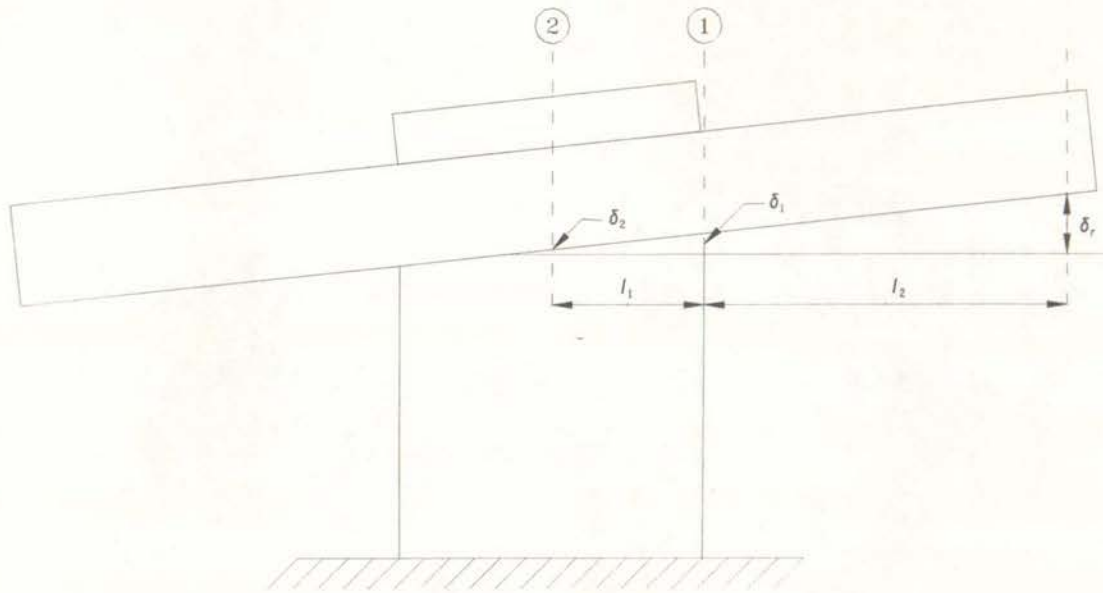


Figure 4-18 Rocking Displacement

## 5.0 Analytical Modelling

A model of the ten-storey building presented in Section 4.1 was generated in the computer programme Ruaumoko (Carr 1998) so that the seismic response of the building could be simulated. Ruaumoko was chosen because of the following reasons: Firstly, it is able to produce piece-wise time-history analyses for non-linear two-dimensional framed structures subjected to ground accelerations and secondly, damage indices form part of the analysis output and this feature was not available on other computer programmes.

Section 5.1 provides information on the model parameters and how the model was calibrated using experimental data from testing conducted using the New Zealand loading history and monotonic loading. Section 5.2 details the formation of the earthquake excitations that enabled the seismic response of the building to be simulated.

### 5.1 Model of Ten-Storey Building

The model set up in Ruaumoko was based initially on the ETABS model presented in 'The Red Book' (C&CA 1998). However, several changes were made to the model. The most significant change was that the building was modelled at two-thirds scale for four of the five acceleration histories. This change was made after testing using the first acceleration history, when it was concluded that modelling the building at the reduced scale avoided scaling issues associated with damage indices and the displacement time history of the critical section.

Four different structural elements were defined in the Ruaumoko model with Section 5.1.1 describing modelling of the beams, columns, beam-column joints, and floors. Section 5.1.2 details how the material and section properties of the structural elements were established. Section 5.1.3 and Section 5.1.4 describe how experimental data from testing conducted using the New Zealand loading history and the monotonic loading history were used to calibrate various model parameters and the chosen hysteresis model respectively. Section 5.1.5 reports on the properties of the mass and

damping matrices and Section 5.1.6 details the parameters on which the time-history analyses were based. Lastly, Section 5.1.7 explains how the necessary output data was obtained from the computer analysis.

Figure 5-1 and Table 5-1 present summary details of the two-thirds model of the ten-storey building presented in Section 4.1. A complete transcript of the model input file for the two-thirds scale model of the ten-storey building is provided in Appendix A.

### 5.1.1 Structural Members

Beam members were modelled as a one component (Giberson) beam member. Figure 5-2 illustrates that the model allowed a plastic hinge to form at one or both ends while the central length of the member remained elastic. The stiffness of the hinge was controlled by the tangent stiffness of the current point of the Modified Takeda hysteresis rule. Ruaumoko required the effective shear area to be input so that shear deformations could be calculated. However, this model took the effective shear area of the beams to be zero and thus, suppressed any shear deformation. This was justified due to the shear component only accounting for an extremely low percentage

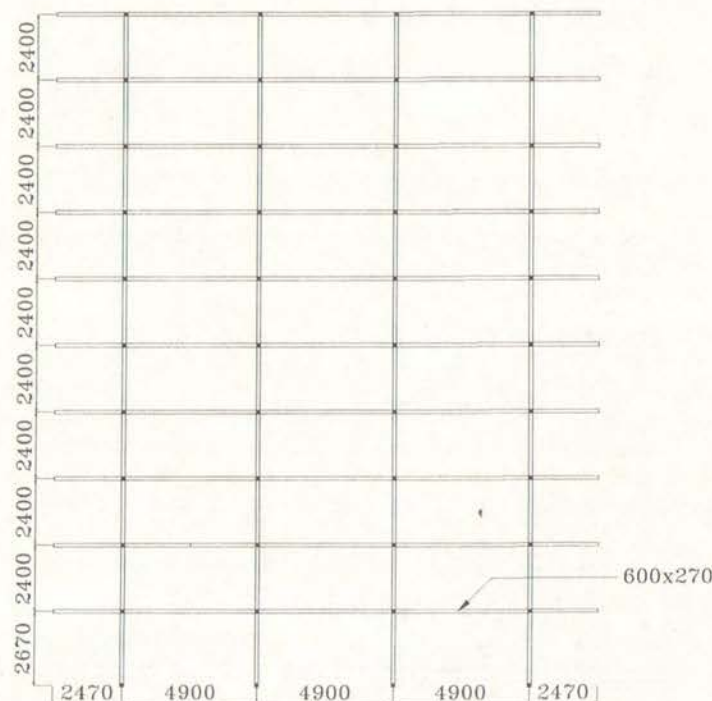


Figure 5-1 Model Dimensions

Table 5-2 Summary of Frame Properties

$T_1$ (s)	2.226
$T_2$ (s)	0.707
$I_b$ (mm <sup>4</sup> )	$1.28 \times 10^6$
$I_c$ (mm <sup>4</sup> )	$3.32 \times 10^6$
$E_c$ (MPa)	29200
Mass of Roof Level (kN)	1609.2
Mass of Typical Level (kN)	1472.65
Mass of First Level (kN)	1490.1
Rigid End Zone (mm)	300

of the elastic deflection.

Columns were modelled in Ruaumoko in one of two ways. The first floor columns were modelled as beam-column members using the elasto-plastic hysteresis model, whereas columns located on floors two through ten were modelled using the linear-elastic model. This is consistent with the design procedure outlined in the New Zealand Standard for the Design of Concrete Structures (Standards New Zealand 1995) where plastic hinges are only allowed to form at the base of the first storey column to ensure that a beam-sway mechanism forms. A yield interaction surface, based on section details presented in 'The Red Book', was provided for the first storey columns.

Ruaumoko allows beam-column joints to be modelled as either fully rigid joints or as elastic members. It was decided that modelling the joints as fully rigid instead of as elastic members was more realistic, even though modelling the joints as fully rigid elements failed to account for strain penetration into the joint. Modelling the joints as fully rigid was also consistent with experimental behaviour where strain penetration into the joint had been eliminated by welding additional reinforcement bars to the

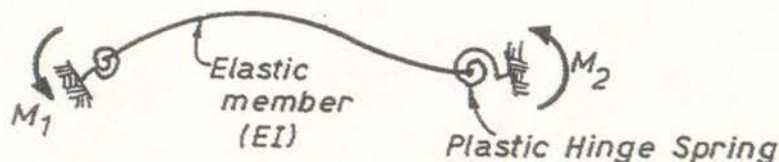


Figure 5-2 Giberson One Component Beam Model (Carr 1998)

longitudinal reinforcement in the joint region. The rigid beam-column joints are illustrated in Figure 5-3 as shaded regions.

The floor was modelled as a rigid diaphragm. This followed the approach in 'The Red Book' and was accomplished by coupling the horizontal displacements for each member at the same floor level.

### 5.1.2 Material Strengths

As previously mentioned, the model set up in Ruaumoko was based on the ETABS model presented in 'The Red book'. However, whereas material and section properties in the ETABS model were based on design values, the Ruaumoko model

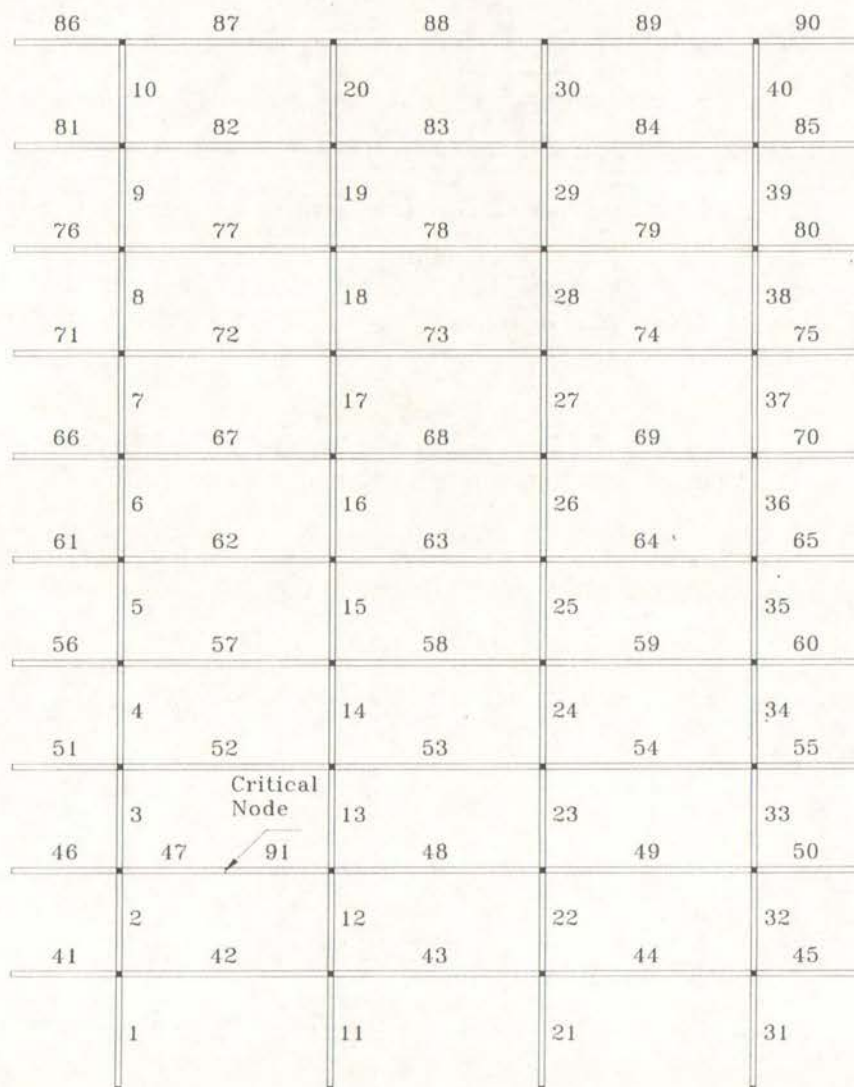


Figure 5-3 Ten-Storey Model with Beam Elements Numbered and Joint Elements Shaded

made use of actual material and section properties derived from experimental data. The section properties established experimentally were the yield strength and the initial stiffness of the beam. Material properties of concrete and reinforcing steel were found through the testing of random samples: the results of which are presented in Section 3.1. Actual material and section properties were used so that output from the Ruaumoko analysis would be consistent with experimental results obtained from applying the load histories detailed in Sections 6.2 through 6.4.

### 5.1.3 Calibration of Model Parameters

Experimental data from testing using the New Zealand loading history and from monotonic loading were used to model strength degradation, to determine the length of plastic hinges, and to calibrate damage indices. Experimental data from testing using the New Zealand loading history was used because the New Zealand loading history was the control for this experimental study.

To model strength degradation, Ruaumoko required the input of the ductility at which strength degradation began and the ductility and residual strength at which degradation ended. As reported in Section 7.1.1, the test unit subjected to the New Zealand loading history failed prematurely at ductility 10. It was estimated that the test subassembly would have dropped to 80% of its strength at ductility 12, if this premature failure had not occurred. A model of the test set-up presented in Section 4.5 was developed in Ruaumoko to replicate the loading sequence from the New Zealand loading history. The ductility at which strength degradation began was then altered in an iterative approach so that the strength degradation from the model matched the experimental behaviour from testing using the New Zealand loading history. Consistent behaviour was obtained by setting strength degradation to begin at ductility 6.8.

The length of the plastic hinge zone was established using measured experimental data from testing using the New Zealand loading history and formulae published by Paulay and Priestley (1992). Firstly, the yield curvature was established through rearranging

$$\delta_y = \phi_y \frac{l^2}{3}, \quad \dots \text{Equation 5.1}$$

where  $\delta_y$  is the yield displacement and from testing was found to be equal to 8.75mm, and  $l$  is the distance from the face of the concrete pedestal to the actuator and was equal to 2150mm. Section 6.2 outlines the procedures that were applied to determine the yield displacement. The plastic hinge length was then calculated through rearranging

$$\delta_p = \delta_{ult} - \delta_y = \theta_p \left( l - \frac{l_p}{2} \right) = (\phi_{ult} - \phi_y) l_p \left( l - \frac{l_p}{2} \right) \quad \dots \text{Equation 5.2}$$

and utilising the yield curvature from Equation 5.1 and an ultimate displacement and corresponding curvature of 70.59mm and 0.07947/m from testing using the New Zealand loading history. This gave a plastic hinge length of 430mm, which was consistent with the observed behaviour during testing. In Equation 5.2,  $\delta_p$  was the plastic deformation,  $\phi_{ult}$  was the ultimate curvature, and  $l_p$  was the length of the plastic hinge zone.

The calculation of damage indices required the ultimate ductility of the beam to be determined. As reported in Section 7.1.1, the stroke of the actuator was reached at ductility 22 under monotonic loading. Extrapolation of the force-displacement response gave an ultimate ductility equal to 23.

#### 5.1.4 Verification of Hysteresis Model

Ruaumoko contains 36 hysteresis models representing the inelastic behaviour of frame and spring members. Of the 36 models, many could not be selected due to their oversimplification of hysteresis behaviour or because they represented other elements and situations; for example, the behaviour of face-loaded masonry wall units. The remaining models were then judged on the failure mechanism inherent in the model. Lastly, modelling of pinching in the hysteresis loops was compared with that observed in experimental data. Through applying the above criteria, the Modified Takeda hysteresis model was chosen.

The Modified Takeda hysteresis model was developed by Otani (1974) so that the inelastic behaviour of a frame member could be simulated. It was based on the model proposed by Takeda et al. (1970) but was derived using a bilinear primary curve and included more rules for small amplitude load reversals. The model was formed on an assumption that the member would fail under a flexural failure mode, and that extensive damage due to shear deformations or bond deterioration would not occur.

As was discussed in Section 5.1.3, a model of the test set-up presented in Section 4.5 was developed in Ruaumoko to replicate the loading sequence from the New Zealand loading history. The variables were then altered in an iterative approach so that the hysteresis behaviour from the model matched the experimental behaviour from the New Zealand loading history.

The five variables that need to be determined were variables associated with the unloading stiffness ( $\alpha$ ), the reloading stiffness ( $\beta$ ), the flexural bilinear factor ( $r$ ), the reloading stiffness power factor, and the type of unloading behaviour. The lower bound for  $\alpha$  and  $\beta$  was 0 and the upper bound was 0.5 and 1.0 respectively. Increasing  $\alpha$  decreases the unloading stiffness and increasing  $\beta$  increases the reloading stiffness. It was established from the model of the test set-up that the appropriate parameter values were  $\alpha = 0.42$ ,  $\beta = 0.90$ ,  $r = 0.035$ , and the reloading stiffness power factor was equal to 1.0. The unloading behaviour could be modelled through either the method proposed by Emori and Schnobrich (1978) or by the method applied in the computer programme DRAIN-2D (Kanaan and Powell 1973). The test model applied the method proposed by Emori and Schnobrich, which is illustrated in Figure 5-4.

Figure 5-5 presents A comparison of hysteresis behaviour from testing using the New Zealand loading history and the Modified Takeda model. It can be seen that there is excellent agreement until ductility six and reasonable agreement thereafter. The adaptability of the model parameters to other loading histories was investigated with comparison of the hysteresis behaviour from testing using the Berkeley loading history and the Modified Takeda hysteresis rule located in Appendix B. It was established that  $\alpha$  and  $r$  were consistent for testing using different loading histories

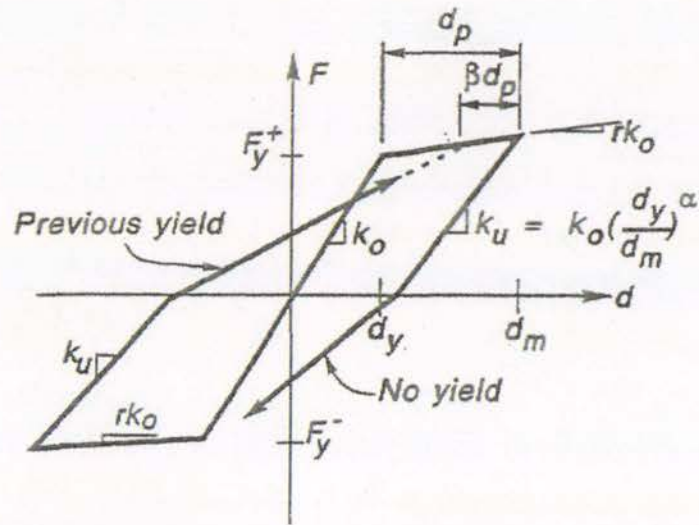


Figure 5-4 Emori and Schnobrich Unloading Curve (Carr 1998)

whereas it was necessary to calibrate  $\beta$  and the strength degradation parameters for each test.

### 5.1.5 Mass and Damping Matrices

Ruaumoko contains five damping model options ranging from Rayleigh or Proportional damping models through to Caughey damping. The model reported herein applied the Rayleigh damping model where the damping matrix is given by

$$C = \alpha M + \beta K \quad \dots \text{Equation 5.3}$$

where  $M$  and  $K$  are the mass and stiffness matrices for the structure. The initial

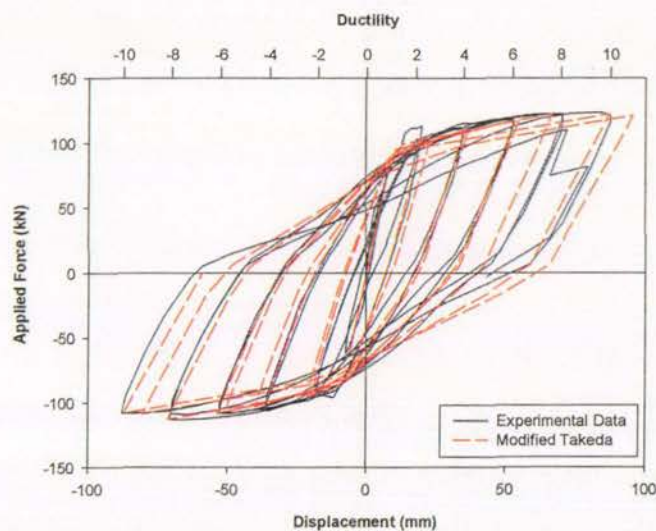


Figure 5-5 Comparison of Experimental Data and Takeda Model

stiffness matrix was used in the analysis. The Rayleigh damping model required the user to specify the amount of damping for two modes. Specification of these two points enabled the damping for all modes to be established. In this model, 5% of critical damping was specified for modes one and ten. This ensured that the fraction of critical damping was less than 100% for the highest modes.

Ruaumoko contained three options for modelling of the mass matrix: lumped mass matrix, diagonal mass matrix, and consistent mass matrix. The model reported herein applied the lumped mass matrix because this reduced the required computational effort.

#### 5.1.6 Time History Analysis

A dynamic time history analysis using the Newmark constant average acceleration method to integrate the dynamic equation of equilibrium was performed. Further iteration could be carried out at each time step, but this option was suppressed in the model reported herein. The time step for the analysis was chosen to be 0.01s. This method was unconditionally stable and had the advantage that not all the degrees of freedom were required to have an associated mass. The analysis assumed that the displacements were of insufficient size to affect members' stiffness and thus, the nodal coordinates did not change during the analysis. P-delta effects were ignored in the analysis.

#### 5.1.7 Model Output Data

The model was set up so that displacements, velocities, and accelerations of nodes and member forces were sent to the post-processor dynaplot file at each time step. This enabled information such as force-time histories, displacement-time histories, and hysteresis plots to be displayed in graphical form.

The elevation of the building frame presented in Figure 5-3 reveals that an additional node was positioned midway between the first and second columns at Level 2. This was the critical design level discussed in Section 4.1, and hence this node allowed the vertical-displacement-time history of the test unit to be established.

The displacement-time history applied in the laboratory was established through fixing the beam at the right hand end of member 91 and taking the relative deflection between the two ends. Figure 5-6 illustrates that the total displacement obtained from the model consisted of three components: the vertical deflection of the beam at the critical node, the vertical deflection of the joint, and the deflection corresponding to the rotation of the joint. Thus the total displacement,

$$v_{total} = v_{joint} + v_{rot} + v_{node}, \quad \dots \text{Equation 5.4}$$

was calculated at the critical node for each time step, and digitised so that the displacement sequence could be applied in the laboratory.

## 5.2 Earthquake Excitations

Four separate earthquake acceleration records were applied sequentially at differing scales and in various orders to generate five simulated acceleration histories. At the end of each record, approximately 10 seconds of free vibration was applied. This was to ensure that the building was at rest before the next record was applied and also to give an indication of the viscous damping decay curve. Table 5-2 presents details of the four earthquake records that were chosen to generate the five acceleration histories used in this study with Table 5-3 summarising the sequence of the records and the corresponding scale factors. Sections 5.2.1 through 5.2.5 provide specific details of the five acceleration histories summarised in Table 5-3.

In Ruaumoko, earthquakes can be applied in one of five formats. Each earthquake

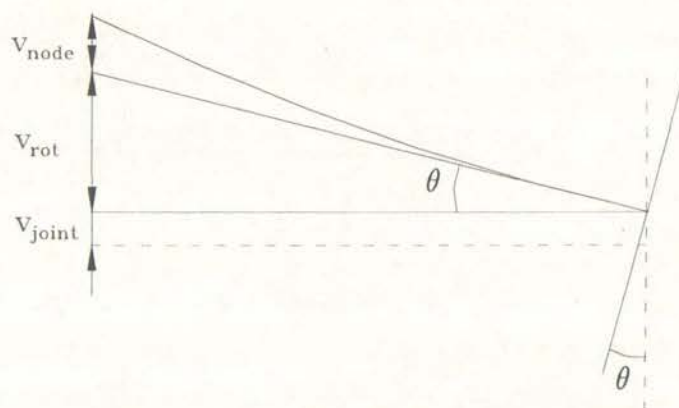


Figure 5-6 Components of Relative Vertical Deflection at Critical Node

Table 5-2 Earthquakes Records Selected for Generating Acceleration Histories

Earthquake	Acceleration Record	Recording Station	PGA (g)
Normalised El Centro		Artificial Earthquake	0.36
Northridge		Pacoima Dam	1.28
El Centro NS		Imperial Valley	0.35
Kobe EW		Kobe JMA Observatory	0.63

record for this study was converted into the FREE format. This enabled separate earthquake records to be combined into an earthquake sequence that was then applied to the computer model. This sequence of earthquakes was only applied in the x-direction. Each earthquake record was digitised at 0.02s and the initial ground velocity and the initial ground displacement were both assumed to equal zero for each earthquake.

Table 5.3 reveals that some of the base records were scaled differently for acceleration history A than for acceleration histories B–E. This was due to the change in computer model from the full-scale model to the two-thirds model and also because an increase in damage was sought. This is detailed further in Section 5.2.2. Scaling was conducted by multiplying the acceleration amplitude by the scale factors in Table 5-3.

Table 5.3 also reveals that an additional earthquake record was applied for the final three acceleration histories. The inclusion of another damaging earthquake record was to ensure that the test subassembly would fail during the application of the acceleration sequence.

Table 5-3 Summary of Five Earthquake Histories

Acceleration History	Event	Earthquake	Scale Factor	PGA (g)
A	1	Normalised El Centro	1.10	0.39
	2	Northridge	1.00	1.28
	3	El Centro NS	2.00	0.70
	4	Kobe EW	1.61	1.02
B	1	Normalised El Centro	1.10	0.39
	2	Northridge	1.20	1.54
	3	El Centro NS	1.00	0.35
	4	Kobe EW	1.20	0.76
C	1	Normalised El Centro	1.10	0.39
	2	Kobe EW	1.20	0.76
	3	Northridge	1.20	1.54
	4	El Centro NS	1.00	0.35
	5	Kobe EW	1.50	0.95
D	1	Northridge	1.20	1.54
	2	El Centro NS	1.00	0.35
	3	Normalised El Centro	1.10	0.39
	4	Kobe EW	-1.20	0.76
	5	Kobe EW	1.50	0.95
E	1	Northridge	1.20	1.54
	2	Kobe EW	1.20	0.76
	3	El Centro NS	1.00	0.35
	4	Normalised El Centro	1.10	0.39
	5	Kobe EW	1.50	0.95

### 5.2.1 Acceleration History A

Acceleration history A was used to calibrate the scale factors for each of the earthquake records in the following four acceleration histories. The order of the individual records within the acceleration sequence was selected randomly.

Figure 5-7 details that acceleration history A consisted of four sequentially applied records. This was used to generate the displacement sequence for the test subassemblage. The first record was the artificial earthquake based upon the North-South component from the El Centro earthquake. Its ductility 1 response spectrum matches the NZS 4203: 1992 intermediate soil 'C' coefficient. When scaled by  $Z = 0.8$  and increased by 10% it could be expected to force the frame to a ductility 6 response. The second record was recorded from the Pacoima dam station during the Northridge earthquake and was not scaled. The third record was the North-South

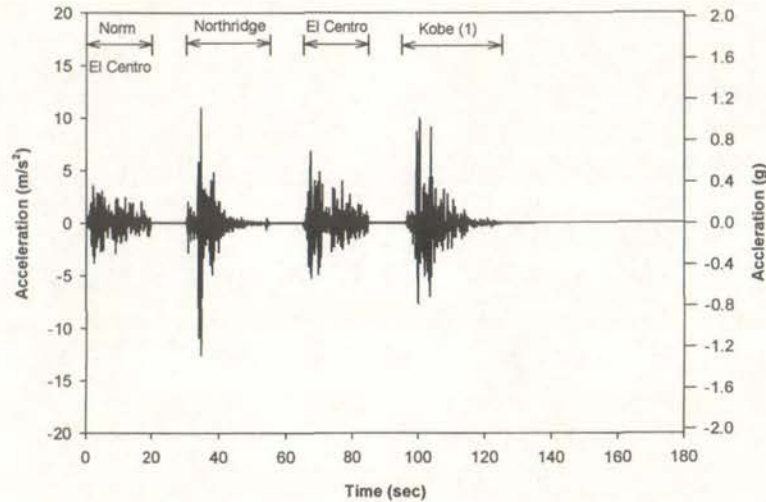


Figure 5-7 Acceleration History A

component from the El Centro earthquake scaled up by 100%. The last earthquake was the East–West component of the Kobe earthquake. This was scaled up by 61% to obtain ductility 6 response of the frame.

Scaling of the earthquake records was necessary because of two reasons. The first was because the analysis in 'The Red Book' was three-dimensional, whereas the analysis conducted for this report was two-dimensional. Hence, torsion was not included for the analysis reported herein, and this resulted in a lower response. The second reason was due to scaling of the intermediate soil 'C' coefficient by a structural performance factor and a zone factor. This further reduced the response of the building to seismic excitation.

The displacement-time history for the critical beam was isolated and scaled by two-thirds to give the displacement-time history to be applied in the laboratory. This can be seen in Figure 5-8. Figure 5-8 reveals that the maximum ductility resulting from the Normalised El Centro record was equal to 3.3. This is significantly less than the ductility 6 response that was expected and was due to the computer model being based on actual properties of the test specimens.

Figure 5-9 presents the displacement-time history of the top storey. It reveals that the top storey underwent an approximate maximum ductility equal to 3, which was significantly lower than the maximum ductility recorded at the critical beam. This

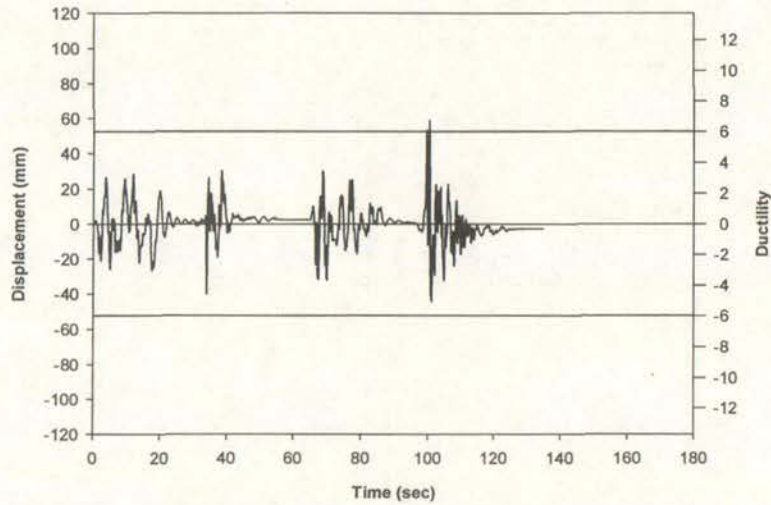


Figure 5-8 Critical Beam Displacement-Time History (Acceleration History A)

was because the profile of the deflected shape at the maximum deflection was parabolic instead of triangular. Thus, the plastic hinges in the critical beam formed prior to the plastic hinges in the upper levels and hence, the critical beam was required to resist greater ductility demand than the entire structure. This was due to modelling the beam-column joints as rigid joints and also not reducing member sizes for the upper levels. The ductility 1 displacement at the top storey was determined through a pushover analysis: the results of which are presented in Section 5.2.2.

Values for the five damage indices calculated as part of the Ruaumoko analysis were recorded. It was at this stage that a discrepancy was discovered between the damage

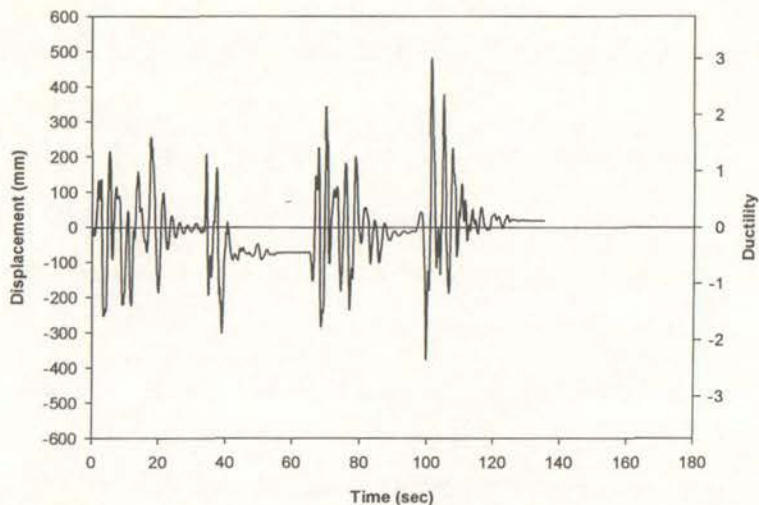


Figure 5-9 Top Storey Displacement History (Acceleration History A)

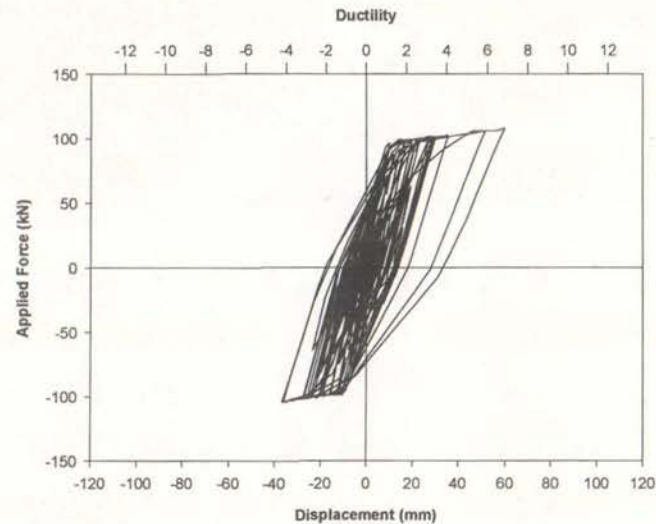


Figure 5-10 Predicted Force-Displacement Response (Acceleration History A)

indices calculated from the Ruaumoko analysis and the damage indices calculated using the predicted force-displacement response from the Ruaumoko analysis. It was postulated that because ductility values in Ruaumoko were based on curvature, the plastic hinge length specified in the input data would effect the values of the damage indices. This was confirmed through varying the plastic hinge length and re-running the analysis. It was found that the values of each damage index were strongly dependent on the plastic hinge length. However, the plastic hinge length did not affect the displacement-time history. Hence, for the remaining analyses the damage indices were calculated using the predicted force-displacement response from the Ruaumoko analysis.

The predicted force-displacement response of the corresponding test subassemblage from the Ruaumoko analysis is shown in Figure 5-10 with the resulting damage indices presented in Table 5-4. Figure 5-10 reveals that there were few cycles to large ductility levels resulting from acceleration history A. This led to the low values for

Table 5-3 Predicted Damage Indices (Acceleration History A)

Damage Index	Value
Cosenza et al.	0.26
Roufaiel and Meyer	0.29
Park and Ang	0.54
Banon and Veneziano	0.42
Bracci et al.	0.54

each of the damage indices, with no damage index predicting failure of the test subassemblage.

### 5.2.2 Acceleration History B

As reported previously, the analysis for acceleration histories B–E was conducted using a two-thirds scale model of the frame. This was because it was difficult to translate the damage index calculations from the full-scale model to the laboratory, as some of the damage indices were not dimensionally compatible. It was decided to develop a new numerical model that had the same period as the original model, but with member sizes identical to member sizes from the laboratory subassemblage. The period of the new numerical model and the original model were kept identical so that the results from testing using acceleration histories B–E could be compared with the results from testing using acceleration history A. Modelling the properties of the laboratory subassemblage meant that the damage index calculations were immediately transferable to the laboratory situation.

Using the new model, it was established that the magnitude of the building's displacements was dependent on the model's scale. This was because the period for the full-scale model and the two-thirds model were both equal to 2.226s. Reducing the scale of the model from a full-scale model to a two-thirds model also reduced the stiffness of the frame members by two-thirds. Thus, with reference to

$$T = 2\pi \sqrt{\frac{m}{k}}, \quad \dots \text{Equation 5.5}$$

it was necessary to also reduce the mass by a factor of two-thirds so that the period of the two models was kept identical. However, as reported in Table 4-1, reducing the size of a member by two-thirds reduces the member's strength by four-ninths. Hence, the lateral force coefficient in the equation (Equation 4.8.1 in NZS 4203:1992),

$$V = CW_t, \quad \dots \text{Equation 5.6}$$

was reduced by two-thirds, which resulted in the two-thirds model experiencing a higher ductility response than the full-scale model.

This was confirmed by comparing the results from a pushover analysis of the full-scale model and the two-thirds model, as shown in Figures 5-11(a) and 5-11(b). For seismic weights of 29,562kN and 20,019kN respectively for the full-scale model and the two-thirds model, the lateral force coefficients were calculated to be 0.0775 and 0.0544. Thus, reducing the scale of the analytical model was largely responsible for the increase in damage between acceleration history A and acceleration B.

Figure 5-12 illustrates that acceleration history B consisted of four earthquake records applied sequentially in the same order as for acceleration history A. The four records were selected to represent a range of magnitudes and hence were scaled by different factors to achieve this.

The first record was the artificial earthquake based upon the North-South component from the El Centro earthquake. This was scaled up by 10% so that ductility 6 response could be expected. The second record was the Pacoima dam station record from the Northridge earthquake. This record was scaled up by 20% so that ductility 8 response was obtained. The third record was the North-South component from the El

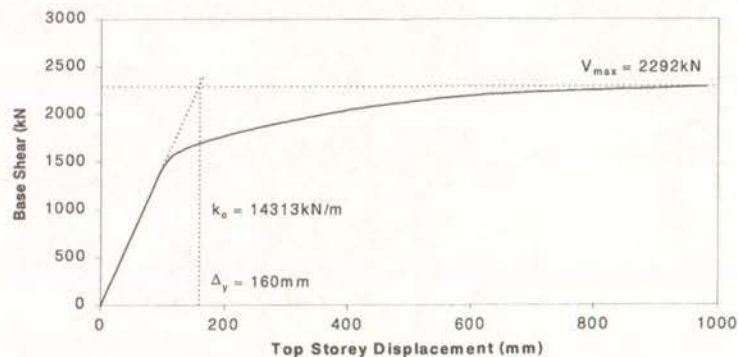


Figure 5-11(a) Pushover Analysis of Full-Scale Model

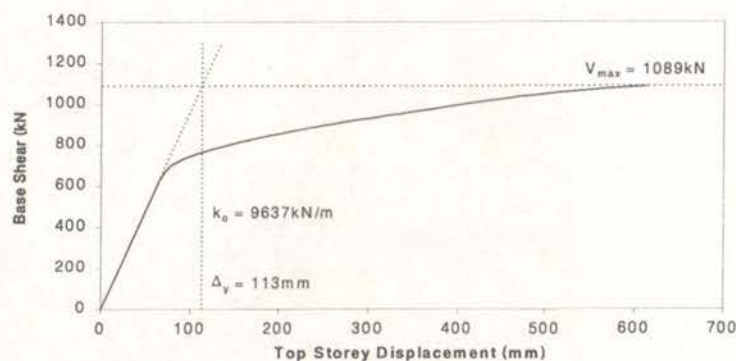


Figure 5-11(b) Pushover Analysis of Two-Thirds Model

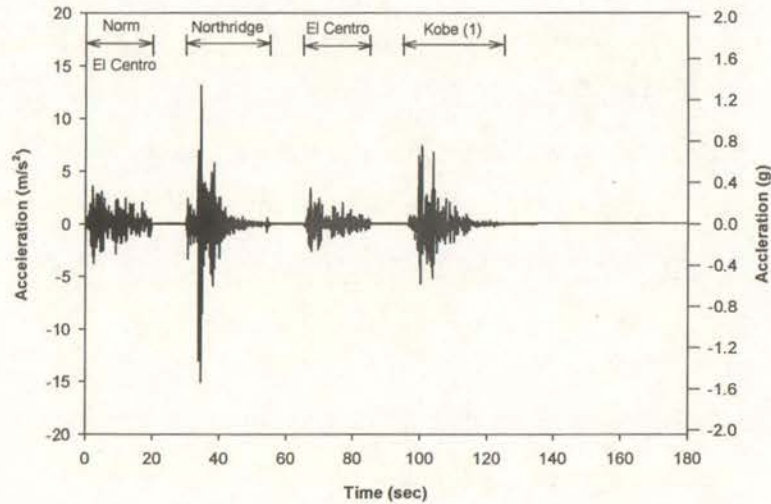


Figure 5-12 Acceleration History B

Centro earthquake. This record was not scaled because an earthquake of low magnitude was determined to be appropriate. This was to represent possible aftershocks or minor events prior to a severe earthquake. The last record was the East–West component from the Kobe earthquake. The record from the Kobe earthquake was scaled up by 20% so that ductility 10 displacements were achieved.

The displacement-time history for the critical beam was isolated. No scaling of the displacement-time history was required because the displacement-time history was established using the two-thirds model in Ruaumoko. Figure 5-13 presents the displacement-time history resulting from application of acceleration history B, and

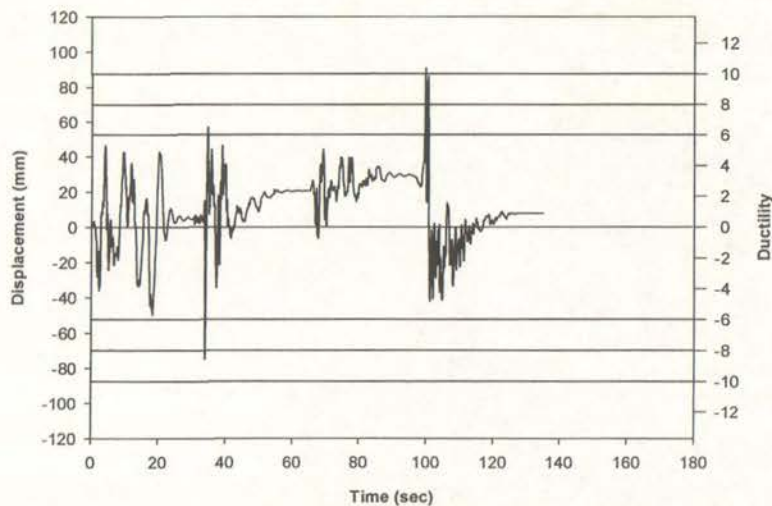


Figure 5-13 Critical Beam Displacement Time History (Acceleration History B)

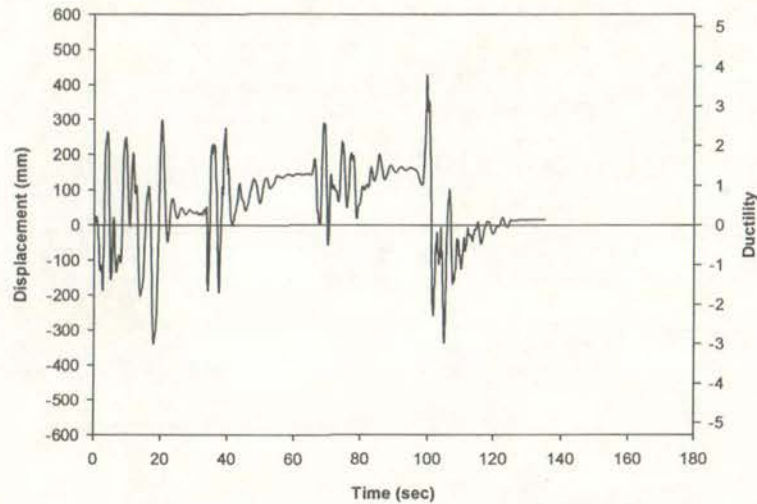


Figure 5-14 Top Storey Displacement-Time History (Acceleration History B)

clearly shows that the various earthquake records resulted in the targeted displacement ductility demands. Figure 5-14 illustrates the displacement-time history for the top storey and reveals that a lower ductility response was again obtained.

Figure 5-15 details the predicted force-displacement response of the test subassembly for acceleration history B. Table 5-5 presents the resulting prediction of the damage indices' values. Figure 5-15 reveals that there were more cycles to high ductility values in this acceleration history than for acceleration history A. This is reflected in the predicted damage indices, where all five damage indices for this acceleration history are larger than the damage indices from acceleration history A.

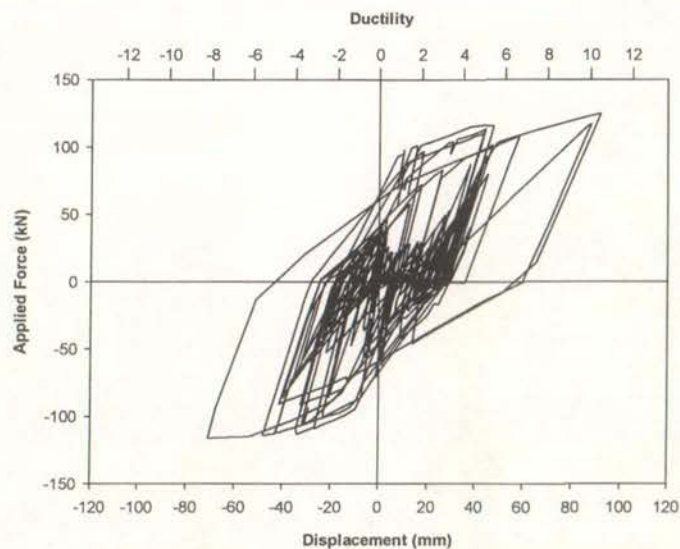


Figure 5-15 Predicted Force-Displacement Response (Acceleration History B)

Table 5-5 Predicted Damage Indices (Acceleration History B)

Damage Index	Value
Cosenza et al.	0.42
Roufaiel and Meyer	0.45
Park and Ang	0.75
Banon and Veneziano	0.55
Bracci et al.	0.70

However, failure was still not predicted by any of the five damage indices although the Park and Ang index did predict that severe damage would occur.

### 5.2.3 Acceleration History C

Figure 5-16 illustrates that an additional earthquake record was included in acceleration history C to ensure that failure occurred. The first four records in acceleration history C were scaled by the same factors as in acceleration history B. This enabled comparisons between the observed response and derived experimental data for the two tests to be made. However, the records were applied in a different order in this acceleration history than in acceleration history B. As with acceleration histories A and B, the first record was the artificial earthquake based upon the North-South component from the El Centro earthquake. The second and third records were the East-West component from the Kobe earthquake and the Northridge earthquake recorded at the Pacoima dam station respectively. The fourth record was the North-

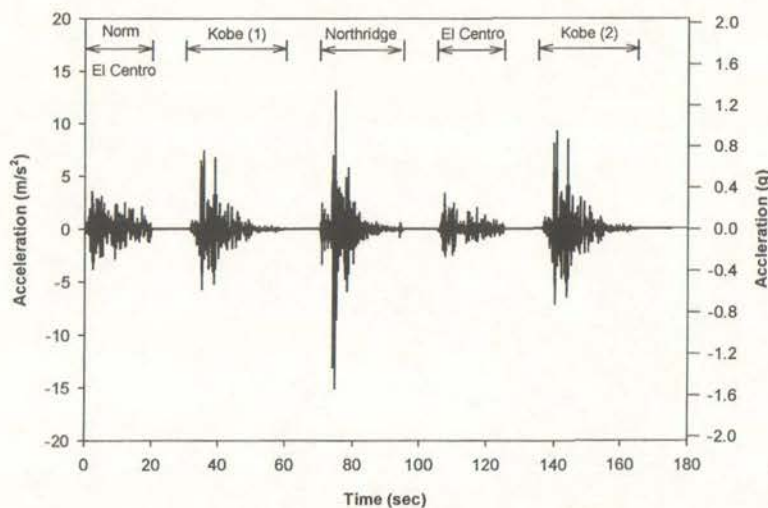


Figure 5-16 Acceleration History C

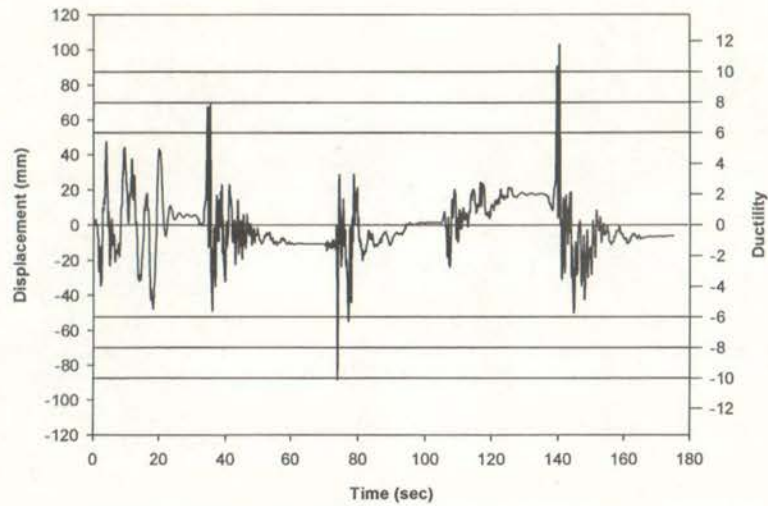


Figure 5-17 Critical Beam Displacement Time History (Acceleration History C)

South component from the El Centro earthquake. The last record was a repeat of the East-West component from the Kobe earthquake. However, the second Kobe record was scaled up by 50%, which was in contrast to the first Kobe record that was scaled up by 20%. This was to ensure that failure of the test subassemblage would be induced.

The displacement-time history for the critical beam was isolated, with the subassemblage displacement-time history resulting from application of acceleration history C presented in Figure 5-17. The displacement-time history of the top storey is displayed in Figure 5-18. As with previously reported acceleration histories, much

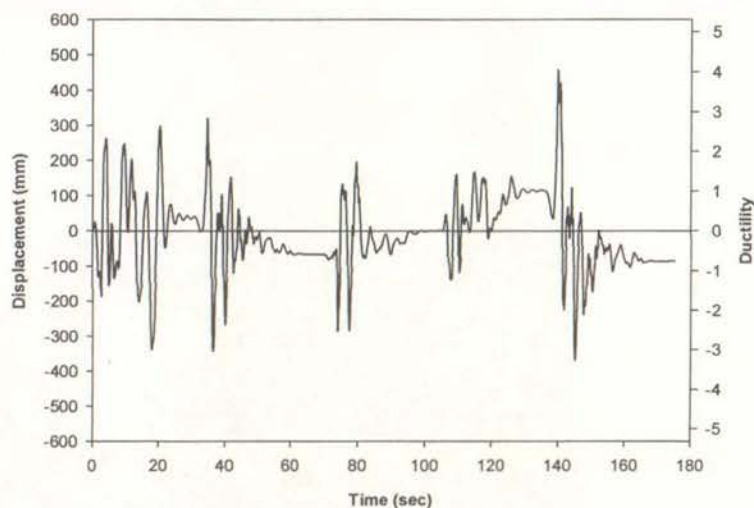


Figure 5-18 Top Storey Displacement-Time History (Acceleration History C)

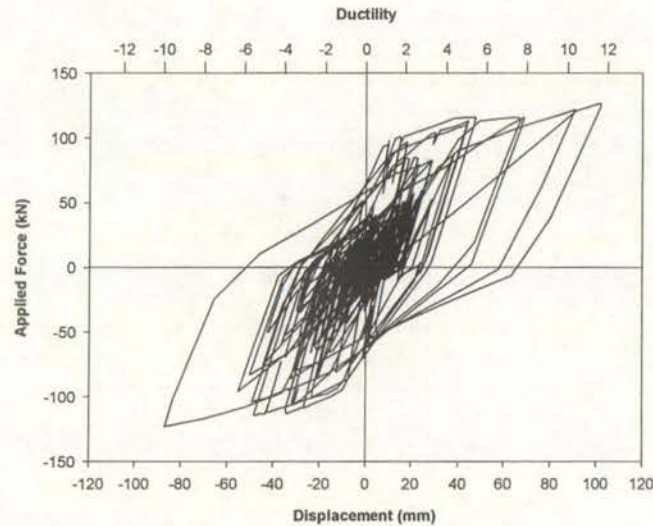


Figure 5-19 Predicted Force-Displacement Response (Acceleration History C)

lower response was obtained for the top storey than the critical beam located on Level 2.

Figure 5-19 presents the predicted force-displacement response of the test subassembly subjected to acceleration history C with Table 5-6 listing the resulting damage indices. Figure 5-19 reveals that the predicted force-displacement response from acceleration history C had the highest number of high ductility cycles of acceleration histories A–C. This is reflected in Table 5-6 where failure is predicted by the Park and Ang index and severe damage is predicted by the Bracci et al index. This increase in predicted damage was due to the extremely large ductility half cycle applied in the second Kobe record near the conclusion of the test. Thus, the application of an additional earthquake had the desired effect on the predicted response.

Table 5-6 Predicted Damage Indices (Acceleration History C)

Damage Index	Value
Cosenza et al.	0.49
Roufaiel and Meyer	0.50
Park and Ang	0.96
Banon and Veneziano	0.64
Bracci et al.	0.84

#### 5.2.4 Acceleration History D

Figure 5-20 illustrates that acceleration history D consisted of five earthquake records scaled by the same factors as in acceleration history C but applied in a different sequence. The first record was the Northridge earthquake recorded at the Pacoima dam station. A severe earthquake was applied first in this acceleration history so that the results from testing using this acceleration history could be compared against acceleration histories C–E where a moderate earthquake was applied first. The second and third records were the North–South component from the El Centro earthquake and the artificial earthquake based upon North–South component from the El Centro earthquake. The fourth record was the East–West component from the Kobe earthquake. As with acceleration history C, the last record was a repeat of the East-

West component from the Kobe earthquake scaled up by 50% instead of 20%.

Figure 5-21 displays the displacement-time history for the test subassemblage resulting from acceleration history D. Figure 5-22 details the displacement-time history from the top storey, with comparable characteristics evident to previously reported acceleration histories.

Figure 5-23 illustrates the predicted force-displacement response of the test subassemblage from application of acceleration history D with Table 5-7 detailing the

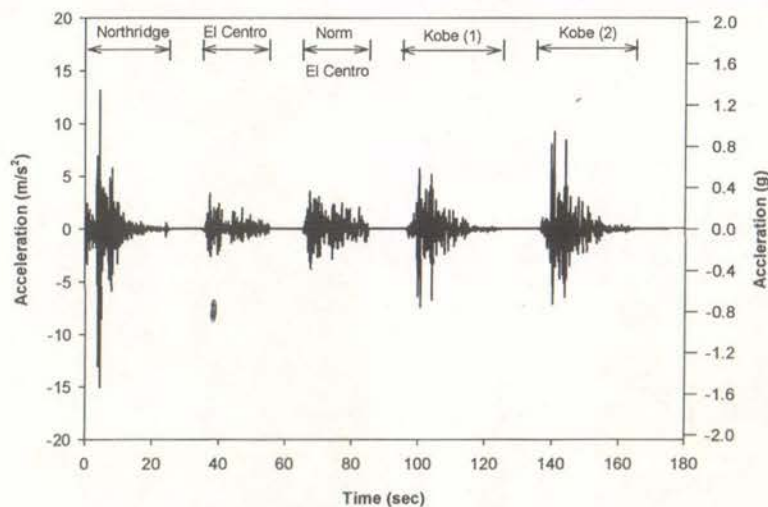


Figure 5-20 Acceleration History D

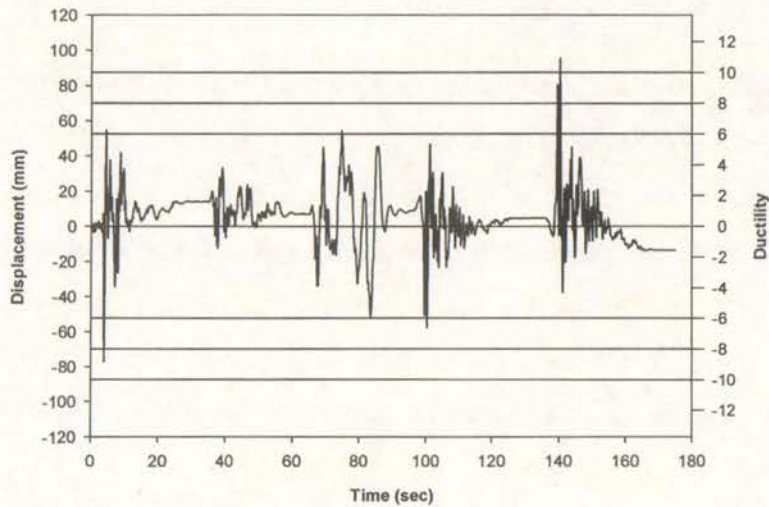


Figure 5-21 Critical Beam Displacement Time History (Acceleration History D)

resulting damage indices. A feature of the predicted force-displacement response is the reduction in force required to achieve positive and negative displacements after the application of the large negative displacement early in the test sequence. This reduction in force decreased the area inside the hysteresis loops and hence, decreased the values of damage indices that included energy dissipation in their formulation. This was reflected in Table 5-7 where values from the Park and Ang index, the Banon and Veneziano index, and the Bracci et al. index were all smaller than the corresponding values from acceleration history C.

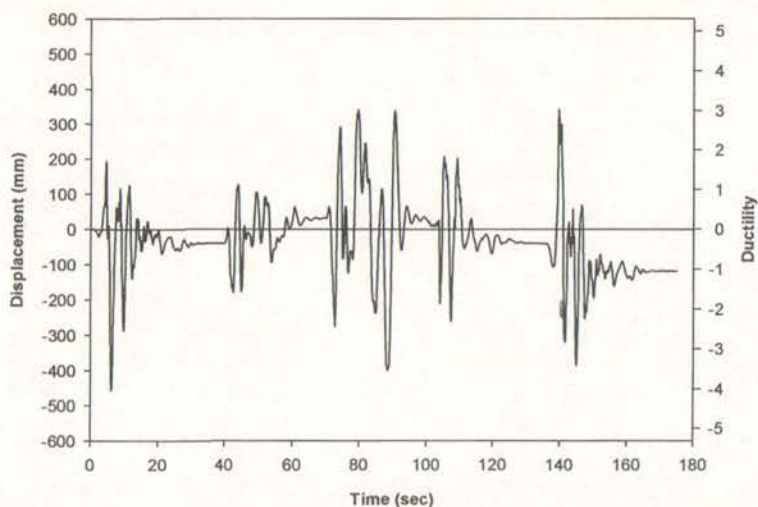


Figure 5-22 Top Storey Displacement-Time History (Acceleration History D)

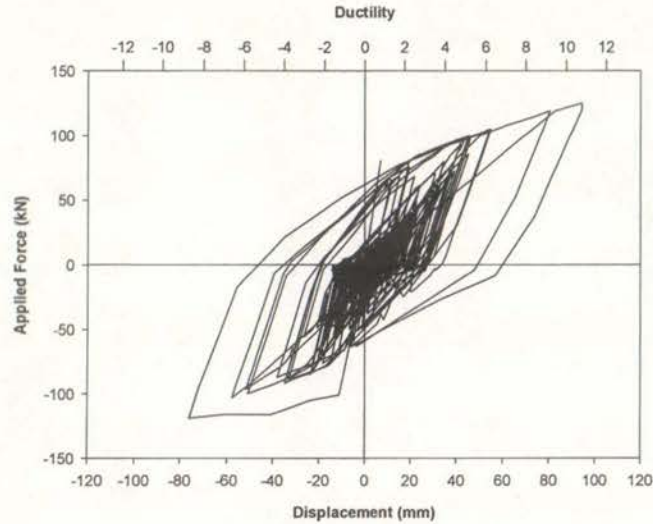


Figure 5-23 Predicted Force-Displacement Response (Acceleration History D)

### 5.2.5 Acceleration History E

As with acceleration history D, the first record in acceleration history E was the Northridge earthquake recorded at the Pacoima dam station. The second record was the East–West component from the Kobe earthquake. The third and fourth records were the North–South component and the artificial earthquake based upon the North–South component from the El Centro earthquake. As for acceleration histories B and C, the final record was the East–West component from the Kobe earthquake scaled by a factor of 1.5. Figure 5-24 details acceleration history E.

Figure 5-25 and Figure 5-26 present the resulting displacement-time history for the critical beam and the top storey for acceleration history E. Similar response to previously reported acceleration histories were observed.

Figure 5-27 illustrates the predicted force-displacement response for the test

Table 5-7 Predicted Damage Indices (Acceleration History D)

Damage Index	Value
Cosenza et al.	0.45
Roufaiel and Meyer	0.47
Park and Ang	0.89
Banon and Veneziano	0.60
Bracci et al.	0.81

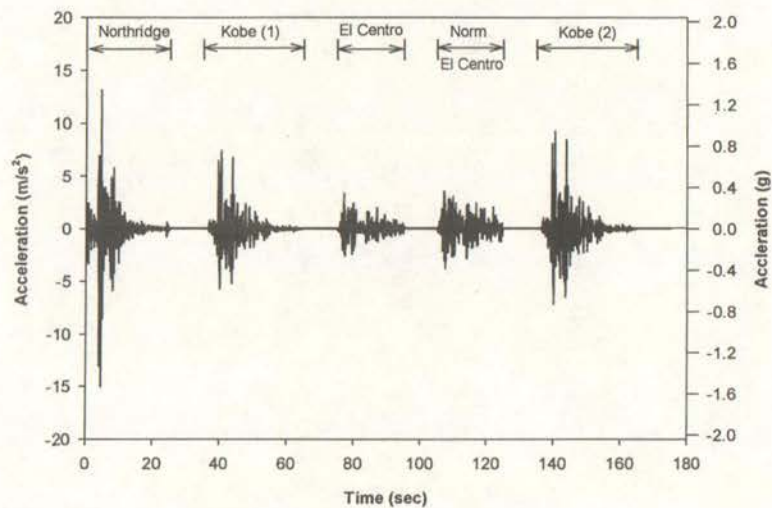


Figure 5-24 Acceleration History E

subassemblage from acceleration history E with Table 5-8 detailing the resulting damage indices. As for acceleration history D, the predicted force-displacement response shows that a reduced force is required to achieve positive and negative displacements after the application of the large negative displacement early in the test sequence.

However, the effect on the predicted damage indices was offset by the application of a higher maximum displacement near the conclusion of the acceleration history. This is evident in Table 5-8 where values for the first four damage indices are slightly higher

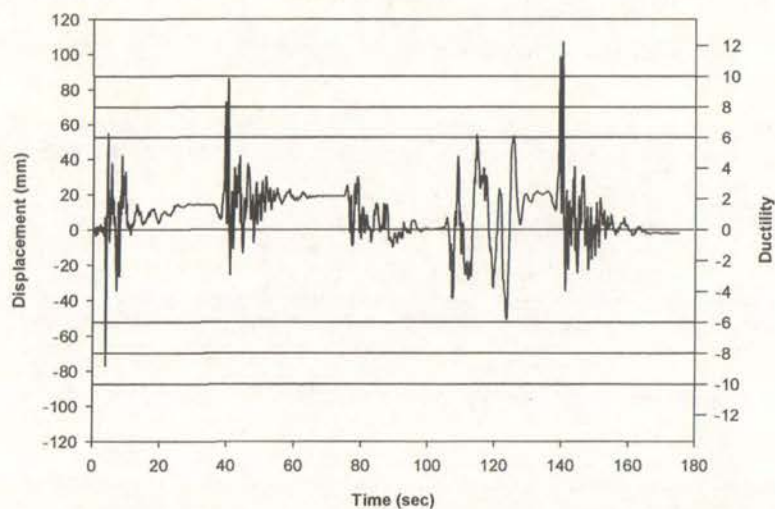


Figure 5-25 Critical Beam Displacement Time History (Acceleration History E)

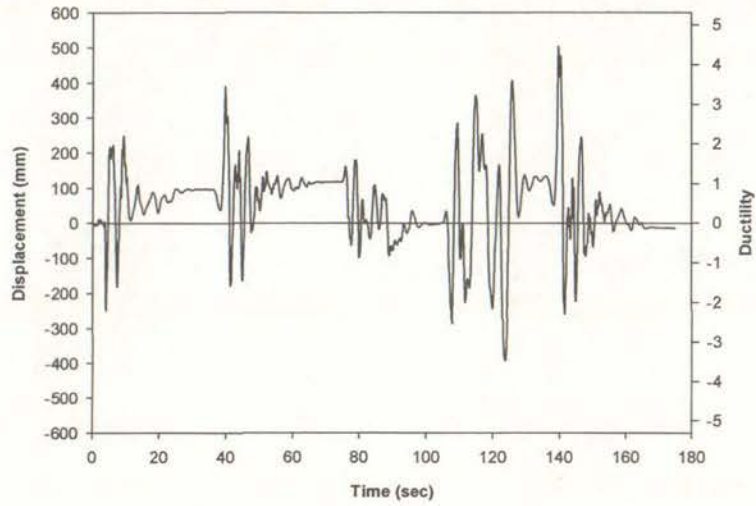


Figure 5-26 Top Storey Displacement-Time History (Acceleration History E)

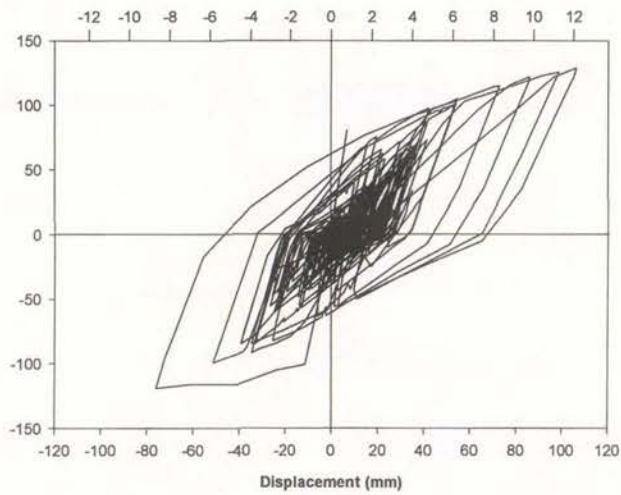


Figure 5-27 Predicted Force-Displacement Response (Acceleration History E)

than the corresponding values from acceleration history D.

Table 5-8 Predicted Damage Indices (Earthquake History E)

Damage Index	Value
Cosenza et al.	0.51
Roufaiel and Meyer	0.52
Park and Ang	0.92
Banon and Veneziano	0.64
Bracci et al.	0.81

## 6.0 Applied Loading Histories

To determine the influence of the applied loading history on the performance and failure characteristics of reinforced concrete plastic hinges, twelve different loading histories were applied to twelve nominally identically reinforced concrete beams. However, before laboratory testing could begin, a common definition of failure was required so that the experimental results from the twelve tests could be compared. Section 6.1 presents a review of failure definitions that have been applied to previous experimental studies. The control for the testing reported herein was the New Zealand loading history. This is detailed in Section 6.2. The other eleven loading histories consisted of three loading histories commonly applied in research institutions in the United States and Japan, three fabricated histories, and five simulated responses of a ten-storey building to different acceleration sequences. Section 6.3 describes the loading histories applied at research institutions in the United States and Japan and Section 6.4 defines the three fabricated histories. Finally, Section 6.5 reports on the five displacement histories that were developed from the model generated in the computer programme Ruaumoko.

### 6.1 Definition of Failure

An important parameter for interpretation of the testing reported herein was the definition of failure. In the past, investigators have used various definitions of what constitutes failure.

Bracci et al. (1989) defined failure as having occurred when a transverse hoop fractured, the longitudinal steel fractured or buckled, or when the member's strength capacity was reduced by more than 20%. Other investigators to use the 20% strength reduction criterion include Park (1989) and the Precast Seismic Structural Systems programme (Stone et al. 1995). Alternative forms of the strength criterion mentioned above include Rao et al. (1998) who suspended testing once there was a strength reduction of 15% and Darwin and Nmai (1986) who considered that a strength reduction of 25% represented the failure point.

Some investigators have considered the strength criteria mentioned above to be too imprecise and have proposed more complex failure definitions; for example, Chung et al. (1989) who related failure to the actual strength reserve. Subjective measures have also been used as a definition of failure; for example, when there was a sudden drop in strength.

As stated in Section 3.5, damage indices attempt to quantify numerically the damage sustained in concrete structures due to seismic loading. For each damage index, failure is defined as having occurred once the damage index reaches a value greater than or equal to 1.0

However, of the aforementioned definitions, the most commonly applied definition was that testing is stopped once the measured strength in a cycle is less than 80% of the maximum measured flexural strength for that direction of loading. Hence this definition was adopted for the twelve tests reported herein.

## 6.2 New Zealand Loading History

The control for this series of experiments was the conventional New Zealand loading history. This procedure is presented schematically in Figure 6-1.

Analytical methods detailed in Equations 4.3 through 4.5 are used to predict the theoretical nominal strength of the beam based on specified material strengths. In

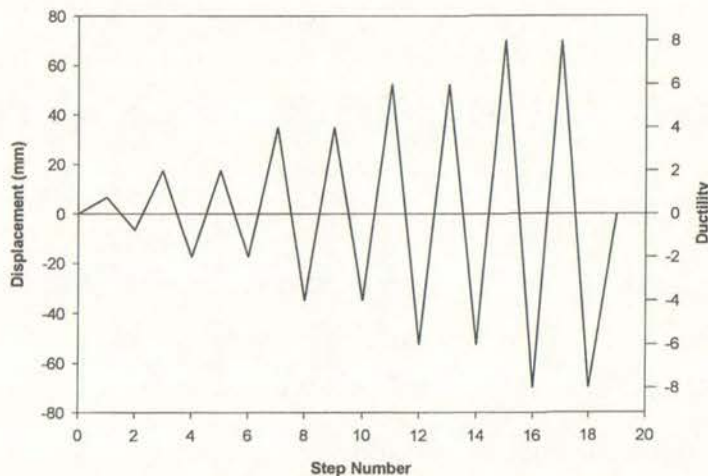


Figure 6-1 New Zealand Loading History

Section 4.2.2, the nominal strength of the beam detail used in this study was calculated to be 185.0kNm. The beam is then loaded to 3/4 of the theoretical nominal strength in both directions with the corresponding displacement being recorded. The necessary actuator force,  $F$ , was calculated to equal

$$\frac{0.75M_n}{l} = \frac{0.75 \times 185.0}{2.15} = 64.5kN.$$

The average displacement,  $\delta'_y$ , for the two directions of loading is established and extrapolated, as presented in Figure 6-2, to the nominal strength to give the yield displacement  $\delta_y$ . A yield displacement equal to 8.75mm was established using these procedures. This is also termed the ductility one displacement. The beam is then loaded by controlling vertical displacements, with applied displacements to integer multiples of  $\delta_y$ . The ductility level is increased in increments of two, and two bilinear loading cycles are applied at each level, as depicted in Figure 6-1. This procedure is repeated until failure occurs.

### 6.3 Comparison with International Procedures

A large percentage of the earthquake engineering research conducted worldwide is undertaken by research institutions in the United States and Japan. Three test assemblies were subjected to conventional loading histories from the United States and Japan so that experimental results from those countries could be compared with results obtained under the New Zealand loading history.

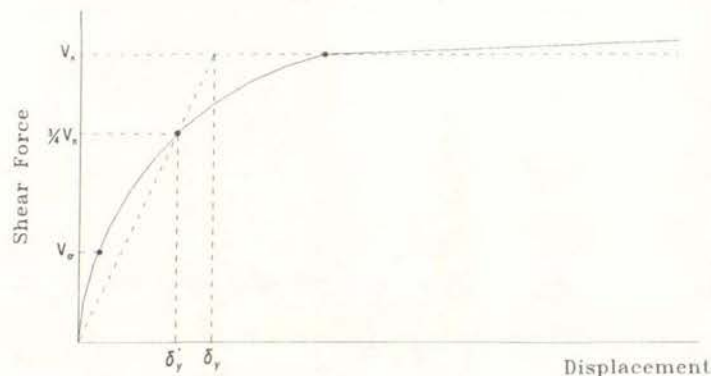


Figure 6-2 Bilinear Approach

The chosen research institution from the United States was the University of California at Berkeley. Section 6.3.1 details the loading history adopted from the University of California at Berkeley. However, it should be noted that the loading history applied at the University of California at Berkeley was similar to loading histories applied at other universities located in the State of California; for example, the University of California at San Diego. Hence the loading history applied at the University of California at Berkeley was taken to be indicative of general practice in universities located on the West Coast of the United States.

In 1987 an experimental programme to investigate the behaviour of precast concrete beam-column connections was initiated at the National Institute of Standards and Technology. The fourth phase of this research programme applied the conventional approach from the PREcast Seismic Structural Systems (PRESSSS) programme so that results from the aforementioned programme could be compared with experimental work conducted under the PRESSSS programme. The PRESSSS programme employed a large number of research institutions throughout the United States and was applied in this testing series due to this wide coverage. Section 6.3.2 details the loading history that was applied in the PRESSSS programme.

The chosen research institution from Japan was the Public Works Research Institute. Section 6.3.3 describes the loading history from the Public Works Research Institute.

### 6.3.1 Conventional Approach from the University of California at Berkeley

Figure 6-3 illustrates the conventional approach from the University of California at Berkeley. The loading history consisted of two components: a force-controlled regime and a displacement-controlled regime.

A literature review of testing procedures applied at the University of California at Berkeley found that procedures when the loading history was under force control varied. Different procedures included subjective measures based on the appearance of flexural cracks and diagonal tension cracks, multiple cycling at fractions of the calculated yield force, or increasing cycles up to the calculated service load. This

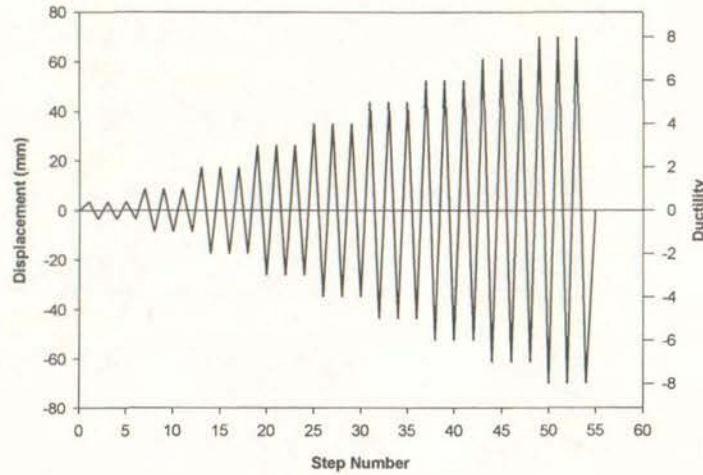


Figure 6-3 Loading History Applied at the University of California at Berkeley

project followed the approach reported on in EERC Report 76-2 (Ma et al. 1976) where three cycles at  $0.4F_y$  was applied.

Once yielding has occurred, the loading is controlled by selected tip displacements that increase in single ductility increments. Three complete cycles at each ductility level are carried out to enable the degradation of strength and stiffness at each ductility level to be calculated. The process is repeated until the failure criterion is met.

### 6.3.2 Conventional Approach from the PRESSS Research Programme

The loading history adopted by the PRESSS research programme (Stone 1995) is based on storey drift. Storey drifts were converted to ductility levels in this report to assist in the comparison of experimental results from this test with other tests. Figure 6-4 illustrates the definition of storey drift for a single-bay portal frame. The displacement ductility of the test subassembly was found through relating the storey drift of the frame to the rotation of the beam as follows:

$$\text{Storey Drift} = \theta = \frac{\Delta}{H} = \frac{\delta}{l} \text{—that is,} \quad \dots \text{Equation 6.1}$$

$$\mu = \frac{\delta}{\delta_y} = \frac{\text{StoreyDrift} \times l}{100\delta_y} \quad \dots \text{Equation 6.2}$$

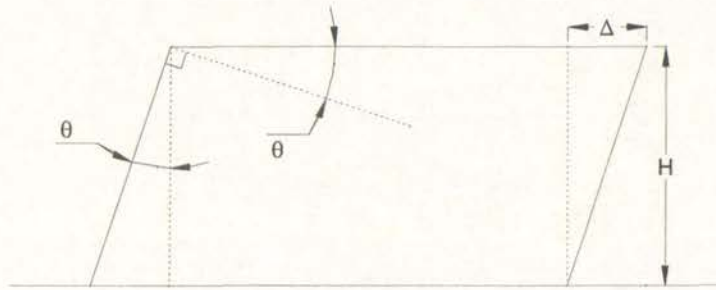


Figure 6-4 Storey Drift

The initial drift level is 0.1% and the drift level increased in increments of 0.05% until 0.25%. The drift level is then increased in increments of 0.1%, 0.15%, and two increments of 0.25%. After these cycles, the drift level is increased in increments of 0.5% until failure occurs. As shown in Figure 6-5, three cycles are completed at each drift level, followed by an intermediate elastic cycle. In the elastic cycle, the specimen is loaded to 30 percent of the peak load in the preceding three cycles.

### 6.3.3 Conventional approach from the Public Works Research Institute in Japan

As with the New Zealand loading history, the procedure adopted by the Public Works Research Institute in Japan consists of a force-controlled component and a displacement-controlled component. Figure 6-6 illustrates the procedure adopted by the Public Works Research Institute.

The force-controlled component consists of several increasing force cycles up to the

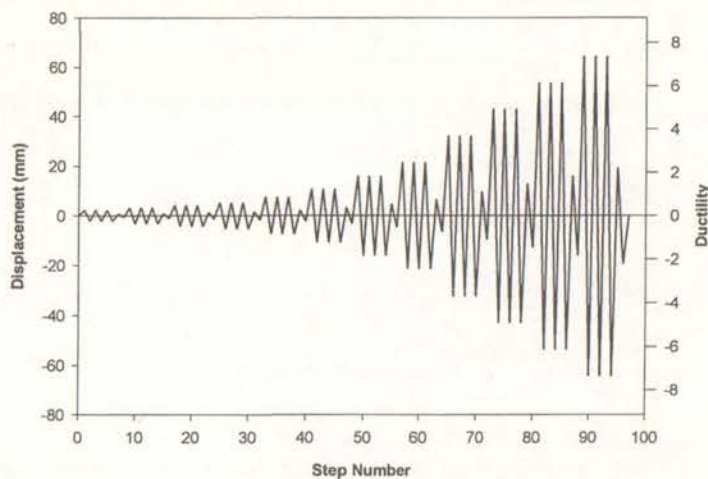


Figure 6-5 PRESSS Loading History

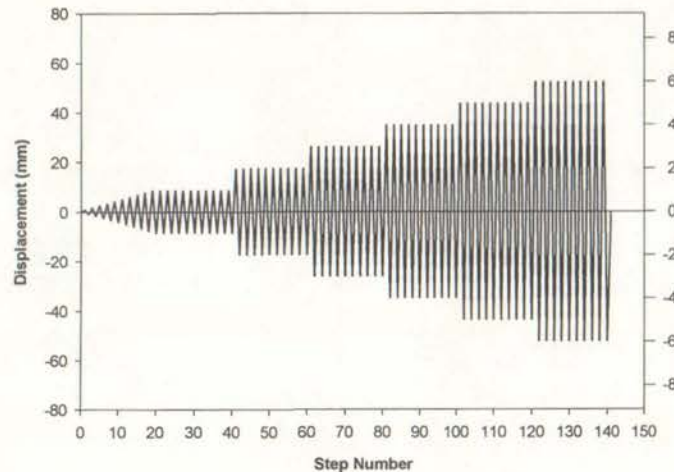


Figure 6-6 Public Works Research Institute Loading History

calculated yield force. The initial force is 10% of the calculated yield force with the force then being increased in increments of 10% of the yield force until the yield force is reached.

Once the force-controlled component has been completed, the loading is controlled by selected tip displacements that increase in single ductility increments. The number of cycles to each ductility step varies according to the member and ground motion characteristics. One cycle at each ductility step is applied if the member is not affected by the load history. Three cycles are applied if the ground motion is an inter-plate earthquake whereas ten cycles are applied if the ground motion is from a large plate-boundary earthquake. Ten cycles are applied at each ductility level in this report because the majority of earthquakes of engineering significance are large plate-boundary earthquakes; for example, in the Cascada subduction zone on the West Coast of the United States (Atwater et al. 1995).

#### 6.4 Fabricated Loading Histories

The three fabricated loading histories applied in this experimental study were monotonic loading, bi-directional cycling at ductility 8, and unidirectional cycling. Section 6.4.1 details the monotonic loading regime, Section 6.4.2 details bi-directional cycling at ductility 8, and Section 6.4.3 details unidirectional cycling.

### 6.4.1 Monotonic Loading

One of the test subassemblies was subjected to monotonic loading, as presented in Figure 6-7, for two reasons. The first reason was to establish the skeleton force-displacement response of the test subassemblage. The second reason was because strength and deformation characteristics established from monotonic loading forms the basis of several damage indices; for example, Banon and Veneziano (1982) who normalised their damage index with respect to monotonic loading. Also Park and Ang (1985) compared the maximum deflection under cyclic or earthquake loading to the maximum displacement under monotonic loading.

### 6.4.2 Bi-directional Cycling at Ductility 8

Bi-directional cycling at ductility 8, as illustrated in Figure 6-8, was conducted to give an indication of the fatigue characteristics of the test subassemblage. Examples of investigators who have applied direct cycling at constant amplitudes include Kunnath et al. (1997) who subjected columns to cyclic loading at various constant amplitudes so that a fatigue-based damage model for flexural members could be calibrated.

### 6.4.3 Uni-Directional Cycling

The third fabricated loading history consisted of the New Zealand loading history applied to a test subassemblage in a single direction so that a comparison could be

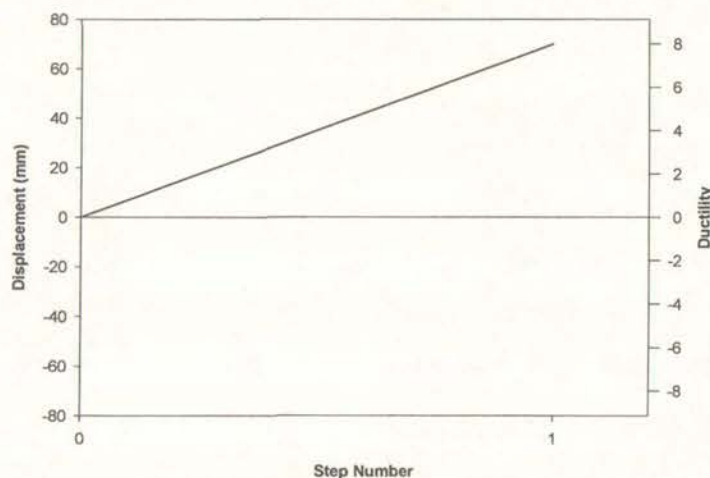


Figure 6-7 Monotonic Loading

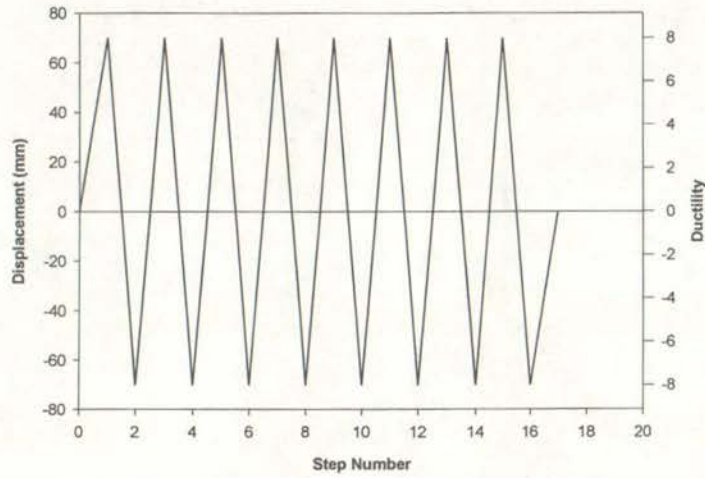


Figure 6-8 Direct Cycling at Ductility 8

made between results from reversed cyclic loading and uni-directional cyclic loading. This is illustrated in Figure 6-9.

### 6.5 Simulated Response of a Ten-Storey Building

One of the objectives of this report was to determine whether the order of earthquake records within an acceleration history affects the experimental results. In Chapter 5.0, the procedures followed to simulate the seismic response of a ten-storey building were discussed. Five acceleration histories consisting of four or five scaled earthquake records were developed. Table 6-1 summarises the scale factors for the individual records in each acceleration history. Table 5-2 summarises the order of the individual records within the acceleration history with the order of the records within each

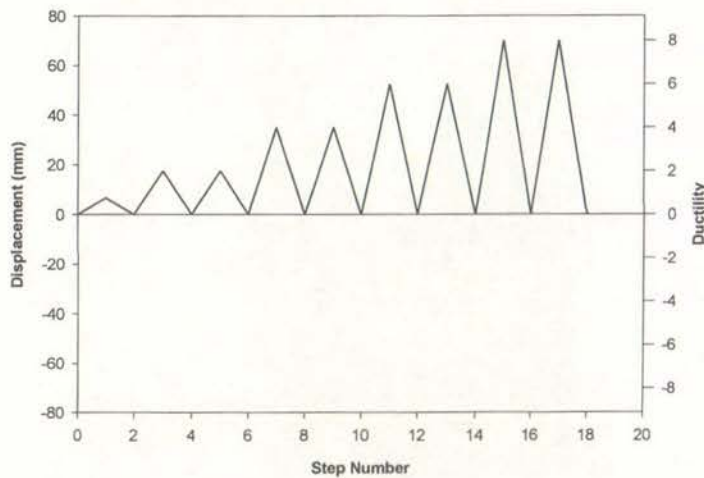


Figure 6-9 Unidirectional Cycling

Table 6-1 Summary of Earthquake Records' Scale Factors

	Earthquake	Acceleration History A	Acceleration Histories B-E
1	Normalised El Centro NS	1.10	1.10
2	Pacoima / Northridge	1.00	1.20
3	El Centro NS	2.00	1.00
4	Kobe (1) EW	1.61	1.20
5	Kobe (2) EW	-	1.50

acceleration history also displayed in the displacement sequence plots shown in this section. Section 5.2 explains the strategy behind the scaling and order of individual records for each acceleration history.

The displacement-time history for the critical beam within the prototype structure was isolated and digitised so that the displacement steps could be applied to the test subassembly. Sections 6.5.1 through 6.5.5 present the five displacement sequences that were applied in the laboratory. All five sequences were applied under displacement control and in each case, the entire loading sequence was completed regardless of the subassembly degradation.

### 6.5.1 Acceleration History A

Acceleration history A consisted of four earthquake records applied in sequential order. The first record was the artificial earthquake based upon the North-South component from the El Centro earthquake. The second record was obtained from the

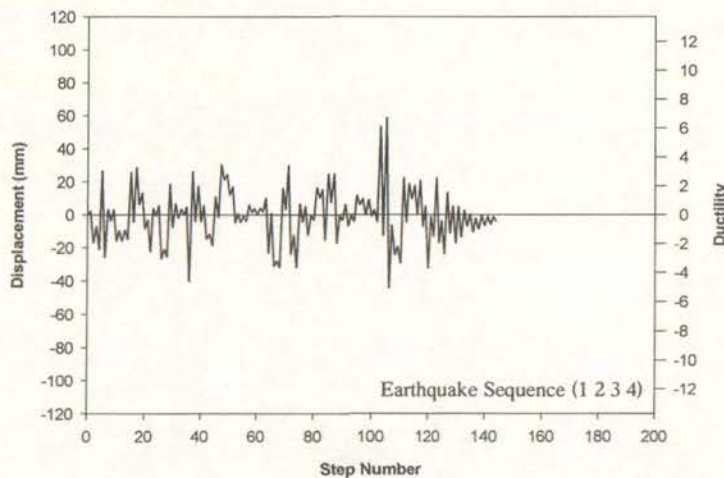


Figure 6-10 Acceleration History A

Pacoima dam station during the Northridge earthquake. The third record was the North–South component from the El Centro earthquake and the final record was the East–West component from the Kobe earthquake. Figure 6-10 presents the displacement sequence from acceleration history A.

### 6.5.2 Acceleration History B

Acceleration history B consisted of four earthquake records applied in the same order as for acceleration history A but with different scale factors. Figure 6-11 details the displacement sequence from acceleration history B.

### 6.5.3 Acceleration History C

An additional earthquake record was included in acceleration histories C–E to ensure that the test subassembly failed. As for acceleration histories A and B, the first record was the artificial earthquake based upon the North–South component from the El Centro earthquake. The second record was the East–West component from the Kobe earthquake (denoted Kobe (1) in Table 6-1). The third record was from the Pacoima dam station during the Northridge earthquake. The fourth record was the North–South component from the El Centro earthquake and the final record was a repeat of the East–West component from the Kobe earthquake (denoted Kobe (2) in Table 6-1) but was scaled by a larger scale factor. Figure 6-12 displays the

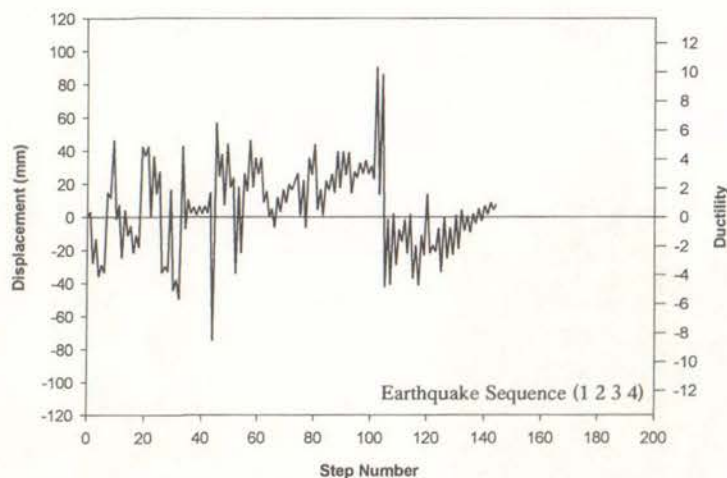


Figure 6-11 Earthquake History B

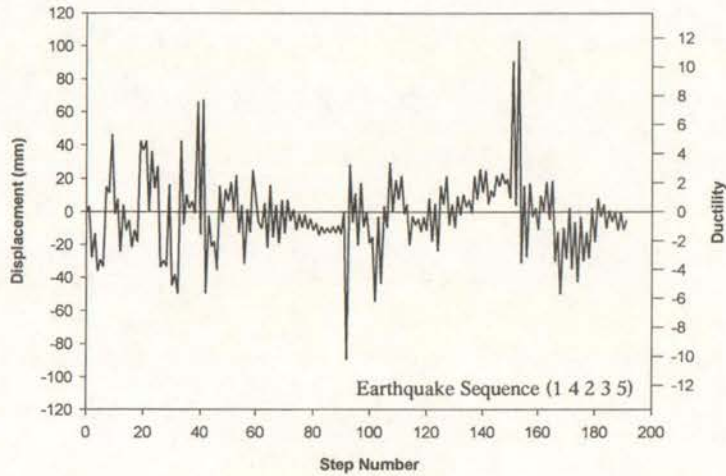


Figure 6-12 Earthquake History C

displacement sequence from acceleration history C.

#### 6.5.4 Acceleration History D

The record obtained from the Pacoima dam station during the Northridge was the first record in acceleration history D. The second and third records were the North-South component from the El Centro earthquake followed by was the artificial earthquake based upon the North-South component from the El Centro earthquake. The fourth and fifth records were the East-West components from Kobe (1) and Kobe (2) respectively. Figure 6-13 illustrates the displacement sequence from acceleration history D.

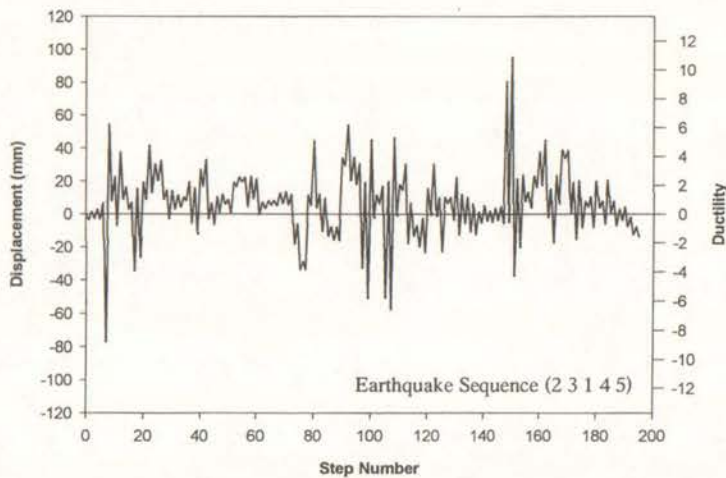


Figure 6-13 Acceleration History D

## 6.5.5 Acceleration History E

Figure 6-14 illustrates the displacement sequence resulting from application of acceleration history E. The first record in acceleration history E was the record obtained from the Pacoima dam station during the Northridge earthquake. The second record was the East–West component from Kobe (1). The third and fourth records were the North–South component and the artificial earthquake based upon the North–South component from the El Centro earthquake respectively. As for acceleration histories C and D, the final record was the East–West component from the Kobe (2) earthquake.

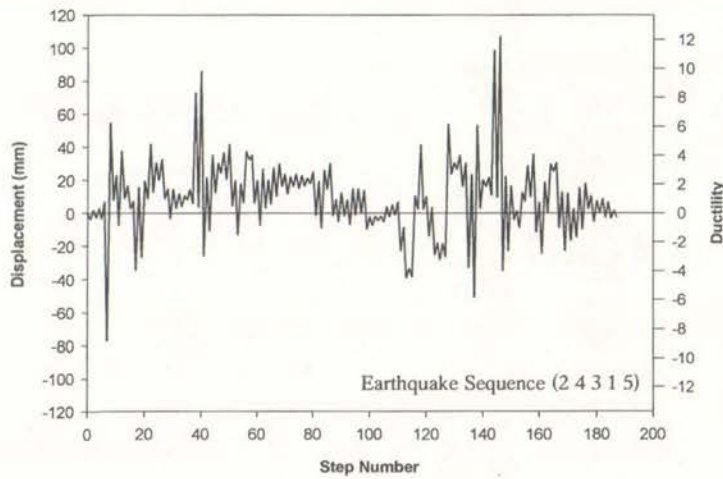


Figure 6-14 Acceleration History E

## 7.0 Analysis of Results

A significant amount of data was obtained from the twelve tests conducted in the experimental component of this study. However, it was established that including the entire data set in this chapter would endanger obscuring the objectives of this study. Therefore, this chapter summarises the experimental results that were relevant to the objectives of this study, whereas Appendix C provides full details of the experimental data. This chapter compares the overall force-displacement response from the twelve tests, the response from each test for various ductility levels, the energy dissipation characteristics of each test specimen, and the strain behaviour of the reinforcement steel from the twelve tests. These are detailed in Sections 7.1 through 7.4 respectively. This chapter also relates the damage indices calculated for each test with the observed behaviour and summarises the observed and measured crack behaviour from the seven laboratory procedures. These are presented in Section 7.5 and Section 7.6.

### 7.1 Ultimate Displacement

The twelve loading histories were separated into two divisions. The first division was comprised of loading histories applied at various research institutions detailed in Section 6.2 and Section 6.3 and the fabricated histories presented in Section 6.4. These are hereafter referred to as the laboratory procedures. The second division was comprised of the five acceleration histories established from modelling of the ten-storey building in the nonlinear time-history analysis programme, Ruaumoko. Section 7.1.1 presents the results from the laboratory procedures and Section 7.1.2 details the force-displacement response from the five acceleration histories.

#### 7.1.1 Laboratory Procedures

Figure 7-1 presents the force-displacement response from testing using the New Zealand loading history and reveals that the beam reached a maximum ductility of 10. Figure 7-1 also indicates that the strength of the test assembly exceeded both the nominal design force and the ideal design force, which were defined in Section 3.1.

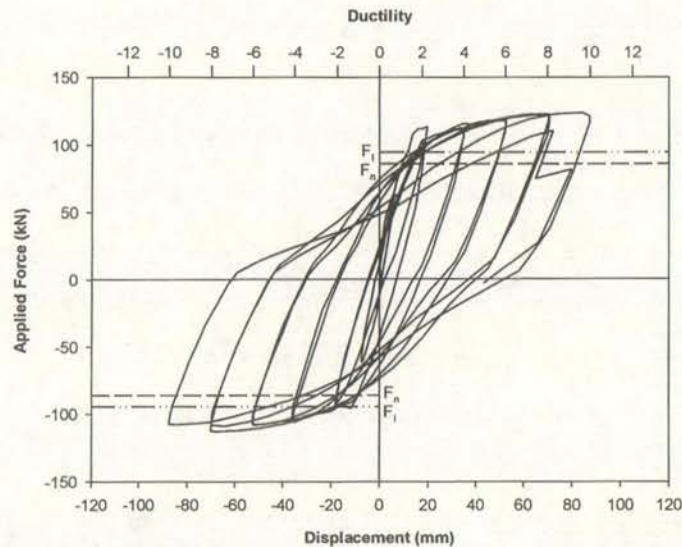


Figure 7-1 Force-Displacement Response (New Zealand Loading History)

This was due to the calculation of nominal and ideal design strengths not including strain hardening in the longitudinal reinforcement and confinement from transverse reinforcement. The beam failed suddenly through the rupture of a longitudinal reinforcement bar immediately next to an instrumentation stud. This resulted in the strength of the test specimen dropping below 80% of the maximum-recorded strength for this test. However, it was postulated that this was a premature failure, as the beam had shown no strength loss and only minor pinching of the hysteresis loops was observed to that point. Therefore, it was proposed that welding of steel studs to the longitudinal reinforcement influenced the local material properties of the bar next to the instrumentation stud. This was confirmed by Radaj (1992) in his research on the heat effects of welding. Radaj stated that a reduction in fatigue strength could occur due to microdefects at the boundary of the fusion zone or through distortion resulting from welding.

Figure 7-2 illustrates that the beam also reached an ultimate ductility of 10 when the Berkeley loading history was applied. Failure also occurred after the rupture of a longitudinal reinforcement bar. However, in contrast to the failure from testing using the New Zealand loading history, rupture in this test occurred after significant strength degradation had taken place. Therefore the welding of instrumentation studs to the longitudinal reinforcement did not affect the local material properties of the reinforcement bar and hence, failure was attributed to low-cycle fatigue of the

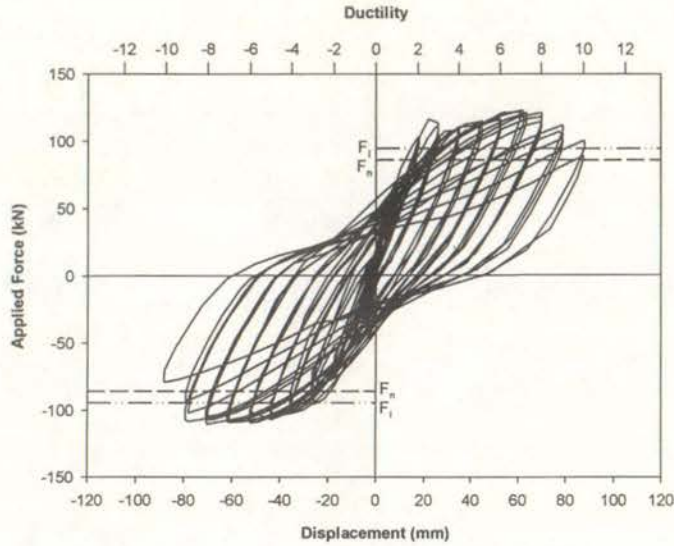


Figure 7-2 Force-Displacement Response (Berkeley Loading History)

reinforcement steel. As with the response from testing that implemented the New Zealand loading history, the nominal and ideal design strengths were both exceeded.

Figure 7-3 presents the force-displacement response from testing that applied the PRESSS loading regime. The beam reached an ultimate ductility of 8.6 in the positive direction and 7.4 in the negative direction. Failure in this test was indicative of conventional tensile flexural failure described in Section 2.5.1.1 because the strength of the test specimen gradually decreased over a number of cycles. As with the response from testing using the New Zealand loading history, the nominal and

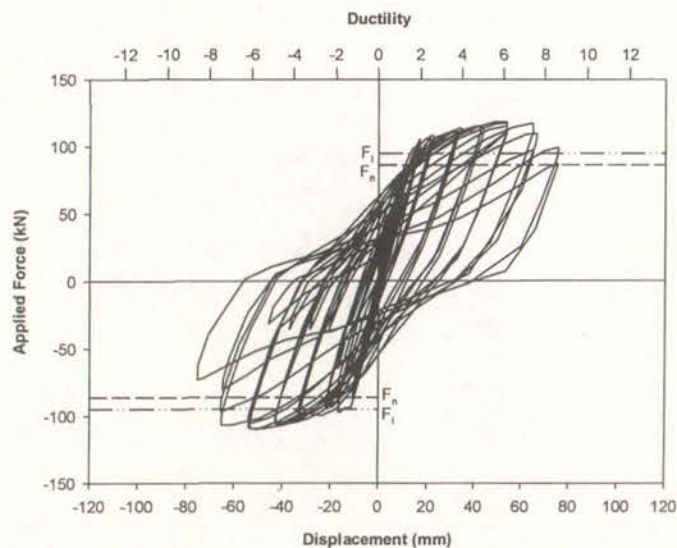


Figure 7-3 Force-Displacement Response (PRESSS Loading History)

ideal design strengths were both exceeded.

Figure 7-4 displays the force-displacement response from testing using the Public Works Research Institute's loading history. The strength of the test specimen dropped below 80% of the maximum-recorded strength for that test on the third cycle at ductility 6 in the positive direction and on the fifth cycle at ductility 6 in the negative direction. As with the failure when the test specimen was subjected to the PRESSS loading history, failure in this test was consistent with the behaviour that occurs when the member fails in a tensile flexural manner. The response of the test specimen was consistent with the response from testing using the New Zealand loading history where both the nominal and ideal design strengths were exceeded.

Figure 7-5 illustrates the force-displacement response of the beam under monotonic loading. The stroke of the actuator was reached after the test subassembly was loaded to ductility 22. However, the strength of the test specimen had begun to reduce and extrapolation of the force-displacement response gave an ultimate ductility of 23. This is far in excess of the maximum displacement obtained from the New Zealand loading history and was directly attributable to the monotonic loading regime. Again, both the nominal and ideal design strengths were exceeded. It should be noted that Figure 7-5 is plotted with an x-axis scale that is twice as large as the figures that plot the force-displacement response from cyclic tests. Plotting the force-displacement response from cyclic tests against a reduced scale enabled the force-

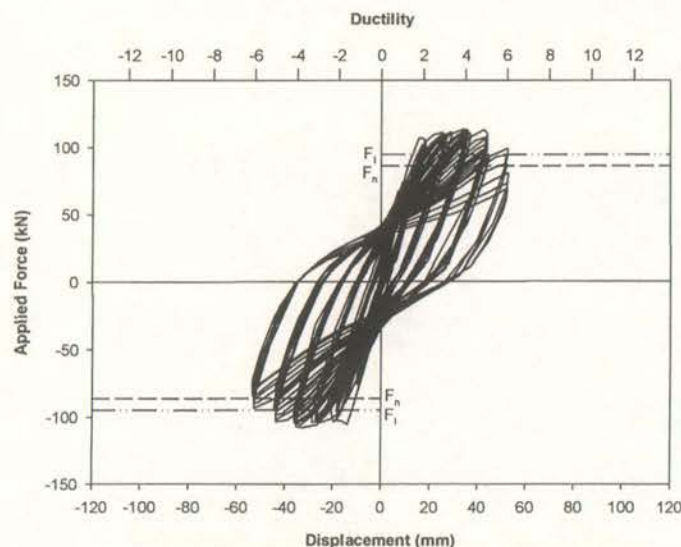


Figure 7-4 Force-Displacement Response (Public Works Research Institute Loading History)

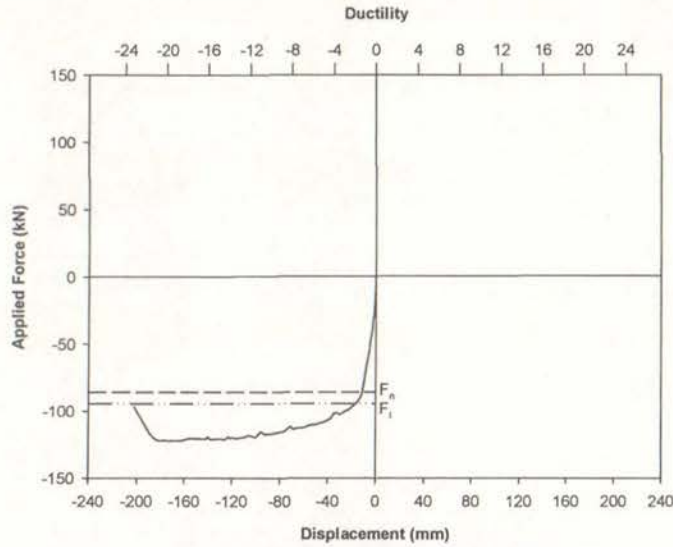


Figure 7-5 Force-Displacement Response (Monotonic Loading)

displacement response to be seen more clearly.

Figure 7-6 presents the force-displacement response from testing that applied bi-directional cycling at ductility 8. Five complete cycles at ductility 8 were applied before the strength of the test specimen dropped below 80% of the maximum-recorded strength for that test. The failure was indicative of a tensile flexural failure and, as usual, the nominal and ideal design strengths were both exceeded.

Figure 7-7 reveals that the test subassembly reached an ultimate ductility of 22 under unidirectional loading before failure occurred. Failure was due to rupturing of a

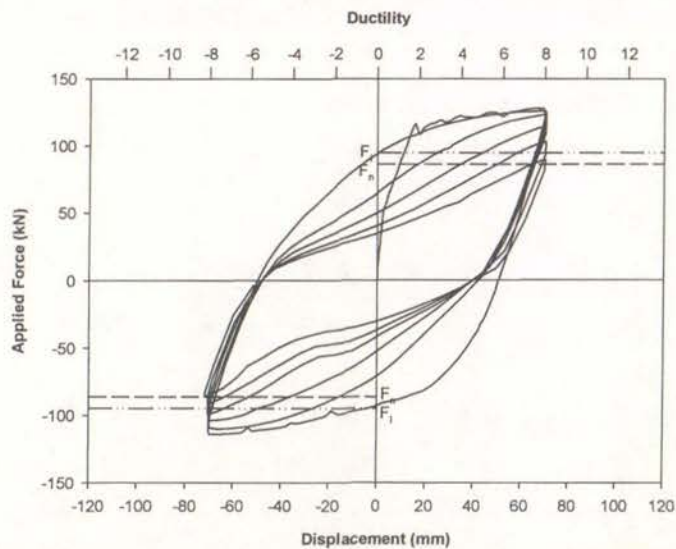


Figure 7-6 Force-Displacement Response (Cycling at Ductility 8)

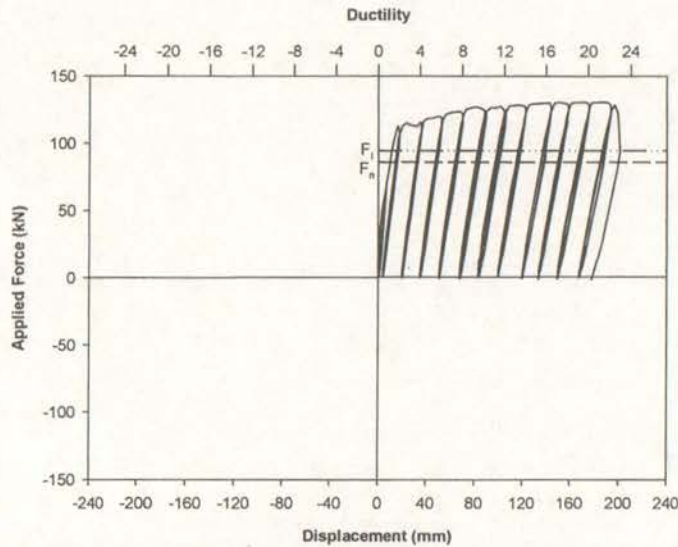


Figure 7-7 Force-Displacement Response (Unidirectional Loading)

longitudinal reinforcement bar after significant strength degradation had taken place. Therefore it was determined that welding of instrumentation studs to the longitudinal reinforcement did not affect the local material properties of the reinforcement bar and hence, failure was attributed to low-cycle fatigue of the reinforcement steel. As with the response from testing that implemented the New Zealand loading history, the nominal and ideal design strengths were both exceeded. Like the force-displacement response from testing under monotonic loading, Figure 7-7 is plotted with an x-axis scale that is twice as large as the figures that illustrate the force-displacement response from cyclic tests.

The seven force-displacement plots presented in Figures 7-1 through 7-7 reveal large discrepancies between the ultimate displacement established from testing using the seven laboratory procedures. Firstly, the ultimate displacement of the test specimen subjected to monotonic loading was far in excess of the ultimate displacement of the test specimens subjected to any of the five bi-directional cyclic procedures. This is consistent with the findings of a previous experimental study by Tomazeivc et al (1996) where it was established that larger ultimate displacements were recorded when testing using monotonic loading than for testing where cyclic loading of any type was applied.

More critically, the ultimate displacement of the test specimens subjected to the loading histories applied at research institutions around the world also varied. Testing

conducted using the loading history from the Public Works Research Institute was the most conservative and returned an ultimate ductility of 6. In contrast, an ultimate ductility equal to 10 was established from testing where the New Zealand and Berkeley loading histories were applied. Of the two, the New Zealand loading history was taken to be the least conservative because the test specimen failed prematurely in that test. Testing using the PRESSS loading regime returned an ultimate ductility of 7.4, which is between the bounds previously reported.

As was reported in Chapter 1.0, the selection of a target ultimate displacement in the displacement-based design process is dependent on the performance of laboratory subassemblies. Clearly, given the above results, structures designed in Japan using displacement-based methods would be designed more conservatively than the corresponding structure on identical ground conditions in New Zealand or the United States.

Creating a statistically accurate means of correlating the ultimate displacement of a nominally identical test specimen subjected to different loading histories would require numerous tests, which are time consuming and expensive. Therefore, there is a need for a consistent loading history to be developed that researchers throughout the world can apply to a laboratory subassemblage.

### 7.1.2 Acceleration Histories

This section details the force-displacement response from acceleration histories A-E. These are presented in Figures 7-8 through 7-12. In all cases the maximum strength exceeded the nominal and ideal design strength. However, in contrast to testing conducted using laboratory procedures, failure was not necessarily induced in these five tests. For acceleration history A, this was because the larger displacements in the displacement sequence established from modelling in Ruaumoko were not of sufficient size or number to promote degradation of the test specimen. For the remaining acceleration histories it also proved difficult to define failure when significant degradation took place. This was because the largest ductility cycles often did not require the application of a large force due to their position in the displacement sequence. Thus, it was difficult to determine whether any strength loss

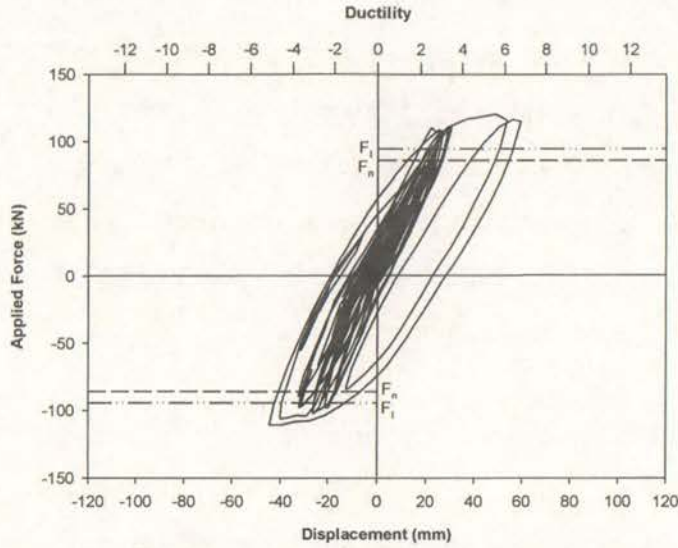


Figure 7-8 Force-Displacement Response (Acceleration History A)

was due to the degradation of the test specimen or the position of the cycle in the displacement sequence.

The loading sequence from acceleration history D was the only loading sequence that definitely induced failure of the test specimen. Figure 7-11 reveals that significant strength degradation occurred during the test. This was due to rupturing of a longitudinal reinforcement bar occurring during application of the third record in the displacement sequence. However, this was a premature failure because the bar ruptured immediately next to an instrumentation stud and the rupture occurred prior to the application of the most damaging records. Therefore, it was established that

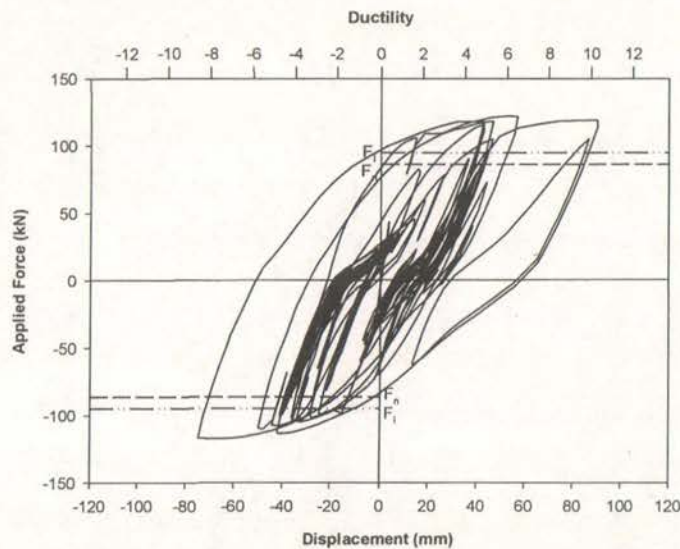


Figure 7-9 Force-Displacement Response (Acceleration History B)

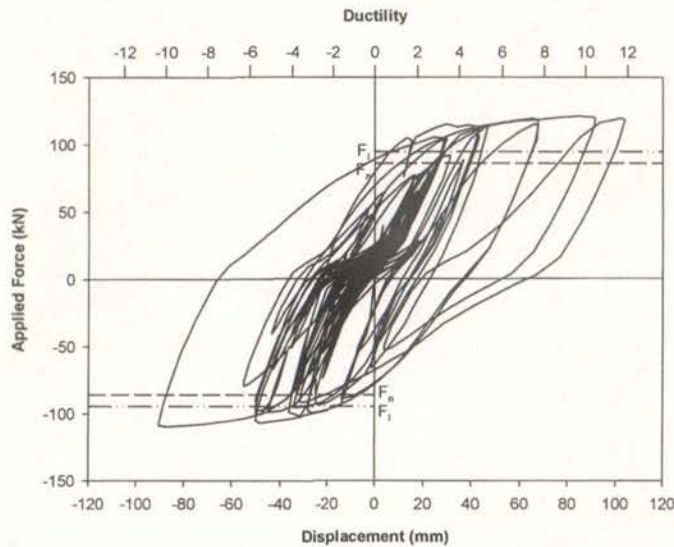


Figure 7-10 Force-Displacement Response (Acceleration History C)

welding instrumentation studs to the longitudinal reinforcement influenced the local material properties of the bar at that point.

As was reported in Section 5.2.3, the Kobe earthquake record was repeated to induce failure of the test subassemblage. Of the four earthquake records applied prior to that record, two were from earthquakes where significant damage occurred. These were the Kobe record and the Pacoima Dam record from the Northridge earthquake (NZNSEE Reconnaissance Team 1995; NZSNEE Reconnaissance Team 1994). Thus, failure of the test subassemblage had still not occurred after being subjected to four earthquake records even though all four records were scaled up by various factors

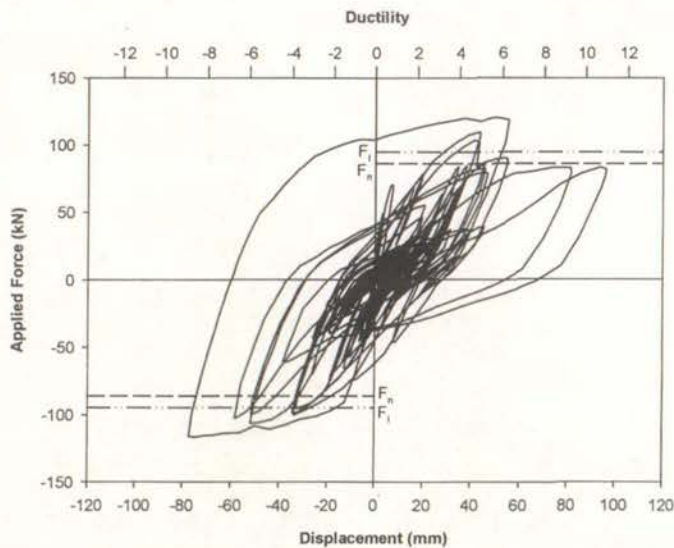


Figure 7-11 Force-Displacement Response (Acceleration History D)

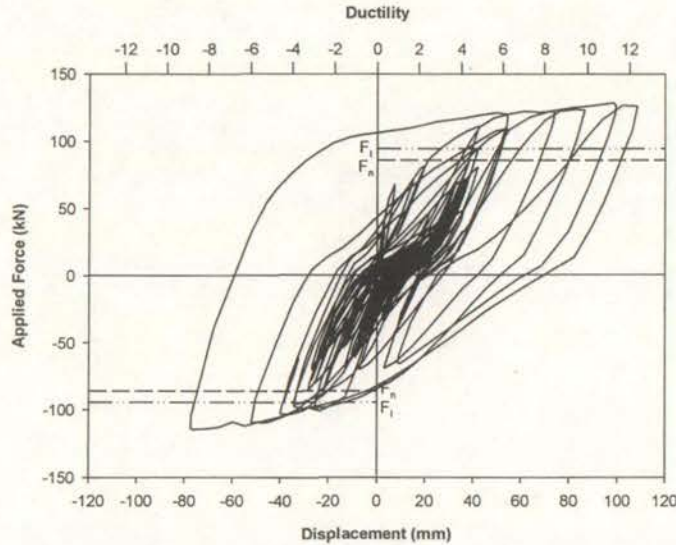


Figure 7-12 Force-Displacement Response (Acceleration History E)

and two records were from severe earthquakes. This could have been exacerbated because the computer model did not include any reduction in member sizes in the upper storey levels. Whether this affected the response of the building to any great extent warrants further consideration. However, on the evidence of the testing reported herein, it is proposed that structures designed using force-based methods have a large degree of conservatism inherent in their design. This has also been noted by Priestley (1997) in his work on displacement-based methods of structural design.

Given that the degradation at the conclusion of acceleration histories B, C, and E were similar, it can be stated that variations in the applied displacement sequence did not cause significant discrepancies in the overall response of the structure. This is consistent with the conclusions made by Hwang and Scribner (1984) in their study on the response of reinforced concrete members to various loading histories.

## 7.2 Comparison of Force-Displacement Hysteresis Loops

It followed that, because the ultimate displacement of the test subassembly varied according to the applied loading history, strength and stiffness degradation also varied between tests. Section 7.2.1 compares the hysteresis loops from the laboratory procedures at various ductility levels and Section 7.2.2 compares the envelopes from the five acceleration histories with the monotonic force-displacement response.

### 7.2.1 Laboratory Procedures

The force-displacement hysteresis loops from each test were isolated for the first cycle at various ductility levels and plotted on the same figure so that the characteristics of the hysteresis loops from each test could be compared. The chosen ductility levels were at ductility 4, ductility 6, and ductility 8. These are reported on in Section 7.2.1.1 through 7.2.1.3 respectively. The force-displacement response at ductility 2 was not presented in this report because there was no significant discrepancies between the tests. It should be noted that the PRESSSS loading history applied irregular ductility levels. Therefore, the ductility level closest to the aforementioned ductility levels was used for comparison purposes.

#### 7.2.1.1 Comparison after Ductility 4 Cycles

Figure 7-13 compares the force-displacement hysteresis loops from six of the seven laboratory procedures after the first cycle at ductility 4, with the response from bi-directional cycling at ductility 8 not included in this comparison. The closest ductility level to ductility 4 in the PRESSSS loading regime was ductility 3.69. Figure 7-13 reveals differences between the six tests regarding the amount of pinching in the hysteresis loops and the reloading stiffness from previous cycles.

The response from the testing using the loading history from the Public Works

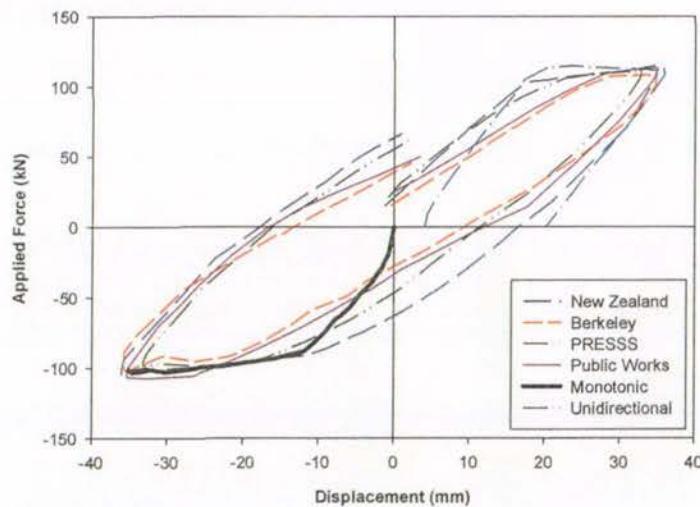


Figure 7-13 Comparison after Loading to Ductility 4

Research Institute and the University of California at Berkeley show more pinching in the hysteresis loops than the response from testing where the New Zealand loading history was applied. This was consistent with the observed behaviour from these tests, with less damage evident at this ductility for testing using the New Zealand loading history than in testing using the aforementioned loading histories. For instance, spalling of cover concrete such that longitudinal reinforcement was visible had occurred by this loading stage in the test that applied the loading history from the Public Works Research Institute whereas spalling was not evident at the corresponding loading stage from testing using the New Zealand loading history.

The reloading stiffness also varied between tests. The highest reloading stiffness was from unidirectional testing whereas the lowest was from testing using the loading history from the Public Works Research Institute and University of California at Berkeley. Again this was consistent with the observed damage at this ductility level from the three tests.

Figure 7-13 also reveals that the post-yield force-displacement response from monotonic loading formed an envelope to the corresponding phase of the force-displacement response from the cyclic tests. This is consistent with the behaviour of concrete under cyclic and monotonic loading, which was reported in Section 2.4.1.1. In their work on the behaviour of concrete under compressive loading, Karsan and Jirsa (1969) concluded that the monotonic stress-strain curve formed an envelope to the cyclic loading stress-strain curve.

#### 7.2.1.2 Comparison after Ductility 6 Cycles

Figure 7-14 compares the force-displacement hysteresis loops from six of the seven laboratory procedures after the first cycle at ductility 6, with the response from cycling at ductility 8 again not included. The closest ductility level to ductility 6 in the PRESSS loading history was ductility 6.14. Figure 7-14 reveals that contrasting behaviour between the six tests concerning the amount of pinching in the hysteresis loops and the reloading stiffness from previous cycles were more apparent at this loading stage than in the comparison made after loading to ductility 4.

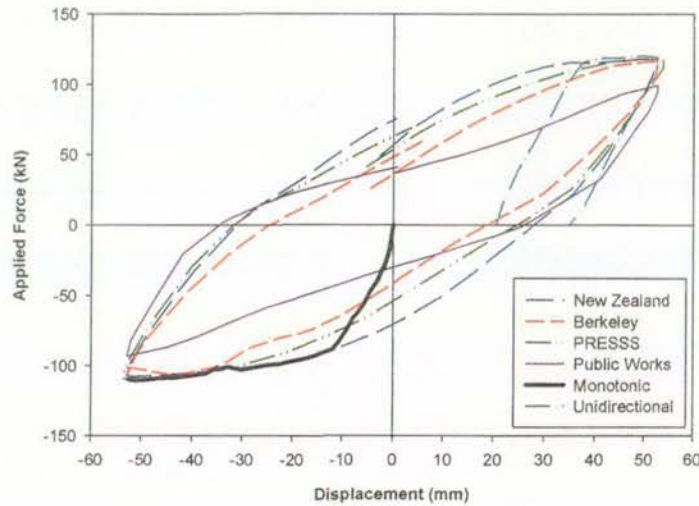


Figure 7-14 Comparison after Loading to Ductility 6

The response from the testing using the loading history from the Public Works Research Institute shows considerably more pinching and a lower reloading stiffness than the response from other cyclic tests. This was consistent with the experimental behaviour from these tests with ductility 6 defined as the ultimate ductility established using the Public Works Research Institute's loading history whereas the other cyclic tests were yet to reach their ultimate ductility.

Figure 7-14 illustrates that the reloading stiffness from testing applying a unidirectional loading history was much greater than the reloading stiffness from any of the bi-directional cyclic tests. This reflected the greater damage incurred in the cyclic tests up to this point compared to damage from tests where a unidirectional loading history was applied.

Figure 7-14 also demonstrates that the post-yield force-displacement response from monotonic loading continued to form an envelope to the corresponding segment of the force-displacement response from the cyclic tests.

### 7.2.1.3 Comparison after Ductility 8 Cycles

Figure 7-15 contrasts the force-displacement hysteresis loops from six of the seven laboratory procedures after the first cycle at ductility 8. The response from testing using the Public Works Research Institute's loading history was not included because

failure had already occurred. The closest ductility level to ductility 8 in the PRESSS loading regime was ductility 7.37. Figure 7-15 demonstrates that variations in the hysteresis response from the six tests increased from previously reported comparison levels.

The response from the testing that applied bi-directional cycling at ductility 8 showed considerably less pinching and a significantly higher reloading stiffness than responses the other cyclic tests. This was because the test specimens subjected to other cyclic tests had suffered considerable damage before the ductility 8 cycles were applied.

Response from testing using the Berkeley and PRESSS loading histories showed similar amounts of pinching. This observation was unusual given that the ultimate displacement established from testing using the PRESSS loading history was lower than the ultimate displacement established from applying the Berkeley loading history. This was attributed to rocking deformations accounting for a much larger percentage of the total vertical displacement in the test that applied the Berkeley loading history compared to the test that applied the PRESSS loading history, as illustrated in Figure C-10 and Figure C-17 in Appendix C. This accounted for the increased pinching in the hysteresis loops from testing using the Berkeley loading history because rocking deformations were elastic and hence dissipated low amounts

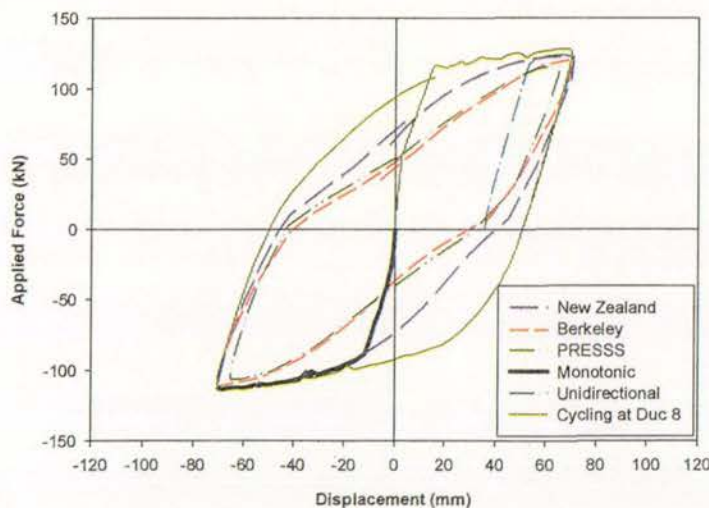


Figure 7-15 Comparison after Loading to Ductility 8

of energy compared to flexural deformations.

It was established from Figure 7-13 through 7-15 that the response from testing using the New Zealand loading history was not reflective of the response from testing using other laboratory procedures applied worldwide. Flexural deformations accounted for a larger percentage of the total displacement when testing using the New Zealand loading history than when testing using loading histories from other research institutions. This was evident in the small shear deformations (presented in Figure C-4(b)) resulting from testing using the New Zealand loading history compared to testing using loading regimes from other research institutions (shown in Figure C-11(b), Figure C-18(b), and Figure C-(25(b)). It was postulated that this behaviour was due to the larger ductility increments that were applied as part of the New Zealand loading history compared to loading histories from research institutions in the United States or Japan.

Figures 7-13 through 7-15 also indicate that the response from testing using the Public Works Research Institute's loading history was not reflective of the response from testing using either of the two loading histories from research institutions in the United States. As demonstrated in Figure C-11(b), Figure C-18(b), and Figure C-25(b), comparable shear deformations were recorded for these three tests even though smaller displacements were applied in testing using the Public Works Research Institute's loading history. It was postulated that this was due to the larger number of cycles that were applied at each ductility level compared to loading histories from research institutions in the United States.

The previous comments indicate that the amount of pinching in the hysteresis loops and the reloading stiffness were not reliable indicators of the amount of degradation that had occurred. Instead these parameters need to be considered in conjunction with the composition of the total displacement and the energy dissipation characteristics of the displacement components before comparisons can be made.

As with the comparisons made after loading to ductility 4 and ductility 6, the post-yield force-displacement response from monotonic loading formed an envelope to the corresponding portion of the force-displacement response from the cyclic tests.

### 7.2.2 Acceleration Histories

Figure 7-16 compares the envelope of the complete force-displacement response from the five acceleration histories to the force-displacement response from monotonic loading. Figure 7-16 illustrates that the post-yield portion of the monotonic curve formed an envelope to the corresponding portion of the force-displacement response from the five acceleration histories. This was consistent with the response plotted in Figures 7-13 through 7-15 from the laboratory procedures.

The influence of the largest displacement cycles' position in the displacement sequence on the shape of the hysteresis loops was illustrated after the largest displacement in the negative direction had been applied. The maximum negative displacement for acceleration histories D and E was at the beginning of the first earthquake record whereas the maximum negative displacement for acceleration histories B and C was during the second and third earthquake records respectively. This was reflected in the greater amount of pinching in the hysteresis loops for acceleration histories B and C because of the degradation that had occurred prior to the application of the maximum displacements in the negative direction. The amount of pinching in the hysteresis loops after application of the maximum displacement in the positive direction was comparable for each acceleration history because these displacements were always applied near the conclusion of the test. However, even though variations in hysteresis behaviour occurred, comparable degradation at the

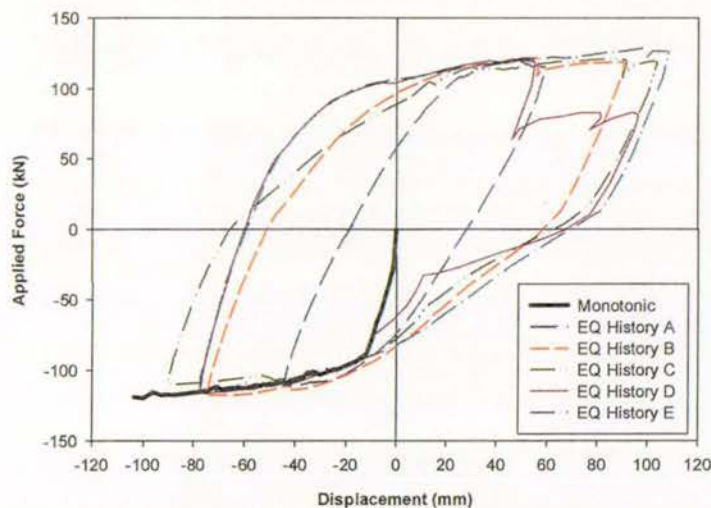


Figure 7-16 Comparison of Acceleration Histories' Envelope with Monotonic Response

conclusion of acceleration histories, B, C, and E was observed. This confirms the conclusions stated in Section 7.2.1.3 regarding the validity of using hysteresis behaviour to compare test results.

The previous comments also indicate that comparisons cannot be made between the hysteresis response from testing using laboratory procedures and testing using the simulated response from acceleration histories because there is no consistency between the displacements applied as part of the simulated seismic response.

Figure 7-16 also provides evidence of the failure that occurred during application of acceleration history D, with significantly lower forces required to apply the larger displacements in the positive direction than for acceleration histories B, C, or E.

### 7.3 Energy Dissipation

The amount of energy dissipated during each test was calculated so that the energy characteristics of each test could be compared. The amount of energy dissipated during the test was defined as the area inside the hysteresis loops until failure occurred. As reported in Section 6.1, the beam was considered to have failed once the maximum strength during a cycle dropped below 80% of the maximum-recorded strength for that direction of loading. Section 7.3.1 compares the energy dissipation characteristics from the seven laboratory procedures and Section 7.3.2 compares the energy dissipation characteristics from the five acceleration histories. Appendix C provides further information regarding separation of the energy dissipated during the test into the energy associated with flexural and shear displacement components.

#### 7.3.1 Laboratory Procedures

Figure 7-17 compares the energy dissipation characteristics from the seven laboratory procedures. Figure 7-17 reveals that the energy dissipation characteristics were strongly load history dependent, with the amount of energy dissipated ranging from 21.8kJ for testing conducted using monotonic loading to 148.1kJ for testing that applied the loading history from the Public Works Research Institute. This was

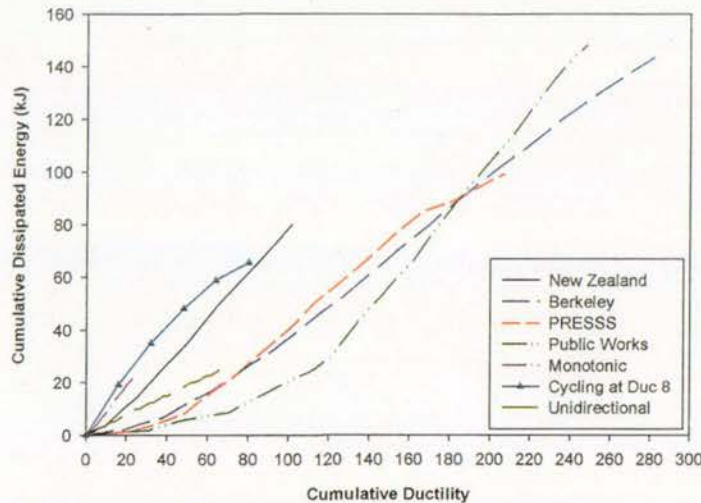


Figure 7-17 Comparison of Energy Dissipated during Laboratory Procedures

consistent with the conclusions reached by Kunnath et al. (1997) in their report on the cumulative seismic damage of reinforced concrete bridge piers.

The effect of the loading history on the energy characteristics of each test specimen was also illustrated in the shape of the envelope curve from each test. The envelope curve from the Public Works Research Institute reveals that only a small amount of energy was dissipated during the first portion of the test, when the test consisted of several cycles to low ductility values. However, large amounts of energy were dissipated later on in the test once ductility levels were increased. This behaviour was consistent with that noted by Lefas and Kotsovos (1990) in their work on reinforced concrete shear walls, which was reported on in Section 2.2.

Figure 7-17 reveals significant differences between the energy dissipated during testing using the four loading histories from research institutions throughout the world. Testing using the New Zealand loading history dissipated the least amount of energy. This was this test had the largest ductility increments and the least number of cycles at each ductility level. In contrast, testing using the loading history from the Public Works Research Institute dissipated the greatest amount of energy. This was reflective of the large number of cycles that were applied at each ductility level in this test.

Figure 7-17 demonstrates that there was little consistency in either the cumulative dissipated energy or the measured cumulative ductility. This and the previous comments imply that these parameters are not sufficiently independent of the applied loading history to be used to compare test results.

### 7.3.2 Acceleration Histories

Figure 7-18 compares the energy dissipation characteristics from testing using the five acceleration histories and demonstrates that the energy dissipation characteristics from acceleration histories B–E were similar. This indicates that the sequence which displacements were applied did not affect the energy dissipation capacity of the test subassembly. Again this was consistent with the conclusions stated by Hwang and Scribner (1984).

The impact of applying an additional earthquake record can be seen in the comparison of the energy dissipated from acceleration histories C and E with the acceleration history B. An additional 15kJ of energy was disbursed because the Kobe record was repeated. Figure 7-18 demonstrates that a lower amount of energy was dissipated during testing using acceleration history D than acceleration histories C and E even though an identical number of earthquake records were applied. This was due to the premature failure that occurred in testing using acceleration history D. This resulted in a reduction of strength and a corresponding reduction in the area inside the force-

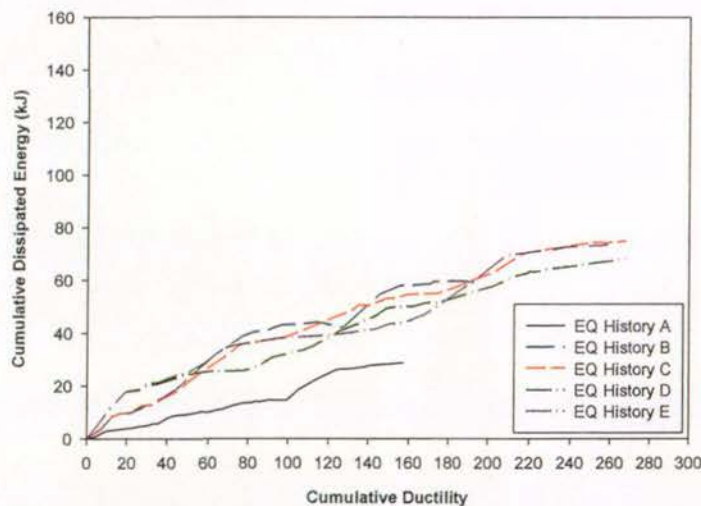


Figure 7-18 Comparison of Energy Dissipated from Acceleration Histories

displacement plot. The low amount of energy expended in acceleration history A compared to acceleration histories B–E reflected the low amount of damage that was incurred during application of acceleration history A.

As stated in Section 7.1.2, it was difficult to strictly define failure of the test specimen for testing using the five acceleration histories. However, the amount of physical degradation that occurred during testing using acceleration histories C through E indicated that failure had either occurred or was about to occur. Comparison of the energy dissipated in these three tests with that plotted in Figure 7-17 determined that testing using the New Zealand loading history returned the most accurate correlation between testing using laboratory procedures and testing using simulated acceleration histories.

#### **7.4 Reinforcement Steel Strain Behaviour**

As with Sections 7.1 and 7.2, the strain behaviour of the longitudinal reinforcement was separated into the seven laboratory procedures and the five acceleration histories. Section 7.4.1 compares the envelope of the strain behaviour of the longitudinal reinforcement from the laboratory procedures and Section 7.4.2 collates the results from the acceleration histories. Appendix C presents the strain histories from which the envelopes of strain behaviour were developed. Both Section 7.4.1 and Section 7.4.2 compare the average reinforcement strain from the first two instrumentation panels. This was equivalent to calculating the average reinforcement strain in the plastic hinge zone and also removed any variations due to different crack distributions.

##### **7.4.1 Laboratory Procedures**

Figure 7-19 presents the reinforcement strain envelopes from the seven laboratory procedures for loading up to and including ductility 8, when the instrumentation devices were removed. At ductility 8 and in the positive direction, the values range from 38600 microstrain from testing using the New Zealand loading history to 27600 microstrain under unidirectional loading. At ductility 8 in the negative direction, the values range from 38900 microstrain from testing that applied the New Zealand

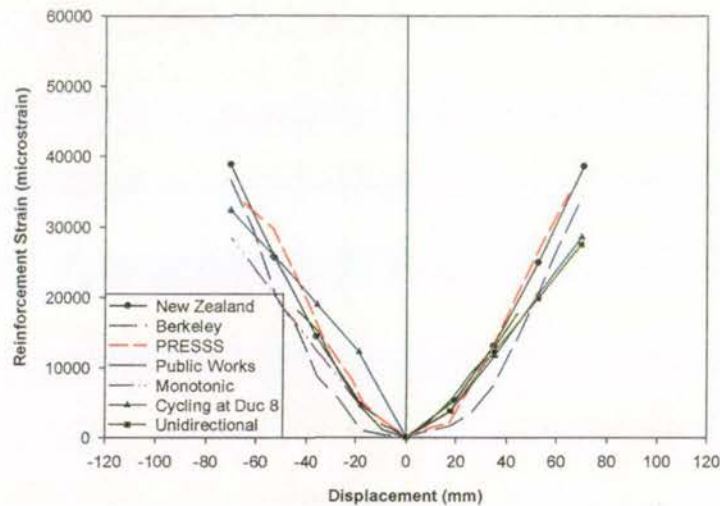


Figure 7-19 Comparison of Reinforcement Strain Envelopes for Laboratory Procedures

loading history to 28400 microstrain under monotonic loading. Figure 7-19 reveals that, apart from bi-directional cycling at ductility 8, the response from the five bi-directional cyclic tests was generally symmetric. Higher reinforcement strains were recorded in the negative direction than the positive direction for testing applying bi-directional cycling at ductility 8.

The low value of strain recorded in the positive direction when bi-directional cycling at ductility 8 was applied was because the strains from the first cycle were taken. Thus, the response from loading the test subassembly directly to ductility 8 (shown on the positive displacement scale) was expected to be similar to the response from monotonic loading (shown on the negative displacement scale).

Figure 7-19 demonstrates that similar strain recordings from monotonic and unidirectional loading were recorded for loading up to and including ductility 8 and these strain recordings formed a lower bound to the strain values recorded during bi-directional cyclic tests. This was consistent with the experimental results published by Kinugasa and Nomura (1992).

#### 7.4.2 Acceleration Histories

Figure 7-20 displays the longitudinal strain envelope from testing using the five acceleration histories. Strains were recorded for the entire test, which in some cases

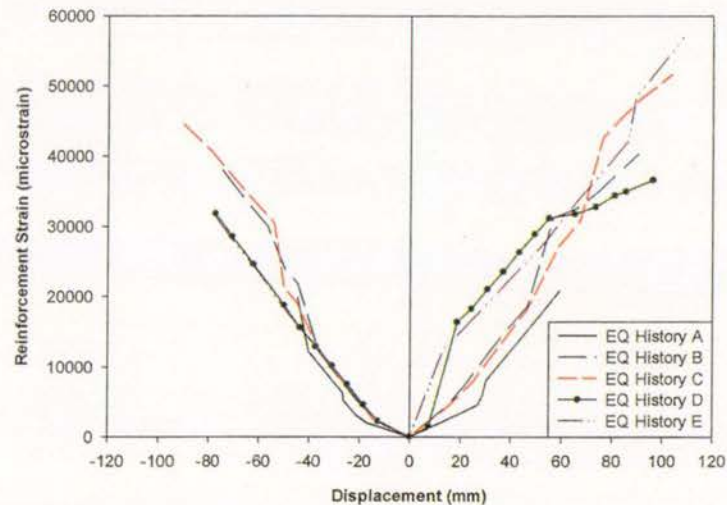


Figure 7-20 Comparison of Reinforcement Strain Envelopes for Acceleration Histories

included cycles above ductility 8. This accounted for the larger strains plotted in Figure 7-20, compared to those plotted in Figure 7-19. The non-symmetrical response was due to the irregular displacement sequences applied.

Different strain accumulation behaviour can be seen in Figure 7-20; for example, larger strains were recorded during application of acceleration histories D and E for low displacements in the positive direction than the corresponding displacements in acceleration histories A–C. This was due to the maximum negative displacement being applied prior to any significant loading in the positive direction for acceleration histories D and E. This resulted in large residual strains being present in the reinforcement prior to loading in the positive direction. This behaviour was comparable to the strain accumulation response from testing using bi-directional loading at ductility 8 that is presented in Figure 7-19.

Kinugasa and Nomura postulated a new failure mode based on the accumulation of strain in the plastic hinge zone. They stated that failure occurred once the strain reached 4–5% (40000–50000 microstrain). However, this finding was only of limited use to this experimental study, because no information was provided regarding the chemical composition of the reinforcement steel. When developing their model for the cyclic behaviour of reinforcing steel, Dodd and Restrepo (1995) established that the chemical composition of the reinforcing steel affected its behaviour under cyclic loading.

The experimental results reported herein also did not endorse the conclusion by Kinugasa and Nomura that failure occurred within a narrow range. The test subassemblage subjected to the loading history from the Public Works Research Institute failed when the longitudinal reinforcement strain was equal to 17700 microstrain. In contrast, failure occurred when testing using the PRESSS loading history at reinforcement strains equal to 34700 microstrain whereas reinforcement strains in excess of 50000 microstrain were recorded during application of acceleration histories C and E. Thus, longitudinal reinforcement strains gave no indication of the point of failure and hence, cannot be used to predict the failure of test subassemblies.

Comparison of Figure 7-19 with Figure 7-20 shows that although the strain behaviour for the twelve tests was generally similar, larger displacements were applied when testing using acceleration histories B through E than for testing using loading histories from research institutions. However, the test specimens subjected to acceleration histories B through E did not necessarily fail by the 20% strength reduction criterion even though larger displacements were applied. This indicates that the loading histories applied at research institutions are more demanding than actual displacements resulting from seismic excitation. This is also evident in Section 7.3, where it was shown that, apart from testing using the New Zealand loading history, more energy was dissipated during testing using laboratory procedures than acceleration histories.

As detailed in Section 7.4.1, the largest strains from the seven laboratory procedures were recorded during testing using the New Zealand loading history. This and the comparison made in Section 7.3.2 regarding energy dissipation indicates that the New Zealand loading history replicates the earthquake demand of a reinforced concrete member more closely than loading histories from other research institutions.

## 7.5 Damage Indices

Damage indices were calculated from the experimental data obtained from the twelve tests. This enabled the damage that occurred when testing using laboratory

procedures to be compared with the damage suffered during application of the five acceleration histories.

Five different damage indices were calculated to enable comparison of the twelve tests. The five damage indices were those proposed by Cosenza et al. (1993), Roufaiel and Meyer (1987), Park and Ang (1985), Banon and Veneziano (1982), and Bracci et al. (1989). These are detailed in Section 3.5.

As reported in Section 5.2, predictions of the maximum damage indices' values were calculated for the five acceleration histories. Section 7.5.1 compares the predicted values with the values established from experimental data. Section 7.5.2 then compares the damage indices calculated from the experimental data for each test with the observed behaviour during testing. Lastly, Section 7.5.3 summarises the findings of Section 7.5.2 and then proposes further details for the damage levels reported on in Section 7.5.2.

#### 7.5.1 Comparison of Predicted Damage Indices with Actual Damage Indices

Prediction of the maximum values for the respective damage indices was based on the predicted force-displacement response from the Ruaumoko analysis. Table 7-1 compares the predicted and actual maximum value for each damage index from each acceleration history.

Comparison of the values in Table 7-1 reveals excellent agreement between the predicted damage indices and the actual damage indices. However, the excellent agreement between the deformation-based damage indices occurred by default because the displacement sequence applied in the laboratory was taken from the displacement-time history that the predicted values were based on. This accounts for the perfect agreement between the predicted and actual values for the Cosenza index and to a lesser extent, the excellent agreement between the predicted and actual values for the Roufaiel and Meyer index. Although the Roufaiel and Meyer index takes into account stiffness and strength degradation, the major variable affecting the damage index is the displacement. The large difference between the predicted and actual value for the Roufaiel and Meyer index for acceleration history D was because of the

Table 7-1 Comparison of Predicted and Actual Damage Indices (At Conclusion of Test)

Acceleration History	Damage Index	Predicted	Actual
A	Roufaiel & Meyer	0.29	0.29
	Park & Ang	0.54	0.43
	Cosenza et al.	0.26	0.26
	Banon and Veneziano	0.42	0.38
	Bracci et al.	0.54	0.40
B	Roufaiel & Meyer	0.45	0.47
	Park & Ang	0.75	0.76
	Cosenza et al.	0.42	0.42
	Banon and Veneziano	0.55	0.55
	Bracci et al.	0.70	0.69
C	Roufaiel & Meyer	0.50	0.56
	Park & Ang	0.96	0.89
	Cosenza et al.	0.49	0.49
	Banon and Veneziano	0.64	0.62
	Bracci et al.	0.84	0.79
D	Roufaiel & Meyer	0.47	0.78
	Park & Ang	0.89	0.81
	Cosenza et al.	0.45	0.45
	Banon and Veneziano	0.60	0.58
	Bracci et al.	0.81	0.74
E	Roufaiel & Meyer	0.52	0.54
	Park & Ang	0.92	0.91
	Cosenza et al.	0.51	0.51
	Banon and Veneziano	0.64	0.64
	Bracci et al.	0.81	0.80

rupturing of the longitudinal bar early in the test sequence. This led to significant strength loss later on in the test that the model was unable to predict.

The other three indices are based on a combination of damage due to deformation and damage due to the dissipated energy. Of the three, the Banon and Veneziano index gives the best correlation between the predicted and actual values. The Bracci et al. index and the Park and Ang index generally over-predicted the amount of damage that occurred. This was due to the hysteresis model failing to accurately account for pinching in the hysteresis loops and strength degradation near the conclusion of the test.

As shown in the following section, the Bracci index and the Park and Ang index provide the most accurate correlation between the calculated index and the observed damage. Therefore, to ensure that failure would occur by the conclusion of the test, it is recommended that a predicted damage index approximately equal to 1.1 be obtained for future testing.

#### 7.5.2 Comparison of Actual Damage Indices with Observed Damage

It was necessary to define the damage evident at each damage level before a comparison of the actual damage indices with the observed damage could be made. However, a review of previously published damage criteria (Applied Technology Council 1989; Williams and Sexsmith 1995; Williams et al. 1997) revealed extremely broad criteria; for example, significant cracking with no mention of the type of cracking, the widths of cracks, or the amount of cracking. Hence the damage criteria previously published have been difficult to apply in this study to the observed behaviour during testing. This report applies these broad terms to the observed behaviour. Further details based on the observed behaviour from the testing reported herein are provided in Section 7.5.3.

Five damage levels with corresponding observed damage were defined in this report. The five levels are no damage, minor damage, moderate damage, severe damage, and collapse. Table 7-2 categorises the observed damage into the five damage levels.

The crack widths in Table 7-2 refer to widths after removal of the load—whether that was the applied actuator force during testing or the conclusion of the earthquake in real-life situations. In contrast, the crack widths after the application of the maximum actuator force were measured for the testing reported herein. Allowance was made for this inconsistency when comparing the crack widths measured during testing and the criteria set out in Table 7-2. However, it was evident from the plots of the horizontal elongation for each test displayed in Appendix C that there was little closure of cracks upon removal of the actuator force.

Table 7-2 Criteria for Damage Levels

Damage State	Observed Behaviour
No Damage	Small amounts of flexural and shear cracking may be evident. However, the widths of these cracks will be less than 0.5mm.
Minor Damage	The widths of any flexural or shear cracks will be less than 1.0mm. No concrete spalling is evident.
Moderate Damage	Damage occurring after this level is generally defined as being irreparable. Flexural or shear cracks will be less than 3.0mm. Limited concrete spalling will occur. However, this will not result in exposure of transverse or longitudinal reinforcement.
Severe Damage	Further crushing of concrete in the plastic hinge zone will occur. Spalling of cover concrete such that longitudinal and transverse reinforcement is visible will occur.
Collapse	Buckling of the longitudinal reinforcement will be evident at this damage level. Rupture of longitudinal reinforcement may occur.

All five damage indices were established so that a value equal to zero implied no damage and a value equal to 1.0 implied failure had occurred. However, of the five damage indices, only the Park and Ang index and the Bracci index gave any indication regarding the meaning of intermediate values. Table 7-3 lists the relationship of the intermediate values for these two damage levels with the five damage levels defined for this report in Table 7-2.

Figure 7-21 displays the damage indices calculated from experimental data obtained from testing that implemented the New Zealand loading history. Damage indices were plotted for this test, and other laboratory procedures, until failure occurred, which was defined as a reduction in strength greater than or equal to 20% of the maximum-recorded strength for that test. Figure 7-21 reveals that of the five damage indices, the Park and Ang index and the Bracci index were the only indices that were close to defining failure of the beam as having occurred. The five damage indices

Table 7-3 Collation of Intermediate Index Values with Observed Damage Levels

	Park & Ang	Bracci
No Damage	$D \leq 0.1$	$D \leq 0.33$
Minor Damage	$0.1 < D \leq 0.25$	
Moderate Damage	$0.25 < D \leq 0.40$	$0.33 < D \leq 0.66$
Severe Damage	$0.40 < D \leq 1.0$	$0.66 < D \leq 1.0$
Collapse	$D > 1.0$	$D > 1.0$

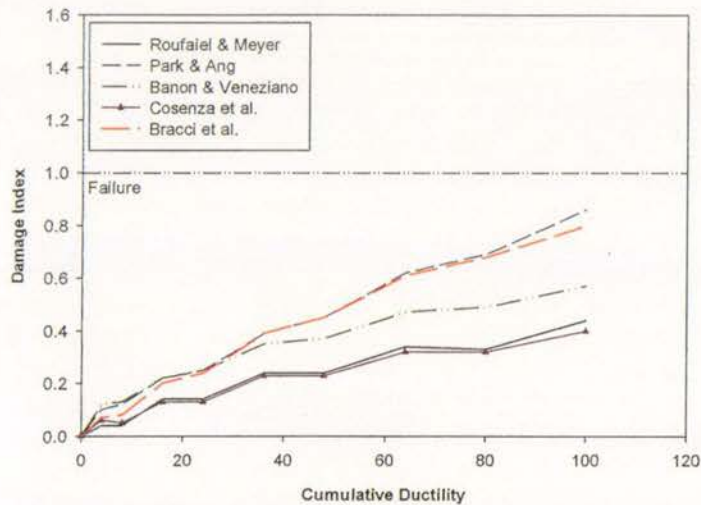


Figure 7-21 Damage Indices (New Zealand Loading History)

increase in a stepwise manner, where the plateau corresponds to the second cycle at each ductility level. This was consistent with observed behaviour from testing where little additional damage was observed during the repeat cycles. Detailed discussion is only provided for the Park and Ang index and the Bracci index because these were the only indices to define intermediate values. The behaviour observed during this test is described in Appendix C.1.1.

The Park and Ang index defined damage incurred for loading up to and including ductility 4 as minor damage. No concrete spalling was evident after these cycles, which was consistent with the description detailed in Table 7-2. However, the largest measured crack width was 5.0mm, which was significantly greater than the crack widths defined under minor damage.

Damage that was observed after loading to ductility 6 was defined as severe damage. The behaviour observed during these cycles is in agreement with the description detailed in Table 7-2. Spalling of cover concrete occurred such that transverse and longitudinal reinforcement was visible. Failure of the test specimen occurred at an index value equal to 0.86. This is slightly lower than the limit listed in Table 7-3 but, as reported in Section 7.1.1, failure was due to the premature rupture of a longitudinal bar. It was likely that the damage index would have reached a value equal to or greater than 1.0 if this premature rupture had not occurred.

The Bracci index exhibited a level of agreement similar to the Park and Ang index. As with the Park and Ang index, the Bracci index defined damage incurred in loading up to and including ductility 4 as minor damage. Damage incurred after ductility 6 cycles was defined as moderate damage. The small amount of spalling that occurred during the ductility 6 cycles is compatible with the damage defined as moderate. By ductility 8, damage was defined as severe, which was consistent with the observed behaviour.

Figure 7-22 presents the damage indices calculated from experimental data derived using the Berkeley loading history. In this figure the Park and Ang index and the Bracci index were the only indices that defined failure of the beam as having occurred. As with testing using the New Zealand loading history, the five damage indices increased in a stepwise manner at low displacements and the plateau corresponded to the second and third cycle at each ductility level.

An identical ultimate ductility was reached in this test to that when using the New Zealand loading history, which accounted for the identical value for the Cosenza index reached in this test. The Roufaiel and Meyer index returned a higher value for this test, which reflected the greater amount of degradation and the premature failure that occurred when testing using the New Zealand loading history.

The values returned by the Park and Ang index were comparable with the observed

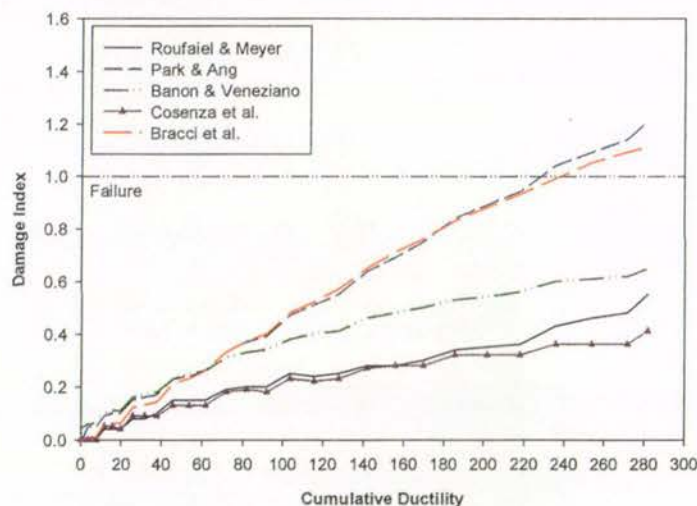


Figure 7-22 Damage Indices (Berkeley Loading History)

damage grouped into the five damage levels near the conclusion of the test. The damage incurred during loading up to and including ductility 4 was defined as minor damage. However, a small amount of spalling was apparent after loading to this stage. A maximum crack width of 3.2mm was measured during the inspection after ductility 4 cycles. This is comparable to the damage grouped under the moderate damage level.

Severe damage was said to have occurred once the loading reached ductility 5, with longitudinal reinforcement becoming visible during the three cycles to ductility 7. The collapse level was reached after the three cycles to ductility 9, with rupture of the longitudinal reinforcement occurring soon after.

The comparison of the calculated Bracci index and the observed damage revealed similar results to the Park and Ang index. Again observed damage was more severe than that defined by the damage index at the minor and moderate damage levels. However, the observed damage was consistent with the calculated index once the severe and collapse damage levels were reached.

Figure 7-23 details the damage indices calculated from experimental data obtained from testing that applied the PRESSS loading history. Figure 7-23 illustrates that, as with the two previously reported tests, the Park and Ang index and the Bracci index were the only indices that were close to defining failure of the beam as having

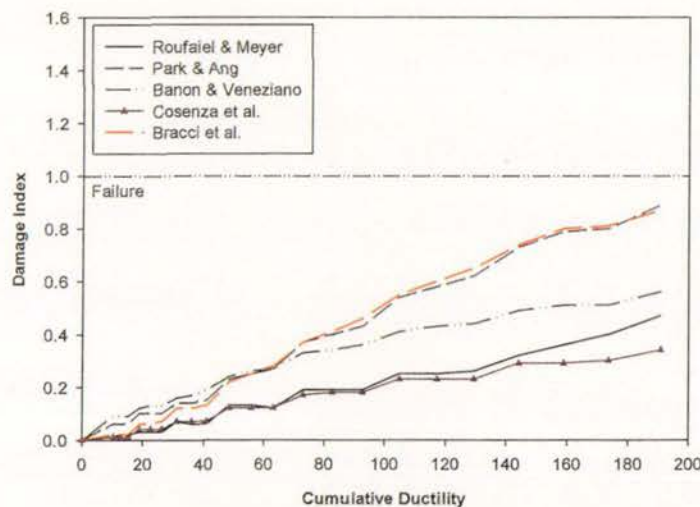


Figure 7-23 Damage Indices (PRESSS Loading History)

eventuated, and that the five damage indices increased in a stepwise manner at low displacements.

A comparison of observed damage with the values conveyed by the damage indices revealed similar results to testing that applied the Berkeley loading history. The damage incurred during loading up to and including ductility 3.69 was defined as minor damage. However, minor spalling was evident after loading to this ductility level and a maximum crack width of 4.0mm was measured during inspection after the third ductility 3.69 cycle. This is wider than the limits defined under the minor damage level. However, the damage observed near the conclusion of the test was consistent with the damage descriptions listed in Table 7-2. Severe damage was determined to have occurred once loading reached ductility 4.91, with longitudinal reinforcement becoming visible during the three cycles at ductility 6.14. Buckling of longitudinal reinforcement occurred during the three cycles at ductility 7.37. This type of damage is defined as occurring during failure of the test subassembly.

Comparison of the calculated Bracci index with observed damage revealed poor correlation between the calculated index and the observed damage. As with the Park and Ang index, damage was more severe in the minor and moderate damage levels. However, in contrast to the Park and Ang index, the Bracci index also showed poor correlation once the damage reached the severe stage.

Figure 7-24 presents the damage indices calculated from the experimental data recorded during testing that applied the loading history from the Public Works Research Institute. Figure 7-24 reveals that the Park and Ang index and the Bracci index were the only indices that identified that failure would occur. The five damage indices increased in a stepwise manner at low displacements with the plateau corresponding to the repeat cycles at each ductility level.

The values returned by the Park and Ang index were comparable with the observed damage grouped into the five damage levels near conclusion of the test. The damage incurred during loading up to and including ductility 2 was defined as minor damage. However the widths of cracks measured after the tenth cycle at ductility 2 were wider than the maximum amount defined under minor damage. Severe damage was said to

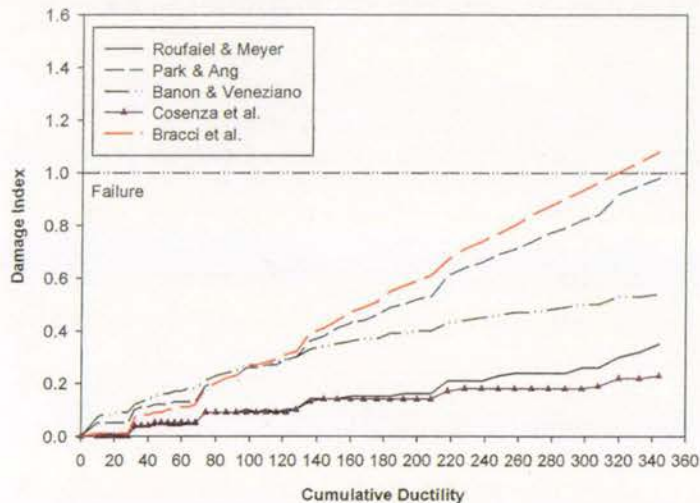


Figure 7-24 Damage Indices (Public Works Research Institute)

have occurred once the loading reached ductility 4. This was consistent with the observed damage from the test, with longitudinal reinforcement becoming visible during the ductility 4 cycles. Failure of the test subassemblage was also defined accurately, with the strength of the test subassemblage dropping below 80% of the maximum-recorded strength at an identical ductility to the designated failure ductility from the damage index.

The comparison of the calculated Bracci index and the observed damage revealed similar results to the Park and Ang index. Again damage was more severe in the minor and moderate damage levels. However, the observed damage was consistent with the calculated index once the severe and collapse damage levels were reached.

Figure 7-25 illustrates the damage indices calculated from testing where monotonic loading was applied. Figure 7-25 reveals that all five damage indices predicted that failure would occur. However, this occurred by default because the ultimate variables in the damage indices were normalised with respect to this test.

The comparison characteristics of the Park and Ang index and the Bracci index were similar to the previously reported tests, where the crack widths were wider than the allowable limits. Otherwise the damage of the test specimen observed during testing was comparable to the descriptions of each damage level listed in Table 7-2.

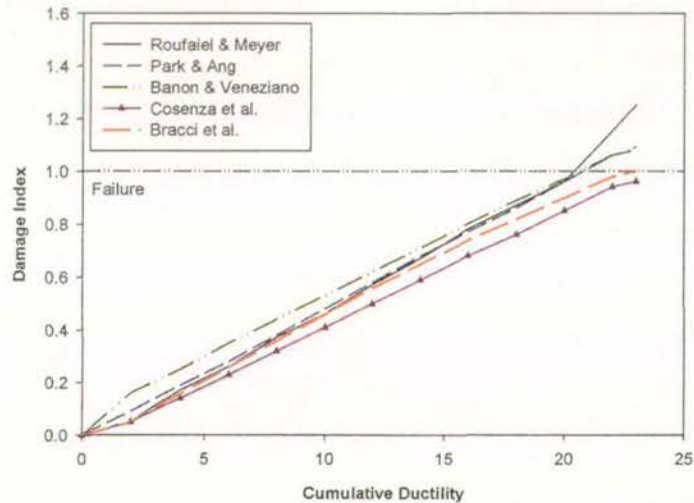


Figure 7-25 Damage Indices (Monotonic Loading)

Figure 7-26 details the damage indices calculated when bi-directional cycling at ductility 8 was applied and reveals that none of the five damage indices defined failure of the beam as having occurred. This was because the five damage indices were not based on the principles of fatigue loading. This was supported in a study by Kunnath et al. (1997) on the development of a fatigue-based cumulative damage model, where it was concluded that indices such as the Park and Ang index and the Roufaei and Meyer index were unable to accurately predict the final damage state of the test subassemblage.

Figure 7-26 illustrates that the indices that accounted for the amount of energy

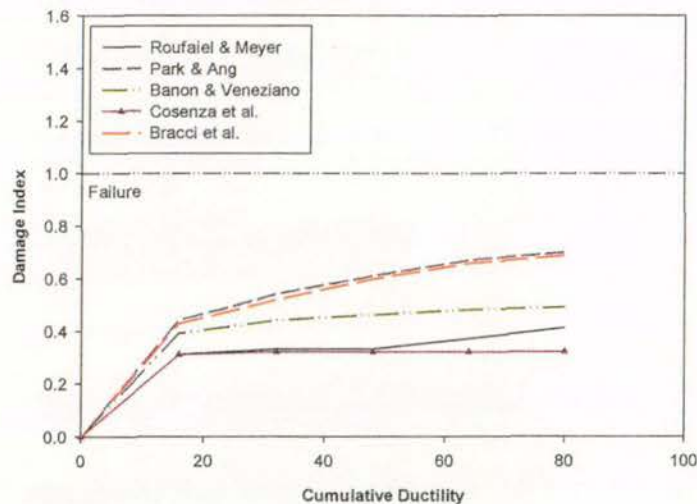


Figure 7-26 Damage Indices (Bi-directional Cycling at Ductility 8)

dissipated during the test gave the best indication of the amount of damage incurred. Fatigue models proposed by Kunnath et al. and Mander (1998) were applied to this test but returned poor correlation to the observed damage. This was not unexpected as these models were calibrated with respect to concrete columns instead of the formation of beam plastic hinges.

The values returned by the Park and Ang index predicted that severe damage had occurred after the first cycle. This was consistent with the observed damage from the test where crushing of concrete and spalling of concrete were both apparent.

The comparison of the calculated Bracci index and the observed damage revealed poor correlation between the observed behaviour and the predicted damage. Severe damage was defined as having occurred by the fourth cycle. However, as has been previously reported, severe damage was observed to have occurred after the first cycle.

Figure 7-27 displays the damage indices calculated for testing applying unidirectional loading. Figure 7-27 reveals that all five damage indices predicted that failure would occur. However, this was expected because the ultimate ductility reached in this test was comparable to the ultimate ductility reached under monotonic loading. All five damage indices increased in a stepwise manner with the plateau corresponding to the

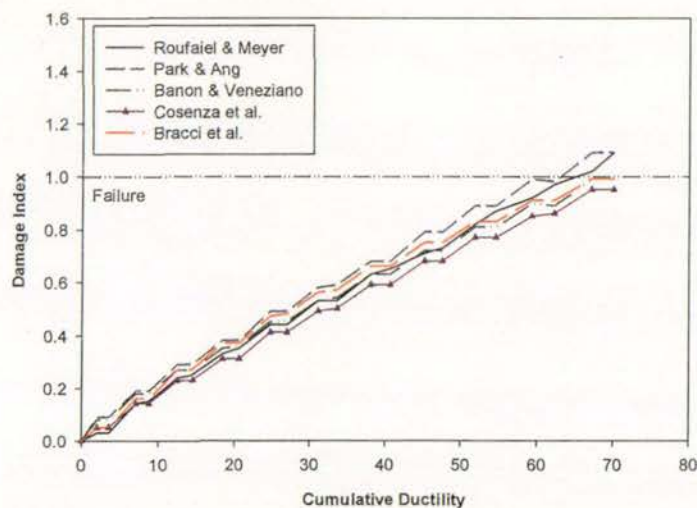


Figure 7-27 Damage Indices (Unidirectional Loading)

second cycle at each ductility level.

As with previously reported tests, the Park and Ang index was comparable with the observed damage for the latter stages of the test only. Damage incurred during loading up to and including ductility 4 was defined as minor damage. However, a maximum crack width of 2.3mm was measured after loading to this stage, which was comparable to the crack widths under the moderate damage level. Severe damage was designated once the loading reached ductility 8. Crushing and spalling of concrete was observed at this load step. This was consistent with the description listed in Table 7-2.

The comparison of the calculated Bracci index and the observed damage again revealed poor correlation between the observed experimental behaviour and the predicted damage, with severe damage only being defined for loading after ductility 14. As was reported earlier, severe damage occurred once the loading reached ductility 8.

Figure 7-28 details the damage indices calculated from testing using acceleration history A. Damage indices were plotted for this test, and other acceleration histories, for points on the force-displacement envelope, because deformation was either the sole indicator of damage or dominated the other terms in the damage index. Hence, plotting damage indices for points inside the force-displacement envelope would

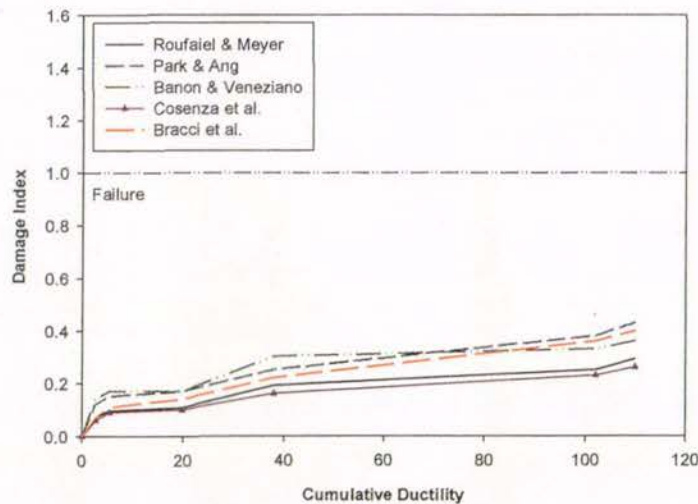


Figure 7-28 Damage Indices (Acceleration History A)

result in reduction of the damage state. It is illogical to predict that minor damage has occurred when, prior to the application of the last cycle, moderate or severe damage had been predicted. Figure 7-28 reveals that all five damage indices specified that failure would not occur. Of the damage indices that defined intermediate values, the Park and Ang index classified the damage as severe whereas the Bracci index classified the damage as moderate.

The values returned by the Park and Ang index revealed poor correlation between the calculated damage index and the observed damage. Spalling was not seen at any stage of the test even though the damage index predicted that severe damage would occur. As with other tests, the widths of cracks were wider than their allowable widths for their respective damage states.

The comparison of the calculated Bracci index and the observed damage revealed slightly better correlation than the Park and Ang index although the measured crack widths were wider than the limits detailed in Table 7-2.

Figure 7-29 presents the damage indices calculated from experimental data recorded during testing using acceleration history B. As with acceleration history A, none of the five damage indices classified the damage incurred as being consistent with the collapse damage level. The Park and Ang index and the Bracci index both specified

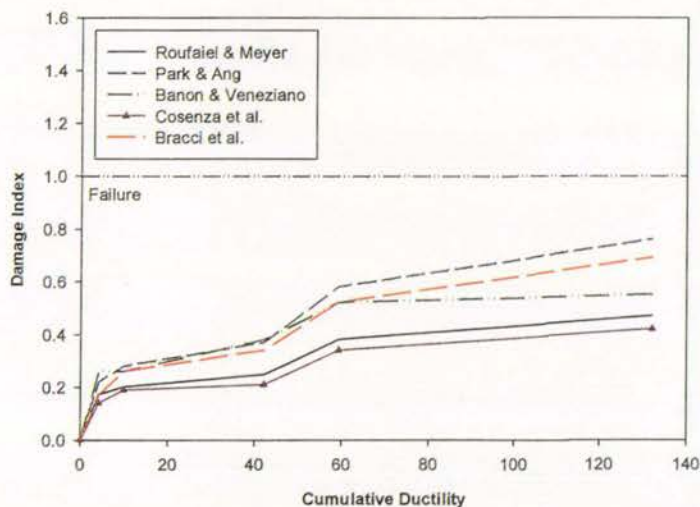


Figure 7-29 Damage Indices (Acceleration History B)

that severe damage occurred.

The Park and Ang index defined the damage incurred during the application of the Normalised El Centro record as moderate damage. However, after loading to this stage, spalling of cover concrete meant that a transverse stirrup was visible. This behaviour is defined as severe damage in Table 7-2. The crack widths were also in excess of the allowable limits. However, the damage observed near the conclusion of the test was consistent with the damage descriptions listed in Table 7-2. Severe damage was said to have occurred during application of the Northridge earthquake record. Crushing of concrete and continued spalling were observed during that record.

The comparison of the calculated Bracci index and the observed damage revealed similar results to the Park and Ang index. Again damage was more severe in the minor and moderate damage levels. However, the observed damage was consistent with the calculated index once the severe and failure damage levels were reached.

Figure 7-30 illustrates the damage indices calculated from testing using acceleration history C. Figure 7-30 reveals that of the five damage indices, the Park and Ang index was the only index that was close to specifying that failure would occur. The Bracci index classified the damage as severe.

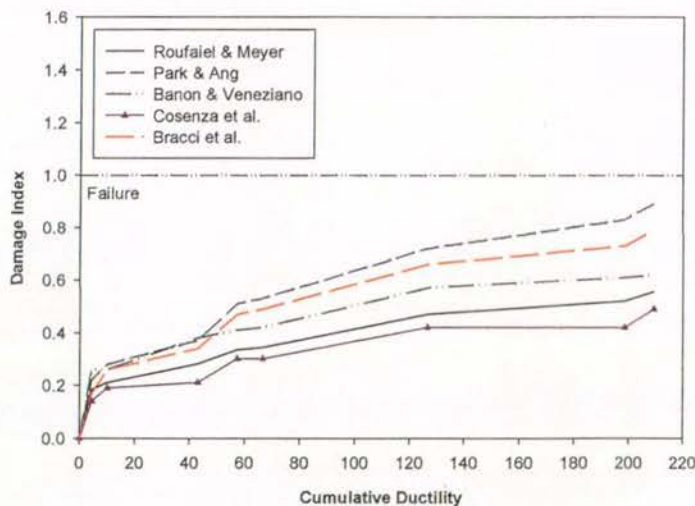


Figure 7-30 Damage Indices (Acceleration History C)

The values returned by the Park and Ang index were comparable with the observed damage grouped into the five damage levels for the entire test. The damage incurred during the Normalised El Centro record was defined as moderate damage with minor spalling of cover concrete being observed. This is consistent with the behaviour described in Table 7-2 as moderate damage. Severe damage was defined as occurring during the first Kobe record. Transverse and longitudinal reinforcement was visible and crushing of concrete was also apparent. Again this is consistent with the behaviour described in Table 7-2. Significant spalling of cover concrete, such that approximately 300mm of longitudinal reinforcement was visible, occurred during the second Kobe record. This reflected the large amount of degradation that had taken place by that stage of the test.

The comparison of the calculated Bracci index and the observed damage revealed similar results to the Park and Ang index, although the crack widths did not correlate to the limits described in Table 7-2.

Figure 7-31 details the damage indices calculated from testing using acceleration history D. Figure 7-31 reveals that none of the five damage indices classified the test specimen as reaching its collapse stage. However, this was largely due to the premature rupture of a longitudinal bar. This led to significant strength reduction and a corresponding loss of energy absorbed, which reduced the values calculated by the

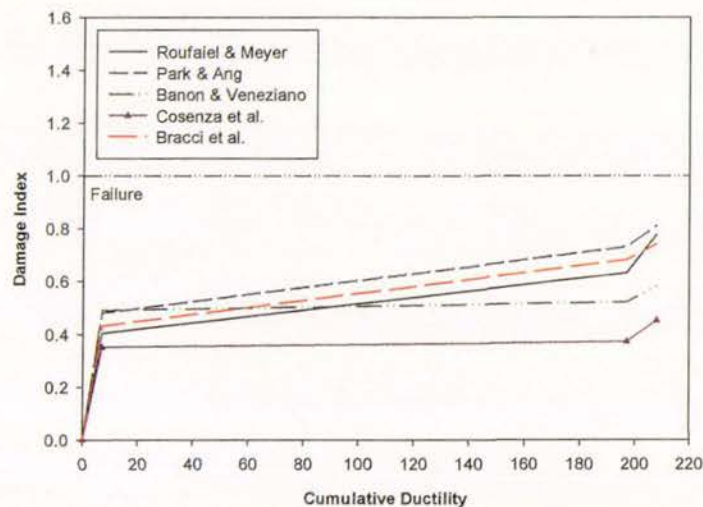


Figure 7-31 Damage Indices (Acceleration History D)

Park and Ang index and the Bracci index.

The Park and Ang index was consistent with the observed damage prior to the rupture of the longitudinal bar. Severe damage was defined as occurring during the application of the Northridge earthquake record, with spalling of cover concrete such that transverse reinforcement was visible occurring during the application of this record. The measured crack widths were also consistent with the limits described in Table 7-2.

The Bracci index did not provide an accurate representation of the physical damage for this test. Damage incurred during the Northridge record was defined as moderate damage when, as previously mentioned, the physical damage was consistent with the characteristics of severe damage.

Figure 7-32 presents the damage indices calculated from experimental data recorded during testing using acceleration history E. Again the Park and Ang index was the only index that specified that failure would occur with the Bracci index classified the damage as belonging to the severe damage level.

The Park and Ang index was consistent with the observed damage for the duration of the test. Severe damage was defined as occurring during the application of the Northridge earthquake, with crushing and spalling of concrete being evident. The

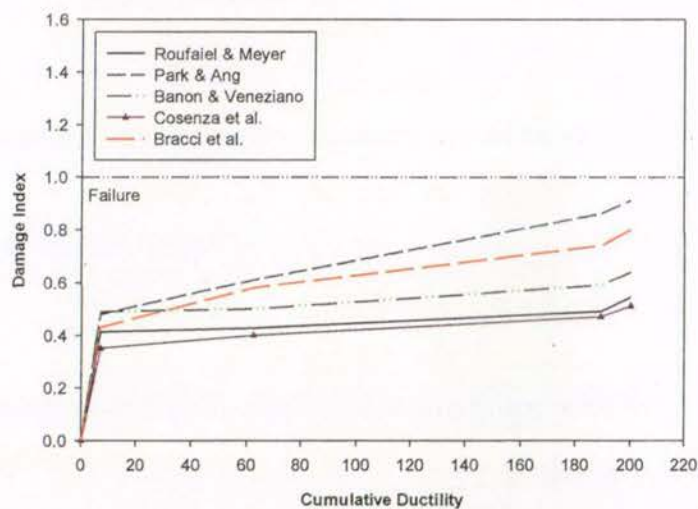


Figure 7-32 Damage Indices (Acceleration History E)

measured crack widths were also consistent with the limits listed in Table 7-2. Spalling continued to occur throughout this test and significant degradation had occurred by the conclusion of this acceleration history.

Poor correlation was obtained between the calculated Bracci index and the observed damage. Damage incurred during the Northridge record was classified as moderate damage, which clearly was not the case.

### 7.5.3 Relevance of Damage Indices

Of the five damage indices, the Park and Ang index and the Bracci index were the only indices that repeatedly returned values at the end of the test that were comparable with the observed damage. This indicates that damage indices that are a combination of damage due to deformation and cumulative cycling return the best correlation to the observed damage. Of the two, the Park and Ang index generally provides the best correlation between the calculated values and the observed damage.

Crushing and spalling of concrete were usually well predicted by the Park and Ang index. In contrast, the measured crack widths were typically wider than the prescribed limits. The exception was for acceleration histories C-E, when the crack widths were consistent with the limits defined in Table 7-2. This was attributed to the acceleration histories consisting of less damaging cycles than the laboratory procedures. This meant that smaller crack widths were recorded during testing using the five acceleration histories. However, this inconsistency was not of major concern because comparisons are unlikely to be made at low damage levels, which was when the widths of cracks were the dominant measure of the amount of damage. Damage in the severe damage level was dominated by the spalling of concrete and the exposure and buckling of longitudinal reinforcement with crack widths generally unreadable once severe damage was reached.

Although the Park and Ang index returned values that were comparable to the observed damage at the end of the test, minor improvements could be made. On several occasions the maximum value for the index was in the range of 0.8 to 0.9. This was slightly less than the value corresponding to collapse listed in Table 7-3.

The value of  $\beta$  calculated from Equation 3.7 in Section 3.5.4 was equal to 0.08. After testing this value was altered so that it was equal to 0.10. This was based on a recommendation made by Kunnath et al. (1992) in their report on the computer programme IDARC. This resulted in the Park and Ang index returning values corresponding to the collapse damage state for six of the seven laboratory procedures. The exception was bi-directional cycling at ductility 8 but, as mentioned previously, this was due to the formation of the Park and Ang index not being based on low-cycle fatigue of reinforced concrete members. Thus, it is recommended that the value for  $\beta$  be set to equal 0.10 for future studies.

Overall, damage indices provide a reasonable means of comparing experimental results derived from testing using different loading regimes. The advantage of calculating damage indices is that behaviour of the test subassemblage at intermediate stages of the test can be compared. In contrast, other criteria such as strength loss can only be applied to establish when failure of the test subassemblage occurs.

The ability of damage indices to facilitate comparison of experimental results at intermediate stages is shown in Figure 7-33—a plot of the Park and Ang damage index for the tests where failure, as defined in Section 6.1, occurred. For example, a moderate damage level can be established for each test, which enables comparison of experimental data recorded while moderate damage is defined. This removes any problems associated with comparing data at a common ductility level because, as

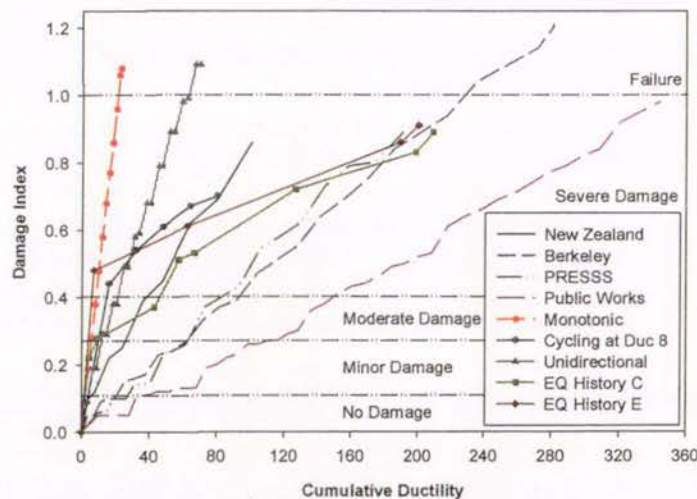


Figure 7-33 Comparison of Park and Ang Damage Index for Tests where Failure Occurred

Figure 7-33 clearly indicates, the behaviour of the test specimen is not consistent with the ductility level. Acceleration histories C and E were included in Figure 7-33 because, although failure was not strictly defined, physical degradation was consistent with that observed during testing using laboratory procedures. Acceleration history D was not included because of the premature failure that occurred early in the test sequence and affected the damage index from that point.

However, one weakness of damage indices is that the criteria for each damage level are extremely broad. Therefore, on the basis of the behaviour observed during this experimental study the descriptions listed in Table 7-2 has been expanded and the criteria presented in Table 7-4.

Table 7-4 specifies the extent of the cracking defined under each classification level and provides more indicators of severe damage and failure of the test specimen; for example, shear deformations becoming more apparent.

Table 7-4 Criteria for Damage Levels (Based on Testing Reported Herein)

Damage State	Observed Behaviour
No Damage	Small amounts of flexural and shear cracking may be evident. However, the widths of these cracks will be less than 0.5mm.
Minor Damage	Widespread cracking within a distance 2h from the face of the beam-column joint will occur. The widths of any flexural or shear cracks will be less than 1.0mm. No concrete spalling is evident.
Moderate Damage	Damage occurring after this level is generally defined as being irreparable. Flexural or shear cracks will be less than 3.0mm. Limited concrete spalling will occur. However, this will not result in exposure of transverse or longitudinal reinforcement
Severe Damage	Little additional cracking will form between this damage level and the moderate damage level. Flexural and shear cracks in the plastic hinge zone will continue to widen with crack widths reaching 10mm. Further crushing of concrete in the plastic hinge zone will occur. Spalling of cover concrete, such that longitudinal and transverse reinforcement is visible, will occur. Shear deformations will become more apparent.
Collapse	Spalling of concrete will continue such that a distance of approximately 0.5h from the face of the beam-column joint will be without cover concrete. Buckling of the longitudinal reinforcement will be evident at this damage level. Rupture of longitudinal reinforcement may occur

## 7.6 Comparison of Crack Behaviour

This section compares the orientation and width of cracks that resulted from testing using the seven laboratory procedures. Comparisons were made at the conclusion of the cycles at ductility 2, ductility 4, and ductility 6 and are reported on in Section 7.6.1, Section 7.6.2, and Section 7.6.3 respectively. No comparisons were made between the crack behaviour from testing using the five acceleration histories. This was because the irregular nature of the acceleration histories made such comparisons meaningless.

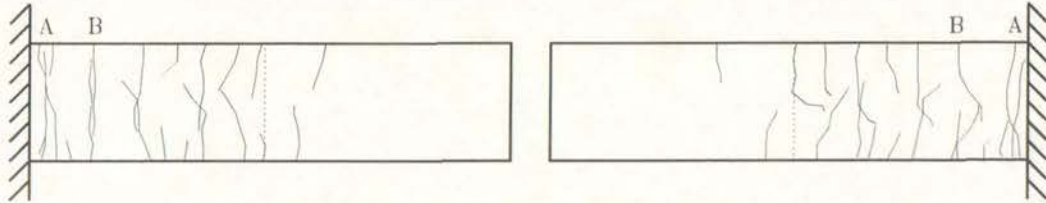
### 7.6.1 Comparison after Loading to Ductility 2

Figure 7-34 illustrates the crack patterns after the conclusion of loading to ductility 2 for the seven laboratory procedures. The dashed vertical line indicates the potential plastic hinge zone as defined by the New Zealand standard for the Design of Concrete Structures (Standards New Zealand 1995) and also the extent of the instrumentation. The letters 'A' and 'B' refer to the two largest cracks on each side. It can be seen in Figure 7-34 that little cracking occurred outside the instrumentation zone. It was observed during testing that, of the cracking that did occur outside the instrumentation zone, cracks did not open for any stage of the test. This indicates that the instrumentation layout depicted in Figure 4-16 recorded all the necessary data. This is further confirmed in Appendix C, where negligible curvature and reinforcement strains from the outmost instrumentation panel were indicated.

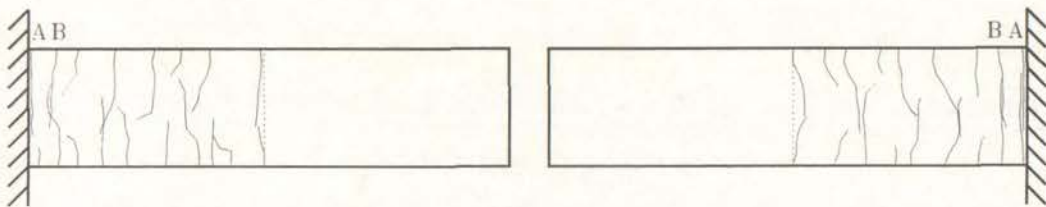
As reported in Section 7.2.1, converting storey drifts from the PRESSSS loading history to ductility levels resulted in irregular ductility increments being applied. Therefore Figure 7-34 illustrates the test specimen subjected to the PRESSSS loading history after three cycles at ductility 1.84 had been applied. Table 7-5 compares the widths of the two major cracks in the plastic hinge zone from each test at this loading stage. Table 7-5 was based on the maximum value measured from both sides of the test unit in both the positive and negative direction of loading.

Figure 7-34 reveals that different crack behaviour resulted from the seven different loading histories. This was largely due to localised discontinuities in each test

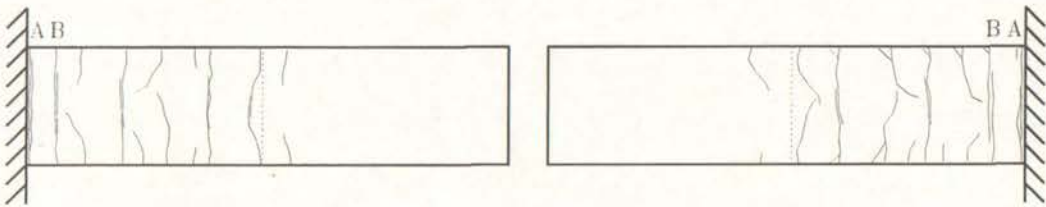
specimen; for example, a plane of concrete that was vibrated less (compared to other parts of the beam) during placement of the concrete. The effect of local discontinuities can be seen in the slightly different crack behaviour when the loading histories were identical; for example, the first half cycle from bi-directional loading at ductility 8 and monotonic loading.



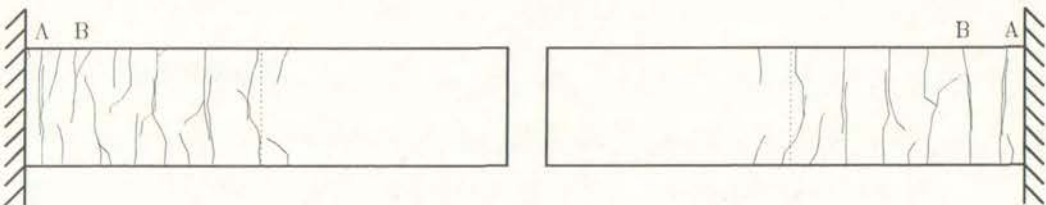
(a) New Zealand



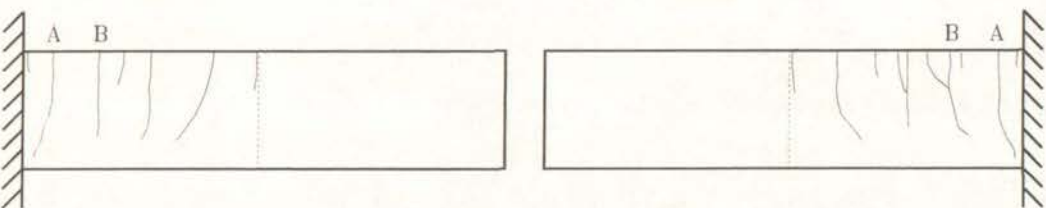
(b) University of California at Berkeley



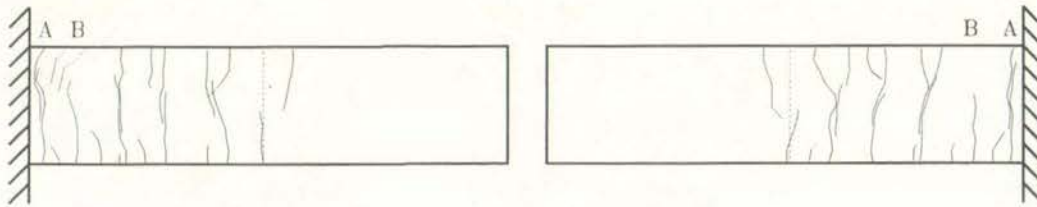
(c) PRESS



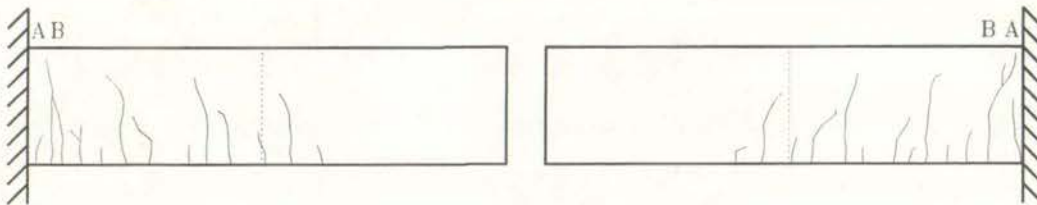
(d) Public Works Research Institute



(e) Monotonic Loading



(f) Bi-directional Cycling at Ductility 8



(g) Unidirectional Loading

Figure 7-34 Crack Patterns after Loading to Ductility 2

Table 7-5 also reveals differences between the widths of cracks from the different tests. Tests where damage was more prominent after the ductility 2 cycles; for example, testing using the loading history from the Public Works Research Institute had wider cracks than tests with little damage at this loading stage such as testing that applied the New Zealand loading history. The narrow cracks measured during testing using the Berkeley loading history reflects the large percentage of the total vertical displacement that was associated with rocking deformations.

The sum of the two crack widths detailed in Table 7-5 generally accounts for between 50 and 70 percent of the total horizontal elongation. The exceptions to this were the crack widths measured during testing using the New Zealand loading history and the Public Works Research Institute. This was due to the width of cracks not being

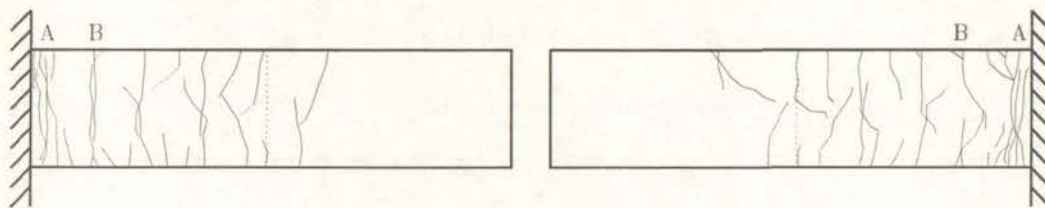
Table 7-5 Comparison of Crack Widths after Loading to Ductility 2

Test	Crack A (mm)	Crack B (mm)	Elongation (mm)
New Zealand	1.5	0.2	1.4
Berkeley	0.3	0.2	0.9
PRESSS	1.2	1.0	3.7
Public Works Research Institute	2.2	0.4	2.3
Monotonic	1.5	0.3	2.7
Cycling at Ductility 8	1.0	0.3	2.7
Unidirectional	0.3	0.8	2.5

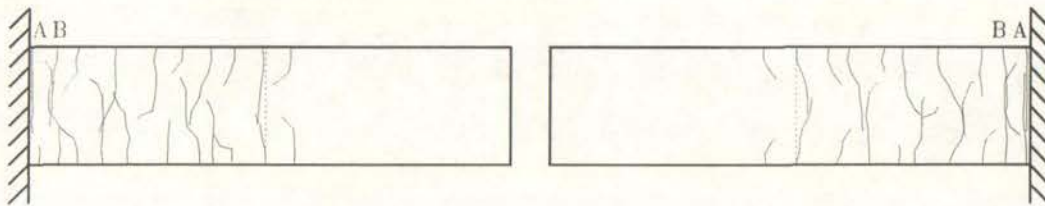
measured immediately next to the strain gauges. Thus, crack widths were measured that were inconsistent with the strains recorded in the gauges at the top and bottom of the beam.

#### 7.6.2 Comparison after Loading to Ductility 4

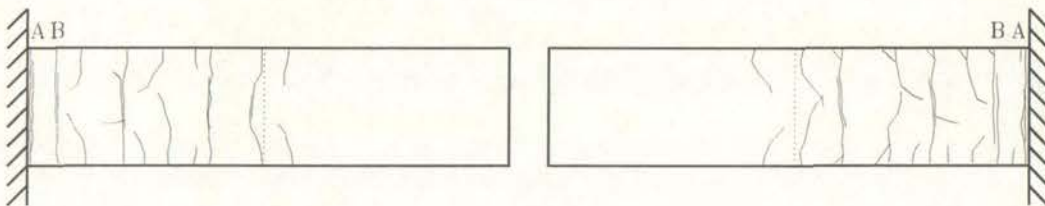
Figure 7-35 illustrates the crack patterns observed after loading to ductility 4 had been completed for the seven laboratory procedures. The crack pattern from testing using the PRESSS loading history is illustrated after the three cycles at ductility 3.69. Table 7-6 compares the widths of the two major cracks in the plastic hinge zone from each



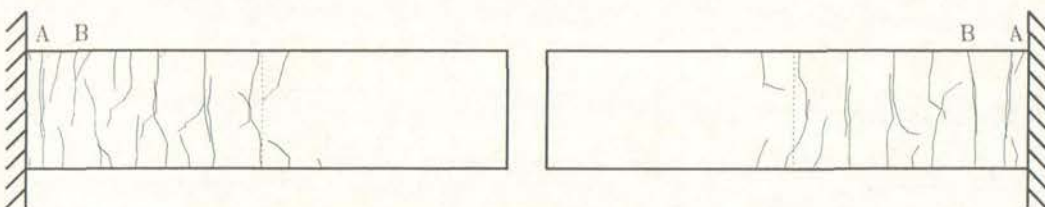
(a) New Zealand



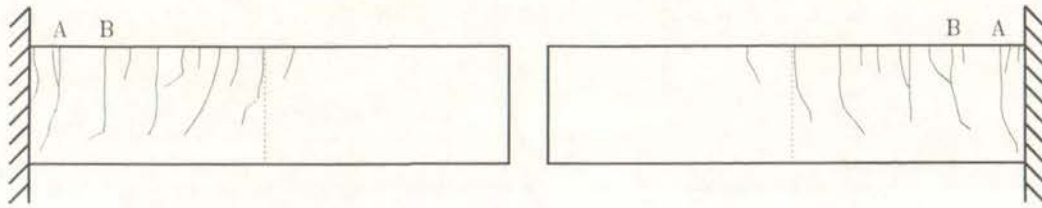
(b) University of California at Berkeley



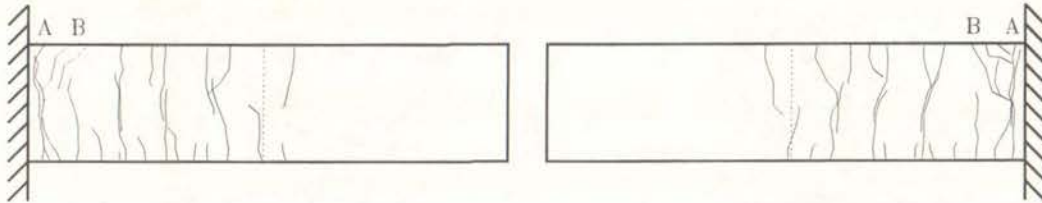
(c) PRESSS



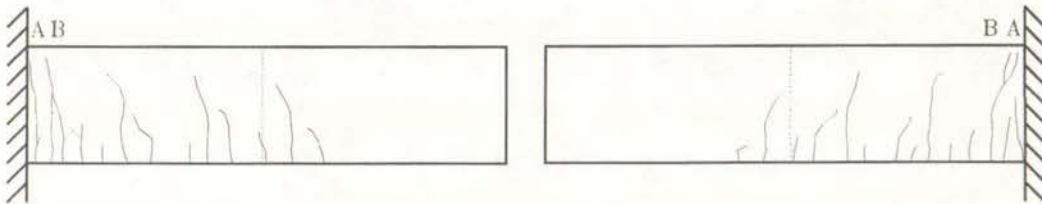
(d) Public Works Research Institute



(e) Monotonic



(f) Bi-directional Cycling at Ductility 8



(g) Unidirectional

Figure 7-35 Crack Patterns after Loading to Ductility 4

test at this loading stage.

Figure 7-35 reveals discrepancies between the crack patterns of the seven laboratory tests. The crack patterns from testing using the New Zealand loading history and bi-directional cycling at ductility 8 depicts more secondary cracking in the plastic hinge zone than the other tests. More testing is required to determine whether this was due to the applied loading history or the physical properties of the beam.

Table 7-6 reveals that varying crack widths were measured after loading to ductility 4 in each test. In general the crack widths reflected the amount of damage that had occurred in the test specimen. The exception to this is the crack widths measured from the test specimen subjected to the New Zealand loading history. It was postulated that this was due to the physical properties of the test specimen varying at that point.

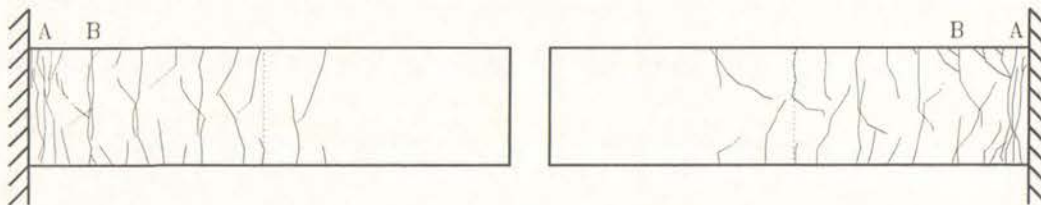
Table 7-6 Comparison of Crack Widths after Loading to Ductility 4

Test	Crack A (mm)	Crack B (mm)	Elongation (mm)
New Zealand	5.0	0.5	5.2
Berkeley	2.8	3.2	6.8
PRESSS	2.8	4.0	11.4
Public Works Research Institute	9.0	0.5	10.7
Monotonic	3.5	0.3	6.7
Cycling at Ductility 8	3.5	0.3	7
Unidirectional	2.5	2.3	6.8

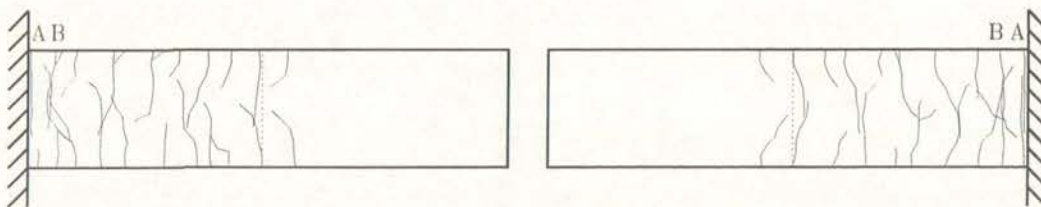
As with the response after loading at ductility 2, the sum of the two crack widths detailed in Table 7-6 generally accounts for between 50 and 70 percent of the total horizontal elongation. Again the exceptions to this were the crack widths measured during testing using the New Zealand loading history and the Public Works Research Institute.

### 7.6.3 Comparisons after Loading to Ductility 6

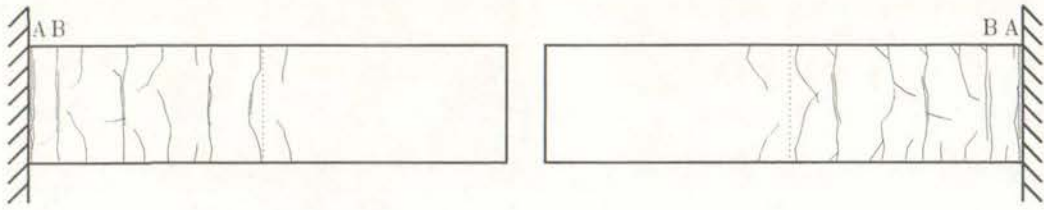
Figure 7-36 presents the crack patterns of the test specimens after loading to ductility 6 had been completed. The crack pattern from testing using the PRESSS loading history is illustrated after the three cycles at ductility 6.14. Table 7-7 compares the widths of the cracks from the seven tests.



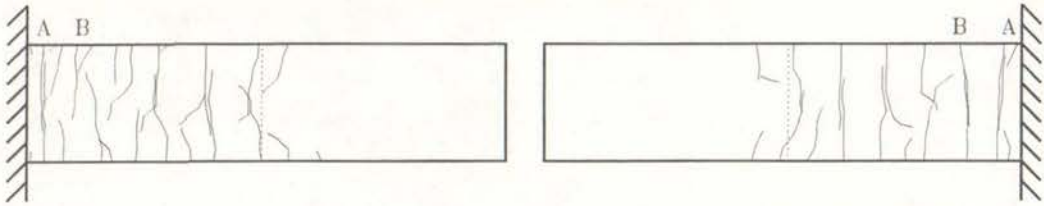
(a) New Zealand



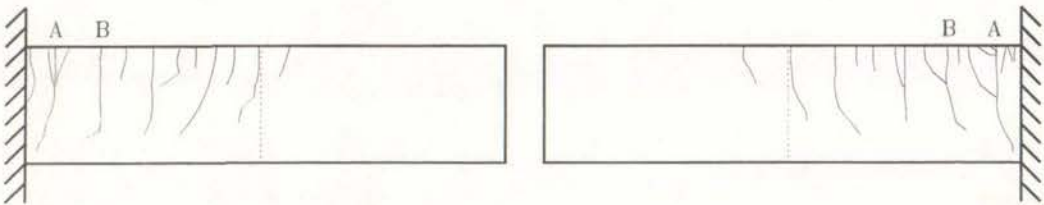
(b) University of California at Berkeley



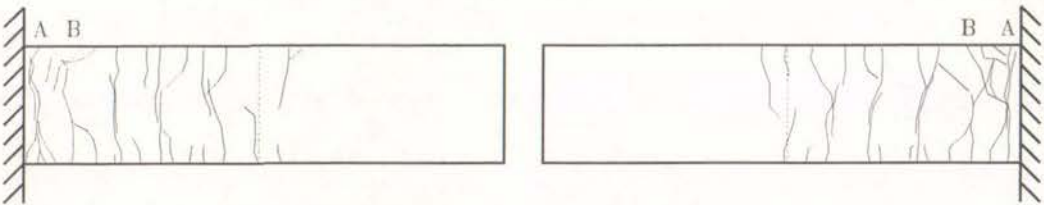
(c) PRESS



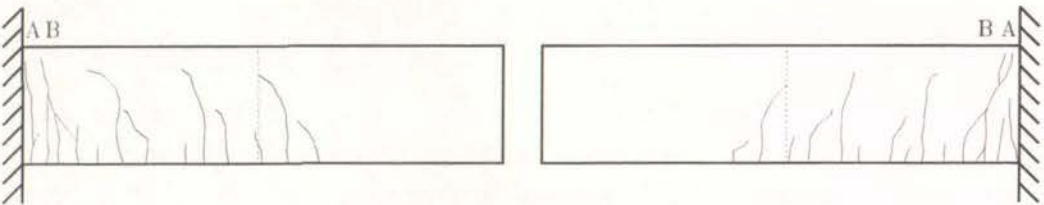
(d) Public Works Research Institute



(e) Monotonic



(f) Bi-directional Cycling at Ductility 8



(g) Unidirectional

Figure 7-36 Comparison of Crack Patterns after Loading to Ductility 6

No additional cracking was observed after the ductility 6 cycles for testing using the PRESSS loading history and the loading history from the Public Works Research Institute. It was observed in the experimental component of this study that the vast majority of cracks formed while damage was defined as no damage, minor damage, or moderate damage. The dominant crack behaviour once severe damage occurred was that existing cracks continued to widen. Therefore, this reflected the greater amount of damage that had been sustained in those tests. Only a small amount of additional cracking was seen in the other tests. Again this is reflective of the degree of damage that had already occurred.

Table 7-7 reveals that different crack widths were measured after loading to ductility 6 in each test. Again, the widest cracks were measured on the test specimens that had suffered the most damage. Trends similar to those derived after loading to ductility 2 and ductility 4 was established after loading to ductility 6.

Crack widths provide a general indication of the amount of damage that has occurred. However, accurate assessment is not possible due to the influence that the differences in the reinforced concrete members (resulting from construction) have on the crack behaviour. This is seen in the different crack behaviour that was observed under the same loading history; for example, the first half-cycle in the positive direction when bi-directional loading to ductility 8 was applied and monotonic loading.

However, although crack widths cannot be used to compare test results, they can be applied during post-earthquake evaluations of buildings to determine the extent of the

Table 7-7 Comparison of Crack Widths after Loading to Ductility 6

Test	Crack A (mm)	Crack B (mm)	Elongation (mm)
New Zealand	7.5	3.5	10.4
Berkeley	5.5	6.5	17.6
PRESSS	6.0	8.0	24.2
Public Works Research Institute	-	-	-
Monotonic	5.0	0.3	10.7
Cycling at Ductility 8	4.5	2.5	11.3
Unidirectional	3.5	3.5	10.6

damage. This is because these inspections are generally more subjective in nature.

Crack patterns do not provide a means for comparison even though differences in crack patterns were observed. This is because defining differences between the crack patterns is largely a subjective exercise. Also the crack behaviour is influenced by the construction of the beam; that is, differences in the amount of vibration between areas of the reinforced concrete members.

## 8.0 Conclusions

This chapter is comprised of two sections with Section 8.1 summarising the conclusions from this experimental study and Section 8.2 listing recommendations for future research on topics associated with this report.

### 8.1 Summary of Findings

Conclusions reported herein are separated into three sections. Section 8.1.1 summarises the findings of the literature review presented in Chapter 2.0. Section 8.1.2 outlines the conclusions made after the analytical modelling in Ruaumoko had been completed and Section 8.1.3 presents the findings from the experimental results that were reported on in Section 7.0.

#### 8.1.1. Literature Review

The following conclusions were established from the literature review presented in Chapter 2.0:

1. The loading procedure adopted in New Zealand is not applied at research institutions in other countries.
2. There is little agreement between research institutions throughout the world regarding the applied loading history.

#### 8.1.2. Analytical Modelling

The following conclusions were based on the analytical modelling that was reported on in Chapter 5.0. The conclusions are as follows:

1. Damage indices from the computer programme, Ruaumoko, are dependent on the value of the plastic hinge zone length entered in the Ruaumoko input file.
2. The model requires extensive calibration against physical tests to determine input variables.
3. The magnitude of the variables modelling the strain hardening and unloading stiffness of the test subassemblage are consistent between tests using different

loading histories. In contrast, the magnitude of the variable modelling the reloading stiffness and the strength degradation require calibration for each individual loading history. Modelling of the hysteresis behaviour of the critical beam in this study was conducted with  $\alpha$  equal to 0.42,  $\beta$  equal to 0.90,  $r$  equal to 0.035, and the reloading stiffness power equal to 1.0. Strength degradation was set to begin at ductility equal to 6.8 and the test subassemblage dropped to 80% of its maximum strength by ductility 12. However, it would be necessary to recalibrate these parameters if a new beam detail was chosen.

4. To ensure that failure would occur by the conclusion of the test, the Bracci index and the Park and Ang index need to be approximately equal to 1.1.

### 8.1.3. Experimental Results

As was mentioned previously, the following conclusions were based on the experimental results reported on in Chapter 7.0. It is recognised that further experimental studies are required to confirm the validity of the conclusions made herein. The conclusions are as follows:

1. Welding of instrumentation studs to the longitudinal reinforcement has the potential to influence the local material properties on the reinforcement bar. This could lead to premature failure occurring during testing.
2. The ultimate displacement from monotonic and unidirectional loading was over twice the value recorded from any bi-directional cyclic tests.
3. More critically, differences were also noted in the ultimate displacements from testing using loading histories adopted by research institutions throughout the world. Testing using the loading history from the Public Works Research Institute was the most conservative whereas testing conducted with the New Zealand loading history was the least conservative.
4. Variations in the applied displacement sequence for the five acceleration histories did not cause significant discrepancies in the overall response of the structure.
5. Failure had not occurred after the test subassemblage was subjected to four magnified earthquake records, even though two of the four records were from severe earthquakes. This indicates that structures designed using force-based methods have a high degree of conservatism inherent in their design.

6. The amount of pinching in the hysteresis loops and the reloading stiffness were not reliable indicators of the amount of degradation that had occurred. Instead these parameters need to be considered in conjunction with the composition of the total displacement and the energy dissipation characteristics of the displacement components.
7. Flexural deformations accounted for a larger percentage of the total displacement for testing using the New Zealand loading history than for testing using other laboratory procedures. This was due to the larger ductility increments that were applied in the New Zealand loading history compared to other loading histories.
8. Cumulative dissipated energy and cumulative ductility were not sufficiently independent of the applied loading history to be used to compare test results.
9. The recorded reinforcement strains at failure of the test subassembly were found to vary. Therefore, as with the amount of energy dissipated, the recorded strains in the longitudinal reinforcement cannot be used as a basis for comparison of experimental results from different loading regimes.
10. The loading histories applied at research institutions are more demanding on the test specimen than actual displacements resulting from seismic excitation. However, of the loading histories from research institutions, the New Zealand loading history replicates the earthquake demand of a reinforced concrete member more closely than loading histories from other research institutions.
11. Damage indices provide a reasonable means of comparing the experimental results derived using different loading regimes. The advantage of applying damage indices is that performance at intermediate damage levels can be compared.
12. The Park and Ang index provides the best correlation between the calculated index and the observed damage. The value for  $\beta$  should be set to equal 0.10.
13. Damage indices should only be calculated for points on the force-displacement envelope when testing using displacement sequences that model acceleration histories. This removes the possibility of damage indices reducing because smaller displacements have been applied.
14. Cracking patterns are too subjective to be used as a measure of the differences between tests and crack widths only provide a general indication of the amount of damage that has occurred. The crack patterns and widths were also influenced by

local discontinuities in the beam that were introduced during construction. However, the widths of cracks can be used during post-earthquake inspections of structures to help determine the extent of the damage, because these inspections are generally more subjective in nature.

## 8.2 Recommendations for Future Research

This study established that several different loading regimes are applied throughout the world and that the ultimate displacement of a test subassembly was dependent on the applied loading procedure. Because of the number of loading procedures applied, it will be too expensive and time consuming to conduct enough tests so that statistically accurate correlation factors can be established. Therefore a common loading history to be applied in research institutions around the world needs to be established.

It was established from this test that welding instrumentation studs to the longitudinal reinforcement could potentially affect the experimental results. Therefore, procedures of connecting instrumentation studs to the longitudinal reinforcement that do not result in changes to local material properties of the longitudinal bar need to be investigated.

Further testing is required to investigate whether the conclusions stated herein are particular to the beam detail adopted in this study; that is, whether the results would change for different beam steel content and moment to shear ratios.

Several issues were raised during computer modelling undertaken to simulate the seismic response of a ten-storey building. The building that the computer model was based on was designed with identical member details for each storey. It is common for buildings to have smaller members for the upper storey levels. Therefore, the influence of modelling each storey with identical member sizes on the seismic response of the building needs to be determined. Also, the effect of Ruaumoko modelling the beam-column joints as fully rigid needs to be investigated further.

The analytical modelling reported on in Chapter 5.0 was based on a building designed to ductility 6 requirements in NZS 3101:1995. It is necessary to investigate whether comparable results would be obtained if this exercise were repeated for structures designed to lower a ductility; for example, ductility 1.25.

## 9.0 References

- Abrams, D. (1996). "Effects of Scale and Loading Rate with Tests of Concrete and Masonry Structures." *Earthquake Spectra*, 12(1), pp. 13-28.
- Applied Technology Council. (1989). "Procedures for Post-earthquake Safety Evaluation of Buildings." *Report ATC-20*.
- Atwater, B. F., Nelson, A. R., Clague, J. J., Carver, G. A., Yamaguchi, D. K., Bobrowsky, P. T., Bourgeois, J., Darienzo, M. E., Grant, W. C., Hemphill-Haley, E., Kelsey, H. M., Jacoby, G. C., Nishenko, S. P., Palmer, S. P., Peterson, C. D., and Reinhart, M. (1995). "Summary of Coastal Geologic Evidence for Past Great Earthquakes at the Cascadia Subduction Zone." *Earthquake Spectra*, 11(1).
- Banon, H., and Veneziano, D. (1982). "Seismic Safety of Reinforced Concrete Members and Structures." *Earthquake Engineering and Structural Dynamics*, 10, pp. 179-193.
- Beres, A., Pessiki, S. P., White, R. N., and Gergely, P. (1996). "Implications of Experiments on the Seismic Behaviour of Gravity Load Design RC Beam to Column Connections." *Earthquake Spectra*, 12(2), pp. 185-198.
- Bracci, J. M., Reinhorn, A. M., Mander, J. B., and Kunnath, S. K. (1989). "Deterministic Model for Seismic Damage Evaluation of Reinforced Concrete Structures." *Technical Report NCEER*, 89-0033.
- Cement and Concrete Association of New Zealand (C&CA). (1998). "Examples of Concrete Structural Design to New Zealand Standard 3101".
- Carr, A. J. (1998). "Ruaumoko User Manual".
- Comite Euro-International Du Beton (CEB). (1996). "RC Elements Under Cyclic Loading".
- Chai, Y. H., Priestley, M. J. N., and Seible, F. (1991). "Seismic Retrofit of Circular columns for Enhanced Flexural Performance." *ACI Structural Journal*, 88(5), pp. 572-584.
- Chung, L., and Shah, P. P. (1989). "Effects of Loading Rate on Anchorage Bond and Beam Column Joints." *ACI Structural Journal*, 86(2), pp. 132-142.
- Chung, Y. S., Meyer, C., and Shinozuka, M. (1989). "Modeling of Concrete Damage." *ACI Structural Journal*, 86(3), pp. 259-271.

- Cosenza, E., Manfredi, G., and Ramasco, R. (1993). "The Use of Damage Functionals in Earthquake Engineering: A Comparison Between Different Methods." *Earthquake Engineering and Structural Dynamics*, 22, pp. 855-868.
- Darwin, D., and Nmai, C. (1986). "Energy Dissipation in RC Beams Under Cyclic Load." *ASCE Journal of Structural Engineering*, 112(8), pp. 1829-1846.
- Dimitrijevic, R. (1992). "Behaviour of Semi-Rigid Prestressed Connections of Concrete Structural Elements Under Cyclic Loading." *10th World Conference on Earthquake Engineering, Madrid, Spain*, 6, pp. 3127-3130.
- Dodd, L. L., and Restrepo-Posada, J. I. (1995). "Model for Predicting Cyclic Behaviour of Reinforcing Steel." *ASCE Journal of Structural Engineering*, 121(3), pp. 433-445.
- Durrani, A. J., and Diaz, A. J. (1992). "Seismic Resistance of Fiber-Reinforced Slab-Column Connections." *10th World Conference on Earthquake Engineering, Madrid, Spain*, 6, pp. 3113-3116.
- Emam, M., Marzouk, H., and Samen Hilal, M. (1997). "Seismic Response of Slab-Column Connections Constructed with High-Strength Concrete." *ACI Structural Journal*, 94(2), pp. 197-205.
- Emori, K., and Schnobrich, W. C. (1978). "Analysis of Reinforced Concrete Frame-Wall Structures for Strong Motion Earthquakes." *Civil Engineering Studies. Structural Research Series No. 434, University of Illinois, Urbana*.
- Fang, I.-K., Wang, C.-S., and Hong, K.-L. (1994). "Cyclic Behaviour of High Strength Concrete Short Beams with Lower Amount of Flexural Reinforcement." *ACI Structural Journal*, 91(1), pp. 10-18.
- Ghee, A. B., Priestley, M. J. N., and Paulay, T. (1989). "Seismic Shear Strength of Circular Reinforced Concrete Columns." *ACI Structural Journal*, 86(1), pp. 45-59.
- Giuffre, A., and Pinto, P. E. (1970). "Comportamento del Cemento Armato per Sollecitazioni Cicliche di Forte Intensita." *Giornale del Genio Civile*, 5.
- Gosain, N. K., Brown, R. H., and Jirsa, J. O. (1977). "Shear Requirements for Load Reversals on RC Members." *ASCE Journal of the Structural Division*, 103(ST7), pp. 1461-1476.

- Hwang, T.-H., and Scribner, M. (1984). "RC Member Cyclic Response During Various Loadings." *ASCE Journal of Structural Engineering*, 110(3), pp. 477-489.
- Ingham, J. M., Priestley, M. J. N., and Seible, F. (1994). "Seismic Performance of Bridge Knee Joints - Volume 1." *Structural Systems Research Report, University of California, San Diego*, 94/12.
- Kanaan, A. E., and Powell, G. H. (1973). "General Purpose Computer Program for Inelastic Dynamic Response of Plane Structures." *Report EERC 73-6, College of Engineering, University of California, Berkeley*.
- Karsan, I. D., and Jirsa, J. O. (1969). "Behaviour of Concrete Under Compressive Loadings." *ASCE Journal of the Structural Division*, 95(ST12), pp. 2543-2563.
- Kawashima, K. (1994). "Seismic Design Force of Bridges." *Proceedings of the Second International Workshop on Seismic Design and Retrofitting of Reinforced Concrete Bridges*, pp. 25-56.
- Kinugasa, H., and Nomura, S. (1992). "Characteristics of Fatigue Damage for Reinforced Concrete Beams Under Reversed Loading." *10th World Conference on Earthquake Engineering, Madrid, Spain*, 6, pp. 3083-3088.
- Krawinkler, H. (1996). "Cyclic Loading Histories for Seismic Experimentation on Structural Components." *Earthquake Spectra*, 12(1), pp. 1-12.
- Kunnath, S. K., El-Bahy, A., Taylor, A., and Stone, W. (1997). "Cumulative Seismic Damage of Reinforced Concrete Walls Under Load Reversals." *Technical Report NCEER*, 97-0006.
- Kunnath, S. K., Reinhorn, A. M., and Lobo, R. F. (1992). "IDARC Version 3.0: A Program for the Inelastic Damage Analysis of Reinforced Concrete Structures." *Technical Report NCEER*, 92-0022.
- Lefas, I. D., and Kotsovos, M. D. (1990). "Strength and Deformation Characteristics of Reinforced Concrete Walls Under Load Reversals." *ACI Structural Journal*, 87(6), pp. 716-726.
- Leon, R. T., and Deierlein, G. G. (1996). "Considerations for the Use of Quasi-Static Testing." *Earthquake Spectra*, 12(1), pp. 87-110.

- Ma, S.-Y. M., Bertero, V. V., and Popov, E. P. (1976). "Experimental and Analytical Studies on the Hysteretic Behavior of Reinforced Concrete Rectangular and T-Beams." *Earthquake Engineering Research Center*, 76-2.
- Mander, J. B., and Dutta, A. (1998). "Capacity Design and Fatigue Analysis of Confined Concrete Columns." *Technical Report - MCEER*, 98-0007.
- Mander, J. B., Kim, J. H., and Ligozio, C. A. (1996a). "Seismic Performance of a Model Reinforced Concrete Bridge Pier Before and After Retrofit." *Technical Report NCEER*, 96-0009.
- Mander, J. B., Mahmoodzadegan, B., Bhadra, S., and Chen, S. S. (1996b). "Seismic Evaluation of a 30-Year Old Non-Ductile Highway Bridge Pier and its Retrofit." *Technical Report NCEER*, 96-0008.
- Mander, J. B., Priestley, M. J. N., and Park, R. (1988). "Theoretical Stress-Strain Model for Confined Concrete." *ASCE Journal of Structural Engineering*, 114(8), pp. 1804-1826.
- Martinez-Rueda, J. E., and Elnashai, A. S. (1997). "Confined Concrete Model Under Cyclic Load." *Materials and Structures*, 30, pp. 139-147.
- Masri, A. C., and Goel, S. C. (1996). "Seismic Design and Testing of an RC Slab-Column Frame Strengthened by Steel Bracing." *Earthquake Spectra*, 12(4), pp. 645-666.
- Mosalam, K. M., White, R. N., and Gergely, P. (1997a). "Seismic Evaluation of Frames with Infill Walls Using Quasi-Static Experiments." *Technical Report NCEER*, 97-0019.
- Mosalam, K. M., White, R. N., and Gergely, P. (1997b). "Static Response of Infilled Frames Using Quasi-Static Experimentation." *ASCE Journal of Structural Engineering*, 123(11), pp. 1462-1469.
- NZNSSEE Reconnaissance Team. (1995). *Bulletin of the New Zealand National Society for Earthquake Engineering*, 28(1), pp. 1-98.
- NZSNEE Reconnaissance Team. (1994). *Bulletin of the New Zealand National Society for Earthquake Engineering*, 27(4), pp. 235-344.
- Otani, S. (1974). "Sake - A Computer Program for Inelastic Analysis of R/C Frames to Earthquakes." *Report UILU-Eng-74-2029 University of Illinois at Urbana-Champaign*.

- Otter, D. E., and Naaman, A. E. (1989). "Model for Response of Concrete to Random Compressive Loads." *ASCE Journal of Structural Engineering*, 115(11), pp. 2794-2809.
- Park, R. (1989). "Evaluation of Ductility of Structures and Structural Assemblages from Laboratory Testing." *Bulletin of the New Zealand National Society of Earthquake Engineering*, 22(3), pp. 155-166.
- Park, Y.-J., and Ang, A. H.-S. (1985). "Mechanistic Seismic Damage Model for Reinforced Concrete." *ASCE Journal of Structural Engineering*, 111(4), pp. 722-739.
- Paulay, T., and Priestley, M. J. N. (1992). "Seismic Design of Reinforced Concrete and Masonry Buildings".
- Powell, G. H., and Allahabai, R. (1988). "Seismic Damage Prediction by Deterministic Methods: Concepts and Procedures." *Earthquake Engineering and Structural Dynamics*, 16, pp. 719-734.
- Priestley, M. J. N. (1997). "Displacement-Based Seismic Assessment of Reinforced Concrete Buildings." *Journal of Earthquake Engineering*, 1(1), pp. 157-192.
- Radaj, D. (1992). "Heat Effects of Welding".
- Raffaella, G. S., and Wight, J. K. (1995). "Reinforced Concrete Eccentric Beam-Column Connections Subjected to Earthquake-Type Loading." *ACI Structural Journal*, 92(1), pp. 45-55.
- Rao, P. S., Sarma, B. S., Lakshmanan, N., and Stangenberg, F. (1998). "Damage Model for Reinforced Concrete Elements Under Cyclic Loading." *ACI Materials Journal*, 95(6), pp. 682-690.
- Roufaiel, M. S. L., and Meyer, C. (1987). "Analytical Modeling of Hysteretic Behavior of R/C Frames." *Journal of Structural Engineering, ASCE*, 113(3), pp. 429-444.
- Saadatmanesh, H., Ehsani, M. R., and Jin, L. (1997). "Seismic Retrofitting of Rectangular Bridge Columns with Composite Straps." *Earthquake Spectra*, 13(2), pp. 281-304.
- Saatcioglu, M., and Ozcebe, G. (1989). "Response of Reinforced Concrete Columns to Simulated Seismic Loading." *ACI Structural Journal*, 86(1), pp. 3-12.

- Scribner, C. F., and Wight, J. K. (1980). "Strength Decay in Reinforced Concrete Beams Under Load Reversals." *ASCE Journal of the Structural Division*, 106(ST4), pp. 861-875.
- Shepherd, R. (1996). "Standardised Experimental Testing Procedures for Low-Rise Structures." *Earthquake Spectra*, 12(1), pp. 111-128.
- Shimazu, T., and Mollick, A. A. (1991). "Vertical Load-Carrying Capacity of Continuous Columns in Multistorey Reinforced Concrete Frames Subjected to Lateral Loading Reversals." *ACI Structural Journal*, 88(3), pp. 359-370.
- Soudki, K. A., Rizkalla, S. H., and LeBlanc, B. (1995). "Horizontal Connections for Precast Concrete Shear Walls Subjected to Cyclic Deformations Part 1: Mild Steel Connections." *PCI Journal*, pp. 78-95.
- Standards New Zealand. (1989). "NZS 3402:1989—Steel Bars for the Reinforcement of Concrete".
- Standards New Zealand. (1992). "NZS 4203:1992—Code of Practice for General Structural Design and Design Loadings for Buildings (Known as the Loading Standard)".
- Standards New Zealand. (1995). "NZS 3101:1995—New Zealand Standard for Design of Concrete Structures".
- Stone, W. C., Cheok, G. S., and Stanton, J. F. (1995). "Performance of Hybrid Moment-Resisting Precast Beam-Column Concrete Connections Subjected to Cyclic Loading." *ACI Structural Journal*, 91(2), pp. 229-249.
- Takeda, T., Sozen, M. A., and Nielsen, N. N. (1970). "Reinforced Concrete Responses to Simulated Earthquakes." *Journal of the Structural Division, ASCE*, 96(ST12), pp. 2557-2573.
- Tomazevic, M., and Lutman, M. (1996). "Seismic Behaviour of Masonry Walls: Modeling of Hysteretic Rules." *ASCE Journal of Structural Engineering*, 122(9), pp. 1049-1054.
- Tomazevic, M., Lutman, M., and Petkovic, L. (1996). "Seismic Behaviour of Masonry Walls: Experimental Simulation." *ASCE Journal of Structural Engineering*, 122(9), pp. 1040-1047.
- Tsonos, A. G., Tegos, I. A., and Penelis, G. G. (1992). "Seismic Resistance of Type 2 Exterior Beam-Column Joints Reinforced with Inclined Bars." *ACI Structural Journal*, 89(1), pp. 3-12.

- Wehbe, N., Saiidi, M., Sanders, D., and Douglas, B. (1996). "Ductility of Rectangular Reinforced Concrete Bridge Columns with Moderate Confinement." *Technical Report NCEER, 96-0003*.
- Williams, M. S., and Sexsmith, R. G. (1995). "Seismic Damage Indices for Concrete Structures: A State-of-the-Art Review." *Earthquake Spectra*, 11(2), pp. 319-349.
- Williams, M. S., Villemure, I., and Sexsmith, R. G. (1997). "Evaluation of Seismic Damage Indices for Concrete Elements Loaded in Combined Shear and Flexure." *ACI Structural Journal*, 94(3), pp. 315-322.

## Appendix A —Ruaumoko In put File

This appendix contains a full transcript of the Ruaumoko data file that was used to establish the five acceleration histories. Further information regarding the terms in the following file can be obtained from the Ruaumoko user manual (Carr 1998).

```

10 Storey Building           !2/3 scale model of Red book building
2,0,1,0,0,0,0,0,0          !Principal analysis options
65,91,5,10,1,10,9.81,5.0,5.0,0.01,175,1.0 !Frame control parameters
0,1,10,0,1,10,0.7,0.1      !Output intervals
0,0                          !Iteration control

NODES
1,2.47,0,1,1,1,0,0,0
2,7.37,0,1,1,1,0,0,0
3,12.27,0,1,1,1,0,0,0
4,17.17,0,1,1,1,0,0,0
5,0,2.67,0,0,0,0,0,0
6,2.47,2.67,0,0,0,5,0,0
7,7.37,2.67,0,0,0,6,0,0
8,12.27,2.67,0,0,0,7,0,0
9,17.17,2.67,0,0,0,8,0,0
10,19.63,2.67,0,0,0,9,0,0
11,0,5.07,0,0,0,0,0,0
12,2.47,5.07,0,0,0,11,0,0
13,7.37,5.07,0,0,0,12,0,0
14,12.27,5.07,0,0,0,13,0,0
15,17.17,5.07,0,0,0,14,0,0
16,19.63,5.07,0,0,0,15,0,0
17,0,7.47,0,0,0,0,0,0
18,2.47,7.47,0,0,0,17,0,0
19,7.37,7.47,0,0,0,18,0,0
20,12.27,7.47,0,0,0,19,0,0
21,17.17,7.47,0,0,0,20,0,0
22,19.63,7.47,0,0,0,21,0,0
23,0,9.87,0,0,0,0,0,0
24,2.47,9.87,0,0,0,23,0,0
25,7.37,9.87,0,0,0,24,0,0
26,12.27,9.87,0,0,0,25,0,0
27,17.17,9.87,0,0,0,26,0,0

```

28,19.63,9.87,0,0,0,27,0,0  
29,0,12.27,0,0,0,0,0,0  
30,2.47,12.27,0,0,0,29,0,0  
31,7.37,12.27,0,0,0,30,0,0  
32,12.27,12.27,0,0,0,31,0,0  
33,17.17,12.27,0,0,0,32,0,0  
34,19.63,12.27,0,0,0,33,0,0  
35,0,14.67,0,0,0,0,0,0  
36,2.47,14.67,0,0,0,35,0,0  
37,7.37,14.67,0,0,0,36,0,0  
38,12.27,14.67,0,0,0,37,0,0  
39,17.17,14.67,0,0,0,38,0,0  
40,19.63,14.67,0,0,0,39,0,0  
41,0,17.07,0,0,0,0,0,0  
42,2.47,17.07,0,0,0,41,0,0  
43,7.37,17.07,0,0,0,42,0,0  
44,12.27,17.07,0,0,0,43,0,0  
45,17.17,17.07,0,0,0,44,0,0  
46,19.63,17.07,0,0,0,45,0,0  
47,0,19.47,0,0,0,0,0,0  
48,2.47,19.47,0,0,0,47,0,0  
49,7.37,19.47,0,0,0,48,0,0  
50,12.27,19.47,0,0,0,49,0,0  
51,17.17,19.47,0,0,0,50,0,0  
52,19.63,19.47,0,0,0,51,0,0  
53,0,21.87,0,0,0,0,0,0  
54,2.47,21.87,0,0,0,53,0,0  
55,7.37,21.87,0,0,0,54,0,0  
56,12.27,21.87,0,0,0,55,0,0  
57,17.17,21.87,0,0,0,56,0,0  
58,19.63,21.87,0,0,0,57,0,0  
59,0,24.27,0,0,0,0,0,0  
60,2.47,24.27,0,0,0,59,0,0  
61,7.37,24.27,0,0,0,60,0,0  
62,12.27,24.27,0,0,0,61,0,0  
63,17.17,24.27,0,0,0,62,0,0  
64,19.63,24.27,0,0,0,63,0,0  
65,4.92,5.07,0,0,0,12,0,0

ELEMENTS

1,5,1,6

2, 1, 6, 12  
3, 1, 12, 18  
4, 1, 18, 24  
5, 1, 24, 30  
6, 1, 30, 36  
7, 1, 36, 42  
8, 1, 42, 48  
9, 1, 48, 54  
10, 1, 54, 60  
11, 5, 2, 7  
12, 1, 7, 13  
13, 1, 13, 19  
14, 1, 19, 25  
15, 1, 25, 31  
16, 1, 31, 37  
17, 1, 37, 43  
18, 1, 43, 49  
19, 1, 49, 55  
20, 1, 55, 61  
21, 5, 3, 8  
22, 1, 8, 14  
23, 1, 14, 20  
24, 1, 20, 26  
25, 1, 26, 32  
26, 1, 32, 38  
27, 1, 38, 44  
28, 1, 44, 50  
29, 1, 50, 56  
30, 1, 56, 62  
31, 5, 4, 9  
32, 1, 9, 15  
33, 1, 15, 21  
34, 1, 21, 27  
35, 1, 27, 33  
36, 1, 33, 39  
37, 1, 39, 45  
38, 1, 45, 51  
39, 1, 51, 57  
40, 1, 57, 63  
41, 3, 5, 6

42,2,6,7  
43,2,7,8  
44,2,8,9  
45,4,9,10  
46,3,11,12  
47,4,12,65  
48,2,13,14  
49,2,14,15  
50,4,15,16  
51,3,17,18  
52,2,18,19  
53,2,19,20  
54,2,20,21  
55,4,21,22  
56,3,23,24  
57,2,24,25  
58,2,25,26  
59,2,26,27  
60,4,27,28  
61,3,29,30  
62,2,30,31  
63,2,31,32  
64,2,32,33  
65,4,33,34  
66,3,35,36  
67,2,36,37  
68,2,37,38  
69,2,38,39  
70,4,39,40  
71,3,41,42  
72,2,42,43  
73,2,43,44  
74,2,44,45  
75,4,45,46  
76,3,47,48  
77,2,48,49  
78,2,49,50  
79,2,50,51  
80,4,51,52  
81,3,53,54

```

82,2,54,55
83,2,55,56
84,2,56,57
85,4,57,58
86,3,59,60
87,2,60,61
88,2,61,62
89,2,62,63
90,4,63,64
91,3,65,13
PROPS
1,FRAME                                !Column
1,0,0,0,0,0,0                          !Section properties
2.92E7,0.0,0.184,0.0,0.00332,4.416,0.30,0.30,0,0 !Elastic properties
2,FRAME                                !Internal Beam
1,0,0,4,3,1,0                          !Section properties
2.92E7,0.0,0.162,0.0,0.00128,3.888,0.30,0.30,0,0 !Elastic properties
0.0,0.035,0.43,0.43                    !Bi-linear factors and hinge properties
0,0,219.00,-196.50,219.00,-196.50     !Yield conditions
6.8,12,0.8,60                          !Strength degradation parameters
0.42,0.90,1,2                          !Stiffness degradation parameters
0.0,0.0,23,23,23,23,0.080,0.080       !Damage indices data
3,FRAME                                !LH Cantilever Beam
1,0,0,4,3,1,0                          !Section properties
2.92E7,0.0,0.162,0.0,0.00128,3.888,0.0,0.30,0,0 !Elastic properties
0.0,0.035,0.0,0.43                    !Bi-linear factors and hinge properties
0,0,219.00,-196.50,219.00,-196.50     !Yield conditions
6.8,12,0.8,60                          !Strength degradation parameters
0.42,0.90,1,2                          !Stiffness degradation parameters
0.0,0.0,23,23,23,23,0.080,0.080       !Damage indices data
4,FRAME                                !RH Cantilever Beam
1,0,0,4,3,1,0                          !Section properties
2.92E7,0.0,0.162,0.0,0.00128,3.88,0.30,0.0,0,0 !Elastic properties
0.0,0.035,0.43,0.0                    !Bi-linear factors and hinge properties
0,0,219.00,-196.50,219.00,-196.50     !Yield conditions
6.8,12,0.8,60                          !Strength degradation parameters
0.42,0.90,1,2                          !Stiffness degradation parameters
0.0,0.0,23,23,23,23,0.080,0.080       !Damage indices data
5,FRAME                                !First Floor Column
2,0,0,1,0,0,0                          !Section properties

```

2.92E7,0.0,0.184,0.0,0.00332,4.416,0.33,0.30,0,0!Elastic properties  
0.0,0.0,0.0,0.0 !Bi-linear factors and hinge properties  
-5152,-3680,397.45,441.6,198.73,1226.67,0 !Beam-column yield surface

## WEIGHTS

1,0,0,0  
2,0,0,0  
3,0,0,0  
4,0,0,0  
5,0,0,0  
6,0,0,0  
7,1490.1,0,0  
8,0,0,0  
9,0,0,0  
10,0,0,0  
11,0,0,0  
12,0,0,0  
13,1472.65,0,0  
14,0,0,0  
15,0,0,0  
16,0,0,0  
17,0,0,0  
18,0,0,0  
19,1472.65,0,0  
20,0,0,0  
21,0,0,0  
22,0,0,0  
23,0,0,0  
24,0,0,0  
25,1472.65,0,0  
26,0,0,0  
27,0,0,0  
28,0,0,0  
29,0,0,0  
30,0,0,0  
31,1472.65,0,0  
32,0,0,0  
33,0,0,0  
34,0,0,0  
35,0,0,0  
36,0,0,0

37,1472.65,0,0  
38,0,0,0  
39,0,0,0  
40,0,0,0  
41,0,0,0  
42,0,0,0  
43,1472.65,0,0  
44,0,0,0  
45,0,0,0  
46,0,0,0  
47,0,0,0  
48,0,0,0  
49,1472.65,0,0  
50,0,0,0  
51,0,0,0  
52,0,0,0  
53,0,0,0  
54,0,0,0  
55,1472.65,0,0  
56,0,0,0  
57,0,0,0  
58,0,0,0  
59,0,0,0  
60,0,0,0  
61,1609.2,0,0  
62,0,0,0  
63,0,0,0  
64,0,0,0  
LOADS  
1,0,0,0  
65,0,0,0  
EQUAKE  
3,1,0.02,1.0,-1,0,0,1.0,1           !Earthquake control parameters

## Appendix B —Adaptability of Hysteresis Model

Section 5.1.4 reports on the verification of the hysteresis model chosen to replicate the force-displacement response from testing using the New Zealand loading history. Data from testing using the New Zealand loading history was used to calibrate the hysteresis model because the New Zealand loading history was the control for the experimental study reported herein.

However, it would be necessary to investigate the influence of the model parameters reported on in Section 5.1.4 for future studies where different loading histories may be modelled. Therefore, the Berkeley loading history was applied to the model detailed in Section 5.1.4. Figure B-1 presents the comparison of the experimental data and the predicted response using the Modified Takeda hysteresis rule. Figure B-1 does not reveal the excellent agreement between the experimental response and the predicted response observed in Figure 5-4, with the model not distinguishing between the three cycles at each ductility level. The ultimate displacement of the test subassembly was predicted accurately. However, this was due to the ultimate displacement from testing using the Berkeley loading history being identical to that established from testing using the New Zealand loading history.

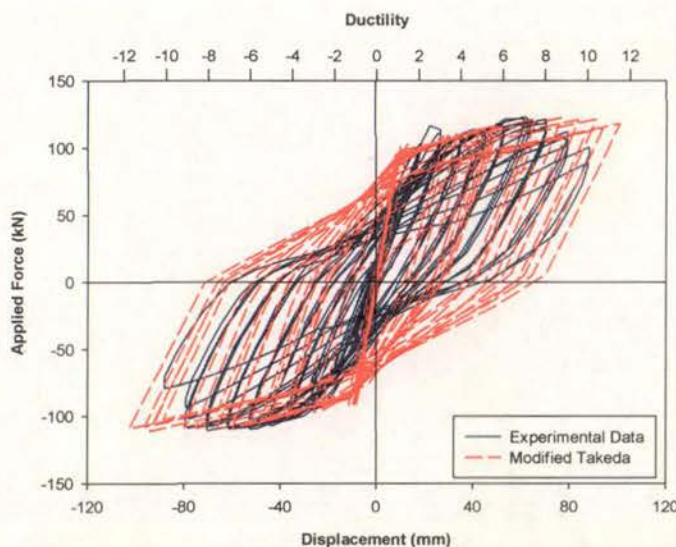


Figure B-1 Comparison of Experimental Data and Modified Takeda Model  
(Berkeley Loading History)

Figure B-1 demonstrates that the unloading stiffness and strain hardening slope from the predicted response was comparable to the experimental data. However, the amount of pinching and the strength degradation was not modelled accurately. This indicates that although the value of  $\alpha$  and  $r$  can remain constant between tests, the value for  $\beta$  and the strength degradation parameters require calibration for each individual loading history.

## Appendix C – Experimental Results

Appendix C presents the experimental results from the twelve tests in this experimental series. These results did not play a direct role in formulating the conclusions of this report, but were further processed to provide the data presented in Chapter 7.0, which led to the report conclusions. Nevertheless, the base data is provided here to permit greater scrutiny of the results.

A feature of this appendix is that graphs detailing the separate displacement components, the moment–curvature response, the strains in the longitudinal reinforcement, and the horizontal elongation of the beam are plotted at the same scale. This facilitates comparison between experimental results from testing using the twelve loading histories. It also should be noted that the yield displacement established as part of applying the New Zealand loading history was taken to be the yield displacement for all twelve tests.

The aforementioned graphs were only plotted for loading up to and including ductility 8 when testing using the seven laboratory procedures. This was to ensure that the portal gauges, which recorded the strains illustrated in Figure 4-16, were not damaged due to measuring excessive deformations. However, the location of the high ductility cycles within the displacement sequence established from each acceleration history meant that the portal gauges were not removed for the high ductility cycles. It was pointless to remove the gauges during a large ductility cycle early in the displacement sequence because that would result in data not being recorded for a significant portion of the test.

Appendices C.1 through C.7 present the experimental results from the seven laboratory procedures. The seven laboratory procedures in reported order are the New Zealand loading history, the loading history from the University of California at Berkeley, the PRESSS loading history, the loading history from the Public Works Research Institute, monotonic loading, direct cycling at ductility 8, and unidirectional cycling. Appendices C.8 through C.12 present the experimental results from testing using the five acceleration histories.

## C.1 New Zealand Loading History

Results from testing conducted using the New Zealand loading history are presented in Sections C.1.1 through C.1.6, with the results summarised in Section C.1.7. Section C.1.1 describes the observed behaviour of the test specimen during testing. Section C.1.2 identifies the separate displacement components that were calculated from the experimental data. These results were used in Section C.1.3 to separate the total energy accumulated during the test into the energy associated with each separate displacement component. Section C.1.4 compares the predicted moment-curvature relationship with the experimental behaviour and Section C.1.5 presents the average strains in the longitudinal reinforcement from the three instrumentation cells. Lastly, Section C.1.6 presents the horizontal elongation of the beam arising from plastic hinge formation.

### C.1.1 Test Observations

The New Zealand loading history was separated into two components: force-controlled regime and displacement-controlled regime. Section C.1.1.1 details the force-controlled section of the test whereas Section C.1.1.2 details the displacement-controlled section.

#### C.1.1.1 Force Control

The initial stages of the test were carried out under force control. An actuator force of 64.5kN was applied in each direction. This is equal to three-quarters of the predicted nominal design strength based on specified material strengths. During the application of this force, testing was halted at the theoretical cracking force (calculated using actual material values) so that an inspection could be carried out. No cracks were observed at this stage in either direction. An inspection was carried out upon completion of the applied force in both directions to  $0.75F_n$ . Three flexural cracks appeared on both sides during loading in the positive direction whereas four flexural cracks appeared on both sides during loading in the negative direction. Section 3.2 defines positive and negative loading for the test set-up reported herein. The recorded

displacements in the positive and negative directions were 5.83mm and 7.29mm respectively. Procedures outlined in Section 6.2 were then followed to give a yield displacement of 8.75mm.

#### C.1.1.2 Displacement Control

Once the yield displacement was determined, testing was carried out under displacement control. The loading steps followed the procedures summarised in Section 6.2. The observed behaviour of the test assembly during the displacement-controlled component of the New Zealand loading history is listed below and on the following three pages. The widths of cracks were measured at the completion of each loading step. Photos of the damage incurred were also taken at various stages of the test. Comparison of the measured crack widths and orientation for the twelve tests is presented in Section 7.6.

#### **Ductility 2:**

Six cracks were identified on both sides after the beam was loaded to ductility 2 in the positive direction. Some of the cracks showed minor shear inclination. The beam was then loaded to ductility 2 in the negative direction. Eight cracks were observed on each side with some cracks showing shear inclinations. More cracks formed under loading in the negative direction than in the positive direction because the self-weight of the test subassembly provided an additional force in the negative direction. The behaviour on Side A was identical to that of Side B for both loading directions. Side A and Side B are defined in Section 3.2.

Hairline cracks formed in the joint region during the second cycle to ductility 2 in the positive direction. However, even though these cracks formed at an early stage in the test, they did not open further during the test. Small extensions to existing cracks were observed. These crack extensions were inclined at an angle of approximately 45° to the horizontal. More cracking in the joint region occurred during the second cycle to ductility 2 in the negative direction. As with the positive direction, there were small extensions (inclined at an angle of 45°) to existing cracks. The behaviour

was again identical on both sides during the second positive and negative loading cycle at ductility 2.

**Ductility 4:**

Small extensions to existing cracks were observed after the beam was loaded in the positive direction to ductility 4. As with the crack extensions at previous load steps, these cracks were inclined at an angle of  $45^\circ$ . Secondary cracks also formed at this load step. No crushing or spalling of cover concrete was observed at this load step. The beam was then loaded to ductility 4 in the negative direction. The response was similar to that of the previous half cycle where the crack extensions were inclined at an angle of  $45^\circ$  and secondary cracking was apparent.

There was a minor increase in observed damage as the beam was loaded on the second ductility 4 cycle, with a small amount of secondary cracking and extensions to existing cracks being noted.

**Ductility 6:**

The first indication of cover concrete spalling was observed after the first positive cycle to ductility 6. Significant extensions to existing cracks were also observed. As shown in Figure C-1, these were inclined at  $45^\circ$  to the horizontal. Minor spalling on both sides was observed at the conclusion of the first complete ductility 6 cycle. There was a small amount of additional cracking but the predominant behaviour by this stage of the test was that existing crack widths were expanding.

Behaviour in the second positive and negative cycle was similar. Limited amounts of additional cracking and minor spalling of cover concrete were observed. It was noted that there was no strength loss between the first and second cycles in either direction.

**Ductility 8:**

A small amount of additional cracking was identified after the first positive cycle to ductility 8. Further spalling of the cover concrete was also observed. Localised

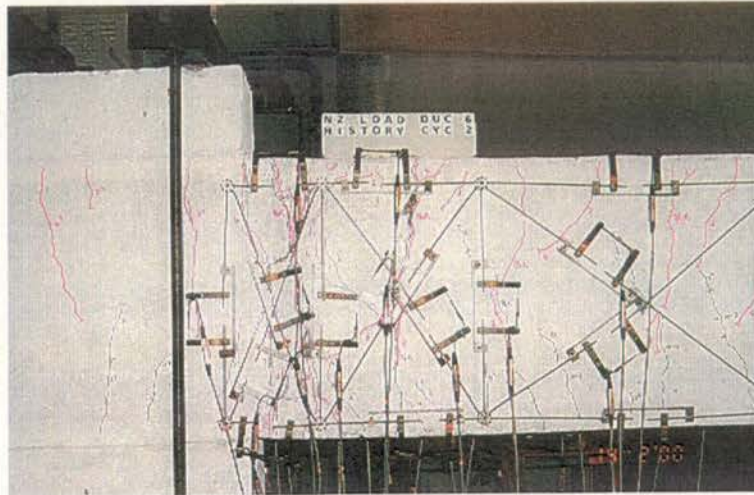


Figure C-1 Test Subassembly Condition at Ductility 6 (Cycle 2)

spalling along cracks in the plastic hinge zone during the first negative cycle to ductility 8 resulted in a section of transverse reinforcement becoming visible.

Severe spalling of concrete from the bottom of the beam during the second cycle to ductility 8 meant that the longitudinal reinforcement was visible. A minor loss of strength was observed between the two cycles in the negative direction.

#### Ductility 10:

Further spalling of cover concrete occurred while the beam was being loaded to ductility 10. Figure C-2 illustrates the total amount of spalling that occurred up to and including loading to ductility 10. A longitudinal bar ruptured next to an instrumentation stud during the second positive cycle. This caused the maximum

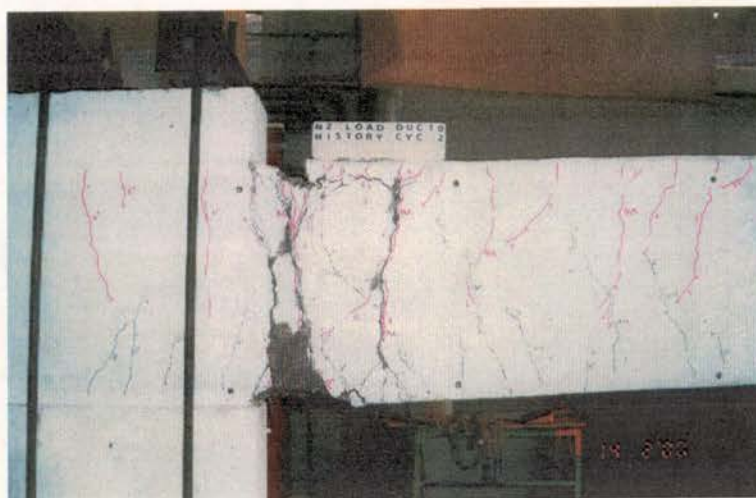


Figure C-2 Test Subassembly Condition at Ductility 10 (Cycle 2)

strength recorded during this cycle to drop below 80% of the maximum-recorded strength for this test and hence the test was terminated at this point. However, this was a premature failure as the beam had only shown minor strength loss in the previous cycles and only limited pinching was evident in the force-displacement response. Hence, it was proposed that welding instrumentation studs to the longitudinal reinforcement affected the local material properties of the longitudinal bar.

### C.1.2 Displacement Components

The total vertical displacement of the test subassembly at the actuator was separated into three components. These were the vertical displacement due to flexural deformation, shear deformation, and the rocking of the beam on its base. Section 3.6 outlines the procedures that enabled the three displacement components to be isolated. Figure C-3 provides an indication of the relative size of each component for various stages of the displacement envelope until ductility 8. It can be seen that there is reasonable agreement in the positive direction and until 50mm in the negative direction. As expected, flexural deformations accounted for the majority of the total deflection.

Figure C-4(a) shows the relationship between the applied actuator force against the flexural deformation component for loading up to and including ductility 8. Figure C-

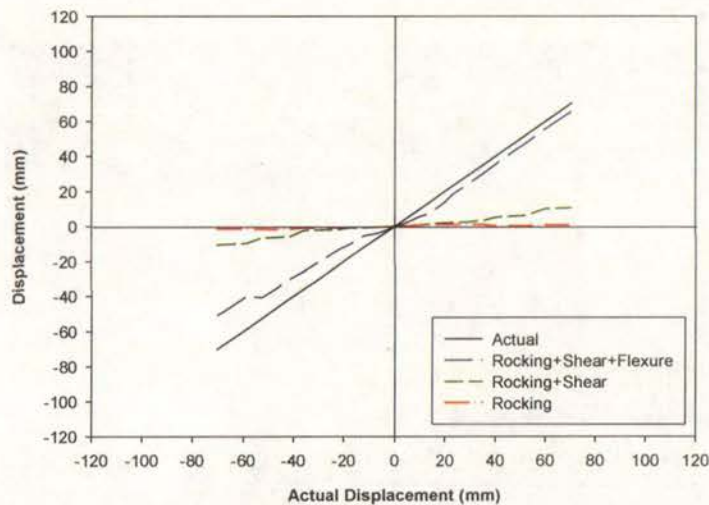


Figure C-3 Components of Displacement

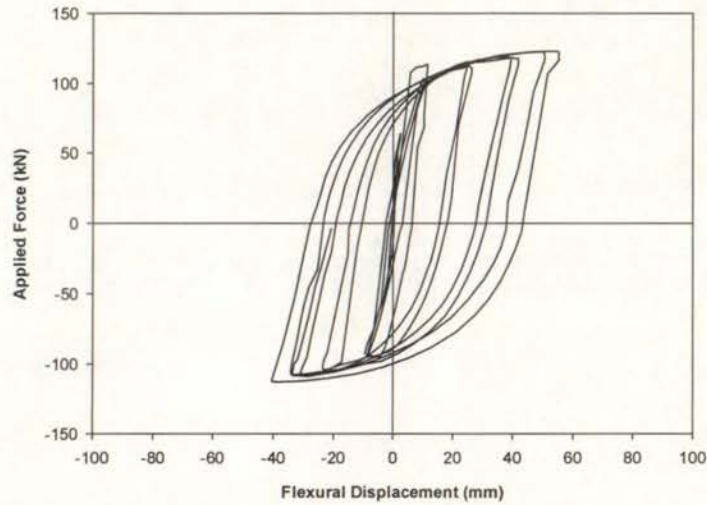


Figure C-4(a) Flexural Displacement Component

4(a) reveals that the flexural deformations were symmetrical and their hysteresis shape followed conventional behaviour. Figure C-4(b) details the shear deformations for the same loading stages. As with the flexural deformations, the shear deformations were symmetrical and followed conventional behaviour. Figure C-4(c) presents the rocking deformation for the aforementioned period. Figure C-4(c) reveals that, as expected, the rocking deformations were elastic. However, the rocking deformations from testing using the New Zealand loading history were offset in the negative direction. This was due to crushing of the mortar base between the beam and its base occurring during negative cycles.



Figure C-4(b) Shear Displacement Component

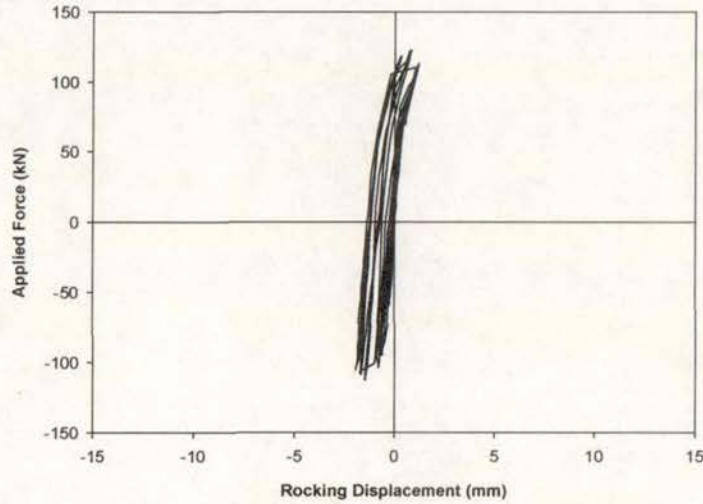


Figure C-4(c) Rocking Displacement Component

### C.1.3 Energy Components

Figure C-5 presents the amount of energy dissipated through the flexural and shear deformation components and compares the sum of the two components to the total amount of energy dissipated. The amount of energy dissipated during the test was defined as the area inside the force-displacement hysteresis loops until failure occurred. As reported in Section 6.1, the beam was considered to have failed once the maximum strength during a cycle dropped below 80% of the maximum measured strength for that direction of loading.

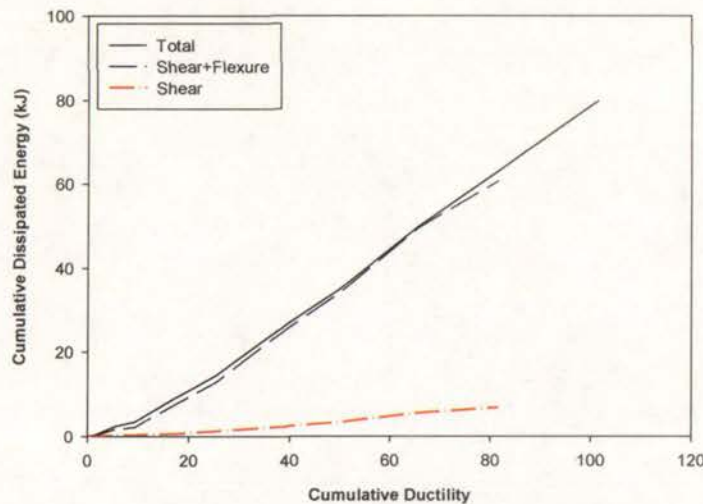


Figure C-5 Components of Energy Dissipation

Only the energy dissipated through flexural and shear deformations were included from the three displacement components. As Figure C-4c indicates, rocking deformations were effectively elastic, and hence no energy was expended as the beam rocked on its base. Figure C-5 demonstrates that as expected, flexural deformations accounted for the majority of the total energy dissipated.

#### C.1.4 Moment–Curvature Response

Moment–curvature relationships were obtained for the three instrumentation cells illustrated in Figure 4-16. The maximum moment was plotted against the average curvature for the particular cell. Section 3.6 summarises the procedures that enabled the average curvature for each instrumentation cell to be determined. The experimental data was then compared with the predicted moment–curvature curve. The predicted moment–curvature envelope was developed using actual material strengths and a computer program developed by Ingham (1994).

Figure C-6(a) and Figure C-6(b) reveal that the beam had a much shorter yield plateau than the predicted response. This was due to the cyclic loading regime, which resulted in the stress–strain behaviour of the longitudinal steel departing from the monotonic stress–strain curve under tensile loading. This was confirmed through accurate correlation between the predicted and actual response being obtained for monotonic loading. Even though there was poor correlation between the predicted

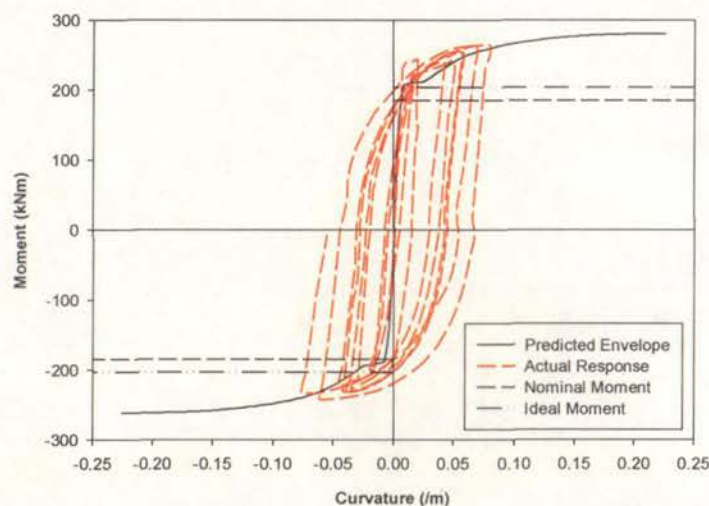


Figure C-6(a) Moment–Curvature Response (Panel 1)

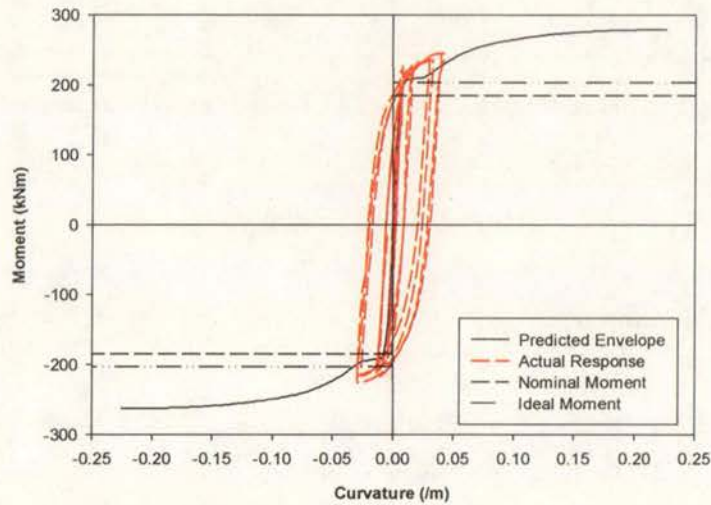


Figure C-6(b) Moment–Curvature Response (Panel 2)

yield plateau and the actual yield plateau, the maximum strength of the beam was accurately predicted. Figure C-6(c) reveals that there was no curvature demand in the third panel. This justified the assumptions made in Section 4.6 that three instrumentation panels would capture all the necessary data.

#### C.1.5 Reinforcement Strains

The average strain in the bottom and top longitudinal reinforcement was plotted for each instrumentation panel. The reinforcement strains from panel 1, panel 2, and panel 3 are presented in Figures C-7(a), C-7(b), and C-7(c) respectively.

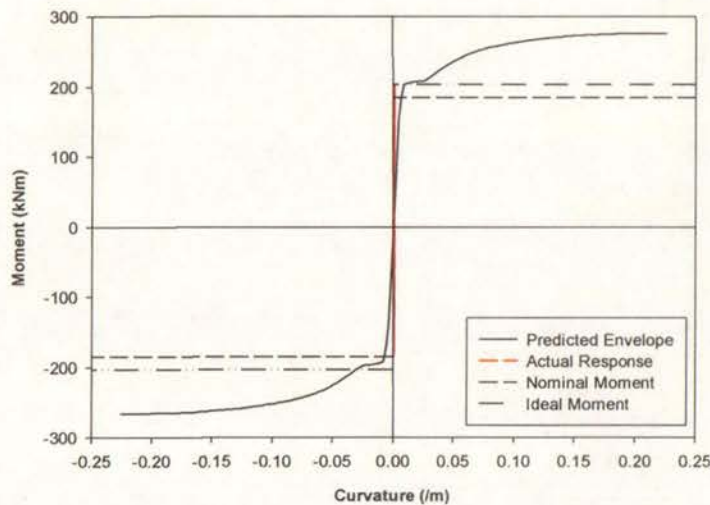


Figure C-6(c) Moment–Curvature Response (Panel 3)

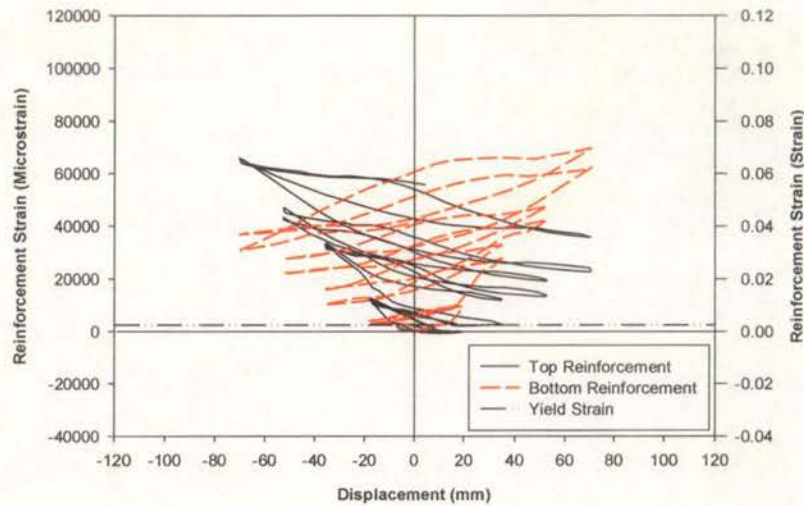


Figure C-7(a) Reinforcement Strains (Panel 1)

Figure C-7(a) and Figure C-7(b) illustrate that the cracks did not close under reversal of load from ductility 2 in the first panel and ductility 4 in the second panel. This indicated the region of plasticity. From Figure C-7(c), it was established that the longitudinal reinforcement in panel 3 did not yield. This confirmed the conclusion reached in Section C.1.4 regarding the location of the instrumentation panels.

It has been observed in previous experimental studies on reinforced concrete frame members that the member's depth increases during testing. However the change in beam depth during the test was not included in this experimental study. It was established in Section 5.1.3 that the length of the plastic hinge zone was 430mm.

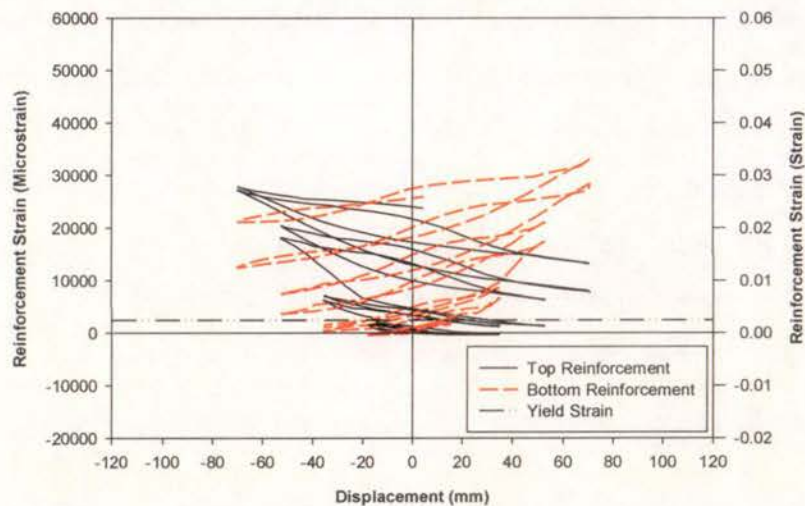


Figure C-7(b) Reinforcement Strains (Panel 2)

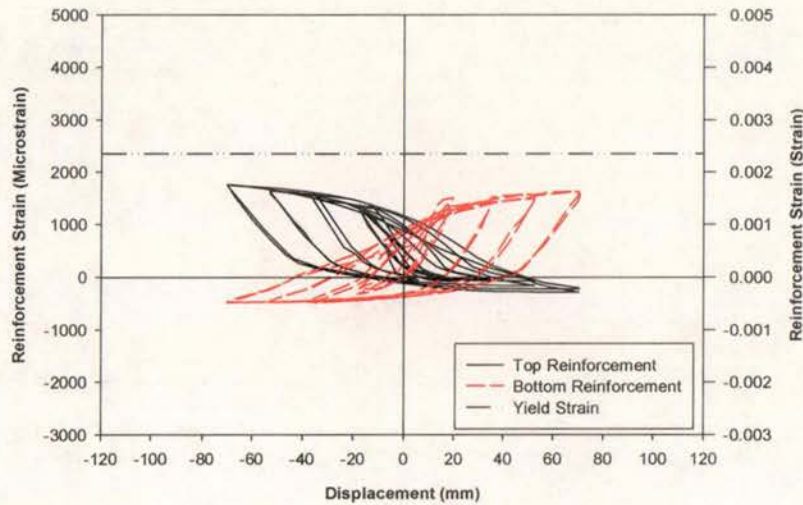


Figure C-7(c) Reinforcement Strains (Panel 3)

Therefore, as revealed in Figure 4-16, the instrumentation set-up for this testing series consisted of a portal gauge measuring the vertical strain either side of the plastic hinge zone with only one portal gauge measuring the vertical strain in the plastic hinge zone. Building an accurate picture of the depth-increase (“bulging”) profile requires several gauges measuring the vertical strain in the plastic hinge zone. Therefore the instrumentation set-up for this testing series was unable to accurately portray the bulging behaviour.

#### C.1.6 Beam Elongation

The horizontal elongation at the beam centreline was recorded for the loading stages up to and including ductility 8. The horizontal elongation at the beam centreline was calculated by summing the average of the two horizontal strain gauge recordings over the three instrumentation cells. Figure C-8 graphs the actuator force versus the horizontal elongation. It reveals that the beam’s length had extended by 16mm, or 2.66% of the total beam depth, as a result of the applied loading and that the majority of this elongation occurred after the beam was loaded to ductility 4.

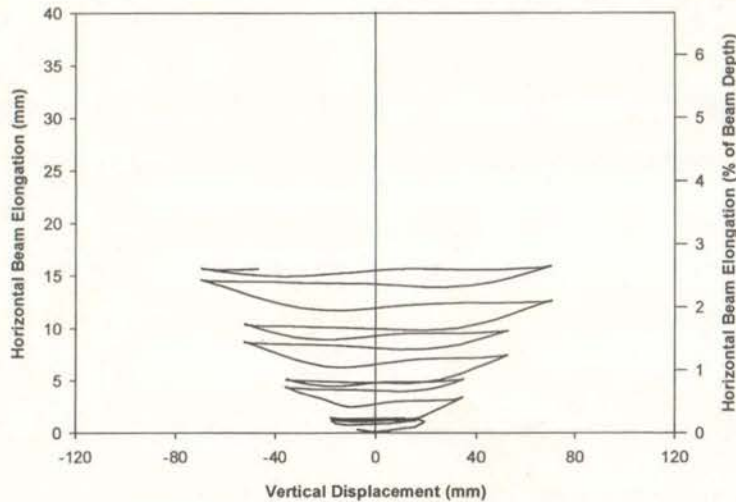


Figure C-8 Horizontal Beam Elongation

### C.1.7 Summary of Results

Reasonable agreement was obtained between the sum of the three displacement components and the actual displacement for the positive direction and until 50mm in the negative direction.

Flexural deformations accounted for the majority of the total displacement and the total amount of energy dissipated. Flexural and shear deformations followed conventional behaviour and were symmetrical about the origin. Rocking deformations were elastic and were slightly offset in the negative direction.

There was poor correlation between the predicted yield plateau and the actual yield plateau. However, the maximum strength of the beam was predicted accurately.

Cracks did not close under reversal of load from ductility 2 in the first instrumentation panel and from ductility 4 in the second instrumentation panel. The longitudinal reinforcement in the third instrumentation panel did not yield.

A total horizontal elongation equal to 2.66% of the total beam depth was recorded for loading up to and including ductility 8.

## C.2 University of California at Berkeley Loading History

Results from testing conducted using the loading history from the University of California at Berkeley are detailed in Sections C.2.1 through C.2.6. Section C.2.7 then outlines the main points from this test. Section C.2.1 describes the observed behaviour of the test specimen during testing. Section C.2.2 identifies the separate displacement components that were established from the experimental data. Section C.2.3 then separates the total energy accumulated during the test into the energy absorbed through the flexural and shear displacement components. Section C.2.4 compares the predicted moment–curvature relationship with the experimental moment–curvature response, and Section C.2.5 details the average strains in the longitudinal reinforcement for the three instrumentation cells. Lastly, Section C.2.6 reports on the horizontal elongation of the beam during the test.

### C.2.1 Test Observations

As with the New Zealand loading history, the loading history from the University of California at Berkeley was separated into a force-controlled regime and a displacement-controlled regime. Section C.2.1.1 reports on the force-controlled section of the test whereas Section C.2.1.2 describes the behaviour observed during the displacement-controlled section.

#### C.2.1.1 Force Control

The initial stages of the test were carried out under force control. An actuator force of 29.0kN was applied in each direction for three cycles. This corresponded to 40% of the yield force established experimentally from testing using the New Zealand loading history. A visual inspection was made at the conclusion of the load application in each direction for each cycle. No cracks were observed at any of the inspections.

### C.2.1.2 Displacement Control

Once the three cycles at 40% of the yield force had been completed, testing was carried out under displacement control. The loading steps followed the procedures outlined in Section 6.3.1.

#### **Ductility 1:**

Six flexural cracks were identified on each side of the beam after the first positive cycle. No shear inclination was seen on any of the cracks. Five flexural cracks were located on each side after the first negative cycle. Again, none of the cracks had any shear inclination.

A new crack on each side was the only additional cracking resulting from the second cycle in both directions. No additional cracking was noted after the third cycle in either direction.

#### **Ductility 2:**

Two new primary cracks were identified after the first cycle in the positive direction. Extensions to existing cracks were also noted. These extensions were inclined at 45° to the horizontal. Three new primary cracks were observed on Side A whereas only one was observed on Side B after the first negative cycle. However, on each side the furthest crack was located 1200mm from the pedestal face, which meant that Side A simply had a higher concentration of cracking. This higher crack concentration may have been due to local discontinuities introduced during construction of the beam; for example, variations in the length of time that the concrete was vibrated for. Extensions to existing cracks were also noted. As with loading in the positive direction, these extensions were inclined at 45° to the horizontal.

No further primary cracks were identified in the remaining two cycles at this level. Instead, small extensions to existing cracks continued to occur. As with the first cycle, these extensions were inclined at 45° to the horizontal.

**Ductility 3:**

One new crack was identified on each side after loading to ductility 3 in both directions. These cracks were the last primary cracks to be identified in this test. Minor extensions to existing cracks were also noted. As with the crack extensions at ductility 2, the extensions were inclined at  $45^\circ$  to the horizontal. No distress was noted in the compression zone although there was extremely minor spalling of concrete along cracks in the plastic hinge zone. It was observed that the rocking of the beam on its base was a major component of the total vertical displacement.

The only additional cracking for the second and third cycles was the extension of existing cracks. These extensions were relatively minor and were inclined at  $45^\circ$  to the horizontal. Extremely minor spalling along cracks in the plastic hinge zone was noted during loading in the third negative cycle.

**Ductility 4:**

No distress in the compression zone or additional cracking was noted during the first cycle in the positive and negative direction.

Minor spalling along cracks in the plastic hinge zone was observed during the second and third cycles. The first evidence of distress in the compression zone was seen after the second cycle in the positive direction. The only additional cracking due to the three cycles at ductility 4 was seen after the second cycle in the negative direction.

**Ductility 5:**

The behaviour from the three cycles at ductility 5 was similar. Minor extensions to existing cracks and secondary cracking in the plastic hinge zone were identified. No further distress was evident in the compression zone although minor spalling along cracks in the plastic hinge zone continued.

**Ductility 6:**

Behaviour for the three cycles at ductility 6 was dominated by continued minor spalling along cracks in the plastic hinge zone. Extremely minor distress was observed in the compression zone after the first negative cycle and minor extensions to existing cracks were identified after the second positive cycle.

**Ductility 7:**

The only additional cracking during the three cycles at ductility 7 was the secondary cracking that was occurring in the plastic hinge region. Significant spalling of concrete from the bottom of the beam meant that the longitudinal reinforcement was visible. Spalling of cover concrete continued to occur in the plastic hinge zone. The total amount of spalling that had taken place since the beginning of the test meant that the widths of cracks in the plastic hinge zone were unable to be measured. Pinching in the force-displacement response was observed during the third positive cycle.

**Ductility 8:**

The observed behaviour from the three cycles at ductility 8 was similar. Spalling continued from the side of the beam. Significant pieces of concrete were also removed from the top and bottom of the beam resulting in approximately 100mm on the top and 200mm on the bottom having no cover concrete.

**Ductility 9:**

The observed behaviour during the three cycles at ductility 9 was comparable to the observed behaviour at ductility 8. Significant spalling continued from the top and bottom of the beam. The strength of the test subassemblage dropped to 84% of the maximum-recorded strength in the positive direction and 87% in the negative direction during the third cycle.

**Ductility 10:**

A longitudinal bar ruptured during the first cycle to ductility 10 in the negative direction. Figure C-9 shows that severe degradation had taken place by the time the rupture of the longitudinal reinforcement bar occurred. Hence, it was determined that the properties of the bar were unaffected by welding associated with the instrumentation studs and that the failure was due to the low-cycle fatigue of the reinforcement bar. This caused the strength of the test subassemblage to drop below 80% of the maximum-recorded strength in the positive and negative direction. The test was terminated at this point.

**C.2.2 Displacement Components**

Figure C-10 illustrates separation of the vertical displacement into its three components. Rocking of the beam on its base accounted for a much larger percentage of the total deflection than for testing using the New Zealand loading history. This was because the stress levels in the stressing rods had reduced during the tensioning process. This reduction in force in the stressing rods allowed the beam to rock on its base to a greater extent. Figure C-10 reveals that there was excellent agreement between summed components and the total measured displacement in both the positive and negative direction for the duration of the test.

Figure C-11(a) is a plot of the applied force against the flexural deformation for



Figure C-9 Rupture of Longitudinal Bar

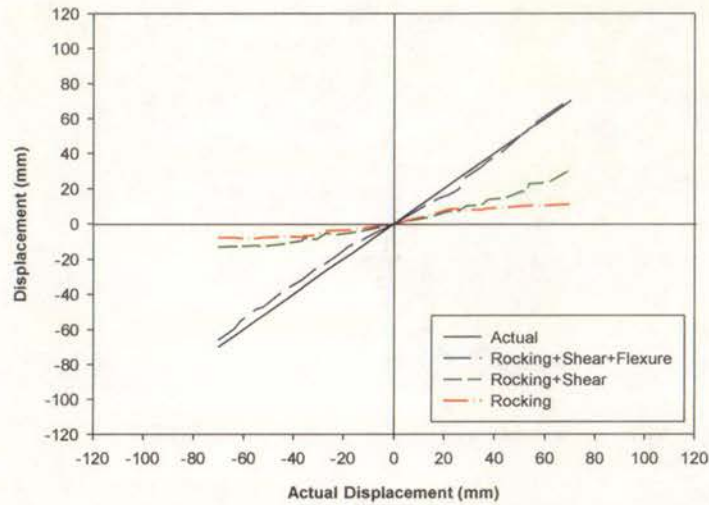


Figure C-10 Components of Displacement

loading up to and including ductility 8. Figure C-11(a) reveals that although the flexural deformations were non-symmetrical, their hysteresis shape followed expected behaviour. Figure C-11(b) shows the applied force versus the shear deformation for the aforementioned loading stages. The shear deformations were highly non-symmetrical although, as with the flexural deformations, their shape followed expected behaviour. Figure C-11(c) presents the relationship between the applied force and rocking deformations. Figure C-11(c) reveals that because of the magnitude of the rocking deformations there were signs of inelastic behaviour. Also rocking displacements were larger in the positive direction. This was due to the concrete pedestal acting as a restraint to the rocking of the beam in the negative direction.

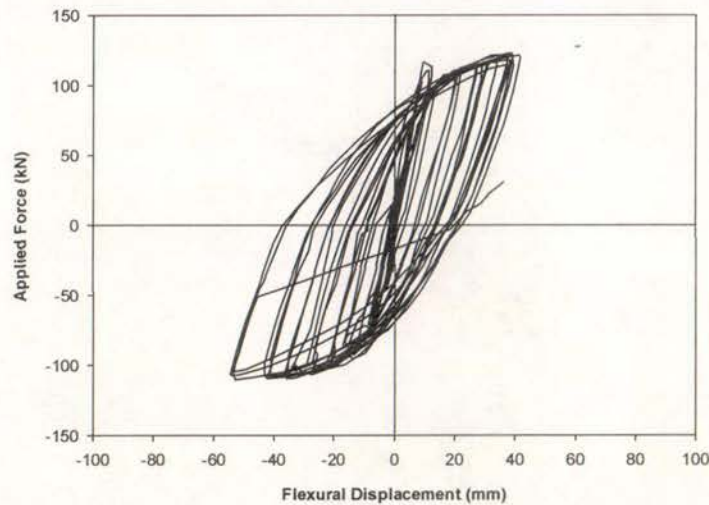


Figure C-11(a) Flexural Displacement Component

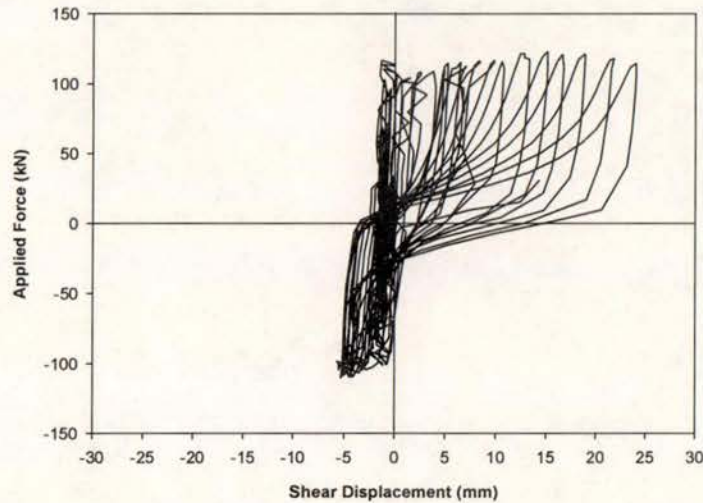


Figure C-11(b) Shear Displacement Component

### C.2.3 Energy Components

Figure C-12 presents the amount of energy expended through the flexural and shear deformation components and compares the sum of the two components to the total amount of energy expended. It was decided to keep the analysis procedures constant for the twelve tests so that data could be compared more easily. Therefore, the amount of energy absorbed through the rocking of the beam on its base was not included in the analysis even though the magnitude of the rocking displacements was significantly greater than that recorded during testing using the New Zealand loading history. Figure C-12 reveals that the sum of the energy expended through flexural and

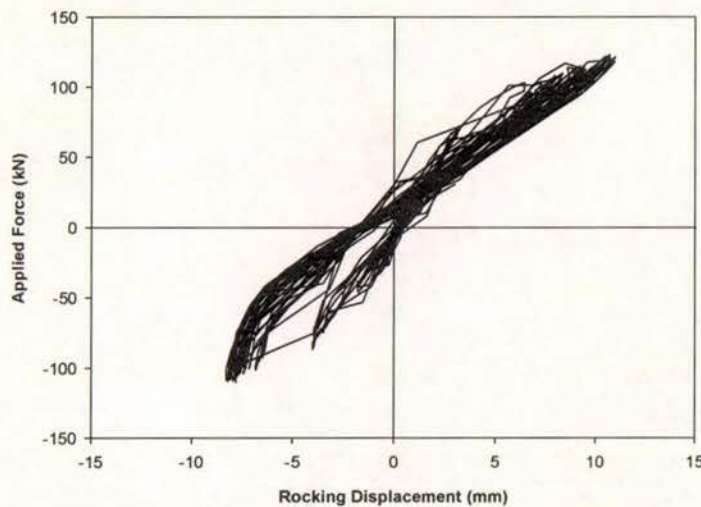


Figure C-11(c) Rocking Displacement Component

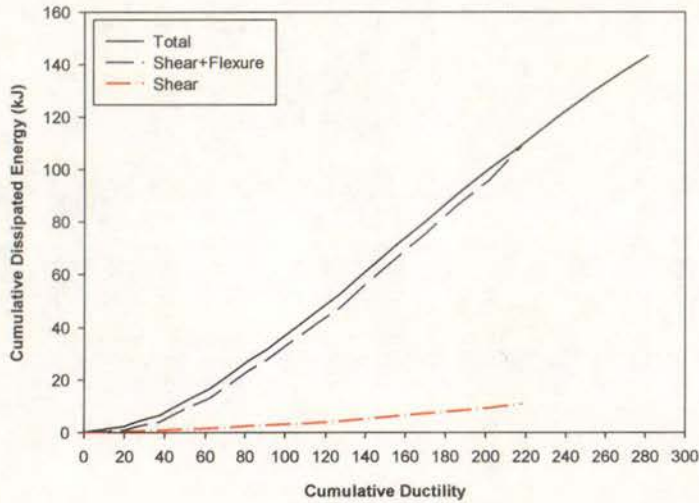


Figure C-12 Components of Energy Dissipation

the analysis failing to include the amount of energy expended through the beam rocking of the beam on its base. As for the New Zealand loading history, flexural deflections accounted for the majority of the expended energy.

#### C.2.4 Moment–Curvature Response

The moment–curvature response for the three instrumentation panels, from testing using the Berkeley loading history, is presented in Figures C-13(a) through C-13(c).

The response followed the trends seen in the moment–curvature response from testing using the New Zealand loading history where the beam had a much shorter yield

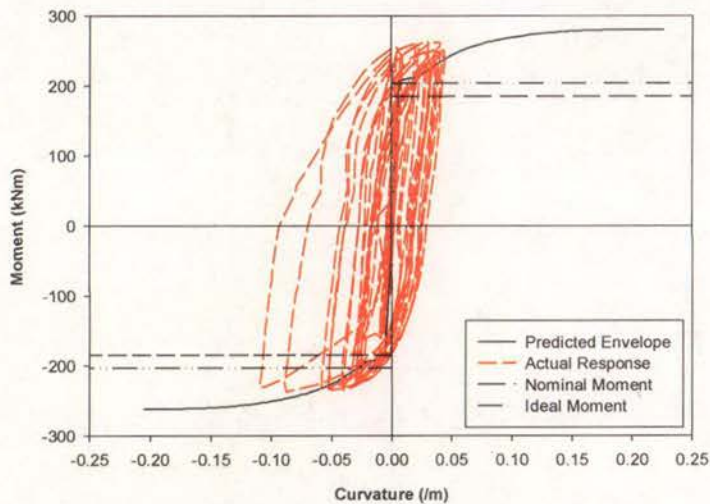


Figure C-13(a) Moment–Curvature Response (Panel 1)

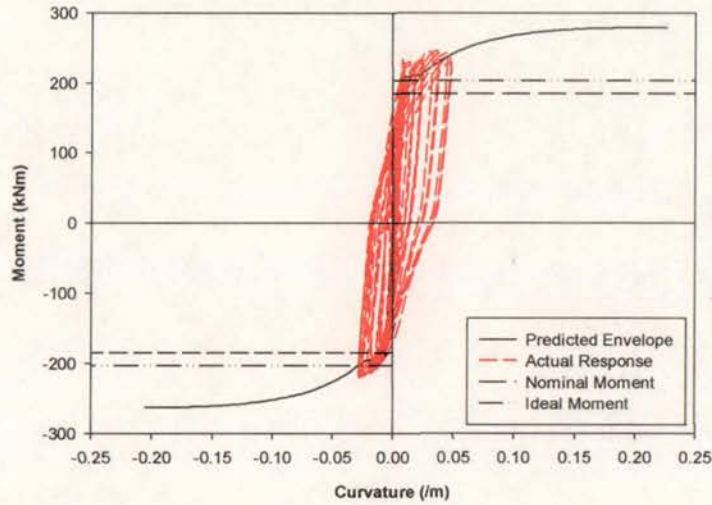


Figure C-13(b) Moment–Curvature Response (Panel 2)

plateau than the predicted response. Figure C-13(a) demonstrates that much larger curvatures were measured in the negative direction than in the positive direction. This is consistent with the negative offset in the calculated flexural deformations. Figure C-13(c) reveals that there was little curvature demand in the third instrumentation panel although the actual response does follow the predicted response accurately.

### C.2.5 Reinforcement Strains

The average strain in the bottom and top longitudinal reinforcement was plotted for each instrumentation panel. The reinforcement strains from panel 1, panel 2, and

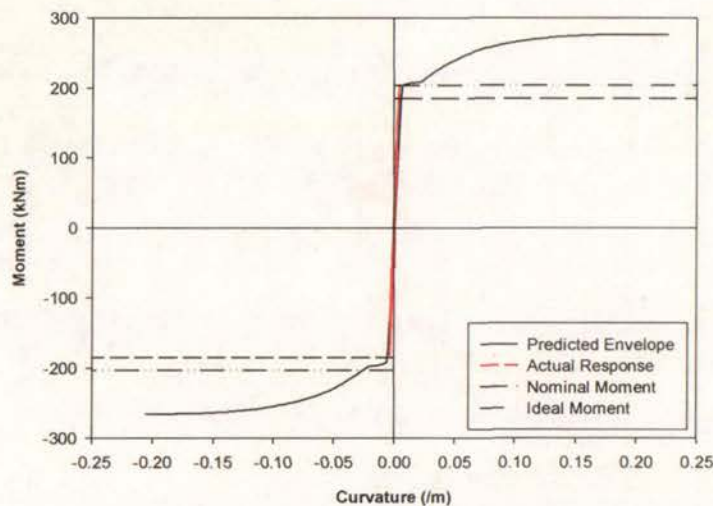


Figure C-13(c) Moment–Curvature Response (Panel 3)

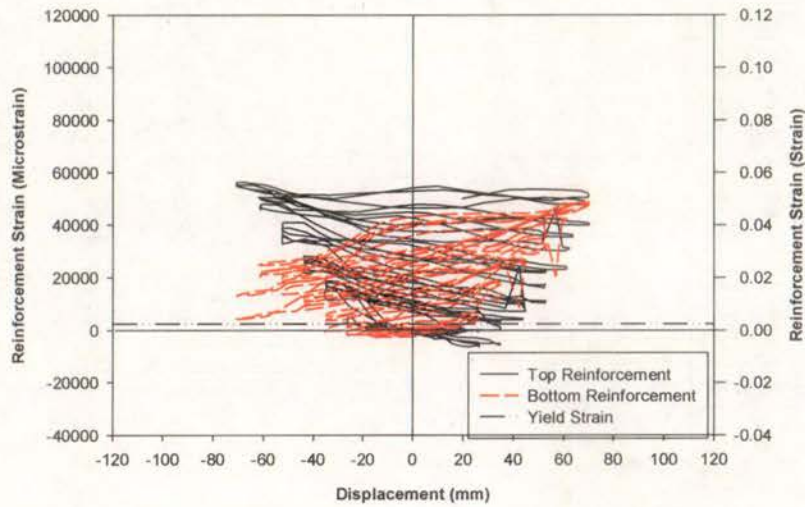


Figure C-14(a) Reinforcement Strains (Panel 1)

panel 3 are presented in Figures C-14(a), C-14(b), and C-14(c) respectively.

The response of the top and bottom reinforcement was symmetrical. Figure C-14(a) and Figure C-14(b) illustrate that the cracks did not close under reversal of load from ductility 3 in the first instrumentation panel and ductility 4 in the second instrumentation panel. This is similar to the results from testing using the New Zealand loading history. Figure C-14(c) demonstrates that yielding did not occur in the third instrumentation panel.

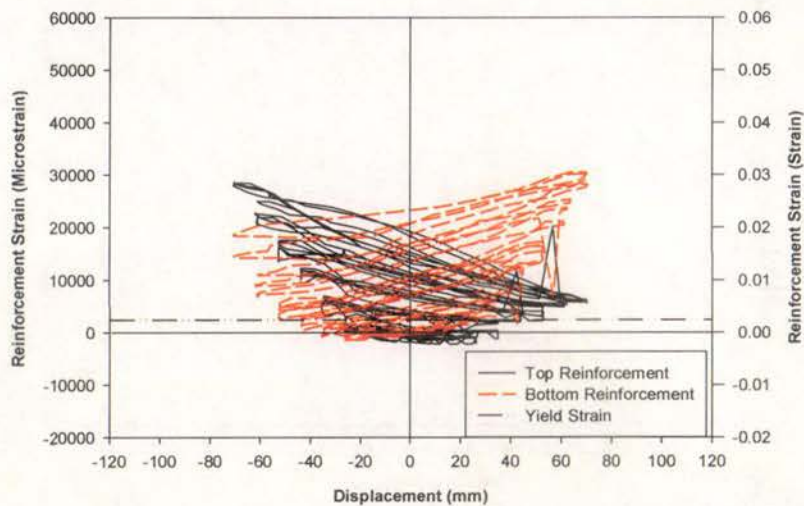


Figure C-14(b) Reinforcement Strains (Panel 2)

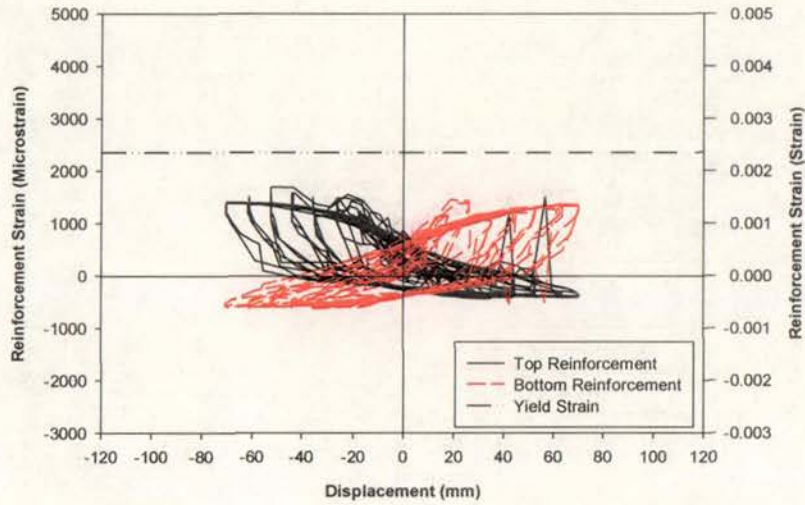


Figure C-14(c) Reinforcement Strains (Panel 3)

### C.2.6 Beam Elongation

The horizontal elongation at the beam centreline was recorded for the loading stages up to and including ductility 8. Figure C-15 plots the applied force against the horizontal elongation and reveals a maximum elongation of 28mm or 4.67% of the total beam depth. It also demonstrates that the horizontal elongation increased at a more uniform rate than the horizontal elongation recorded during testing using the New Zealand loading history. This was due to the smaller ductility increments that were applied as part of this loading history.

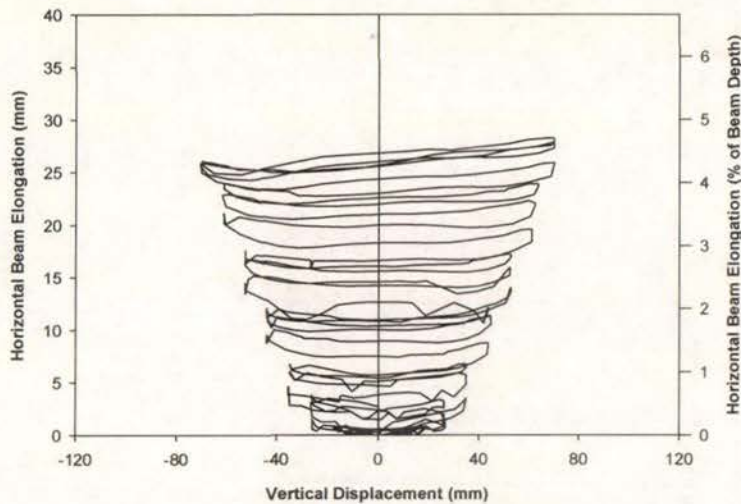


Figure C-15 Horizontal Beam Elongation

### C.2.7 Summary of Test Results

Excellent agreement was obtained between the sum of the three displacement components and the actual displacement for both loading directions.

Flexural deformations accounted for the majority of the total displacement and the total amount of energy absorbed. Flexural deformations were offset in the negative direction whereas shear deformations were offset in the positive direction. However, the shape of the flexural and shear deformations still followed normal behaviour. Rocking deformations accounted for a much larger percentage of the vertical displacement than for testing using the New Zealand loading history.

Poor correlation was obtained between the predicted yield plateau and the actual yield plateau due to the stress-strain behaviour of the longitudinal steel departing from the monotonic stress-strain curve under tensile loading under cyclic loading. However, the maximum strength of the beam was predicted accurately.

Strains recorded in the top and bottom reinforcement were symmetrical. Cracks did not close under reversal of load from ductility 3 in the first instrumentation panel and from ductility 4 in the second instrumentation panel. The longitudinal reinforcement in the third instrumentation panel did not yield.

A total horizontal elongation equal to 4.67% of the total beam depth was recorded for loading up to and including ductility 8.

### C.3 PRESSS Loading History

Results from testing conducted using the PRESSS loading history are presented in Sections C.3.1 through C.3.6. Section C.3.7 encapsulates the main details from the test. Section C.3.1 describes the observed behaviour of the test specimen during testing. Section C.3.2 and Section C.3.3 separate the total vertical displacement and the total energy accumulated during the test into their separate components. Section C.3.4 compares the predicted moment–curvature relationship with the moment–curvature relationship established experimentally, and Section C.3.5 reports on the average strains in the longitudinal reinforcement for the three instrumentation cells. Lastly, Section C.3.6 details the horizontal elongation of the beam during the test.

#### C.3.1 Test Observations

Loading during the PRESSS loading history was completed entirely under displacement control. Inspections were made upon the conclusion of each load step. For the purposes of reporting, observations made during these inspections are grouped into pre-yield cycles, cycles between ductility 1 and 2, cycles between ductility 2 and 4, cycles between ductility 4 and 6, and cycles over ductility 6.

##### **Pre-yield inspections:**

The cycles described in this category are the three cycles at ductility 0.25, 0.37, 0.49, 0.61, and 0.86. At ductility 0.25, contrasting behaviour was observed between loading in the positive direction and loading in the negative direction. No cracks were identified in the positive direction whereas one flexural crack was noted during the inspection after the first cycle in the negative direction. Furthermore, subsequent cycles in the negative direction led to an additional crack forming on Side A and a small extension to existing cracks. This contrasting behaviour occurs because the self-weight of the test subassemblage provides an additional force in the negative direction.

At ductility 0.37, additional flexural cracks formed under loading in both directions. At the conclusion of the three loading cycles, the amount of cracking was approximately symmetric between the positive and negative directions.

New cracks did not form under positive loading to ductility 0.49. Two additional flexural cracks on Side A and one additional flexural crack on Side B formed after the first negative cycle. The dominant behaviour at this ductility level was the small extensions to existing cracks that formed during the first two cycles. No additional cracking was identified in the inspection proceeding the third cycle.

Only a minor increase in force from the previous displacement level was required to load the test subassemblage to ductility 0.61. Therefore, no new cracks were identified after any of the three cycles. However, small extensions to existing cracks were noted.

The formation of new cracks and extensions to existing cracks were observed during the three cycles to ductility 0.86. Some of the crack extensions showed shear inclination. A total of six cracks formed on each side during loading in the positive direction whereas a total of seven cracks formed on each side during loading in the negative direction.

Significantly more cracking occurred during the pre-yield cycles from the PRESSSS loading history than during the pre-yield cycles from the New Zealand loading history. This difference is due to the larger number of cycles that were applied in this range as part of the PRESSSS loading history.

#### **Cycles between ductility 1 and ductility 2:**

Three cycles were applied at ductility 1.23 and at ductility 1.84. No new cracks formed in the beam during the three cycles at ductility 1.23. However, cracking in the joint region was noted. As with other tests, the cracks in the joint region did not open during the test. Significant extensions to existing cracks were identified with these extensions inclined at 45° to the horizontal.

New flexural cracks were identified during inspections made when cycling at ductility 1.84. One flexural crack formed on each side during loading in the negative direction whereas two cracks formed on each side during loading in the positive direction. These cracks were the last flexural cracks to form in this test. The higher number of new cracks formed during loading in the positive direction meant that there was the same number of total cracks from loading in both directions. Extensions to existing cracks were also noted. As with the crack extensions at ductility 1.23, these extensions exhibited shear inclination. The first evidence of secondary cracking in the plastic hinge zone was found. Secondary cracking formed at a lower ductility level than for testing using the New Zealand loading history. Again this was due to the larger number of cycles that were applied in the PRESSSS loading history up to this ductility level than for the corresponding ductility level when testing using the New Zealand loading history.

#### **Cycles between ductility 2 and ductility 4:**

Three cycles were applied at ductility 2.46 and ductility 3.69. The additional cracking from that point consisted of extensions to existing cracks and new cracks in the joint region. Little additional cracking was observed during the three cycles at ductility 2.46. Two cracks on each side of the joint region were observed along with small extensions to existing cracks. These extensions showed shear inclination.

A small number of crack extensions were identified during the three cycles at ductility 3.69. These were all inclined at  $45^\circ$  to the horizontal. The first evidence of crushing of concrete in the compression zone and spalling of cover concrete along cracks in the plastic hinge zone was also observed. Again this behaviour occurred at a lower ductility level than the corresponding behaviour observed during testing using the New Zealand loading history.

#### **Cycles between ductility 4 and 6:**

Three cycles at ductility 4.91 were applied. Spalling along cracks in the plastic hinge zone continued to occur during the three cycles. No further crushing of concrete in the plastic hinge zone or additional cracking was evident during the three cycles.

**Cycles over ductility 6:**

Three cycles at ductility 6.14 and ductility 7.37 were applied. The test was terminated after the completion of two cycles in the positive direction and one cycle in the negative direction to ductility 8.60. Significant spalling of concrete from the top and bottom of the beam, such that the longitudinal reinforcement was visible, occurred during the three cycles to ductility 6.14. Spalling of concrete along cracks in the plastic hinge zone meant that the widths of cracks in the plastic hinge zone were unable to be measured. Figure C-16 illustrates the amount of spalling that had occurred by the third cycle at ductility 6.14.

The behaviour during the three cycles at ductility 7.37 was similar to the behaviour noted at the previous displacement level. Significant spalling from the top and bottom of the beam continued to occur with the longitudinal reinforcement being visible for approximately 300mm. Buckling of the longitudinal reinforcement was apparent. Shear deformations accounted for a much larger percentage of the total vertical displacement and pinching in the hysteresis loops was observed. The strength recorded during the third cycle in the negative direction dropped below 80% of the maximum-recorded strength. Thus, the test subassembly was considered to have failed in the negative direction.

As mentioned previously, two cycles were applied in the positive direction and one in the negative direction at ductility 8.60. The strength recorded during the second cycle

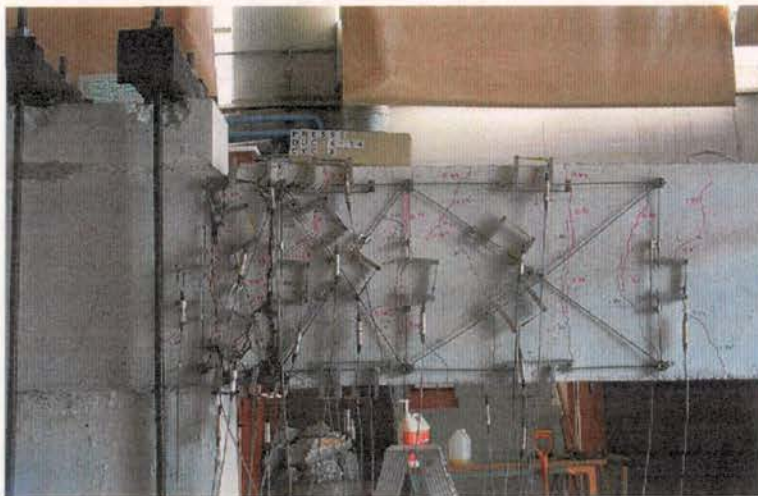


Figure C-16 Test Subassembly Condition at Ductility 6.14 (Cycle 3)

in the positive direction dropped below 80% of the maximum-recorded strength. Thus, the test subassembly was considered to have failed in the positive direction and the test was terminated at that point.

### C.3.2 Displacement Components

Figure C-17 illustrates separation of the vertical displacement into its three components. By the conclusion of the test, shear deformation accounted for a larger percentage of the total vertical displacement than that recorded for the two previously reported tests. Figure C-17 reveals that there was excellent agreement in the positive and negative direction for the duration of the test.

Figure C-18(a) and Figure C-18(b) present the flexural and shear deformation components for loading up to and including ductility 8. Figures C-18(a) and C-18(b) reveal that the flexural and shear deformations were symmetrical and their hysteresis shape was consistent with the standard response. Figure C-18(c) illustrates the rocking deformation for the aforementioned loading period. Figure C-18(c) demonstrates that the characteristics of rocking deformations varied according to the direction of loading. The stiffness in the positive direction was less than the stiffness in the negative direction. This was due to the concrete pedestal acting in conjunction with the stressing rods to restrain any rocking of the beam in the negative direction. The magnitude of rocking deformation in the positive direction was greater than at the

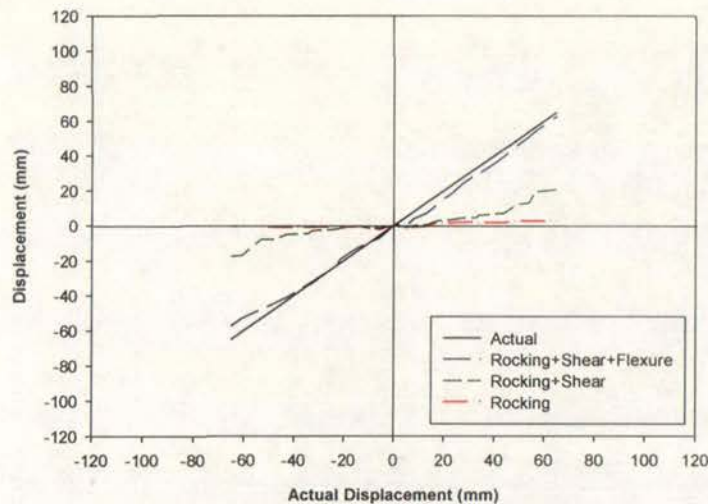


Figure C-17 Components of Displacement

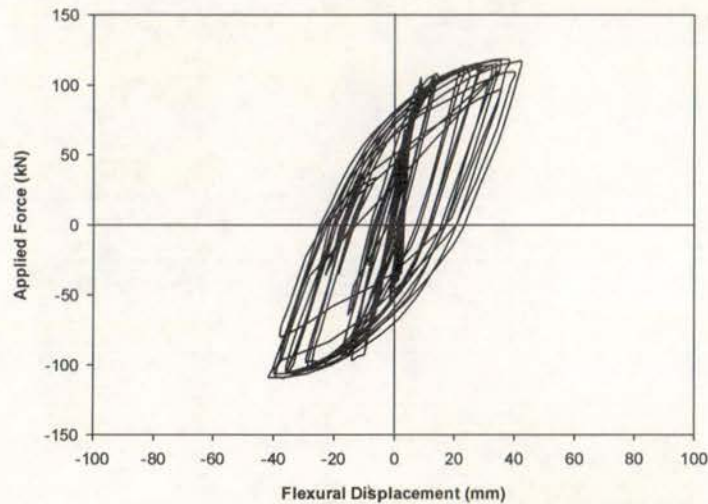


Figure C-18(a) Flexural Displacement Component

corresponding load stage in the negative direction. Again this was due to the influence of the concrete pedestal.

### C.3.3 Energy Components

Figure C-19 illustrates the amount of energy dissipated through flexure and shear deformations. Figure C-19 demonstrates that, as expected, flexural deformations accounted for the majority of the total energy dissipated and that there was excellent agreement between the sum of the two components and the total amount of energy dissipated.

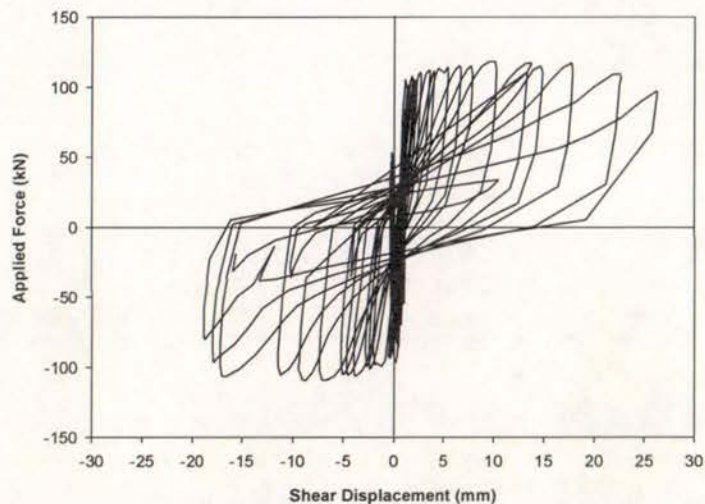


Figure C-18(b) Shear Displacement Component

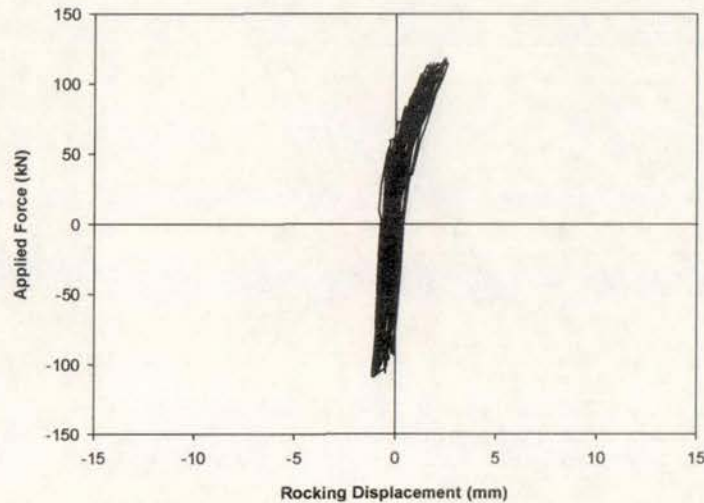


Figure C-18(c) Rocking Displacement Component

### C.3.4 Moment–Curvature Response

The moment–curvature response from testing using the PRESSS loading history followed the trends seen in the moment–curvature response from the New Zealand loading history. Figures C-20(a) through C-20(c) present the moment–curvature response from panel 1, panel 2, and panel 3 respectively.

As for testing reported in Section C.1.4 and C.2.4, the beam had a much shorter yield plateau than the predicted response and there was little curvature demand in the third panel. Figure C-20(a) reveals that larger curvatures were recorded in the positive

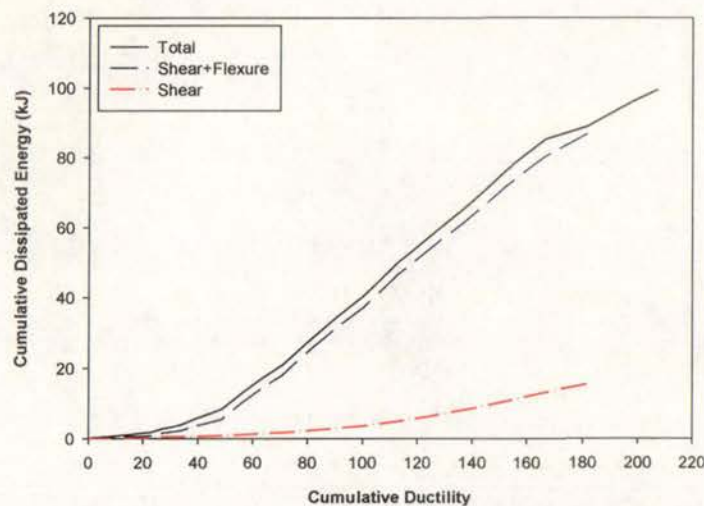


Figure C-19 Components of Energy Dissipation

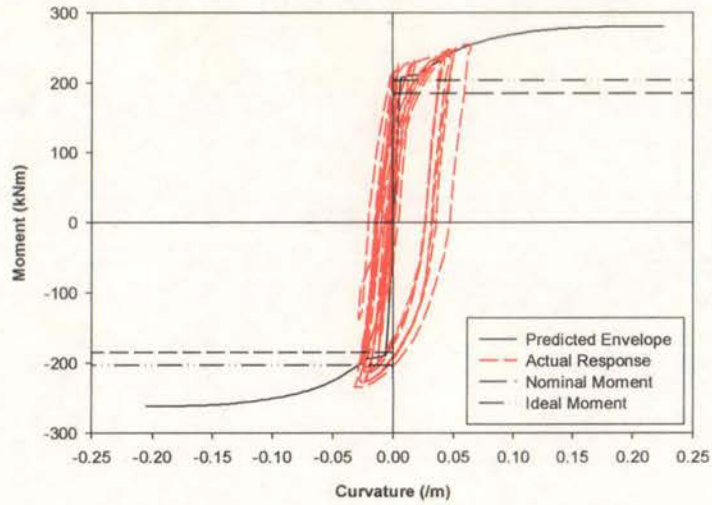


Figure C-20(a) Moment–Curvature Response (Panel 1)

direction than the in negative direction for the first instrumentation panel whereas Figure C-20(b) reveals that the opposite was true for the second instrumentation panel. This is due to the different distribution of cracking in the positive and negative direction.

### C.3.5 Reinforcement Strains

Figures C-21(a), C-21(b), and C-21(c) present the reinforcement strains in the top and bottom longitudinal reinforcement from panel 1, panel 2, and panel 3 respectively.

Figure C-21(a) and Figure C-21(b) illustrate that the cracks did not close under

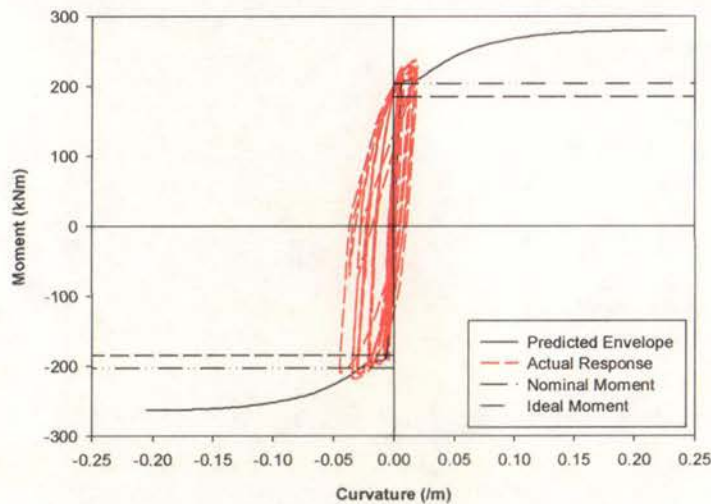


Figure C-20(b) Moment–Curvature Response (Panel 2)

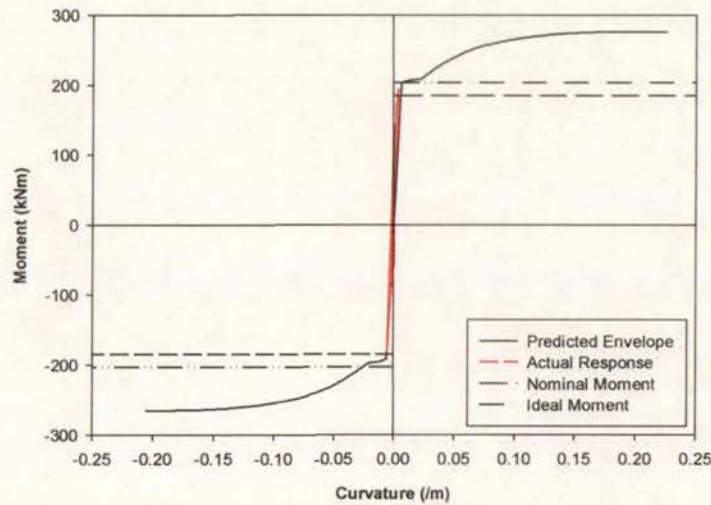


Figure C-20(c) Moment–Curvature Response (Panel 3)

reversal of load from ductility 2.46 in the first panel and ductility 3.69 in the second panel. This is comparable to the results obtained from testing using the New Zealand loading history. Unlike the behaviour from the first two reported tests, the top reinforcement in the third instrumentation panel reached its yield strain. However, this did not effect the overall response of the beam to any extent.

### C.3.6 Beam Elongation

The horizontal elongation at the beam centreline was recorded for loading up to and including ductility 8. Figure C-22 plots the applied force against the horizontal

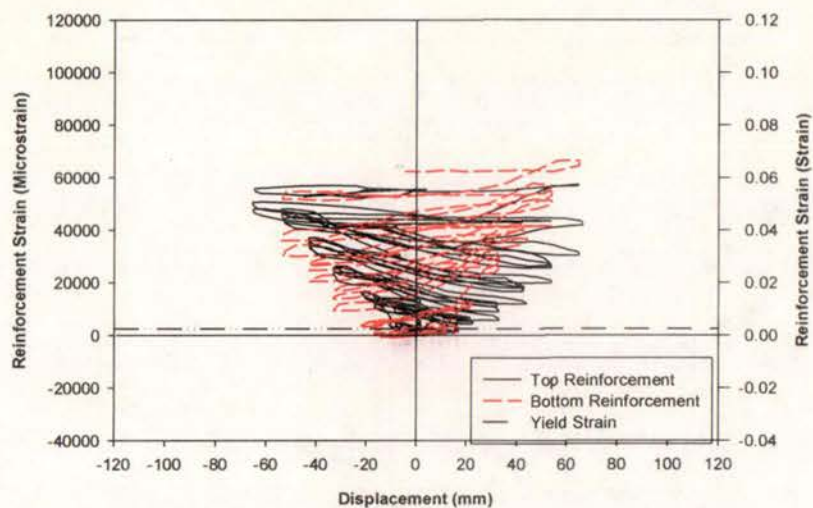


Figure C-21(a) Reinforcement Strains (Panel 1)

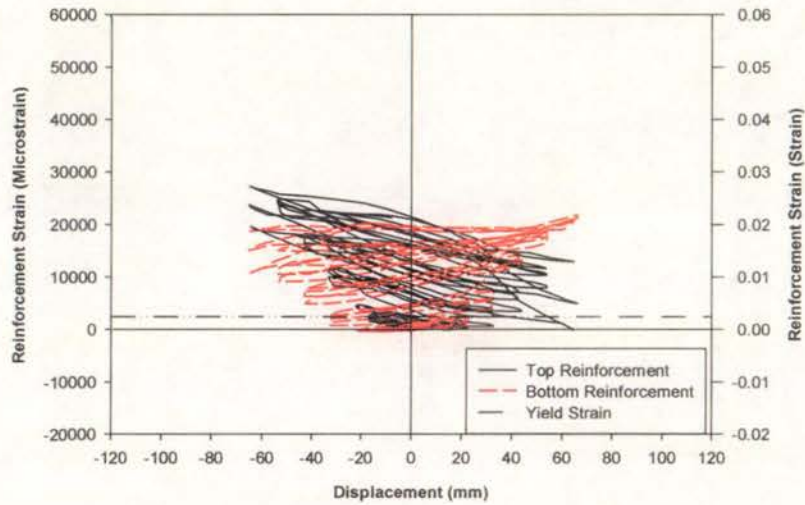


Figure C-21(b) Reinforcement Strains (Panel 2)

elongation and reveals a maximum horizontal elongation of 25mm, or 4.17% of the total beam depth. The horizontal beam elongation increased at a more uniform rate than the horizontal beam elongation measured during testing using the New Zealand loading history. This was due to the smaller ductility increments that were applied as part of this loading history.

### C.3.7 Summary of Test Results

Excellent agreement was obtained between the sum of the three displacement components and the actual displacement for both loading directions.

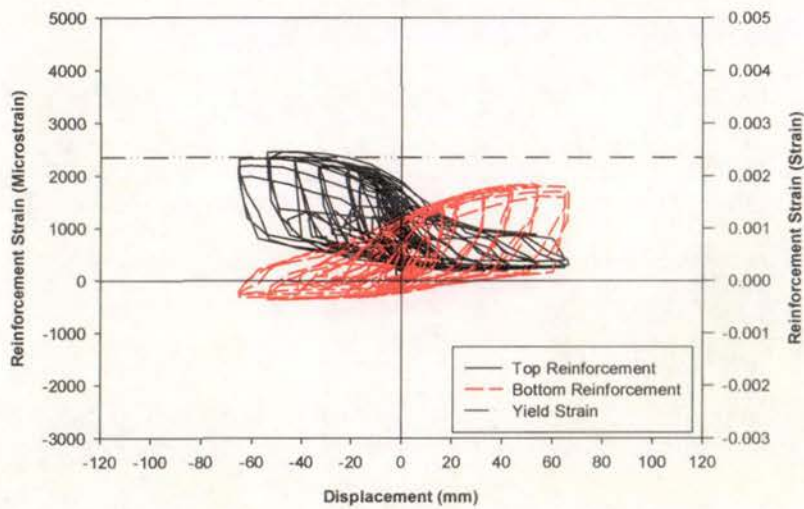


Figure C-21(c) Reinforcement Strains (Panel 3)

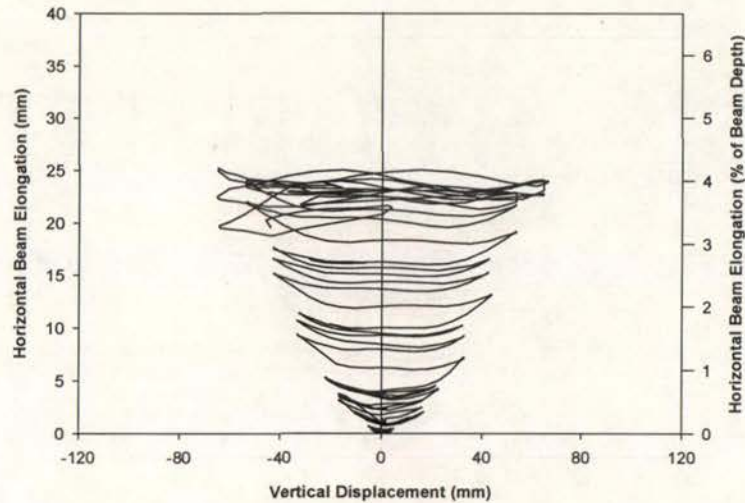


Figure C-22 Horizontal Beam Elongation

Shear deformations accounted for a larger percentage of the total vertical displacement than the shear deformations from testing using the New Zealand loading history. Both the flexural and shear deformations were symmetric and their shape was consistent with standard theory. A graph of rocking deformations showed that there was greater resistance during loading in the negative direction than during loading in the positive direction. This was due to the concrete pedestal acting in conjunction with the stressing rods to resist rocking of the beam on its base.

As for previously reported tests, there was poor correlation between the predicted yield plateau and the actual yield plateau but the maximum strength of the beam was predicted accurately.

Strains recorded in the top and bottom reinforcement were symmetrical. Cracks did not close under reversal of load from ductility 2.46 in the first instrumentation panel and from ductility 3.69 in the second instrumentation panel. In contrast to results from testing using the New Zealand loading history, the top reinforcement in the third instrumentation panel did yield.

A total horizontal elongation equal to 4.17% of the total beam depth was recorded for loading up to and including ductility 8.

## C.4 Public Works Research Institute Loading History

Results from testing undertaken using the loading history from the Public Works Research Institute are presented in Sections C.4.1 through C.4.6 with the main points outlined in Section C.4.7. Section C.4.1 describes the observed behaviour of the test specimen during testing. Section C.4.2 breaks the total vertical displacement into displacement components calculated from the experimental data. These results were applied in Section C.4.3 to separate the total energy expended during the test into the energy expended through the flexural and shear displacement components. Section C.4.4 compares the predicted moment–curvature relationship with the experimental response, and Section C.4.5 details the average strains in the longitudinal reinforcement for the three instrumentation cells. Lastly, Section C.4.6 reports on the horizontal elongation of the beam during the test.

### C.4.1 Test Observations

The loading history from the Public Works Research Institute was separated into a force-controlled regime and a displacement-controlled regime. Section C.4.1.1 details the force-controlled section of the test whereas Section C.4.1.2 describes the observed behaviour from the displacement-controlled section.

#### C.4.1.1 Force Control

The initial stages of the test were carried out under force control. The force-controlled component consists of several increasing force cycles up to the yield force established experimentally from testing using the New Zealand loading history. The initial force was 10% of the yield force, with the force then increased in increments of 10% of the yield force until the yield force was reached. A visual inspection was made at the conclusion of the load application in each direction for each cycle.

The first crack due to loading in the negative direction did not occur until the load reached 40% of the yield force, whereas the first crack under positive loading did not occur until the load reached 60% of the yield force. This difference was due to the

self-weight of the test subassemblage providing an additional force in the negative direction.

By the conclusion of the force-controlled cycles, five cracks had formed on each side during positive and negative loading. Extensions to existing cracks began to show shear inclination once the force reached 80% of the yield force.

Significantly more cracking occurred during the pre-yield cycles from testing using the loading history from the Public Works Research Institute than the pre-yield cycles from the New Zealand loading history. Furthermore, cracks showing shear inclination formed at a much lower ductility level than that observed during testing using the New Zealand loading history. This difference was due to the larger number of cycles that were applied in this range as part of the loading history from the Public Works Research Institute.

#### C.4.1.2 Displacement Control

Once the force-controlled regime had been applied, testing was carried out under displacement control. The loading steps followed the procedures outlined in Section 6.3.3.

##### **Ductility 1:**

One new crack was identified on each side during the first positive cycle. Otherwise, the only additional cracking consisted of extremely small crack extensions. There was no change in recorded crack widths during the ten cycles in either direction. The first cracks in the joint region were identified. However, as with other tests, these cracks did not open further for the duration of the test.

##### **Ductility 2:**

Two new cracks were identified on Side A whereas one new crack was identified on Side B for loading during the first cycle in both directions. Minor extensions to existing cracks were observed in subsequent cycles. The widths of cracks in the

plastic hinge zone expanded during the ten cycles in both directions. Extremely minor distress was evident along cracks in the plastic hinge zone by the fourth cycle in the negative direction and secondary cracking in the plastic hinge zone was identified by the ninth positive cycle.

Secondary cracking and minor distress formed at a lower ductility level than for testing using the New Zealand loading history. As before, this difference was due to the larger number of cycles that were applied up to and including this ductility level as part of the loading history from the Public Works Research Institute.

### **Ductility 3:**

Little additional cracking was noted during the ten cycles at ductility 3. However, the widths of the existing cracks did significantly increase during the ten cycles. Spalling along cracks continued for all ten cycles and minor spalling from the top and bottom of the beam was noted by the sixth cycle.

### **Ductility 4:**

Figure C-23 shows that significant spalling had occurred by the tenth cycle at ductility 4. Removal of several large pieces of concrete from the bottom of the beam meant that the longitudinal reinforcement was visible for a distance of approximately 200mm. Spalling along cracks in the plastic hinge zone continued to occur. Pinching



Figure C-23 Test Subassembly Condition at Ductility 4 (Cycle 10)

was observed in the force-displacement response.

The damage observed at this ductility level was far in excess of the damage observed at the corresponding ductility level when testing using the New Zealand loading history. This increase in damage showed the effects of having more cycles at each ductility level and also having smaller ductility increments.

#### **Ductility 5:**

The behaviour that was observed at ductility 4 continued to occur during the cycles to ductility 5. Severe spalling of cover concrete occurred from the top and bottom of the beam. Spalling along cracks in the plastic hinge zone was also evident. Shear deformations became more apparent during the ten cycles at this level and the strength of the test subassembly had dropped close to the failure criterion by the conclusion of the ten cycles.

#### **Ductility 6:**

The test subassembly had undergone severe degradation by this stage of the test. Horizontal displacements of approximately 15mm were measured in the plastic hinge zone. The beam was also twisting about its y-y axis. The strength of the beam dropped below 80% of the maximum-recorded strength during the third cycle in the positive direction and hence the test was determined to have failed in the positive direction. The strength of the beam dropped below 80% of the maximum-recorded strength during the fifth cycle in the negative direction. The test was considered to have failed in the negative direction and the test was terminated at that point.

#### **C.4.2 Displacement Components**

Figure C-24 illustrates separation of the vertical displacement into its three components. By the conclusion of the test, shear deformation accounted for a larger percentage of the total vertical displacement than that recorded using the New Zealand loading history. Figure C-24 reveals that although there was excellent agreement in the positive direction for the duration of the test, the correlation between

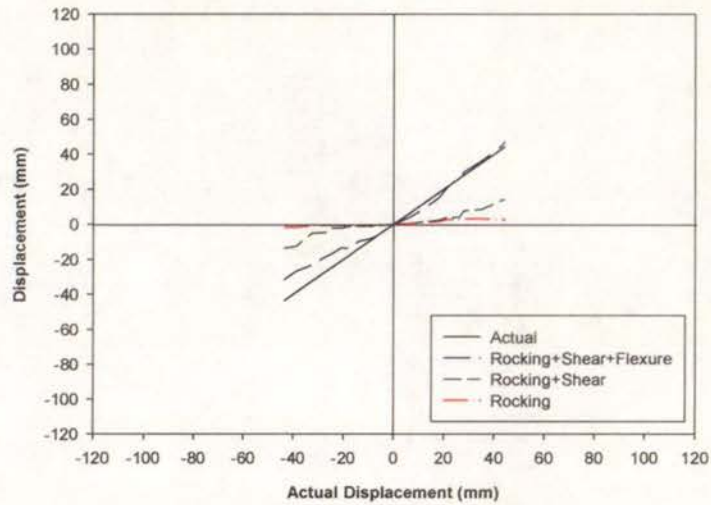


Figure C-24 Components of Displacement

actual and summed displacement components arising in the negative direction was poor.

Figure C-25(a) plots the applied force against the flexural deformation component for the duration of the test. It was discovered that contamination of the data from several strain gauges had occurred during the test. This explains the non-symmetrical behaviour and the unusual hysteresis characteristics evident in Figure C-25(a). It also explains the poor correlation between the total vertical displacement and the sum of the three components in the negative direction. Figure C-25(b) graphs the applied force against the shear deformation and reveals that the shear deformations were non-

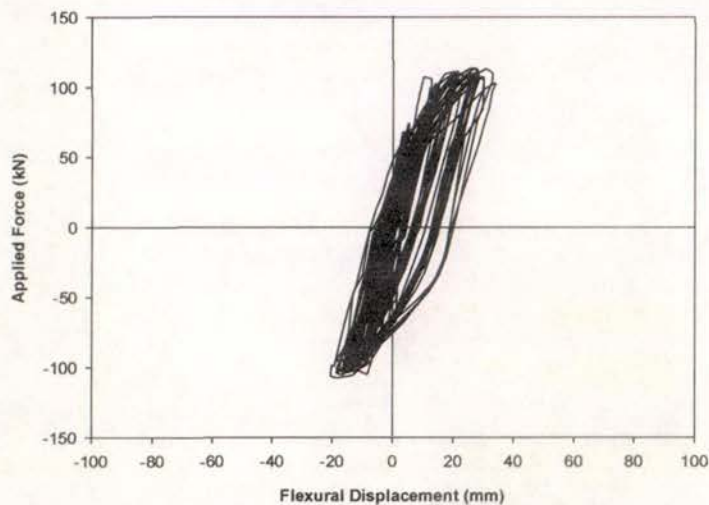


Figure C-25(a) Flexural Displacement Component



Figure C-25(b) Shear Displacement Component

symmetrical although the hysteresis behaviour did exhibit conventional behaviour.

Figure C-25(c) plots the applied force against the rocking deformation for the test duration. Figure C-25(c) reveals that as with testing using the PRESSS loading history, the rocking deformations varied according to the direction of loading. As explained in Section C.3.2, this was due to the influence of the concrete pedestal.

#### C.4.3 Energy Components

Figure C-26 illustrates the amount of energy dissipated through flexure and shear deformations. Figure C-26 demonstrates that, while flexural deformations still

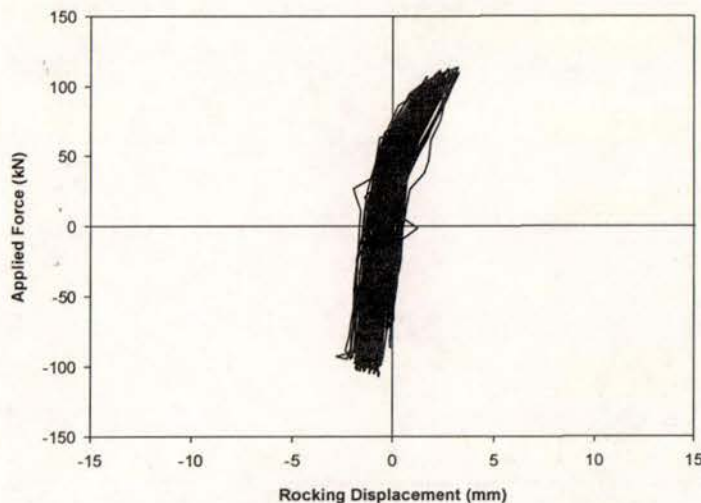


Figure C-25(c) Rocking Displacement Component

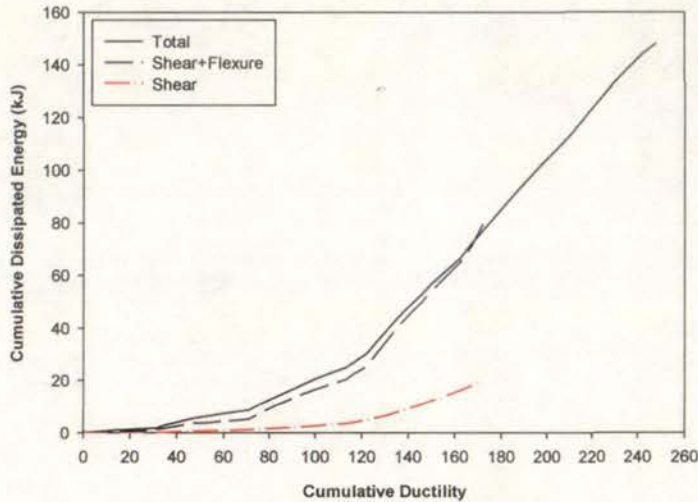


Figure C-26 Components of Energy Dissipation

accounted for the majority of the total energy dissipated, energy dissipated through shear deformation accounted for a larger percentage than that recorded in other tests. Again there was excellent agreement between the sum of the two components and the total amount of energy dissipated.

#### C.4.4 Moment–Curvature Response

The moment–curvature response from testing using the loading history from the Public Works Research Institute for the three instrumentation panels is presented in Figures C-27(a) through C-27(c).

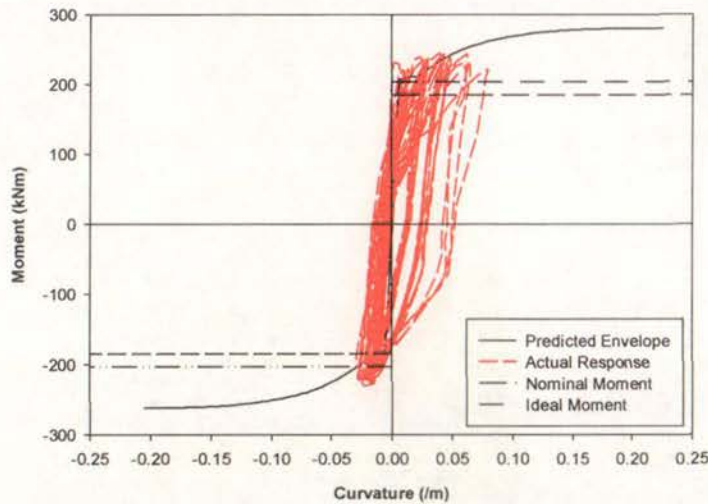


Figure C-27(a) Moment–Curvature Response (Panel 1)

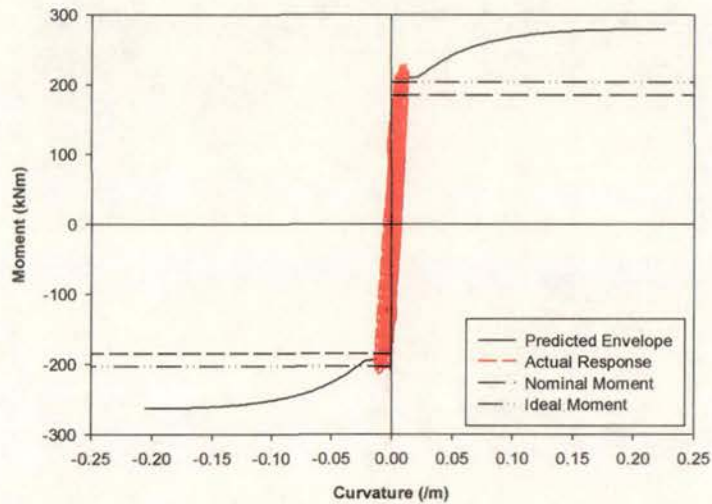


Figure C-27(b) Moment–Curvature Response (Panel 2)

Figure C-27(a) reveals that larger curvatures were recorded in the positive direction than in the negative direction. This is consistent with the non-symmetrical behaviour of the flexural deformations demonstrated in Figure C-25(a). As for testing reported in Section C.1.4 and C.2.4, the beam had a much shorter yield plateau than the predicted response and there was little curvature demand in the third panel.

#### C.4.5 Reinforcement Strains

The average strain in the bottom and top longitudinal reinforcement was plotted for each instrumentation panel. Figures C-28(a), C-28(b), and C-28(c) detail the

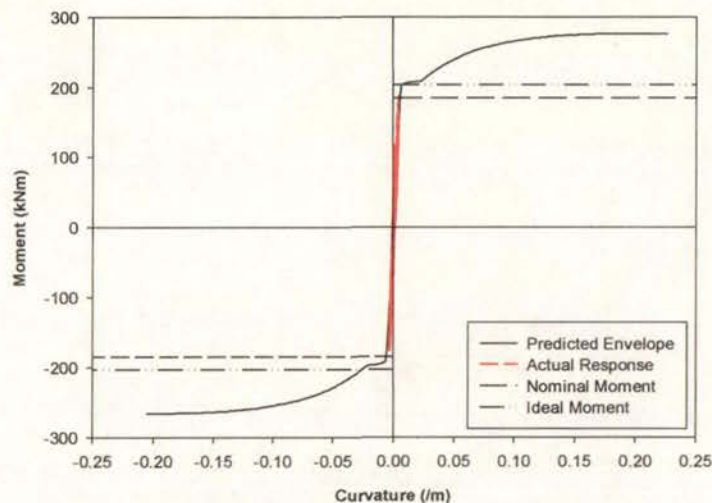


Figure C-27(c) Moment–Curvature Response (Panel 3)

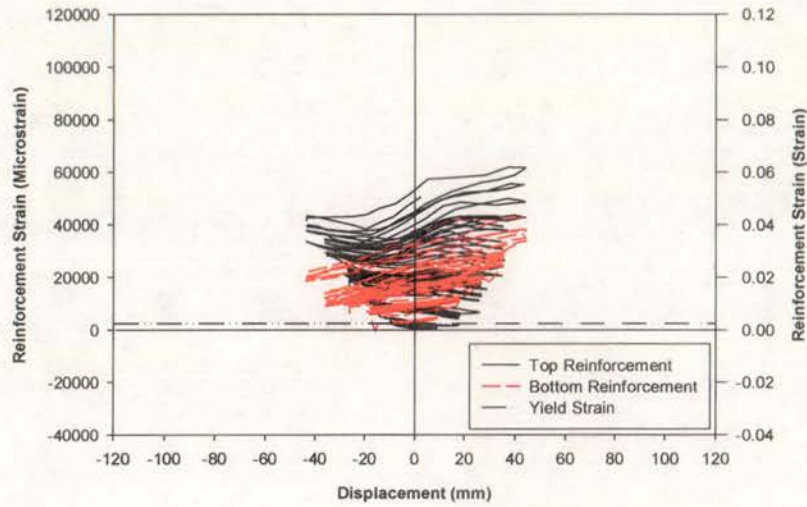


Figure C-28(a) Reinforcement Strains (Panel 1)

reinforcement strains from panel 1, panel 2, and panel 3 respectively.

Figures C-28(a) and Figure C-29(b) reveal that the cracks did not close upon reversal of load from ductility 2 in the first instrumentation panel and from ductility 4 in the second instrumentation panel. This is identical to the response from testing using the New Zealand loading history. The response of the top and bottom reinforcement was non-symmetrical for panel 1 and panel 2. This is consistent with the non-symmetrical behaviour previously noted in Section C.4.2 and C.4.4. Figure C-28c reveals that yielding did not occur in the third instrumentation panel.

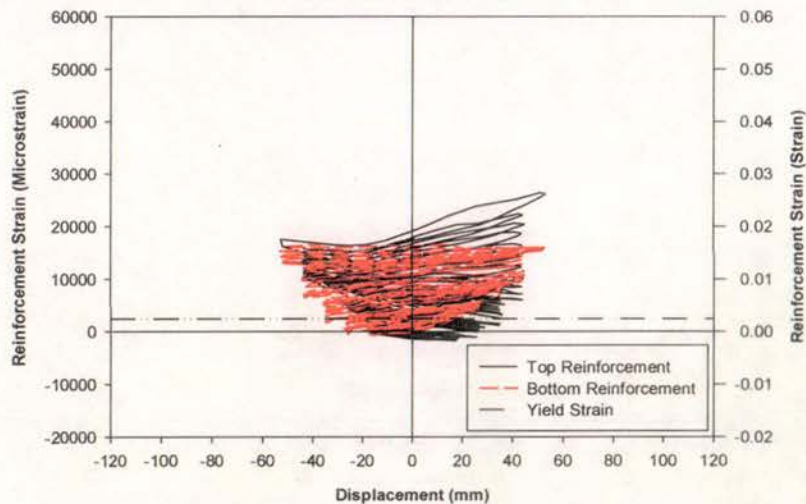


Figure C-28(b) Reinforcement Strains (Panel 2)

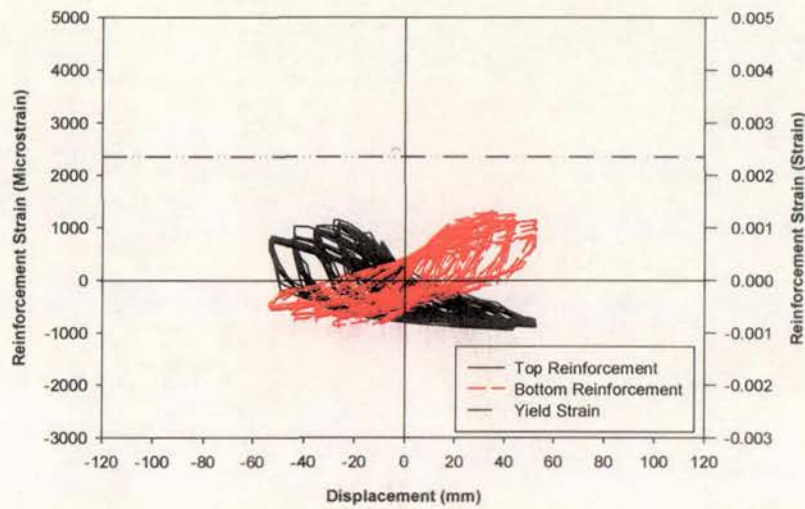


Figure C-28(c) Reinforcement Strains (Panel 3)

#### C.4.6 Beam Elongation

The horizontal elongation at the beam centreline was recorded for the duration of the test. Figure C-29 plots the applied force against the horizontal elongation and reveals a maximum horizontal elongation of 12mm, or 2.0% of the total beam depth. The maximum horizontal elongation from this test is significantly lower than the maximum value from testing using the New Zealand loading history. This difference was because of two reasons: a higher ductility level was applied in the test using the New Zealand loading history and the majority of the horizontal elongation occurs due to flexural deformations. Shear deformations accounted for a much larger percentage

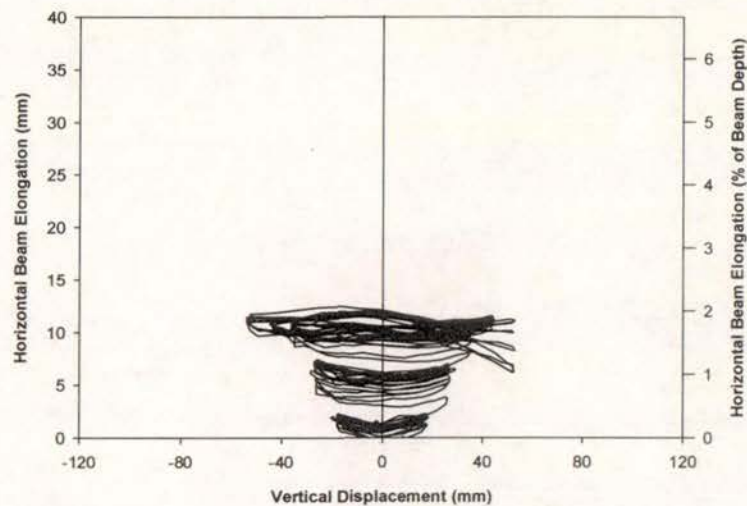


Figure C-29 Horizontal Beam Elongation

of the total displacement in this test, and hence less horizontal elongation occurred.

#### C.4.7 Summary of Test Results

Excellent agreement was obtained between the sum of the three displacement components and the actual displacement for loading in the positive direction. However, poor agreement was recorded for loading in the negative direction.

Shear deformations accounted for a larger percentage of the total vertical displacement than that recorded during testing using the New Zealand loading history. Flexural deformations were non-symmetric and their characteristics differed from conventional response. Shear deformations were also non-symmetric but their shape was consistent with previous experimental studies. There was greater resistance to rocking in the negative direction than in the positive direction. This was due to the concrete pedestal acting in conjunction with the stressing rods to resist rocking of the beam on its base in the negative direction.

There was poor correlation between the predicted yield plateau and the actual yield plateau. However, the maximum strength of the beam was predicted accurately.

Cracks did not close upon reversal of load from ductility 2 from the first instrumentation panel and from ductility 4 from the second instrumentation panel. Reinforcement strains in the first two instrumentation panels were non-symmetric. As for testing using the New Zealand loading history, yielding did not occur in the third instrumentation panel.

A horizontal elongation equal to 2.0% of the total beam depth was recorded for the test. This value was significantly less than the elongation when the New Zealand loading history was applied. This difference was due to the lower ductility level reached in this test and also because shear deformations accounted for a much greater percentage of the vertical displacement.

## C.5 Monotonic Loading

Results from testing where monotonic loading was applied are presented in Sections C.5.1 through C.5.6, with the results outlined in Section C.5.7. Section C.5.1 describes the observed behaviour of the test specimen during testing. Section C.5.2 identifies the separate displacement components that were established from the recorded test data. These results were used in Section C.5.3 to separate the total energy accumulated during the test into the energy associated with the flexural and shear displacement components. Section C.5.4 compares the predicted moment–curvature relationship with the experimental response, and Section C.5.5 details the average strains in the longitudinal reinforcement for the three instrumentation cells. Lastly, Section C.5.6 presents the horizontal elongation of the beam during the test.

### C.5.1 Test Observations

Testing was halted several times during application of the actuator force so that inspections could be carried out at various ductility levels. Loading was applied in the negative direction.

#### **Pre-yield inspections:**

Loading was halted at the theoretical cracking force. One flexural crack was seen on each side although the length of this crack was only 50mm. Testing was also paused at the load corresponding to three-quarters of the predicted nominal design strength based on specified material strengths. Seven flexural cracks showing no shear inclination were located on each side. The displacement at this point was equal to 7.77mm. This is consistent with the displacement observed at this stage in the negative direction during the New Zealand loading history.

#### **Ductility 2:**

Two additional flexural cracks were identified on Side A whereas only one additional flexural crack was located on Side B. Small extensions to existing cracks were noted. These crack extensions began to exhibit shear inclination.

**Ductility 4:**

Two additional flexural cracks were identified on Side B whereas only one additional flexural crack was located on Side A. This resulted in there being an identical number of primary cracks on both sides. Small extensions to cracks outside the plastic hinge zone were identified. These crack extensions were inclined at 45° to the horizontal. Extremely minor spalling was also noted along cracks in the plastic hinge zone on Side B.

**Ductility 6:**

No additional primary cracks or extensions to existing cracks were evident in the beam at this inspection. However, secondary cracking in the plastic hinge zone was apparent. Two small cracks were located in the joint region on Side B. However, as was the case during testing using the New Zealand loading history, these cracks did not open during the test. Minor spalling along cracks in the plastic hinge zone was also visible. Spalling at this stage of the test was consistent with the behaviour observed when testing using the New Zealand loading history.

**Ductility 8:**

Further extensions to existing cracks were identified at this load point. This was the last additional cracking that occurred in the test with the dominant behaviour becoming expansion of the crack widths of existing cracks after this point. This is consistent with the behaviour observed when testing using the New Zealand loading history. No further spalling was identified although crushing of concrete in the compression zone was noted.

**Ductility 10:**

Crushing of concrete in the compression zone led to minor spalling of cover concrete. No further spalling from the cracks in the plastic hinge zone was evident.

**High-ductility inspections:**

Minor spalling in the compression zone but no further spalling along cracks in the plastic hinge zone was observed during inspections at ductility 12, 14, and 16. Significant spalling of concrete in the compression zone was noted during the inspection at ductility 18 although the longitudinal reinforcement was still not visible. The width of cracks in the plastic hinge zone continued to widen. Figure C-30 reveals the extent of the cracking at ductility 20. At displacement ductility of approximately 22, the limiting stroke of the jack was reached. However, the strength of the test subassemblage had begun to drop by that point and extrapolation of the force-displacement response gave an ultimate ductility equal to 23.

**C.5.2 Displacement Components**

Figure C-31 illustrates the separation of the vertical displacement into its three components. In contrast to other tests, shear deformations accounted for only a small percentage of the total vertical displacement. Results from other tests have shown that the percentage of the total displacement relating to shear deformations increases as the level of degradation increases. Small shear deformations were recorded for this test because only minor degradation had occurred up to and including loading to ductility 8. Figure C-31 reveals that there was excellent agreement between the total displacement and the sum of the three components for the recorded phase of the test.

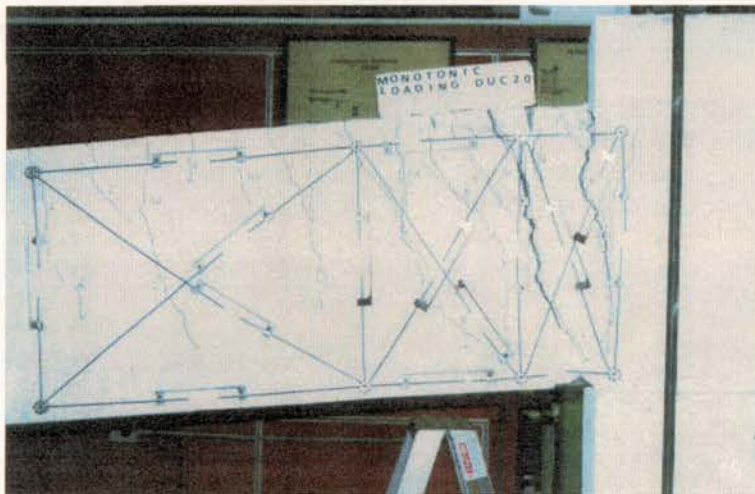


Figure C-30 Test Subassemblage Condition at Ductility 20

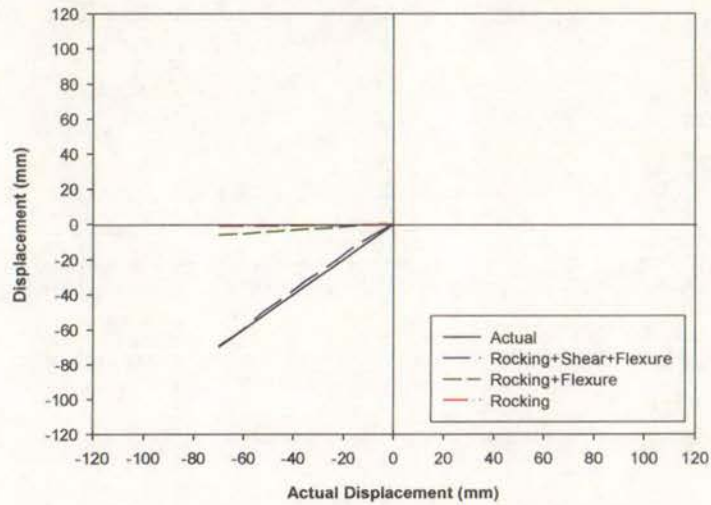


Figure C-31 Components of Displacement

Figures C-32(a), C-32(b), and C-32(c) present the flexural, shear, and rocking displacement components for loading up to and including ductility 8. The three figures show that each displacement component followed a bilinear path. This behaviour was as expected for the flexural and shear deformations. Initially it was thought that the rocking deformation characteristics were in contrast to rocking deformations characteristics recorded during cyclic tests. However, loading the test subassembly monotonically did not allow a reduction in stiffness that was present during cyclic tests. Therefore, although the rocking deformation response from monotonic loading appears to be different to that under cyclic loading, the secant

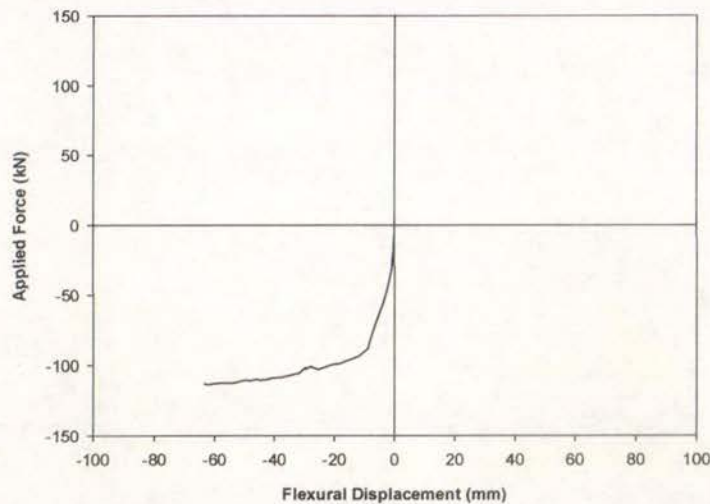


Figure C-32(a) Flexural Displacement Component

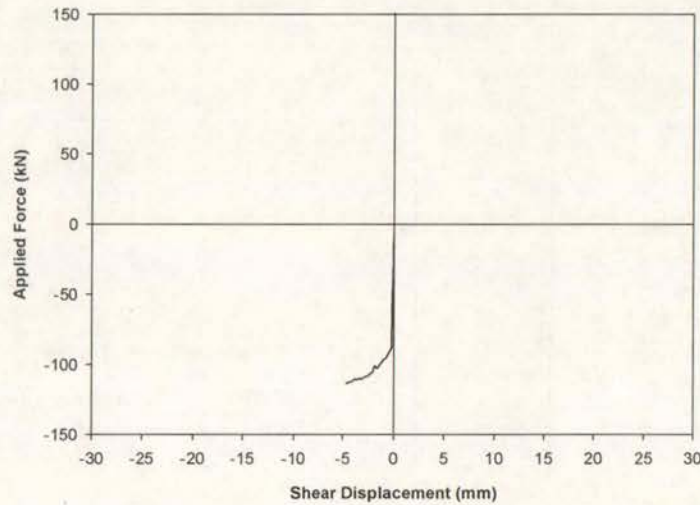


Figure C-32(b) Shear Displacement Component

stiffness at ductility 8 was similar to that recorded in cyclic tests.

### C.5.3 Energy Components

Figure C-33 illustrates the amount of energy expended through flexure and shear deformations and demonstrates that the flexural deformations accounted for the vast majority of the total energy expended. This is consistent with the behaviour noted for previously reported tests. Again there was excellent agreement between the sum of the two components and the total amount of energy absorbed.

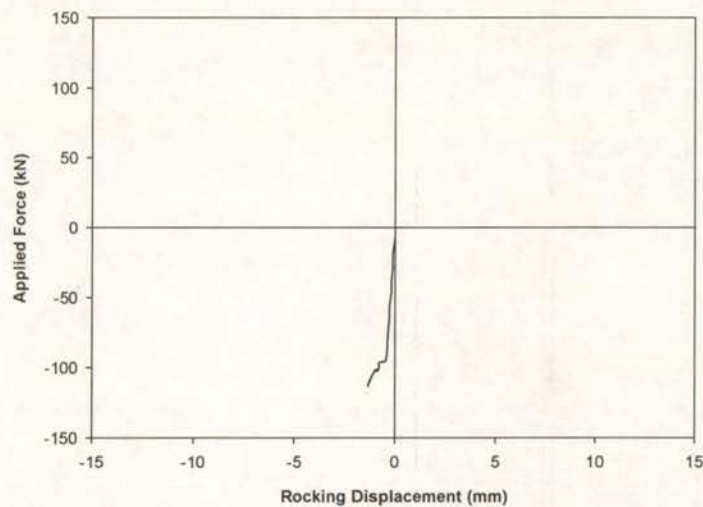


Figure C-32(c) Rocking Displacement Component

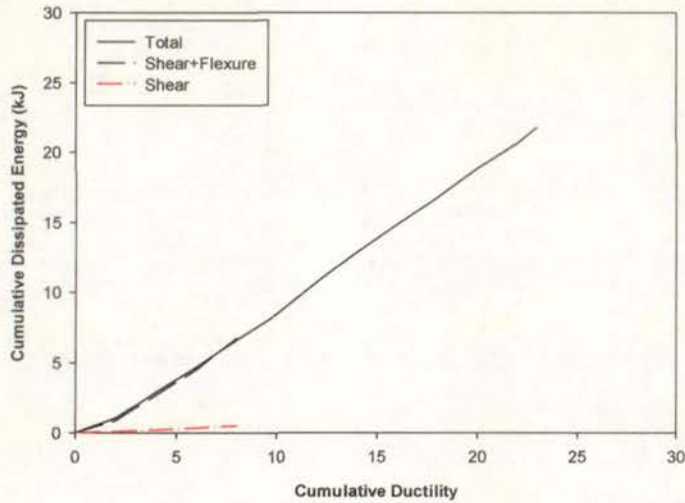


Figure C-33 Components of Energy Dissipation

### C.5.4 Moment–Curvature Response

The moment–curvature response from the first, second, and third instrumentation panels is presented in Figures C-34(a) through C-34(c).

Figure C-34(a) and C-34(b) reveal that the yield plateau recorded experimentally was comparable to the predicted response. This indicates that applying cyclic loading histories was the cause of the longitudinal steel departing from the monotonic stress–strain curve. Figure C-34(c) demonstrates that there was little curvature demand in the third panel. This is consistent with the trends seen in the moment–curvature

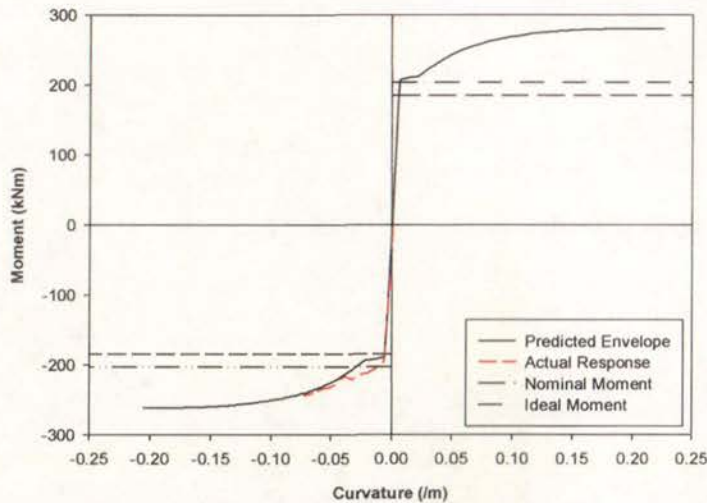


Figure C-34(a) Moment–Curvature Response (Panel 1)

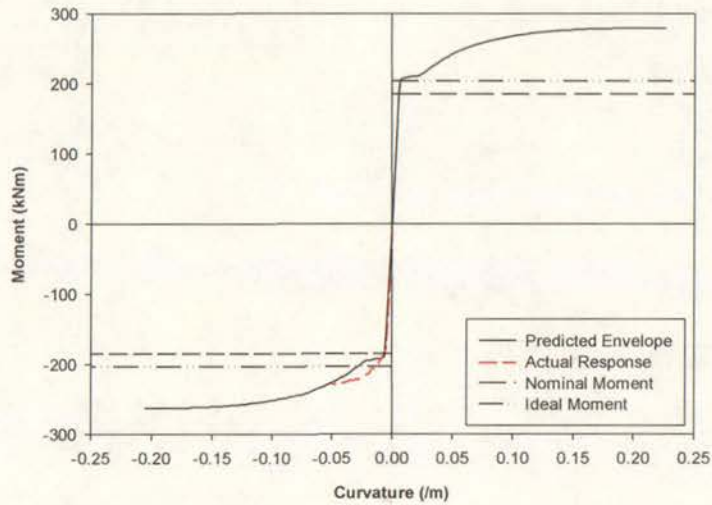


Figure C-34(b) Moment–Curvature Response (Panel 2)

response from previously reported tests.

#### C.5.5 Reinforcement Strains

Figure C-35(a) through C-35(c) plot the average strain in the bottom and top longitudinal reinforcement against the total vertical displacement for each instrumentation panel.

Significantly lower reinforcement strains were recorded from this test than for testing using the New Zealand loading history. This partially accounted for the significantly larger ultimate displacement recorded in this test compared to the ultimate

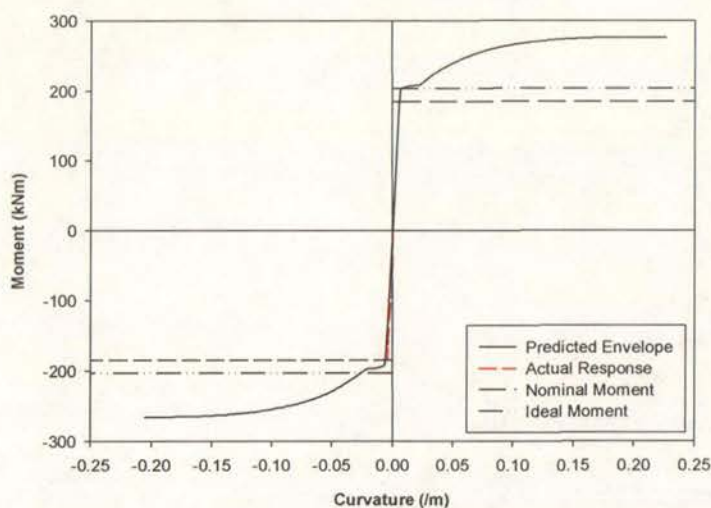


Figure C-34(c) Moment–Curvature Response (Panel 3)

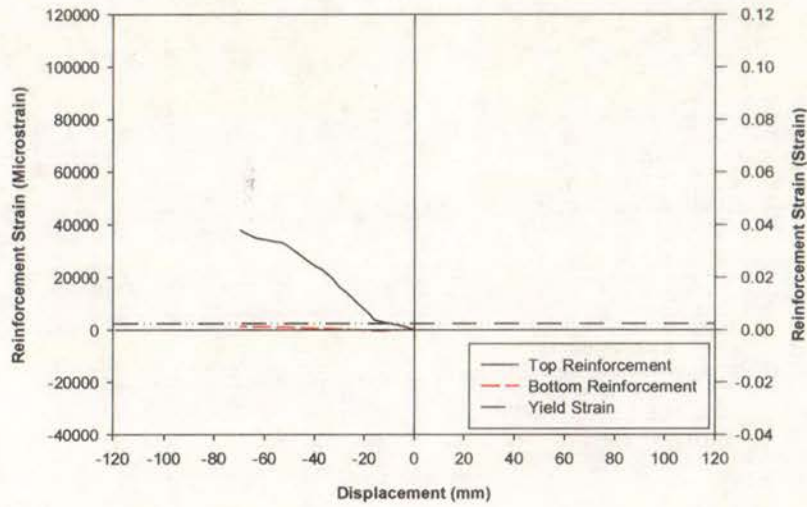


Figure C-35(a) Reinforcement Strains (Panel 1)

displacement from testing which applied the New Zealand loading history. Figure C-35(c) reveals that yielding had not occurred in the third instrumentation panel by ductility 8.

#### C.5.6 Beam Elongation

The horizontal elongation at the beam centreline was recorded for the loading stages up to and including ductility 8. Figure C-36 plots the applied force against the horizontal elongation and reveals a maximum horizontal elongation of 15mm, which is equal to 2.5% of the total beam depth. This value is significantly lower than the

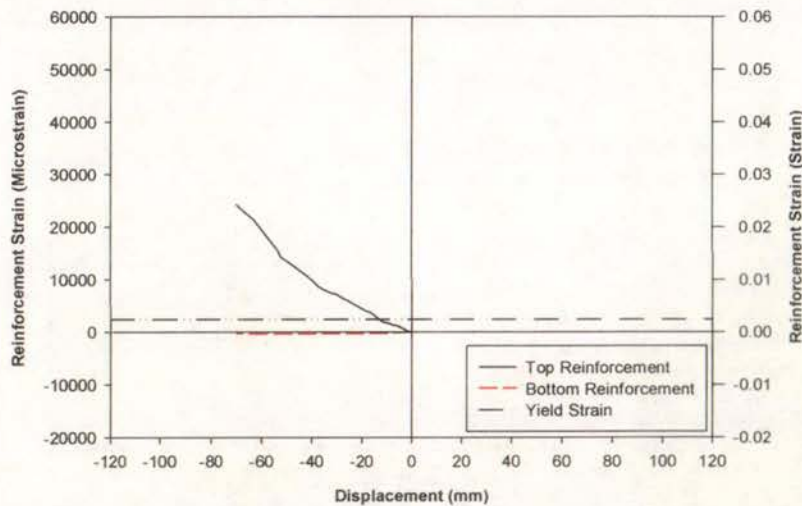


Figure C-35(b) Reinforcement Strains (Panel 2)

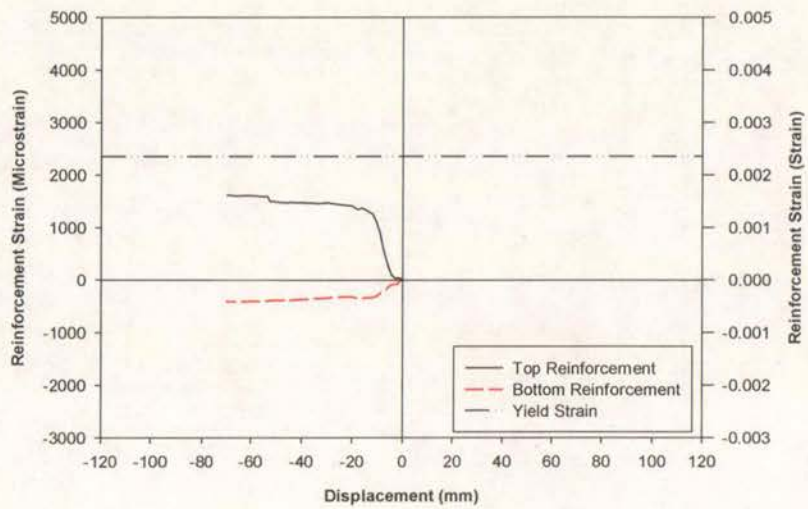


Figure C-35(c) Reinforcement Strains (Panel 3)

elongation that occurred when testing was carried out using the New Zealand loading history. This is consistent with the comparison of the reinforcement strains discussed in the previous section.

#### C.5.7 Summary of Test Results

Excellent agreement was obtained between the sum of the three displacement components and the actual displacement for loading up to ductility 8.

Shear deformations accounted for a low percentage of the total vertical displacement compared to that recorded during testing using the New Zealand loading history. All

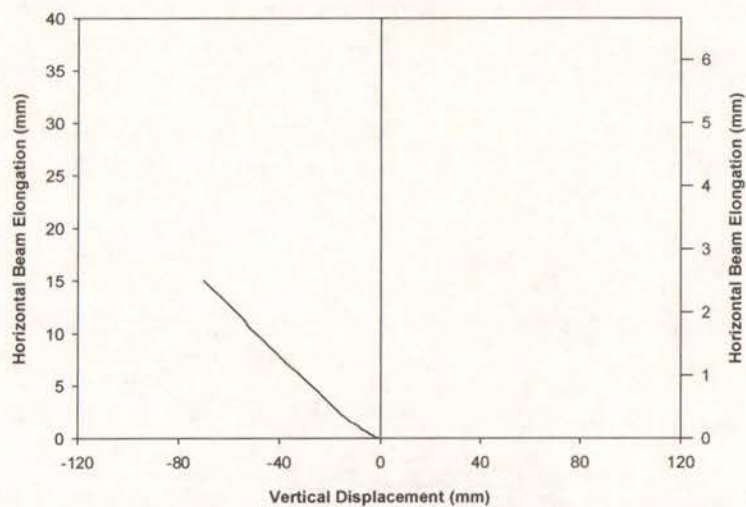


Figure C-36 Horizontal Beam Elongation

three displacement components followed bilinear behaviour.

The yield plateau recorded experimentally was comparable to the predicted yield plateau. As for previously reported tests, the maximum strength of the beam was predicted accurately.

Reinforcement strains measured in the first instrumentation panel were significantly lower than the strains measured at the corresponding ductility from testing using the New Zealand loading history. Yielding did not occur in the third instrumentation panel.

A horizontal elongation equal to 2.5% of the total beam depth was recorded for loading up to and including ductility 8. This was significantly lower than the horizontal elongation resulting from testing that implemented the New Zealand loading history.

## C.6 Bi-directional Cycling at Ductility 8

Results from testing where bi-directional cycling to ductility 8 was applied are presented in Sections C.6.1 through C.6.6. Section C.6.7 encapsulates the main points from the test. Section C.6.1 describes the observed behaviour of the test specimen during testing. Section C.6.2 separates the vertical displacement into the separate displacement components that were established from the experimental data. These components were used in Section C.6.3 to separate the total energy accumulated during the test into the energy associated with the flexural and shear displacement components. Section C.6.4 compares the predicted moment–curvature relationship with the experimental moment–curvature relationship, and Section C.6.5 presents the average strains in the longitudinal reinforcement for the three instrumentation cells. Lastly, Section C.6.6 details the horizontal elongation of the beam during the test.

### C.6.1 Test Observations

During the first half-cycle to ductility 8 in each direction, testing was halted at several ductility values to permit an inspection of the test specimen to take place. This enabled comparisons to be made between the observed data from this test and the observed data from other cyclic tests.

#### Cycle 1:

The first inspection point was at the ductility 2 displacement. Six flexural cracks were visible on each side of the beam. Some of the cracks were beginning to show shear inclination and secondary cracking was also apparent. The second inspection point was at the ductility 4 displacement. No new cracks were identified although there were small extensions to existing cracks. The third inspection point was at the ductility 6 displacement. Crushing and minor spalling of cover concrete in the compression zone was evident. Again there were minor extensions to existing cracks. The test subassembly was then loaded to its ductility 8 displacement. No additional cracks were observed at this point. Minor spalling from the compression zone was apparent.

Inspections were made at the same ductility levels in the negative direction as for loading in the positive direction. At ductility 2, concrete was removed from the compression zone of the previous cycle. Six flexural cracks were seen on each side with some of the cracks showing shear inclination. Secondary cracking in the plastic hinge zone was the only additional cracking identified during the inspection at ductility 4. Small crack extensions were visible during the inspection made at ductility 6. Extremely minor crushing of concrete in the compression zone and spalling along cracks in the plastic hinge zone was also evident. Further crushing of concrete in the compression zone and secondary cracking was apparent during the inspection at ductility 8.

**Cycle 2:**

Several large pieces of concrete were removed from the top and bottom of the beam during the second cycle to ductility 8, such that the longitudinal reinforcement was visible. Further spalling of cover concrete along cracks in the plastic hinge zone also occurred.

**Cycle 3:**

Pinching was observed in the force-displacement response during the third cycle to ductility 8. However, no loss of strength was noted. Spalling of cover concrete from the compression zone and from along cracks in the plastic hinge zone continued to occur.

**Cycle 4:**

Pinching in the force-displacement response became even more prevalent during this cycle. This resulted in a 10% loss of strength. Spalling of cover concrete from the compression zone and from along cracks in the plastic hinge zone continued to occur.

**Cycle 5:**

Further pinching in the force-displacement response was observed during this cycle. This resulted in a 20% loss of strength, which was right on the failure criterion. Spalling of cover concrete from the compression zone and from along cracks in the plastic hinge zone was also apparent.

**Cycle 6:**

The force in this cycle dropped below 80% of the maximum-recorded strength during the test. Figure C-37 illustrates the physical degradation that had taken place during the test. The test was terminated at this point.

**C.6.2 Displacement Components**

Figure C-38 illustrates the separation of the vertical displacement into its three components and shows that shear deformations accounted for only a small percentage of the total vertical displacement. However, this was due to the envelope curve that Figure C-38 was based on being from the first cycle to ductility 8. It was expected that the shear deformations would increase during the test. This is confirmed in Figures C-39(a) and C-39(b), which plot the applied force against the flexural and shear deformations for the entire test. While the flexural displacements decrease as more cycles are applied, the magnitude of the shear deformations increases. Figure C-



Figure C-37 Test Subassembly Condition at Ductility 8 (Cycle 6)

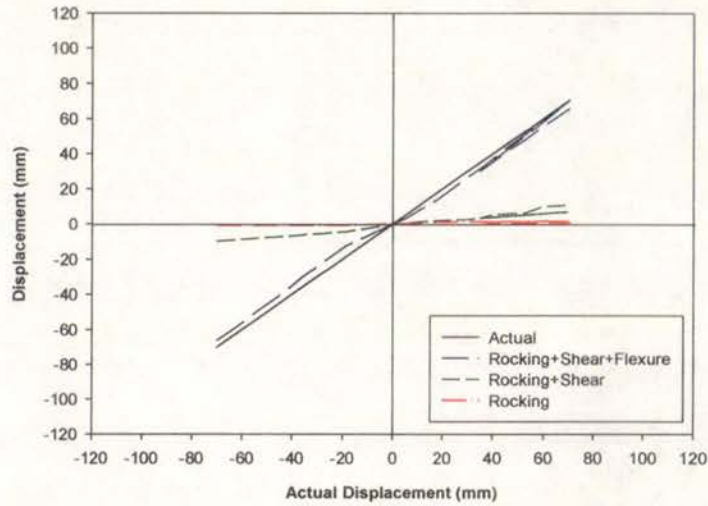


Figure C-38 Components of Displacement

38 reveals that there was excellent agreement during the first cycle to ductility 8.

Figures C-39(a) and C-39(b) demonstrate that the flexural deformations were symmetric and consistent with normal behaviour. The shear deformations are non-symmetric although the shape of the hysteresis curve was as expected. Figure C-39(c) displays the rocking deformations for the test and reveals that the rocking displacements were consistent with behaviour measured from testing using the PRESSS loading history and the loading history from the Public Works Research Institute.

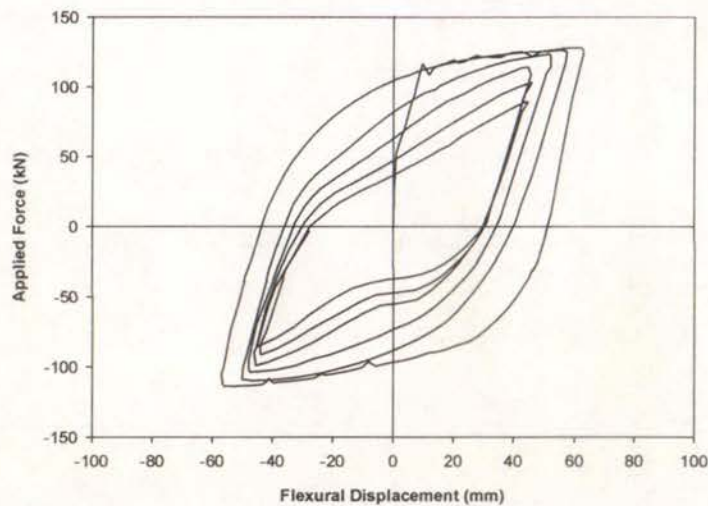


Figure C-39(a) Flexural Displacement Component

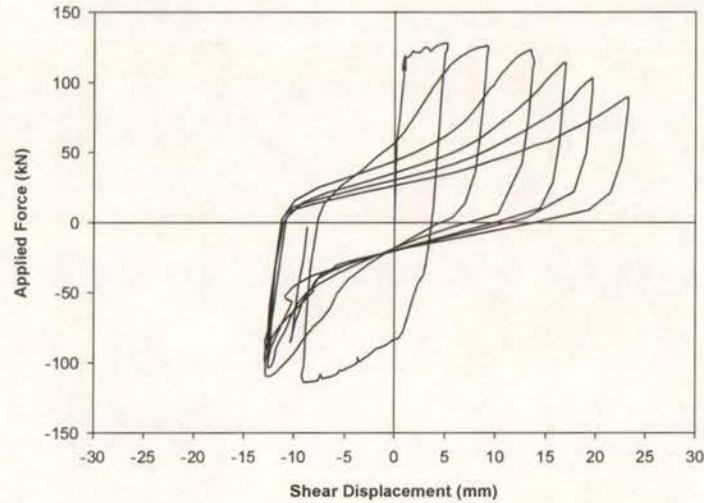


Figure C-39(b) Shear Displacement Component

### C.6.3 Energy Components

Figure C-40 illustrates the amount of energy dissipated through flexure and shear deformations. Figure C-40 demonstrates that, as with other tests, the flexural deformations accounted for the vast majority of the total energy dissipated. Figure C-40 also reveals that there was reasonable agreement between the sum of the two components and the total amount of energy dissipated for the test duration.

### C.6.4 Moment–Curvature Response

Figures C-41(a) through C-41(c) present the moment–curvature response from panel

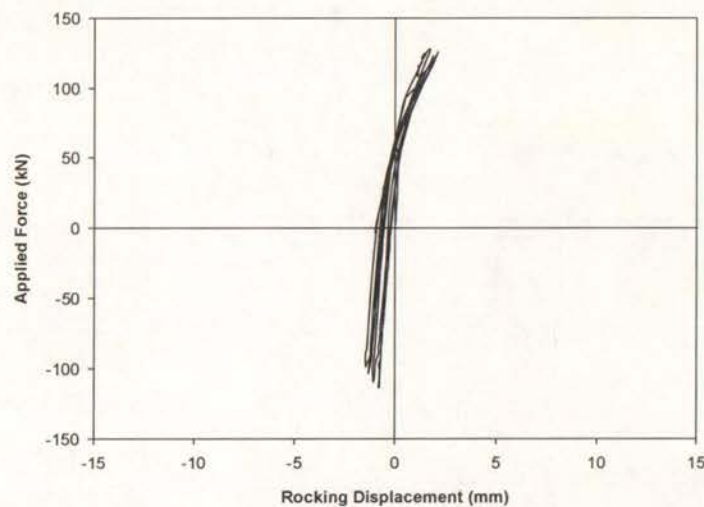


Figure C-39(c) Rocking Displacement Component

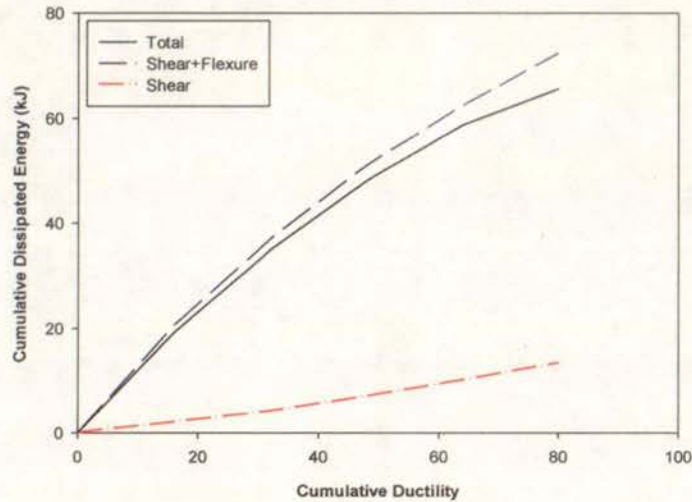


Figure C-40 Components of Energy Dissipation

1, panel 2, and panel 3 respectively.

The moment–curvature response from testing where direct cycling at ductility 8 was applied followed the trends seen in the moment–curvature response from the New Zealand loading history: The beam had a much shorter yield plateau than the predicted response and there was little curvature demand in the third panel. Figure C-41(a) illustrates that the moment–curvature response was symmetric, and this was consistent with the behaviour of the flexural deformations described in Section C.6.2.

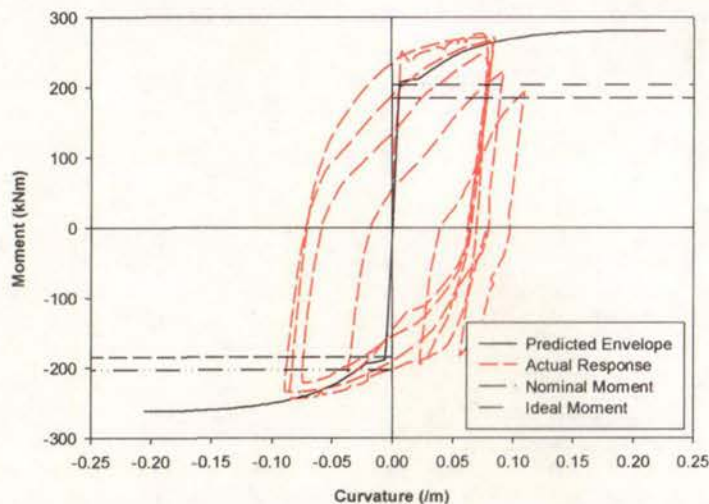


Figure C-41(a) Moment–Curvature Response (Panel 1)

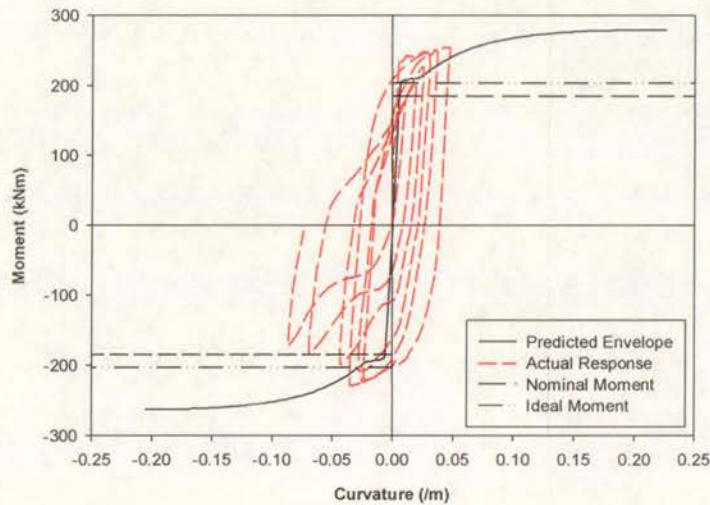


Figure C-41(b) Moment–Curvature Response (Panel 2)

### C.6.5 Reinforcement Strains

The average strain in the bottom and top longitudinal reinforcement was calculated for each instrumentation panel with the reinforcement strains from panel 1, panel 2, and panel 3 plotted in Figures C-42(a), C-42(b), and C-42(c) respectively.

The response of the top and bottom reinforcement was symmetrical for all three panels. As expected, cracks that formed in the first two instrumentation panels did not close under reversal of load. Figure C-42(c) reveals that yielding did not occur in the third instrumentation panel.

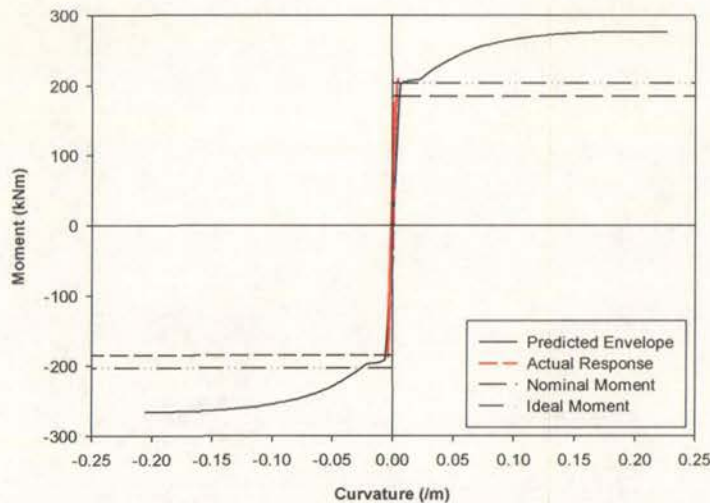


Figure C-41(c) Moment–Curvature Response (Panel 3)

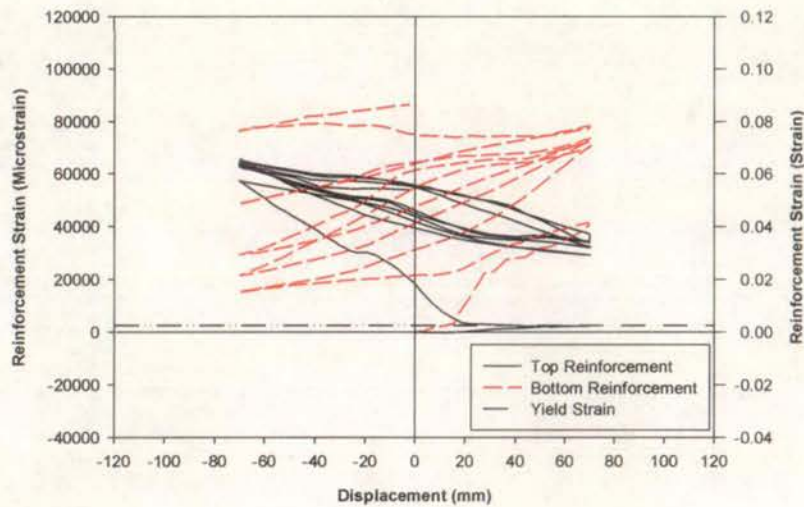


Figure C-42(a) Reinforcement Strains (Panel 1)

### C.6.6 Beam Elongation

The horizontal elongation at the beam centreline was recorded for the duration of the test. Figure C-43 graphs the applied force versus the horizontal elongation and reveals a maximum horizontal elongation of 32mm, which is equal to 5.33% of the total beam depth.

Figure C-43 reveals that the vast majority of the horizontal elongation occurred in the first three half-cycles. Afterwards, the horizontal elongation cycled about the same point. This was due to the large loss of stiffness due to the large displacements that

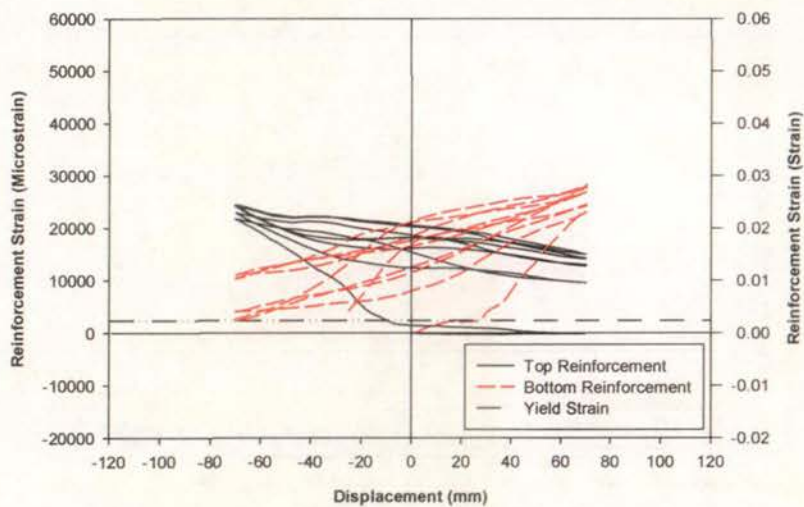


Figure C-42(b) Reinforcement Strains (Panel 2)

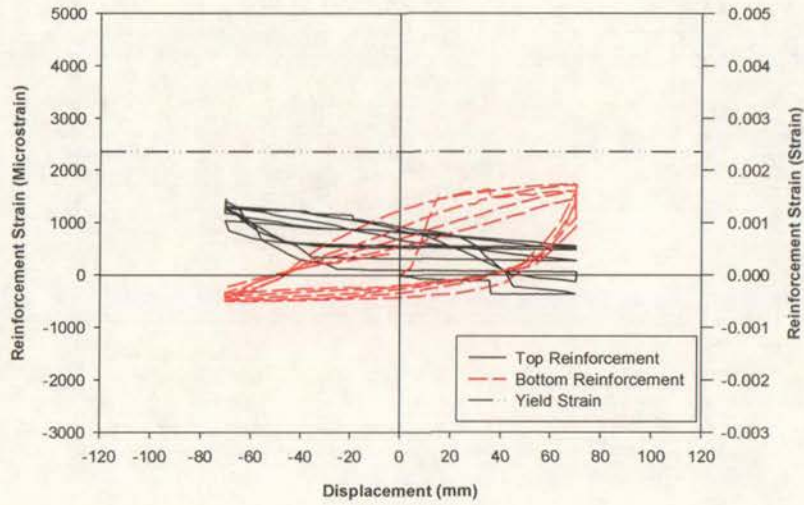


Figure C-42(c) Reinforcement Strains (Panel 3)

were applied early in the test. Cycling of the horizontal elongation about a common point is consistent with the large shear deformations and pinching in the hysteresis loops that were evident in this test.

#### C.6.7 Summary of Test Results

Excellent agreement was obtained between the sum of the three displacement components and the actual displacement in both loading directions for the first cycle to ductility 8.

Shear deformation increased and flexural deformation decreased as degradation of the

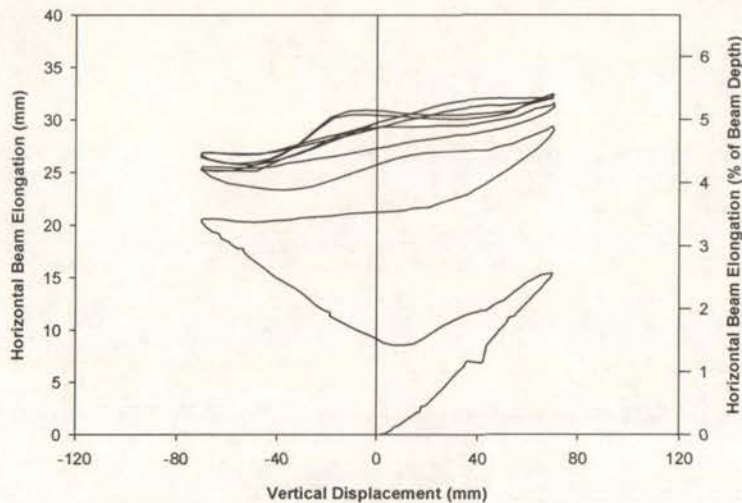


Figure C-43 Horizontal Beam Elongation

test subassemblage progressed. Flexural deformations were symmetric and were consistent with conventional behaviour. Shear deformations were non-symmetric but the hysteresis response was as expected. The characteristics of the rocking deformations were consistent with the behaviour established from testing using the PRESSS loading history and using the loading history from the Public Works Research Institute.

Extremely poor correlation was obtained between the predicted yield plateau of the moment–curvature response and the actual yield plateau. However, the maximum strength of the beam was predicted accurately.

Comparable reinforcement strains measured all three instrumentation panels for loading in the positive and negative direction. Cracks in the first two instrumentation panels did not close under reversal of load, and yielding did not occur in the third instrumentation panel.

A total horizontal elongation equal to 5.33% of the total beam depth was recorded for the duration of the test, although the vast majority of this was recorded during the first three half-cycles.

## C.7 Unidirectional Cycling

Results from testing conducted using the New Zealand loading history in a single direction are presented in Sections C.7.1 through C.7.6, with Section C.7.7 summarising the results. Section C.7.1 describes the observed behaviour of the test specimen during testing. Section C.7.2 presents separate displacement components that were calculated from the experimental data. Section C.7.3 details the separation of the total energy disbursed during the test into the energy disbursed through the flexure and shear displacement components. Section C.7.4 compares the predicted moment—curvature relationship with the experimental moment—curvature relationship, and Section C.7.5 details the average strains in the longitudinal reinforcement for the three instrumentation cells. Lastly, Section C.7.6 reports on the horizontal elongation of the beam during the test.

### C.7.1 Test Observations

The New Zealand loading history was applied in a single direction to determine the effects of unidirectional loading. Section C.7.1.1 details the force-controlled phase of the test whereas Section C.7.1.2 describes the behaviour of the test specimen from the displacement-controlled phase.

#### C.7.1.1 Force Control

The initial stages of the test were carried out under force control. An actuator force of 64.5kN was applied in the positive direction. This is equal to three-quarters of the predicted nominal design strength based on specified material strengths. During the application of this force, testing was paused at the theoretical cracking force (calculated using actual material values) so that an inspection could be carried out. No cracks were observed at this stage. An inspection was carried out upon completion of the applied force to  $0.75F_n$ . The displacement at this point was 5.83mm. This was identical to the value recorded at the corresponding point when testing using the New Zealand loading history. Six flexural cracks with no shear inclination were seen on each side.

### C.7.1.2 Displacement Control

The displacement-controlled loading steps followed the procedures outlined in Section 6.4.3.

#### **Ductility 2:**

Four new flexural cracks were identified after the first cycle to ductility 2. Extensions were also observed to cracks that formed in the force-controlled section of the test. These extensions were inclined at approximately  $45^\circ$  to the horizontal. No additional cracking was observed during the second cycle to ductility 2.

#### **Ductility 4:**

Further cracking in the plastic hinge zone was observed after the first cycle to ductility 4. There were also a couple of minor extensions to cracks outside the instrumentation zone. No distress in the compression zone was evident at this load step. No additional cracking was observed after the second cycle at ductility 4.

#### **Ductility 6:**

Extensions to existing cracks were identified after the first cycle. These extensions were inclined at  $45^\circ$  to the horizontal. Crushing of concrete in the compression zone was also apparent. As with previous ductility levels, no additional cracking was visible after the second cycle.

#### **Ductility 8:**

Secondary cracking in the plastic hinge zone was the only additional cracking observed at this ductility level. Crushing of cover concrete in the compression zone continued and minor spalling occurred as a result. The behaviour observed after the second cycle at ductility 8 was identical to the behaviour observed after the first cycle.

**Ductility 10:**

Further crushing of concrete in the compression zone and spalling along cracks in the plastic hinge zone was evident after the two cycles to ductility 10. Secondary cracking in the plastic hinge zone was the only additional cracking identified at this load step.

**High Ductility Cycles:**

The behaviour observed during the high ductility cycles was consistent with that observed after the two cycles at ductility 10. At ductility 18, several large pieces of concrete fell out from the tension zone of the beam, such that the longitudinal reinforcement became visible. An extremely large piece of concrete was removed from the top of the beam after the first cycle to ductility 22. Figure C-44 illustrates that there was no cover concrete for a length of approximately 700mm on Side B after this event.

A longitudinal bar ruptured while the test subassembly was being loaded to ductility 24. This resulted in the strength of the test subassembly dropping below 80% of the maximum-recorded strength, and hence, the test was terminated at this point.

**C.7.2 Displacement Components**

Figure C-45 illustrates the separation of the vertical displacement into its three



Figure C-44 Spalling of Cover Concrete (Ductility 22)

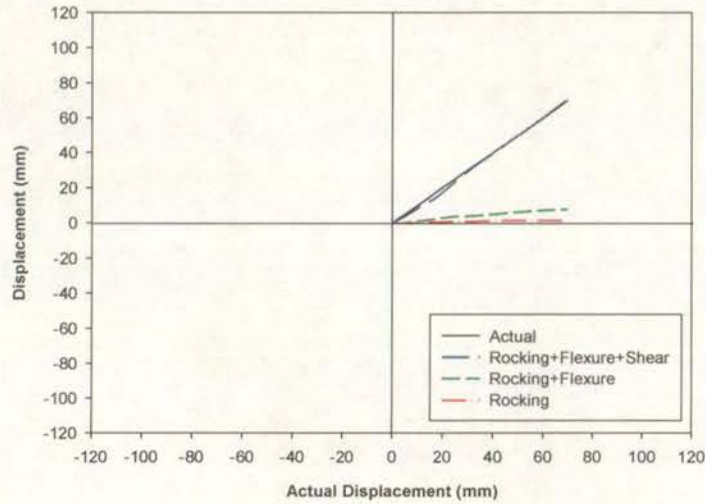


Figure C-45 Components of Displacement

components and reveals that shear deformations accounted for only a small percentage of the total vertical displacement. This was comparable to the results developed from testing using monotonic loading, and again was due to the low amount of degradation that had occurred during loading up to and including ductility 8. Figure C-45 reveals that there was excellent agreement during the recorded phase of the test.

Figures C-46(a), C-46(b), and C-46(c) detail the flexural, shear, and rocking displacement components for loading up to and including ductility 8. These three figures show that the envelope of all three displacement components follow a bilinear

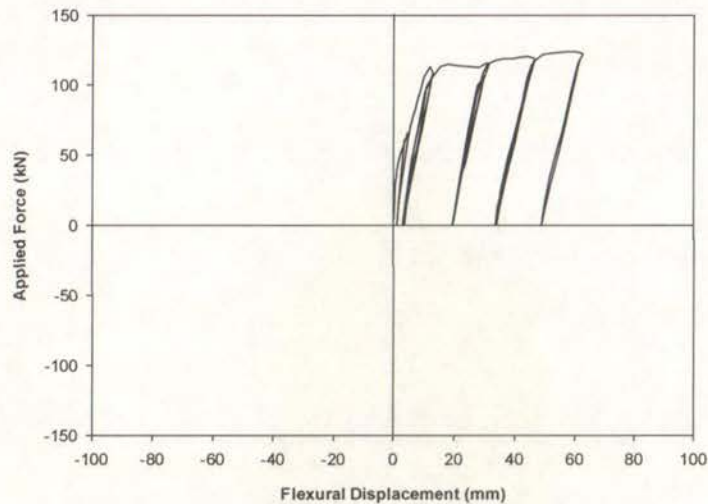


Figure C-46(a) Flexural Displacement Component

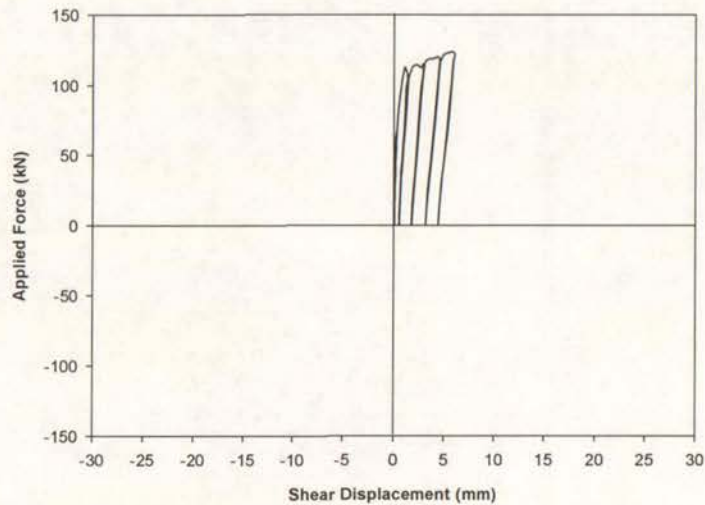


Figure C-46(b) Shear Displacement Component

path. This behaviour is consistent with the behaviour observed from testing where monotonic loading was applied.

### C.7.3 Energy Components

Figure C-47 exhibits the amount of energy disbursed through flexure and shear deformations and demonstrates that the flexural deformations accounted for the vast majority of the total energy disbursed. Figure C-47 reveals that there was reasonable agreement between the sum of the two components and the total amount of energy disbursed.

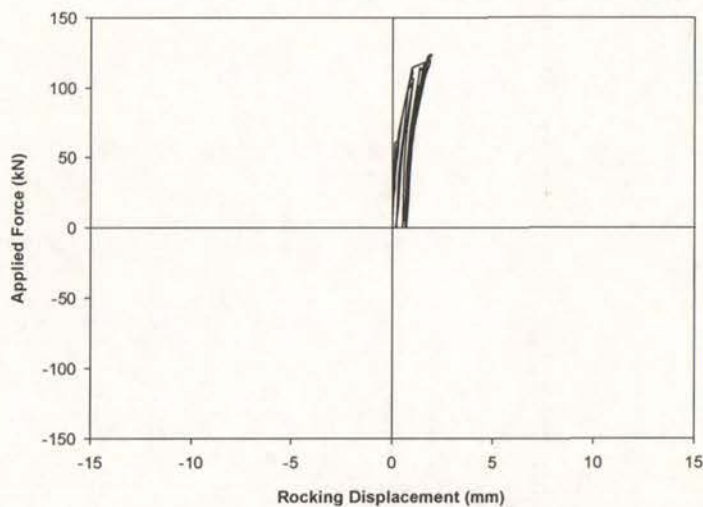


Figure C-46(c) Rocking Displacement Component

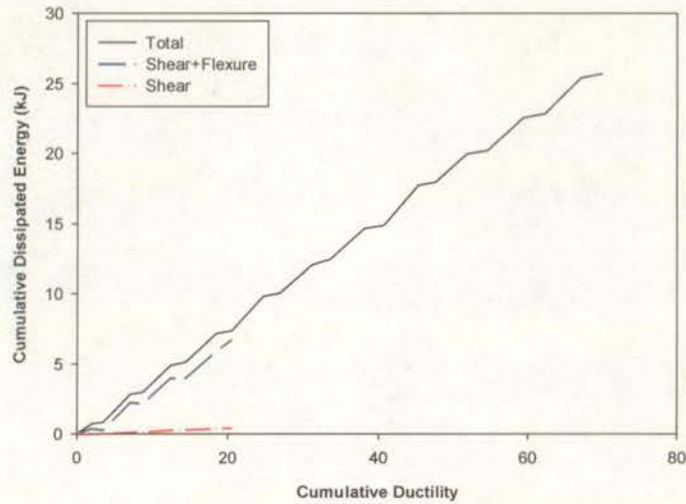


Figure C-47 Components of Energy Dissipation

#### C.7.4 Moment–Curvature Response

Figures C-48(a) through C-48(c) illustrate the moment–curvature response from panel 1, panel 2, and panel 3. The moment–curvature response from unidirectional cycling followed the trends seen in the moment–curvature response from the New Zealand loading history. Extremely poor response is seen in Figure C-48(a) and C-48(b), which depicts the data from the first two instrumentation panels. Figure C-48(c) reveals, that as usual, there was little curvature demand in the third panel.

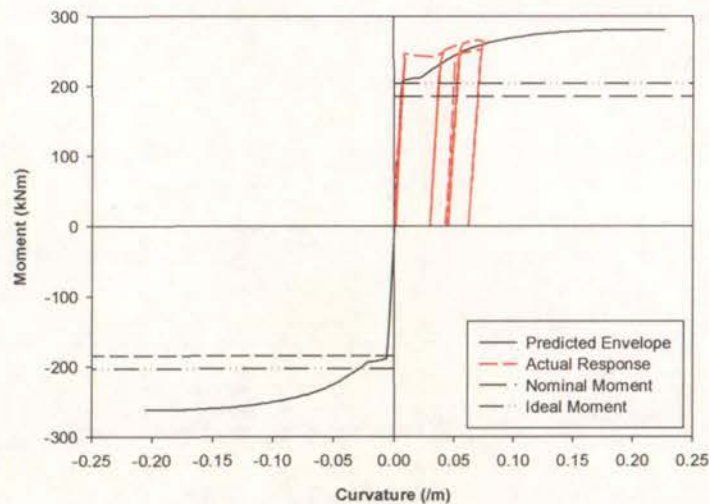


Figure C-48(a) Moment–Curvature Response (Panel 1)

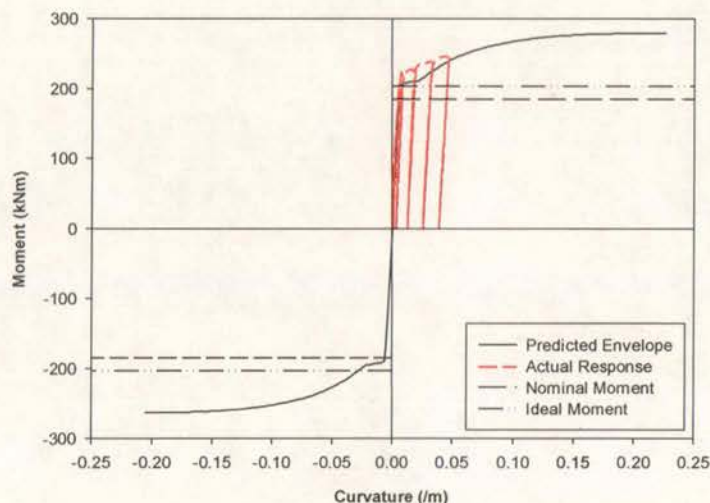


Figure C-48(b) Moment–Curvature Response (Panel 2)

### C.7.5 Reinforcement Strains

The average strain in the bottom and top longitudinal reinforcement was plotted for each instrumentation panel. Figures C-49(a) through C-49(c) detail the reinforcement strains from panel 1, panel 2, and panel 3.

The reinforcement strains from the first two instrumentation panels were significantly lower than the strains recorded during testing using the New Zealand loading history. This behaviour is consistent with the strains recorded when monotonic loading was applied. The low reinforcement strains partially account for the significantly larger

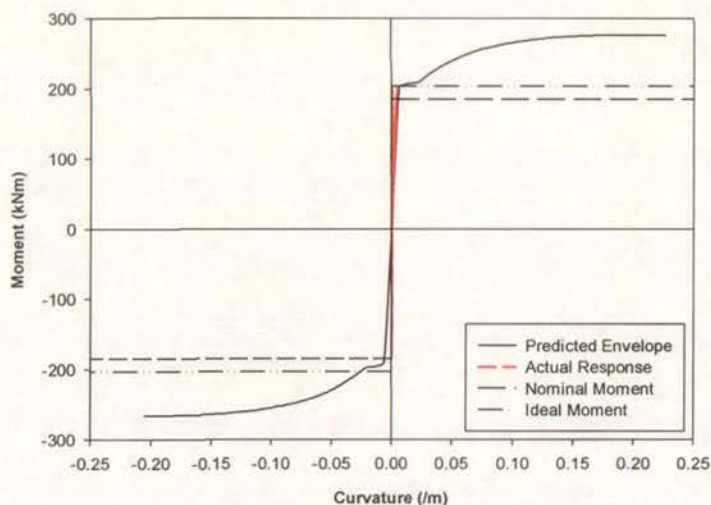


Figure C-48(c) Moment–Curvature Response (Panel 3)

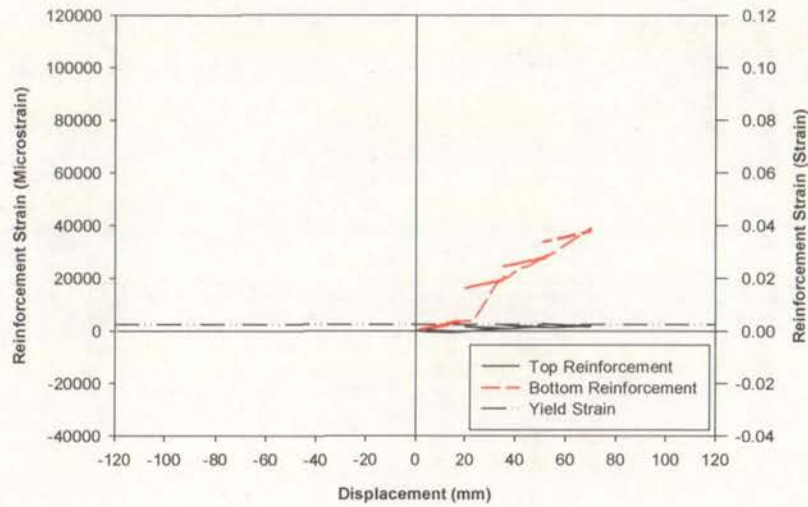


Figure C-49(a) Reinforcement Strains (Panel 1)

ultimate displacement that was reached in this test, compared to the ultimate displacement when the New Zealand loading history was applied. From Figure C-49(c), it was established that the longitudinal reinforcement in panel 3 did not yield.

#### C.7.6 Beam Elongation

The horizontal elongation at the beam centreline was recorded for the loading stages up to and including ductility 8. Figure C-50 displays the horizontal elongation and reveals a maximum horizontal elongation of 15mm, or 2.5% of the total beam depth. This value is consistent with horizontal elongation recorded for tests where little

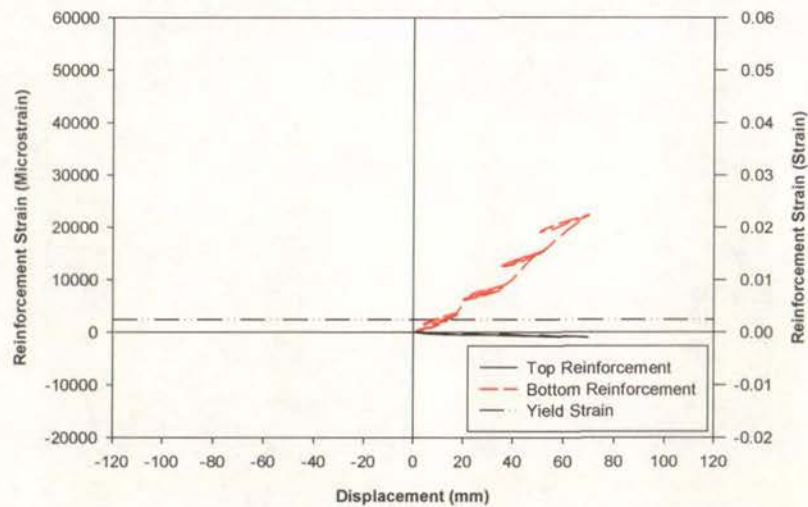


Figure C-49(b) Reinforcement Strains (Panel 2)

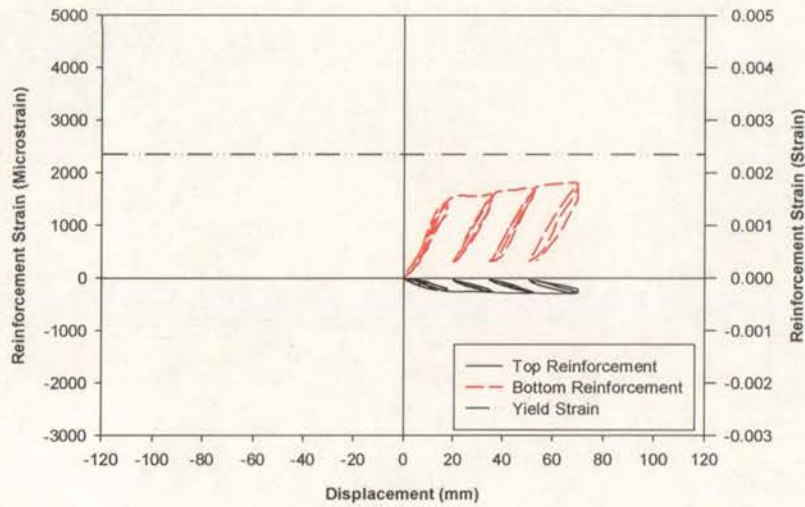


Figure C-49(c) Reinforcement Strains (Panel 3)

physical degradation had taken place during loading up to and including ductility 8.

### C.7.7 Summary of Test Results

Excellent agreement was obtained between the sum of the three displacement components and the actual displacement for loading up to ductility 8.

Shear deformations accounted for a low percentage of the total vertical displacement compared to that recorded during testing using the New Zealand loading history. All envelopes of the three displacement components followed bilinear behaviour.

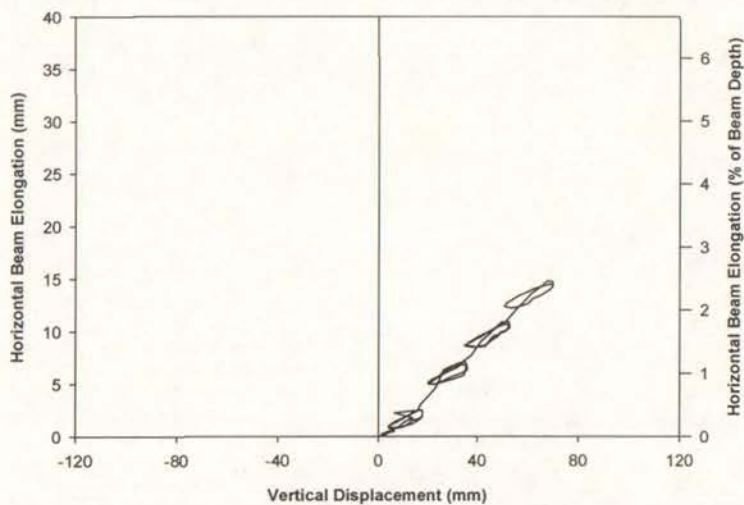


Figure C-50 Horizontal Beam Elongation

Extremely poor response was observed between the predicted yield plateau and the actual yield plateau. However, the maximum strength of the beam was predicted accurately.

Reinforcement strains measured in the first instrumentation panel were significantly lower than the strains measured at the corresponding ductility from testing where the New Zealand loading history was applied. Yielding did not occur in the third instrumentation panel.

A total horizontal elongation equal to 2.5% of the total beam depth was recorded for loading up to and including ductility 8.

The observed behaviour during testing and the experimental results obtained from testing using unidirectional loading was consistent with the response from the test where monotonic loading was applied.

## C.8 Acceleration History A

Results from testing conducted using acceleration history A are presented in Sections C.8.1 through C.8.6, with the results outlined in Section C.8.7. Section C.8.1 describes the observed behaviour of the test specimen during the application of the acceleration history. Section C.8.2 identifies separate displacement components that were established from the experimental data. Section C.8.3 reports on the separation of the total energy dissipated during the test into the energy dissipated through the flexural and shear displacement components. Section C.8.4 compares the predicted moment–curvature relationship with the experimental response and Section C.8.5 details the average strains in the longitudinal reinforcement for the three instrumentation cells. Lastly, Section C.8.6 presents the horizontal elongation of the beam during the test.

### C.8.1 Test Observations

The displacement-time history established from the Ruaumoko analysis outlined in Section 5.2.1 was digitised so that an equivalent displacement record could be applied to the test subassemblage. Four individual earthquake records were applied as part of the first acceleration history. The observed behaviour from the four earthquake records is listed below and on the following page.

#### **Normalised El Centro:**

Maximum displacements of 28.81mm and –26.78mm were applied in the positive and negative direction respectively. These displacements were of sufficient size to ensure that crack patterns formed that were consistent with the crack patterns observed from testing using the cyclic laboratory procedures. However, no spalling or crushing of concrete was evident at the conclusion of this earthquake.

#### **Northridge:**

This record was larger than the normalised El Centro record with a maximum displacement of 30.47mm in the positive direction and –40.3mm in the negative

direction. Secondary cracking was apparent in the plastic hinge zone due to the displacements applied in this earthquake. However, no spalling or crushing of concrete was evident at the conclusion of this record even though larger displacements were applied.

#### **El Centro:**

A maximum displacement of 30.16mm and  $-32.27$ mm were applied in the positive and negative direction respectively during the El Centro portion of the displacement sequence. There were small amounts of additional cracking during this record. However, no spalling or crushing of concrete was evident at the conclusion of this record.

#### **Kobe:**

This record was largest of the four earthquake records, with a maximum displacement of 59.06mm in the positive direction and  $-44.57$ mm in the negative direction. There were small amounts of additional cracking during this record. However, there was still no spalling or crushing of concrete evident at the conclusion of this record. Figure C-51 illustrates the amount of damage that was apparent after the application of the four earthquakes. It can be seen that there was very little spalling of cover concrete. The test was concluded after this earthquake even though only minor damage had been incurred, as applying an additional earthquake would not provide any further

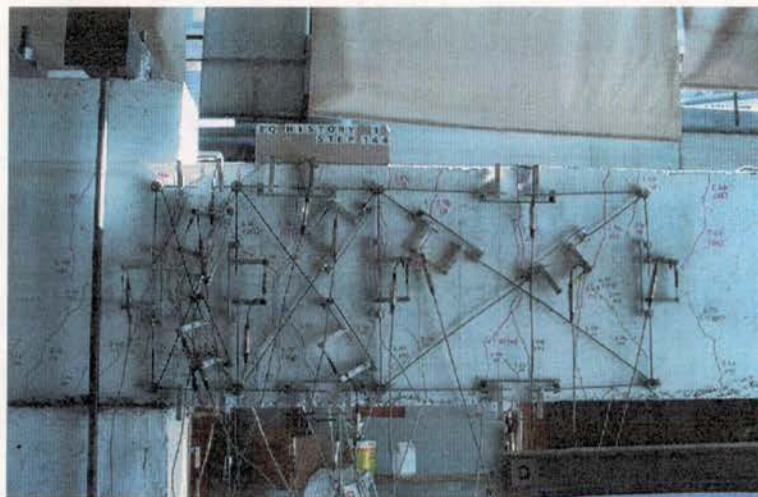


Figure C-51 Test Subassembly Condition at Conclusion of Acceleration History A

information.

### C.8.2 Displacement Components

Figure C-52 illustrates separation of the vertical displacement into its three components and was based on points from the envelope of the force-displacement response. Figure C-52 reveals that there was excellent agreement for the duration of the test.

Figures C-53(a), C-53(b), and C-53(c) present the flexural, shear, and rocking displacement components for the test duration. No comments can be made regarding the symmetrical or non-symmetrical behaviour due to the randomness of the earthquake history. However, the shape of all three displacement components does follow conventional behaviour.

Figure C-52 reveals that the shear deformations accounted for only a small percentage of the total vertical displacement. As reported in Section C.8.1, little degradation occurred during this test. Hence the small shear deformations are consistent with the results from testing under monotonic or unidirectional loading where little physical degradation occurred. Figure C-52 reveals that the rocking deflections accounted for a much larger percentage of the total displacement than from testing using the New Zealand loading history. As explained in Section C.2.2, this was due to the reduction

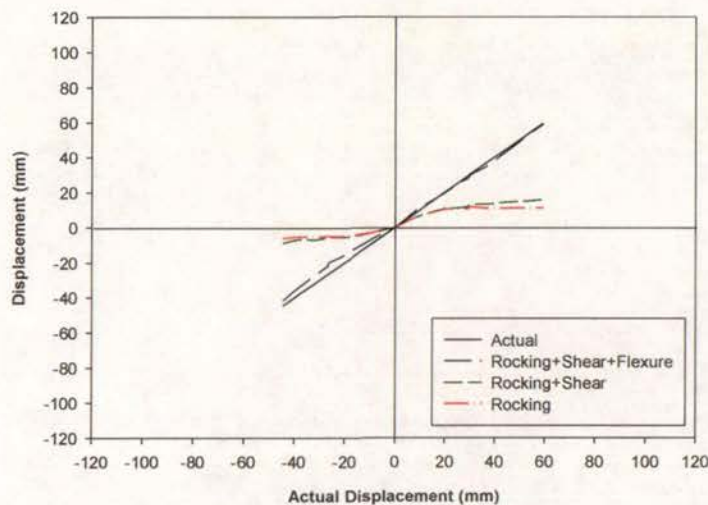


Figure C-52 Components of Displacement

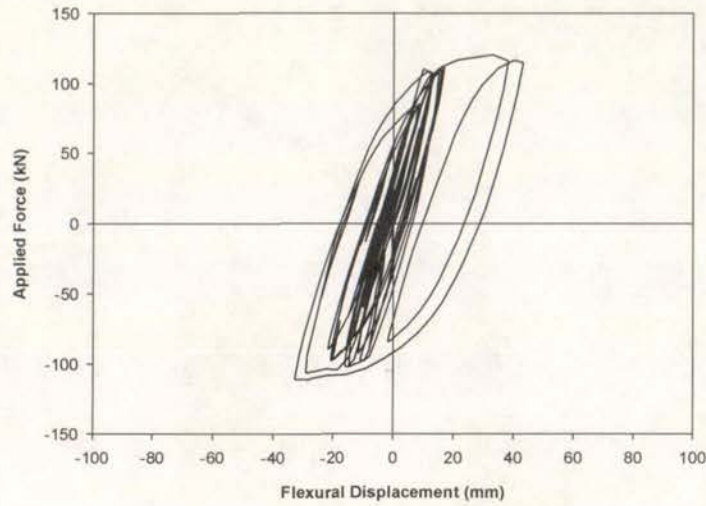


Figure C-53(a) Flexural Displacement Component

of force in the stressing rods during the tensioning process.

### C.8.3 Energy Components

Figure C-54 illustrates the amount of energy dissipated through flexure and shear deformations and demonstrates that, as usual, the flexural deformations accounted for the vast majority of the total energy dissipated. Figure C-54 reveals that there was reasonable agreement between the sum of the two components and the total amount of energy absorbed.

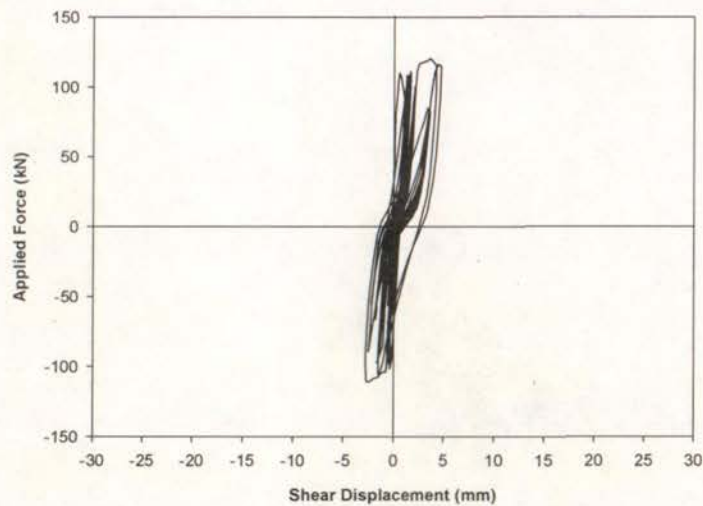


Figure C-53(b) Shear Displacement Component

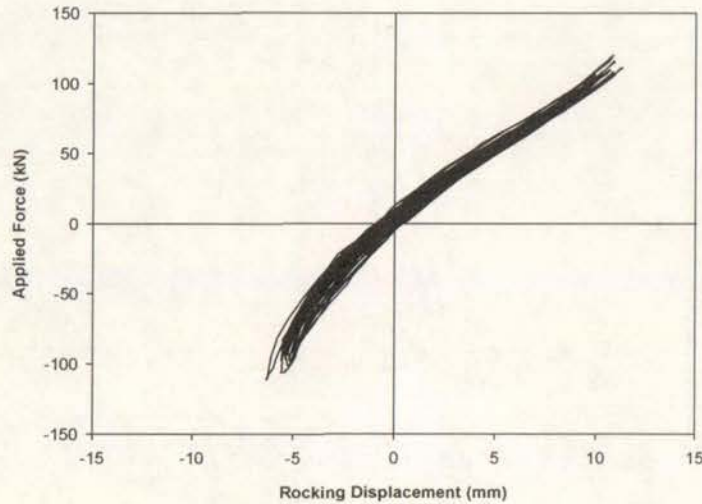


Figure C-53(c) Rocking Displacement Component

#### C.8.4 Moment–Curvature Response

Figures C-55(a) through C-55(c) detail the moment–curvature response for the three instrumentation panels illustrated in Figure 4-16. The moment–curvature response from acceleration history A followed the trends seen in the moment–curvature response from the New Zealand loading history: Poor correlation between the predicted yield plateau and the experimentally determined yield plateau, and little curvature demand in the third panel.

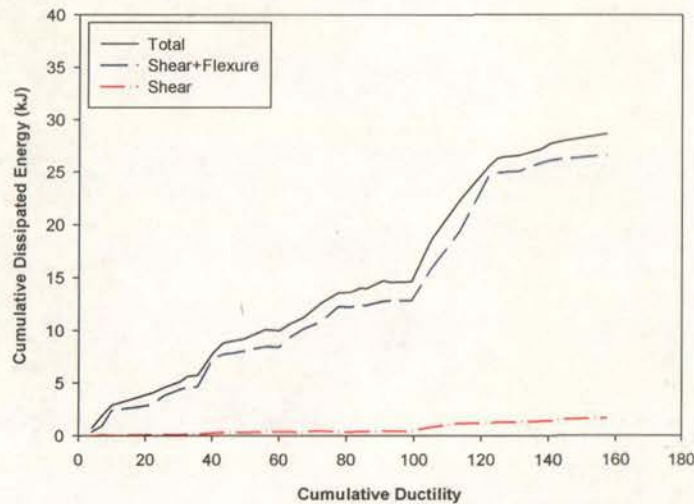


Figure C-54 Components of Energy Dissipation

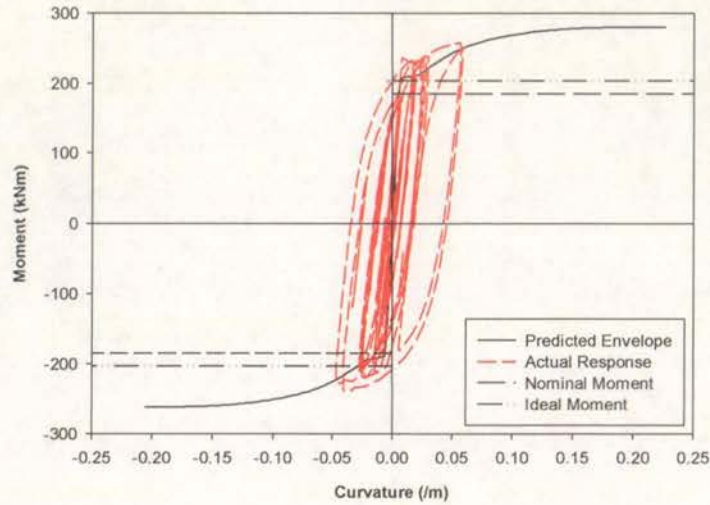


Figure C-55(a) Moment–Curvature Response (Panel 1)

### C.8.5 Reinforcement Strains

The average strain in the bottom and top longitudinal reinforcement was plotted for each instrumentation panel. Figure C-56(a), C-56(b), and C-56(c) present the reinforcement strains from panel 1, panel 2, and panel 3 respectively.

Figure C-56(a) reveals that significantly lower strains were measured in the longitudinal reinforcement during this test than from testing when the New Zealand loading history was applied. This is due to the lower ductility levels that were applied in this displacement sequence. From Figure C-56(c), it was established that the

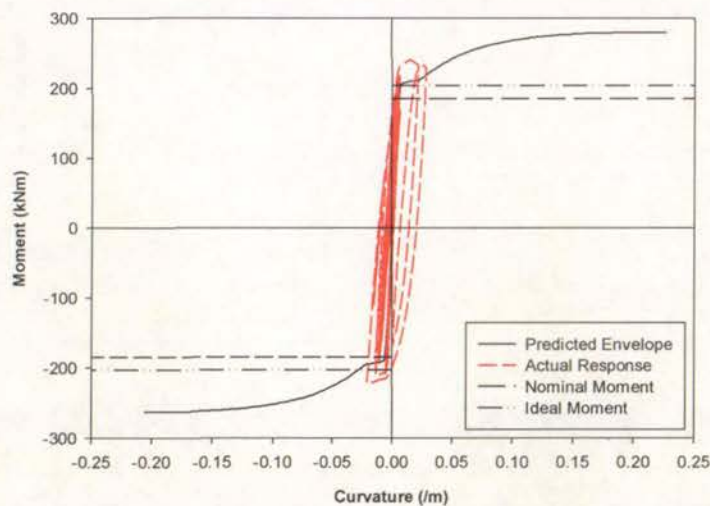


Figure C-55(b) Moment–Curvature Response (Panel 2)

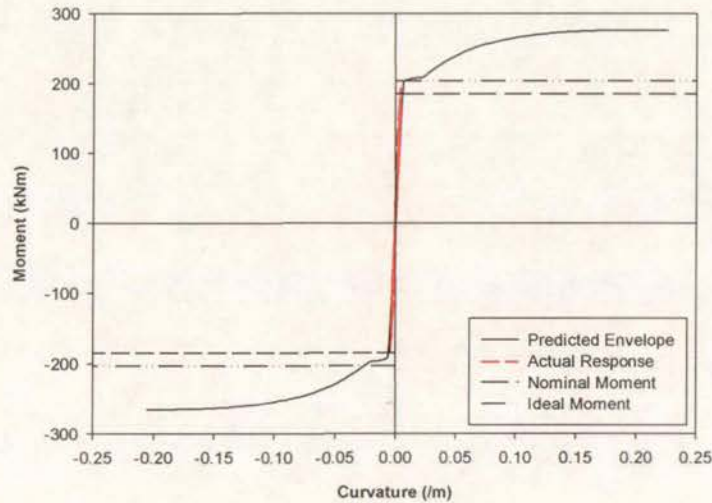


Figure C-55© Moment-Curvature Response (Panel 3)

longitudinal reinforcement in panel 3 did not yield.

### C.8.6 Beam Elongation

The horizontal elongation at the beam centreline was recorded for the duration of the test. Figure C-57 displays the horizontal elongation recorded during the test and reveals a maximum horizontal elongation of 14mm, which is equal to 2.33% of the total beam depth. This low value of horizontal elongation is consistent with the results from other tests that had suffered little damage by ductility 8; for example, testing where monotonic or unidirectional loading was applied.

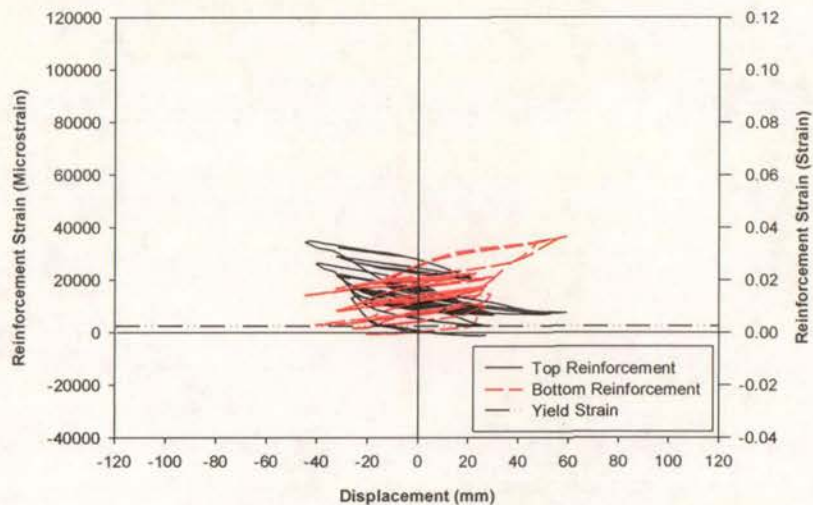


Figure C-56(a) Reinforcement Strains (Panel 1)

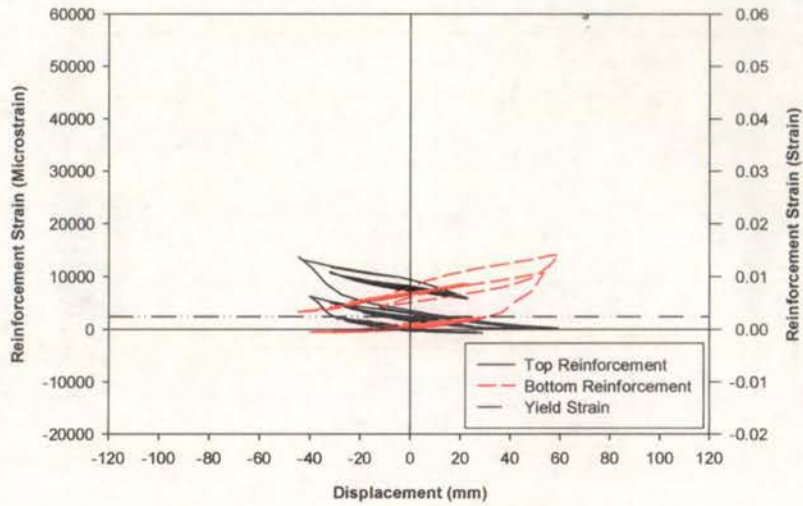


Figure C-56(b) Reinforcement Strains (Panel 2)

### C.8.7 Summary of Test Results

Excellent agreement was obtained between the sum of the three displacement components and the actual displacement for the duration of the test.

Shear deformations accounted for a low percentage of the total vertical displacement compared to that recorded during testing using the New Zealand loading history. All three displacement components followed conventional behaviour.

Poor response was observed between the predicted yield plateau and the actual yield

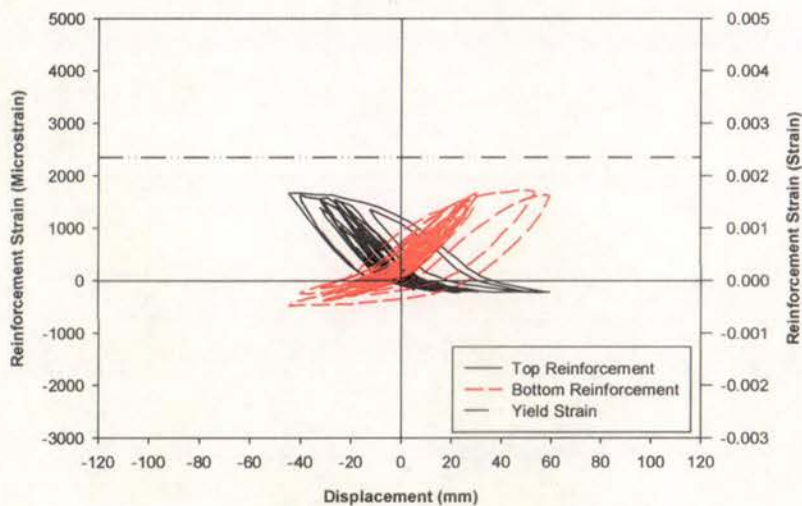


Figure C-56(c) Reinforcement Strains (Panel 3)

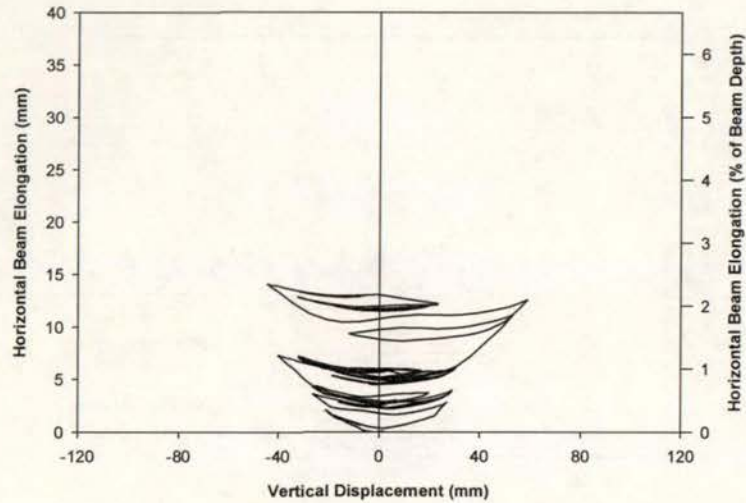


Figure C-57 Horizontal Beam Elongation

plateau. However, the maximum strength of the beam was predicted accurately.

Significantly lower strains were measured in the longitudinal reinforcement from this test compared to testing using the New Zealand loading history. Yielding did not occur in the third instrumentation panel.

A maximum horizontal elongation equal to 2.33% of the total beam depth was recorded during application of acceleration history A.

## C.9 Acceleration History B

Results from testing conducted using acceleration history B are presented in Sections C.9.1 through C.9.6, with the results encapsulated in Section C.9.7. Section C.9.1 describes the observed behaviour of the test specimen during application of acceleration history B. Section C.9.2 identifies the separate displacement components that were established from the recorded data. Section C.9.3 details the separation of the total energy dissipated during the test into the energy dissipated through the flexural and shear displacement components. Section C.9.4 compares the predicted moment–curvature relationship with the experimental relationship and Section C.9.5 reports on the average strains in the longitudinal reinforcement for the three instrumentation cells. Lastly, Section C.9.6 details the horizontal elongation of the beam during the test.

### C.9.1 Test Observations

The displacement-time history established from the Ruaumoko analysis covered in Section 5.2.2 was digitised so that an equivalent displacement record could be applied to the test subassemblage.

#### **Normalised El Centro:**

Maximum displacements of 46.58mm and –49.85mm were applied in the positive and negative direction respectively. These displacements were of sufficient size to ensure that crack patterns formed that were consistent with the crack patterns observed from testing using the cyclic laboratory procedures. Secondary cracking in the plastic hinge zone was also apparent. Cumulative spalling along cracks in the plastic hinge zone meant that a transverse stirrup was visible by the conclusion of this earthquake.

#### **Northridge:**

This record was larger than the normalised El Centro record with a maximum displacement of 56.85mm in the positive direction and –74.96mm in the negative direction. Secondary cracking was apparent in the plastic hinge zone due to the

displacements applied in this record. Spalling continued to occur along cracks in the plastic hinge zone and the first evidence of crushing of concrete in the compression zone was visible.

#### **El Centro:**

A maximum displacement of 44.07mm and  $-6.54$ mm were applied in the positive and negative direction respectively during the El Centro portion of the displacement sequence. No additional cracking was observed during this record. Minor spalling of cover concrete continued to occur although this was due to the order of this record in the acceleration sequence rather than the size of the applied displacements.

#### **Kobe:**

This record was largest of the four records with a maximum displacement of 90.67mm in the positive direction and  $-42.44$ mm in the negative direction. No additional cracking was identified during this record. However, there was significant spalling of concrete from the top and bottom of the beam. Approximately 150mm of longitudinal reinforcement from the top and bottom of the beam were exposed by the conclusion of this record. Figure C-58 illustrates the physical degradation, in particular the substantial amount of spalling, which had taken place by the conclusion of the acceleration history. The test was concluded after this earthquake.

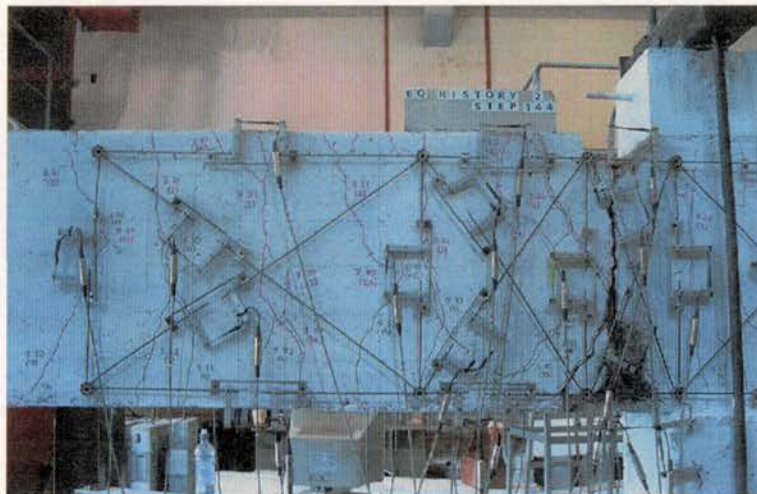


Figure C-58 Test Subassembly Condition at Conclusion of Acceleration History B

### C.9.2 Displacement Components

Figure C-59 illustrates separation of the vertical displacement into its three components and demonstrates that the shear displacement component accounted for a larger percentage of the total displacement than that recorded from testing using the first acceleration history. This was due to the increase in damage resulting from this test. Figure C-59 also reveals that for the duration of the test there was excellent agreement between the sum of the three components and the actual vertical displacement.

Figure C-60(a), C-60(b), and C-60(c) illustrate the flexural, shear, and rocking displacement components for the test duration. The shape of all three displacement components followed conventional behaviour.

### C.9.3 Energy Components

Figure C-61 illustrates the amount of energy dissipated through flexure and shear deformations and demonstrates that, as usual, the flexural deformations accounted for the vast majority of the total energy dissipated. Figure C-61 exhibits the excellent agreement between the sum of the two components and the total amount of energy dissipated.

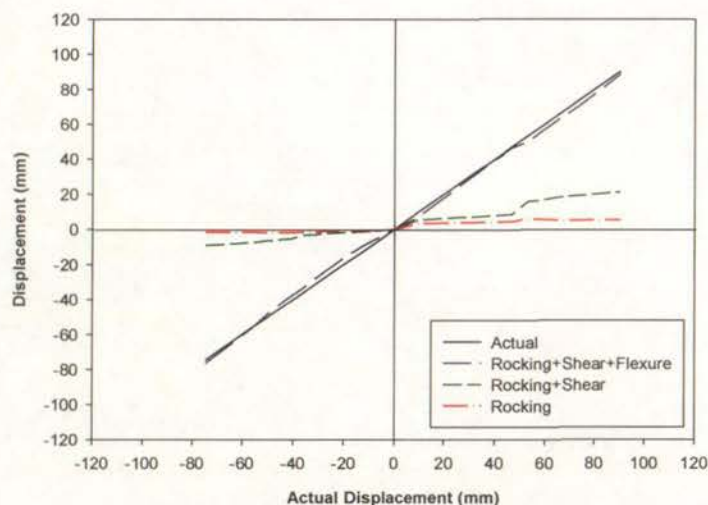


Figure C-59 Components of Displacement

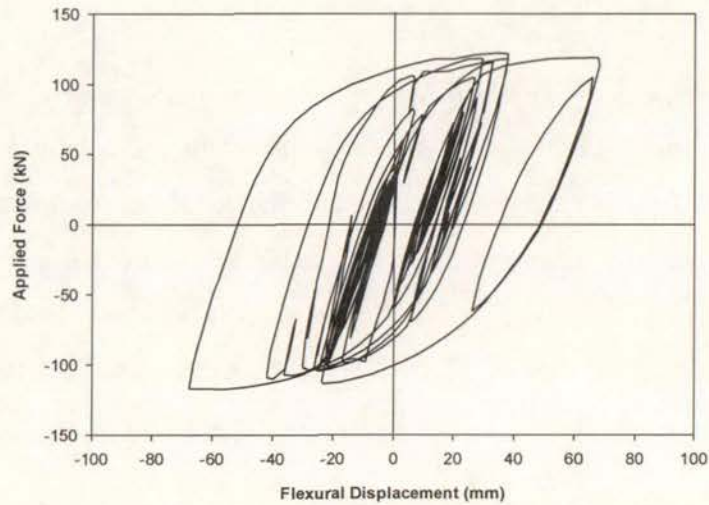


Figure C-60(a) Flexural Displacement Component

#### C.9.4 Moment–Curvature Response

Figures C-62(a) through C-62(c) detail the moment–curvature response from panel 1, panel 2, and panel 3. The moment–curvature response from acceleration history B followed the trends seen in the moment–curvature response from the New Zealand loading history: Poor correlation between the predicted and experimental yield plateau and little curvature demand in the third panel.



Figure C-60(b) Shear Displacement Component

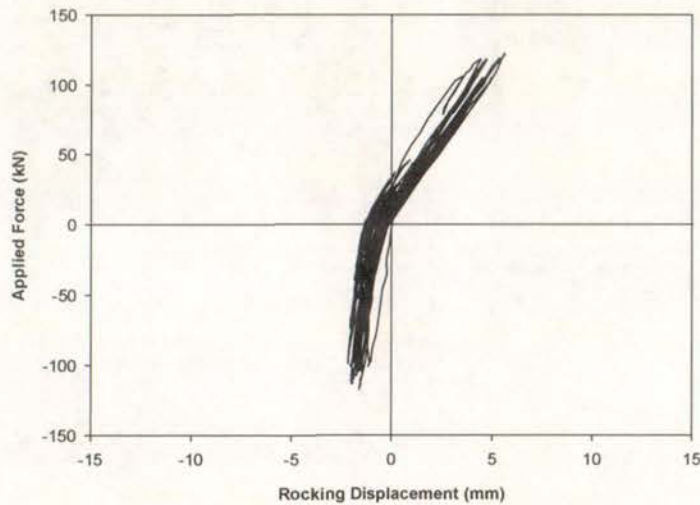


Figure C-60(c) Rocking Displacement Component

### C.9.5 Reinforcement Strains

The average strain in the bottom and top longitudinal reinforcement was plotted for each instrumentation panel. Figures C-63(a) through C-63(c) detail the reinforcement strains from panel 1, panel 2, and panel 3 respectively.

Figure C-63(a) reveals that the strains in the longitudinal reinforcement were slightly larger than the reinforcement strains recorded while testing using the New Zealand loading history. This is because higher ductility levels were recorded in this earthquake history than during the recorded phase using the New Zealand loading

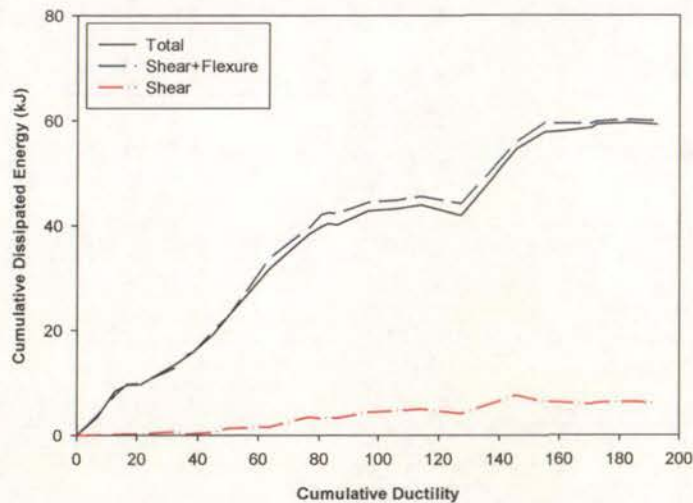


Figure C-61 Components of Energy Dissipation

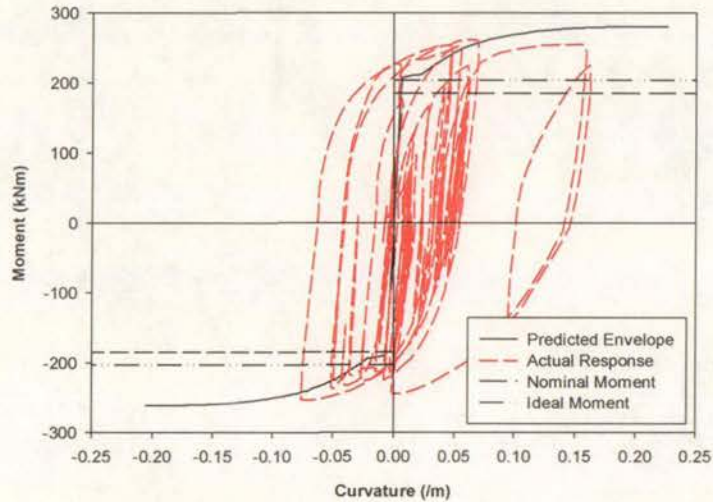


Figure C-62(a) Moment–Curvature Response (Panel 1)

history. From Figure C-63(c), it was established that the longitudinal reinforcement in panel 3 did not yield.

#### C.9.6 Beam Elongation

The horizontal elongation at the beam centreline was recorded for the duration of the test. Figure C-64 presents the horizontal elongation for the test duration and reveals a maximum horizontal elongation of 31mm, which is equal to 5.17% of the total beam depth. This value of horizontal elongation was consistent with maximum-recorded elongation from cyclic tests.

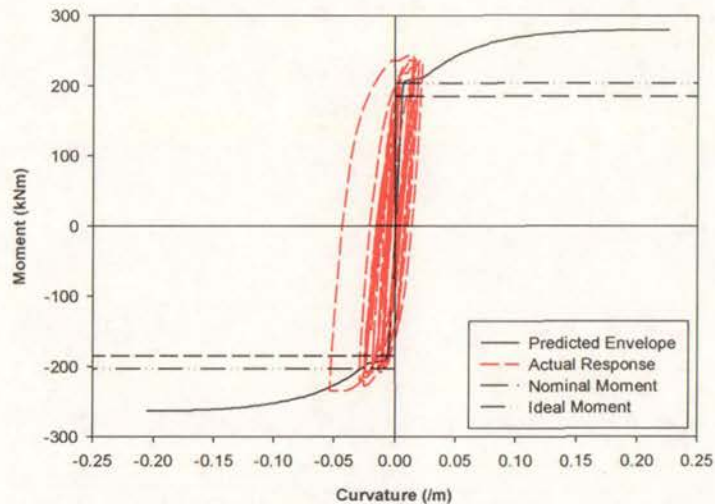


Figure C-62(b) Moment–Curvature Response (Panel 2)

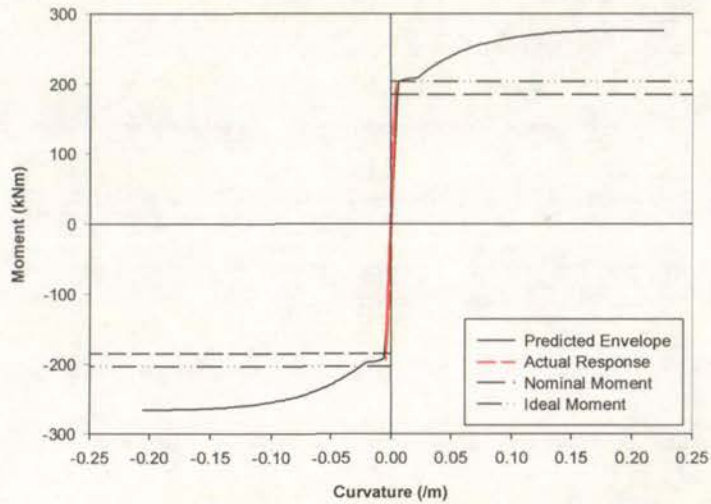


Figure C-62(c) Moment-Curvature Response (Panel 3)

### C.9.7 Summary of Test Results

Excellent agreement was obtained between the sum of the three displacement components and the actual displacement for the duration of the test.

Shear deformations accounted for a higher percentage of the total vertical displacement compared to that recorded during testing using the first earthquake history. All three displacement components followed conventional behaviour.

Poor response was observed between the predicted yield plateau and the actual yield

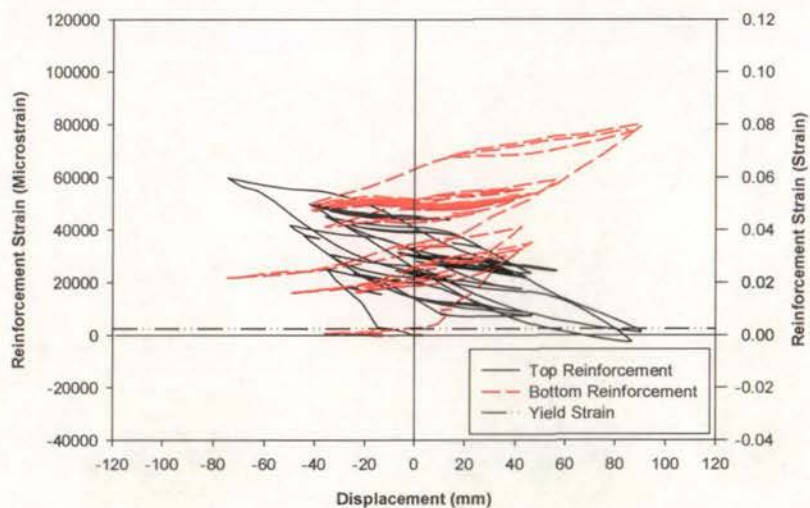


Figure C-63(a) Reinforcement Strains (Panel 1)

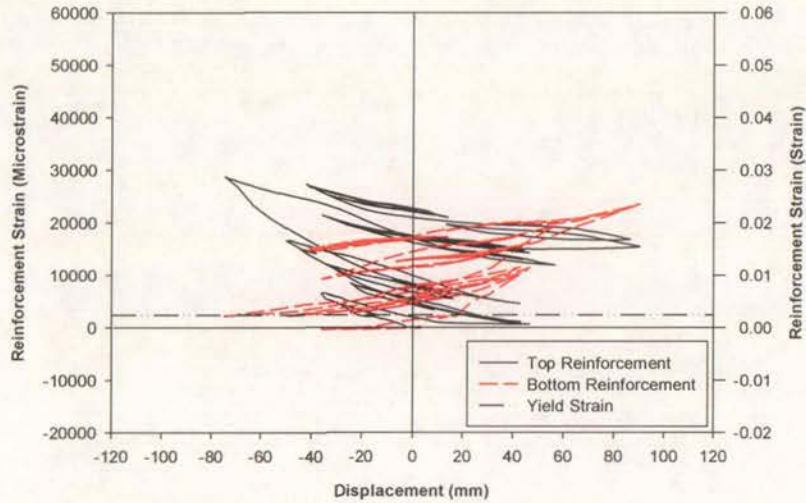


Figure C-63(b) Reinforcement Strains (Panel 2)

plateau. However, the maximum strength of the beam was predicted accurately.

Larger reinforcement strains were measured in the first instrumentation panel during this acceleration history than from testing where the New Zealand loading history was applied. This was due to the larger displacements that were recorded in this acceleration history compared to the displacements recorded while testing using the New Zealand loading history. Yielding did not occur in the third instrumentation panel.

A horizontal elongation equal to 5.17% of the total beam depth was recorded for the

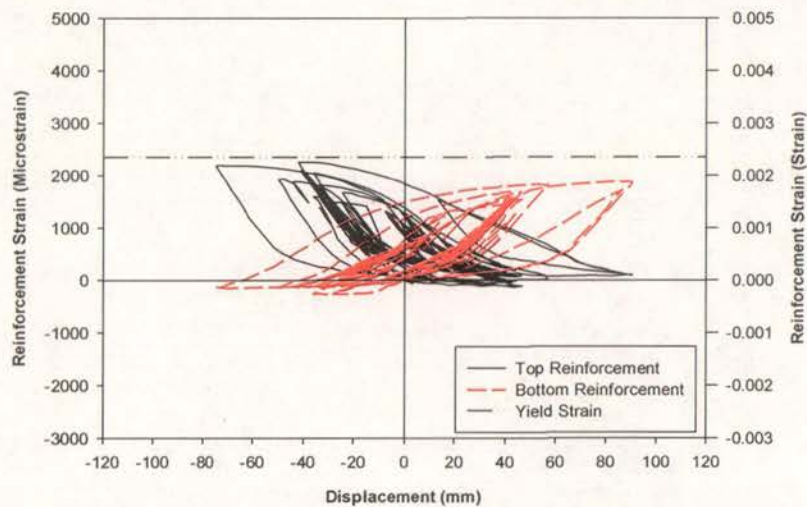


Figure C-63(c) Reinforcement Strains (Panel 3)

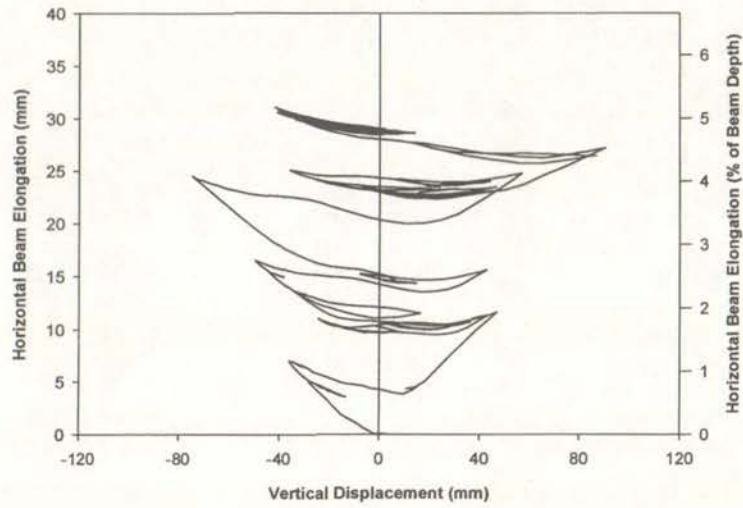


Figure C-64 Horizontal Beam Elongation

duration of the test. This was consistent with the elongation that occurred in cyclic tests.

## C.10 Acceleration History C

Results from testing where acceleration history C was applied are presented in Sections C.10.1 through C.10.6. Section C.10.7 outlines the conclusions reached from this test. Section C.10.1 describes the behaviour of the test specimen observed while testing. Section C.10.2 identifies the separate displacement components that were calculated from the recorded test data. Section C.10.3 applied the results from Section C.10.2 to separate the total energy disbursed during the test into the energy disbursed through the flexural and shear displacement components. Section C.10.4 compares the predicted moment–curvature relationship with the experimental response and Section C.10.5 details the average strains in the longitudinal reinforcement for the three instrumentation cells. Lastly, Section C.10.6 presents the beam horizontal elongation that occurred during the test.

### C.10.1 Test Observations

The displacement-time history established from the Ruaumoko analysis outlined in Section 5.2.3 was digitised so that an equivalent displacement record could be applied to the test subassemblage. The Kobe record was repeated in the final three acceleration histories to ensure that failure of the test subassemblage occurred. For reporting purposes, the repeat Kobe record is denoted as Kobe (2).

#### **Normalised El Centro:**

Maximum displacements of 46.58mm and –49.85mm were applied in the positive and negative direction respectively. These displacements were of sufficient size to ensure that crack patterns formed that were consistent with the crack patterns observed from testing using the cyclic laboratory procedures. Secondary cracking in the plastic hinge zone was also apparent. Minor spalling along cracks in the plastic hinge zone occurred throughout the record although no reinforcement was visible at the conclusion of this record.

**Kobe:**

This record was one of the largest records, with maximum displacements of 67.65mm in the positive direction and -49.52mm in the negative direction. This record resulted in a large amount of damage to the test subassemblage. Small amounts of additional cracking were identified and cumulative spalling along cracks in the plastic hinge zone meant that a transverse stirrup was visible by the conclusion of this record. Also, there was significant spalling of concrete from the bottom of the beam such that a length of longitudinal reinforcement was visible. Crushing of concrete on the top of the beam was observed although only extremely minor spalling resulted.

**Northridge:**

Maximum displacements of 29.59mm in the positive direction and -89.69mm in the negative direction were applied as part of this record. Significant damage occurred during the application of this earthquake. Shearing deformations were observed to become more prevalent with a major shear crack forming during the earthquake, while significant spalling from Side A meant that transverse reinforcement was clearly visible.

**El Centro:**

Maximum displacements of 25.73mm and -24.02mm were applied in the positive and negative direction respectively during the El Centro portion of the displacement sequence. No additional cracking was observed during this record. Minor spalling of cover concrete continued to occur, although this was due to the order within the displacement sequence rather than the size of the applied displacements.

**Kobe (2):**

This record was a magnified version of the Kobe earthquake with, a maximum displacement of 103.26mm in the positive direction and -50.13mm in the negative direction. Another significant shear crack formed during this earthquake. Also, several large pieces of concrete were removed from the top and bottom of the beam,

which meant that approximately 300mm of longitudinal reinforcement from the top and bottom of the beam was visible by the conclusion of this record. Figure C-65 illustrates the significant physical degradation that had taken place by the conclusion of acceleration history C. The test was terminated after the conclusion of this record.

#### C.10.2 Displacement Components

Figure C-66 illustrates the separation of the vertical displacement into the flexural, shear, and rocking displacement components. The shear displacement component in this acceleration history accounted for a similar percentage of the total displacement when compared with response using acceleration history B. Figure C-66 also exhibits excellent agreement during the recorded phase of the test.

Figures C-67(a), C-67(b), and C-67(c) illustrate the flexural, shear, and rocking displacement components for the duration of the test. The shape of all three displacement components followed conventional response.

#### C.10.3 Energy Components

Figure C-68 illustrates the amount of energy disbursed through flexure and shear deformations. Shear deformations accounted for a similar percentage of the total energy disbursed as in the second acceleration history. Figure C-68 reveals that there was excellent agreement between the sum of the two components and the total amount



Figure C-65 Test Subassembly Condition at Conclusion of Acceleration History C

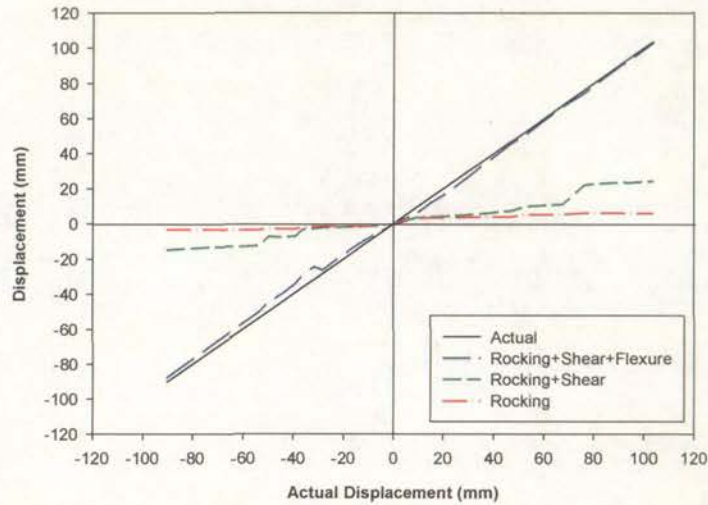


Figure C-66 Components of Displacement

of energy disbursed.

#### C.10.4 Moment Curvature

Figure C-69(a) through C-69(c) illustrates the moment–curvature response from panel 1, panel 2, and panel 3 respectively. The moment–curvature response from the second acceleration history followed the trends seen in the moment–curvature response from testing using the New Zealand loading history, with poor correlation between the predicted and experimental yield plateau and little curvature demand in the third instrumentation panel.

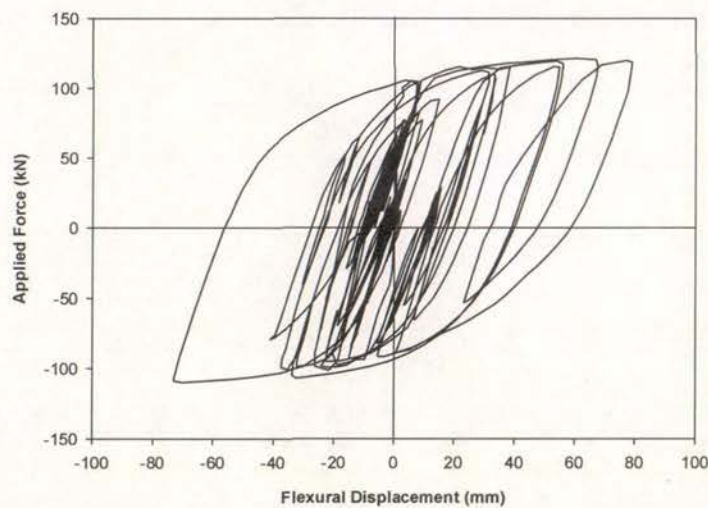


Figure C-67(a) Flexural Displacement Component

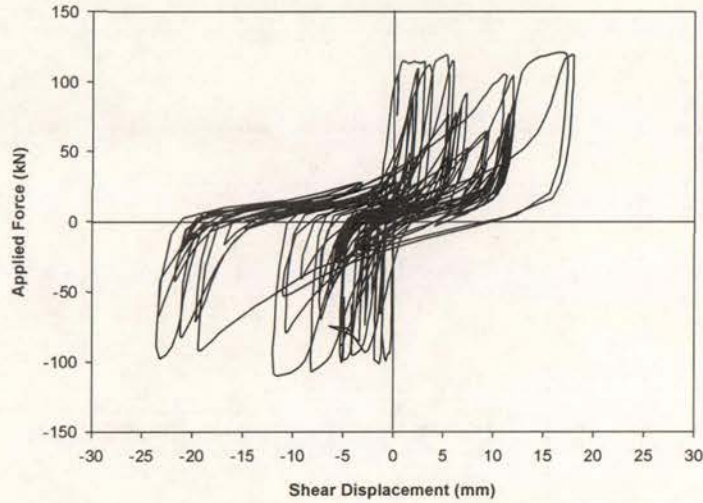


Figure C-67(b) Shear Displacement Component

### C.10.5 Reinforcement Strains

The average strain in the bottom and top longitudinal reinforcement was plotted for each instrumentation panel, with Figures C-70(a) through C-70(c) displaying the reinforcement strains from panel 1, panel 2, and panel 3 respectively.

The reinforcement strains recorded in the first instrumentation panel were similar to those recorded during acceleration history B. However, the reinforcement strains in the second instrumentation panel were slightly higher than those measured during acceleration history B. This reflects the larger displacements that were applied in this

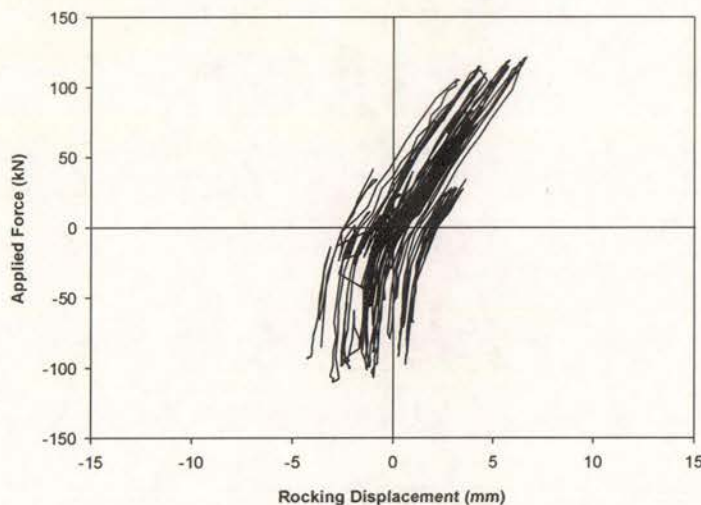


Figure C-67(c) Rocking Displacement Component

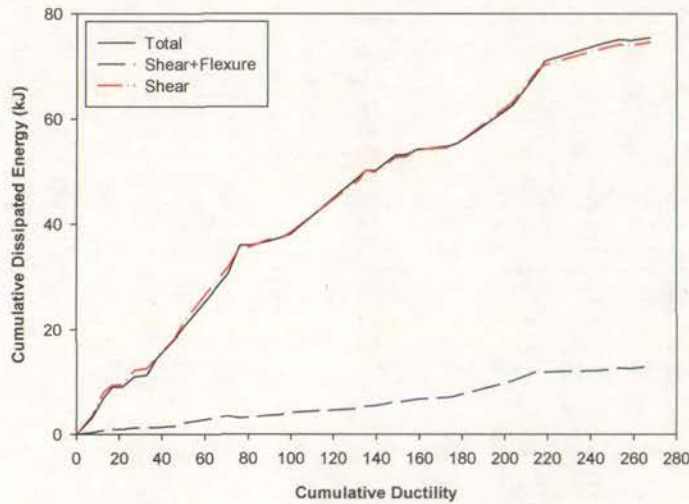


Figure C-68 Components of Energy Dissipation

test. From Figure C-70(c), it was established that the longitudinal reinforcement in the third instrumentation panel did reach its yield strain. Again this was due to the larger displacements that were recorded in this test compared to the displacements that were recorded during application of the laboratory procedures.

#### C.10.6 Beam Elongation

The horizontal elongation at the beam centreline was recorded for the duration of the test. Figure C-71 shows the values of horizontal elongation recorded during the test and reveals a maximum horizontal elongation of 36mm, which is equal to 6.0% of the

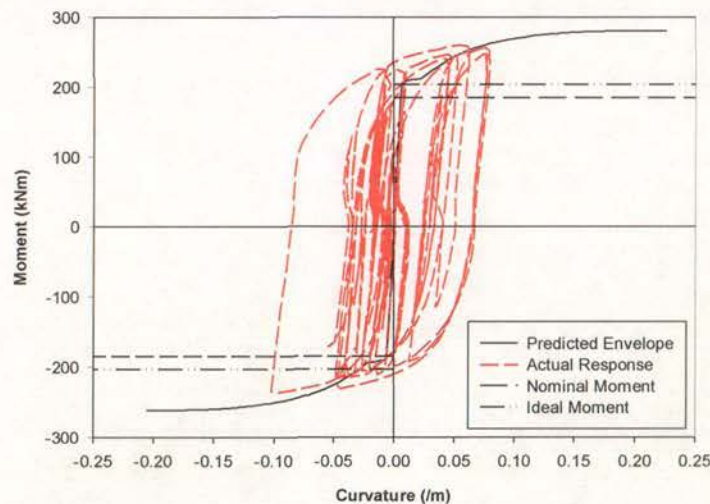


Figure C-69(a) Moment-Curvature Response (Panel 1)

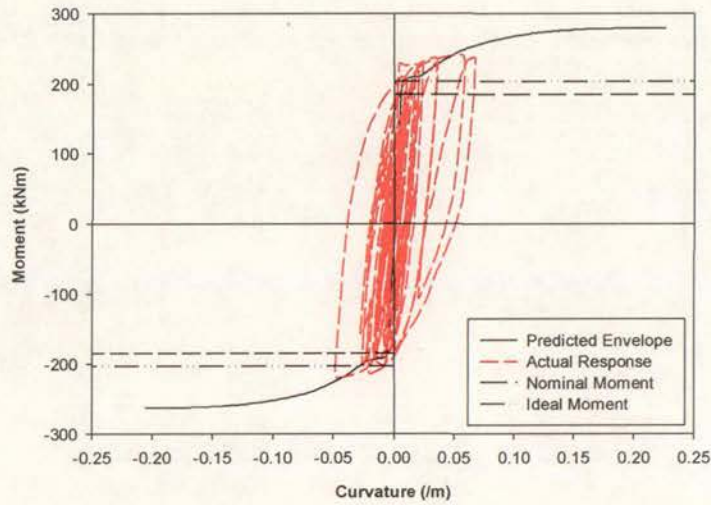


Figure C-69(b) Moment–Curvature Response (Panel 2)

total beam depth. This value of horizontal elongation is slightly larger than the maximum value recorded during testing using acceleration history B and reflects the greater amount of damage that was incurred in this acceleration history.

#### C.10.7 Summary of Test Results

Excellent agreement was obtained between the sum of the three displacement components and the actual displacement for the duration of the test.

Shear deformations accounted for a similar percentage of the total vertical displacement compared to that recorded during testing using acceleration history B.

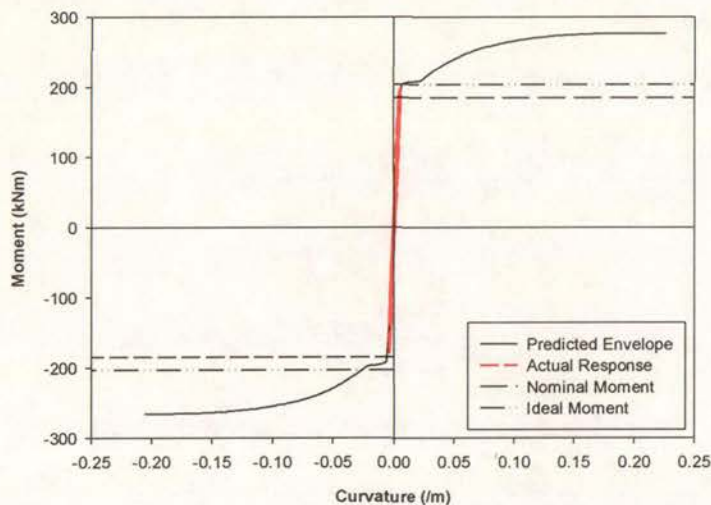


Figure C-69(c) Moment–Curvature Response (Panel 3)

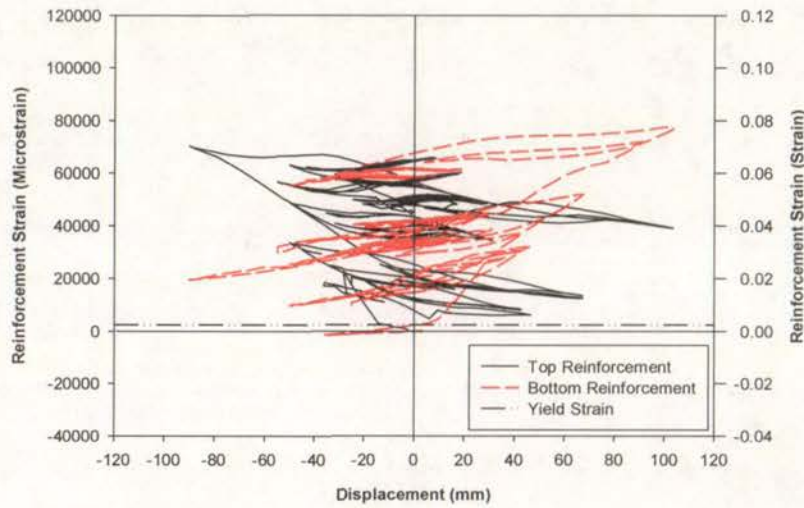


Figure C-70(a) Reinforcement Strains (Panel 1)

All three displacement components followed conventional behaviour.

Poor response was observed between the predicted yield plateau and the actual yield plateau. However, the maximum strength of the beam was predicted accurately.

Similar response was obtained from the first instrumentation panel for acceleration histories B and C, whereas slightly larger strains were recorded in the second instrumentation panel for acceleration history C. This reflected the larger displacements that were applied in the latter acceleration history. Yielding did occur in the third instrumentation panel. Again this was due to the larger displacements

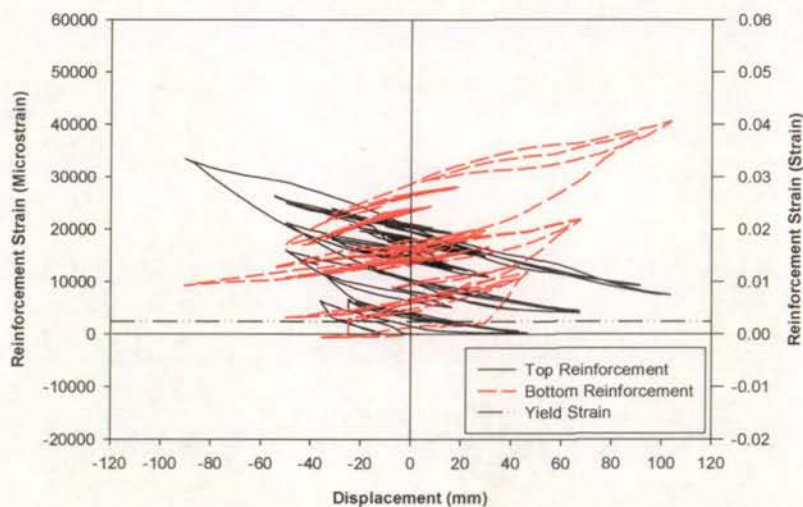


Figure C-70(b) Reinforcement Strains (Panel 2)

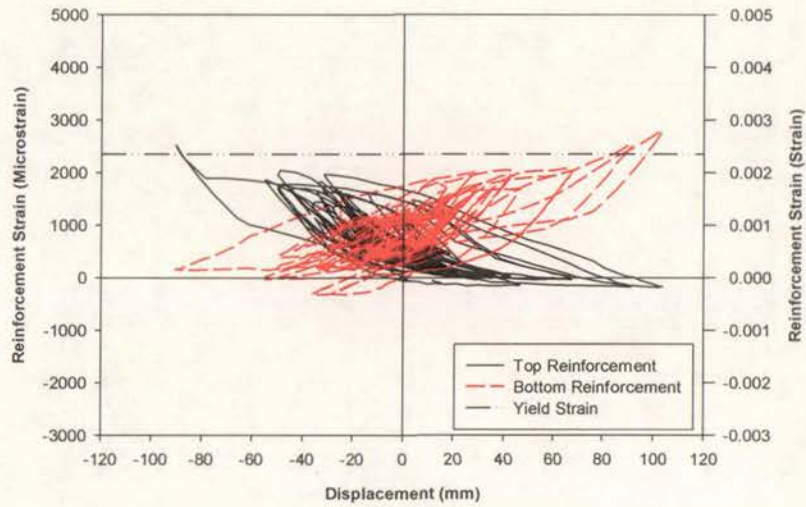


Figure C-70(c) Reinforcement Strains (Panel 3)

applied in this acceleration history.

A horizontal elongation equal to 6.0% of the total beam depth was recorded for the duration of the test. This was slightly larger than the maximum response from testing using acceleration history B or the cyclic tests. This reflects the increase in physical degradation in this test compared to acceleration history B. The increase in elongation during this test compared to the cyclic tests was because larger displacements were recorded in this test.

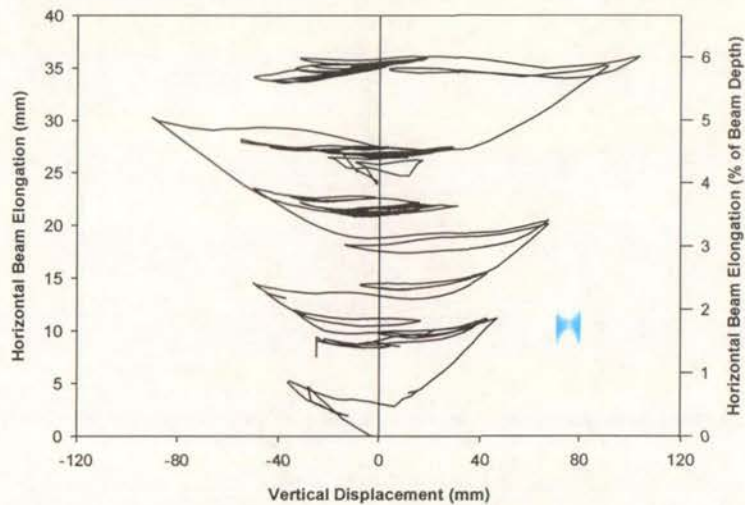


Figure C-71 Horizontal Beam Elongation

## C.11 Acceleration History D

Results from testing conducted using acceleration history D are detailed in Sections C.11.1 through C.11.6, with the results outlined in Section C.11.7. Section C.11.1 describes the observed behaviour of the test specimen during the test. Section C.11.2 identifies the separate displacement components that were established from the experimental data. In Section C.11.3, the total energy expended during the test is separated into the energy expended through the flexural and shear displacements. Section C.11.4 compares the predicted moment–curvature relationship with the experimental moment–curvature response and Section C.11.5 details the average strains in the longitudinal reinforcement for the three instrumentation cells. Lastly, Section C.11.6 reports on the horizontal elongation of the beam during the test.

### C.11.1 Test Observations

The displacement-time history established from the Ruaumoko analysis covered in Section 5.2.4 was digitised so that an equivalent displacement record could be applied to the test subassemblage. Five earthquake records were applied in sequential order with the repeat Kobe record denoted as Kobe (2).

#### **Northridge:**

This record had maximum displacements of 54.82mm in the positive direction and –77.47mm in the negative direction. These displacements were of sufficient size to ensure that crack patterns formed that were consistent with the crack patterns observed from testing using the cyclic laboratory procedures. Secondary cracking in the plastic hinge zone was also apparent. Spalling along cracks in the plastic hinge zone occurred throughout the record and led to transverse reinforcement being visible on both sides of the beam by the conclusion of this record. Minor crushing of concrete in the compression zone was also observed.

**El Centro:**

Maximum displacements of 33.42mm and -12.55mm were applied in the positive and negative direction respectively during the El Centro portion of the displacement sequence. No additional cracking or spalling was observed during this record.

**Normalised El Centro:**

Maximum displacements of 54.45mm and -51.34mm were applied in the positive and negative direction respectively. A longitudinal bar ruptured during application of this record. This was because the welding of an instrumentation stud affected the local material properties of the bar, and hence the failure occurred prematurely. Testing was continued even though failure had occurred. Significant spalling from the side and bottom of the beam occurred during this earthquake. The removal of several large pieces of spalled concrete from the bottom of the beam meant that the longitudinal reinforcement was visible.

**Kobe:**

This record was one of the largest records, with maximum displacements of 46.65mm in the positive direction and -58.12mm in the negative direction. This earthquake resulted in a large amount of damage to the test subassemblage. Spalling continued from the side and the top and bottom of the beam. No additional cracking was observed.

**Kobe (2):**

This record was a magnified version of the Kobe (1) record with maximum displacements of 95.77mm in the positive direction and -37.85mm in the negative direction. Severe damage was observed during application of this record. Shear deformations had become much more prevalent. Significant spalling occurred from the side, top and bottom of the beam. This meant that the widths of cracks in the plastic hinge zone were unable to be measured. Transverse stirrups were rupturing on the large displacement cycles. Figure C-72 illustrates the damage incurred after the

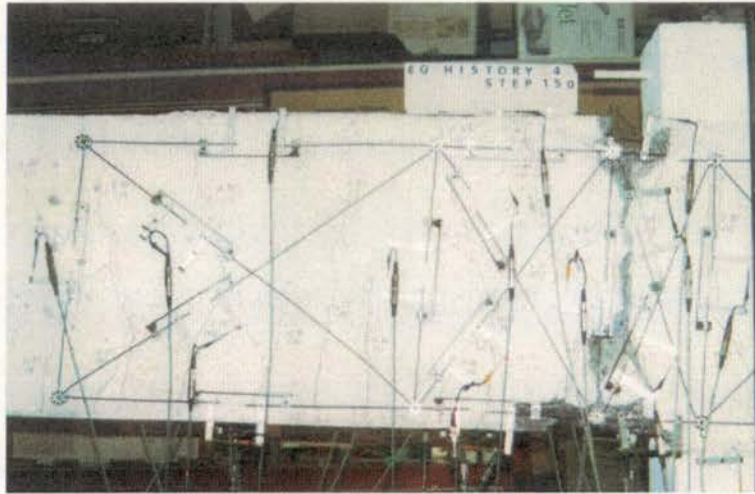


Figure C-72 Test Subassemblage Condition After Application of Maximum Displacement

maximum positive displacement of 95.77mm had been applied. The test was terminated after conclusion of this record.

#### C.11.2 Displacement Components

Figure C-73 illustrates separation of the vertical displacement into its three components. Figure C-73 reveals that the shear displacement component accounted for a low percentage of the total displacement in the negative direction but accounted for a relatively high amount in the positive direction. This was due to the largest displacements in the negative direction being at an early stage of the test where there was little damage and hence, correspondingly small shear deformations were recorded. In the positive direction, the envelope contained points from after

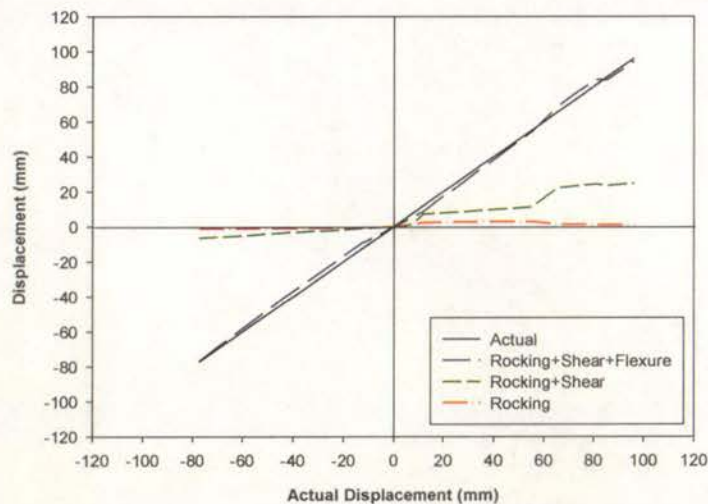


Figure C-73 Components of Displacement

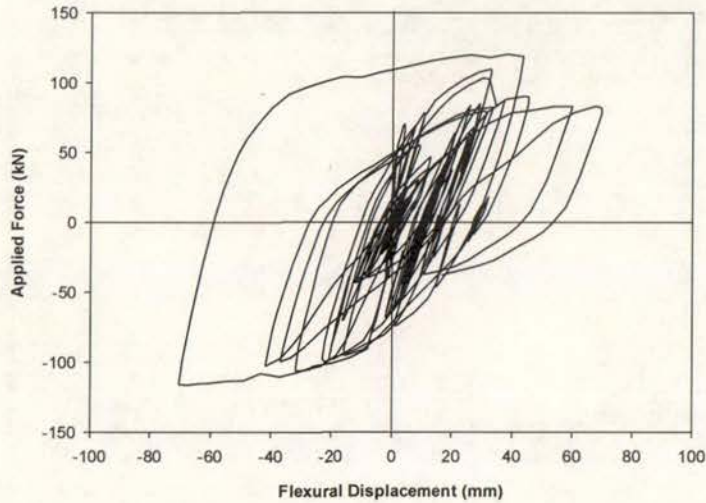


Figure C-74(a) Flexural Displacement Component

premature rupture of the longitudinal bar. This led to significant degradation (as described in Section C.11.1) and hence higher values of shear deformation. Figure C-73 reveals that there was excellent agreement during the recorded phase of the test.

Figures C-74(a), C-74(b), and C-74(c) detail the flexural, shear, and rocking displacement components for the test up until halfway through the fifth record. Contamination of strain gauge recordings meant that the flexural and shear displacement components were unable to be calculated after that point. The shape of all three displacement components follows conventional behaviour.

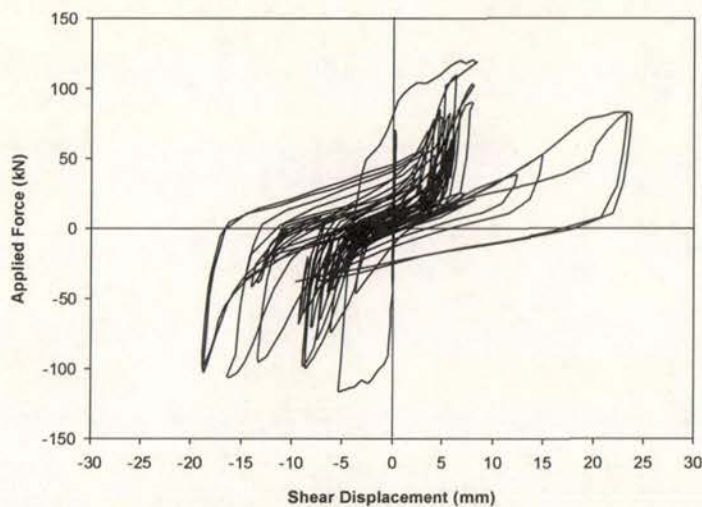


Figure C-74(b) Shear Displacement Component

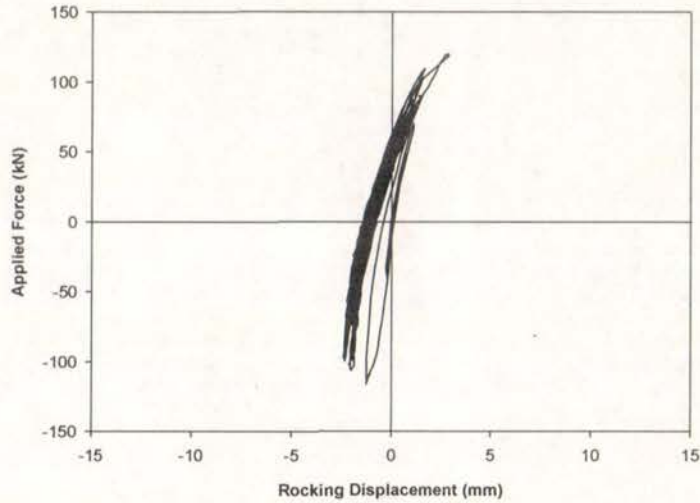


Figure C-74(c) Rocking Displacement Component

### C.11.3 Energy Components

Figure C-75 illustrates the amount of energy expended through flexure and shear deformation, and demonstrates that shear deformations accounted for a larger percentage of the total expended energy than for other tests. This is due to the behaviour described in Section C.11.2 where there was an increase in magnitude of shear deformations due to the premature rupturing of a longitudinal bar. Figure C-75 reveals that there was excellent agreement between the sum of the two components and the total amount of energy expended.

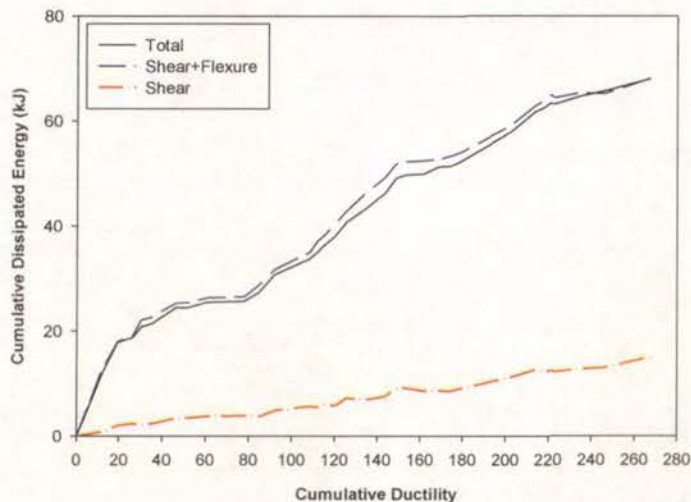


Figure C-75 Components of Energy Dissipation

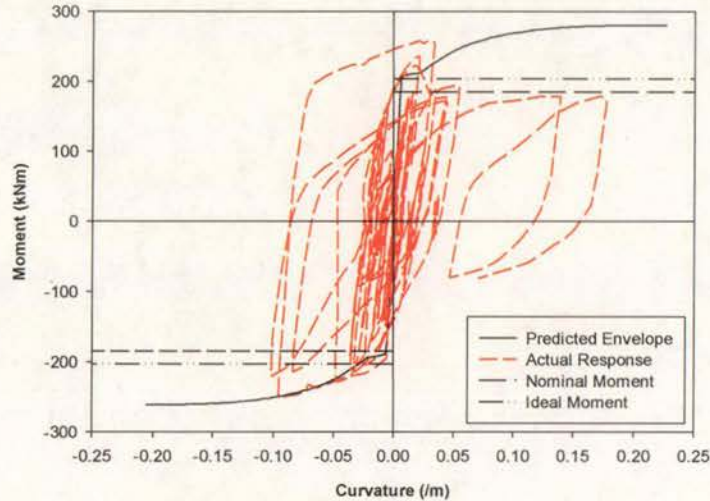


Figure C-76(a) Moment–Curvature Response (Panel 1)

#### C.11.4 Moment–Curvature Response

Figures C-76(a) through C-76(c) display the moment–curvature response from the three instrumentation panels. The moment–curvature response from acceleration history D followed the trends seen in the moment–curvature response from the New Zealand loading history, with poor correlation between the predicted and experimental yield plateau and little curvature demand in the third panel.

#### C.11.5 Reinforcement Strains

The average strain in the bottom and top longitudinal reinforcement was plotted for

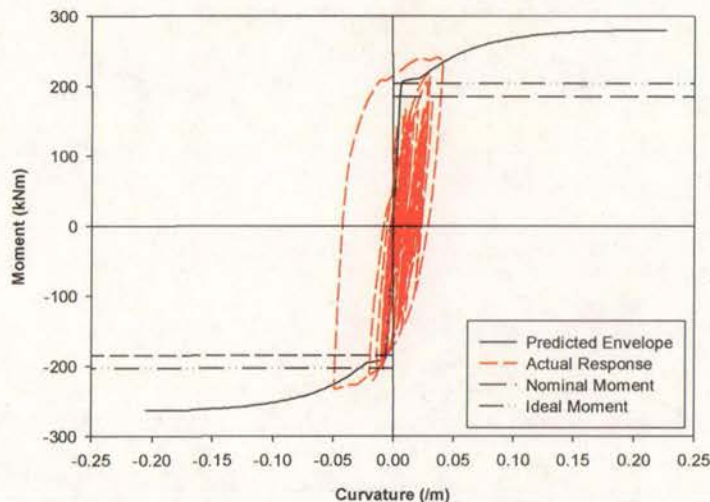


Figure C-76(b) Moment–Curvature Response (Panel 2)

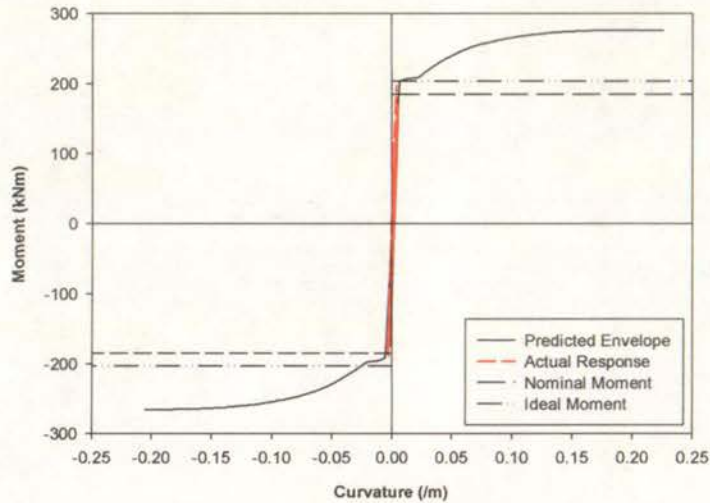


Figure C-76(c) Moment–Curvature Response (Panel 3)

each instrumentation panel, with Figures C-77(a) through C-77(c) detailing the reinforcement strains from panel 1, panel 2, and panel 3 respectively.

The reinforcement strains recorded in the first two instrumentation panels during this earthquake were consistent with the response from the acceleration history C. From Figure C-77(c), it was established that, in contrast to most other tests, the longitudinal reinforcement in panel 3 did reach its yield strain. This was due to the large displacements that were applied late in the test. If these displacements were recorded at the conclusion of the laboratory procedures, it is highly likely that yielding would occur in the third instrumentation panel and thus little can be gained

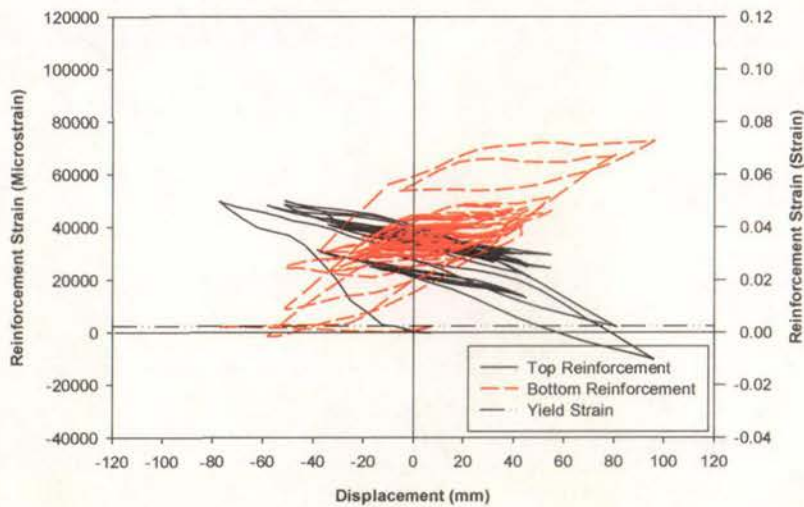


Figure C-77(a) Reinforcement Strains (Panel 1)

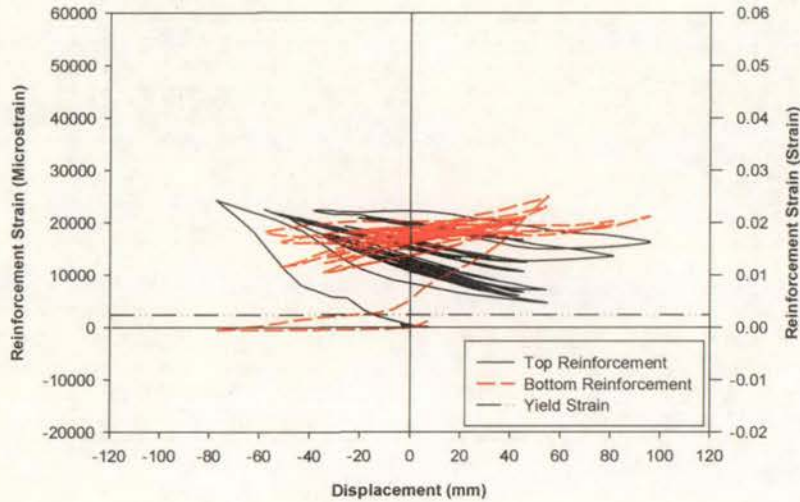


Figure C-77(b) Reinforcement Strains (Panel 2)

from this feature.

### C.11.6 Beam Elongation

The horizontal elongation at the beam centreline was recorded for the duration of the test. Figure C-78 details the beam elongation and reveals a maximum horizontal elongation of 27mm, which is equal to 4.5% of the total beam depth. This value of horizontal elongation is less than the elongation that occurred in acceleration history C. This reflects the greater percentage of total displacement accounted for through shear deformations.

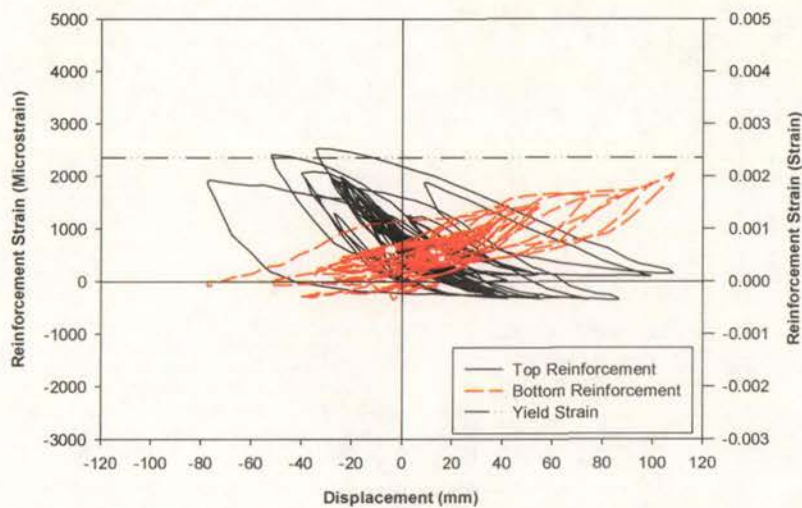


Figure C-77(c) Reinforcement Strains (Panel 3)

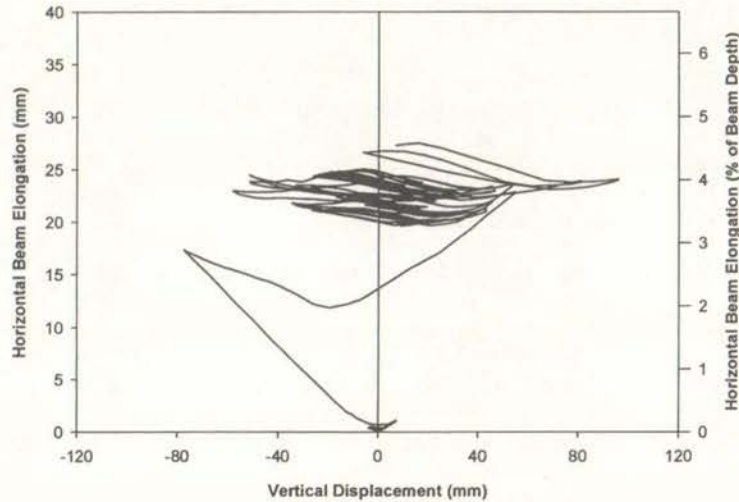


Figure C-78 Horizontal Beam Elongation

### C.11.7 Summary of Test Results

Excellent agreement was obtained between the sum of the three displacement components and the actual displacement for the duration of the test. Shear deformations accounted for a higher percentage of the total vertical displacement compared to that recorded during testing using acceleration history C. This was because premature rupturing of a longitudinal bar led to extensive degradation occurring, which resulted in larger shear deformations. All three displacement components exhibited conventional behaviour.

Poor response was observed between the predicted yield plateau and the actual yield plateau. However, the maximum strength of the beam was predicted accurately.

Reinforcement strains in the first two instrumentation panels were similar to the results from the acceleration history C. Yielding occurred in the third instrumentation panel as a result of the large displacements that were applied in the fifth record.

A total horizontal elongation equal to 4.5% of the total beam depth was recorded for the duration of the test. This is less than the elongation that occurred during application of acceleration history C and was due to shear deformation accounting for a larger percentage of the total displacement.

## C.12 Acceleration History E

Results from testing conducted using the acceleration history E are presented in Sections C.12.1 through C.12.6. Section C.12.7 then outlines the main points from the test results. Section C.12.1 describes the observed behaviour of the test specimen. Section C.12.2 identifies the separate displacement components that were measured during testing. Section C.12.3 then separates the total energy dissipated during the test into the energy associated with flexural and shear deformations. Section C.12.4 compares the predicted moment–curvature relationship with the experimental moment–curvature relationship and Section C.12.5 details the average strains in the longitudinal reinforcement for the three instrumentation cells. Lastly, Section C.12.6 reports on the horizontal elongation of the beam during the test.

### C.12.1 Test Observations

The displacement-time history established from the Ruaumoko analysis detailed in Section 5.2.5 was digitised so that an equivalent displacement record could be applied to the test subassemblage. Five individual earthquake records were applied in sequential order, with the repeat Kobe record denoted as Kobe (2).

#### **Northridge:**

This record had maximum displacements of 54.82mm in the positive direction and –77.47mm in the negative direction. These displacements were of sufficient size to ensure that crack patterns formed that were consistent with the crack patterns observed from testing using the cyclic laboratory procedures. Secondary cracking in the plastic hinge zone was also apparent. Minor spalling along cracks in the plastic hinge zone occurred throughout the record, although no transverse reinforcement had become visible by the conclusion of this record. Minor crushing of concrete in the compression zone was also observed.

**Kobe:**

This record was one of the largest records, with maximum displacements of 86.32mm in the positive direction and -25.94mm in the negative direction. This record resulted in a large amount of damage to the test subassemblage. Spalling from the top and bottom of the beam resulted in a length of longitudinal reinforcement becoming visible. Also spalling along cracks in the plastic hinge zone meant that transverse reinforcement was visible. Minor extensions to existing cracks were also seen after the larger displacement cycles.

**El Centro:**

Maximum displacements of 30.25mm and -9.96mm were applied in the positive and negative direction respectively during the El Centro portion of the displacement sequence. No additional cracking or spalling was observed during this record.

**Normalised El Centro:**

Maximum displacements of 54.02mm and -50.96mm were applied in the positive and negative direction respectively. Significant spalling from the side and bottom of the beam was observed with several large pieces falling out from the bottom of the beam during this record. Further spalling from the side of the beam meant that more transverse reinforcement was visible. Minor extensions to existing cracks were also identified after the largest displacement cycles.

**Kobe (2):**

This record was a magnified version of the Kobe record, with maximum displacements of 107.25mm in the positive direction and -34.88mm in the negative direction. Significant damage was observed during application of this record with major spalling from the side, top, and bottom of the beam. This meant that the width of cracks in the plastic hinge zone were unable to be measured. Extremely minor extensions to existing cracks were observed after application of the largest displacement cycles. Figure C-79 illustrates the total physical degradation that had

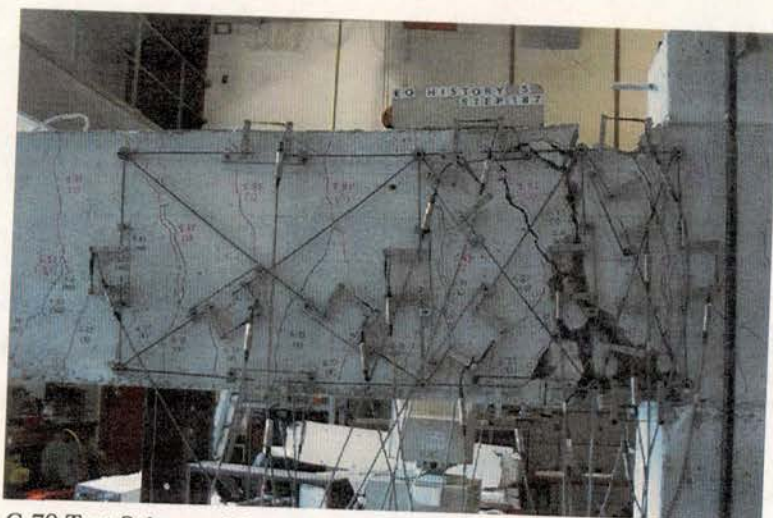


Figure C-79 Test Subassembly Condition at Conclusion of Acceleration History E

taken place by the end of this record. The test was terminated after conclusion of this record.

#### C.12.2 Displacement Components

Figure C-80 illustrates separation of the vertical displacement into its three components, and reveals that the shear displacement response was similar to that from acceleration history D. This was because the same situation applies for this earthquake history as for acceleration history E, where the largest negative displacement occurred early in the test sequence. Figure C-80 reveals that there was excellent agreement during the recorded phase of the test.

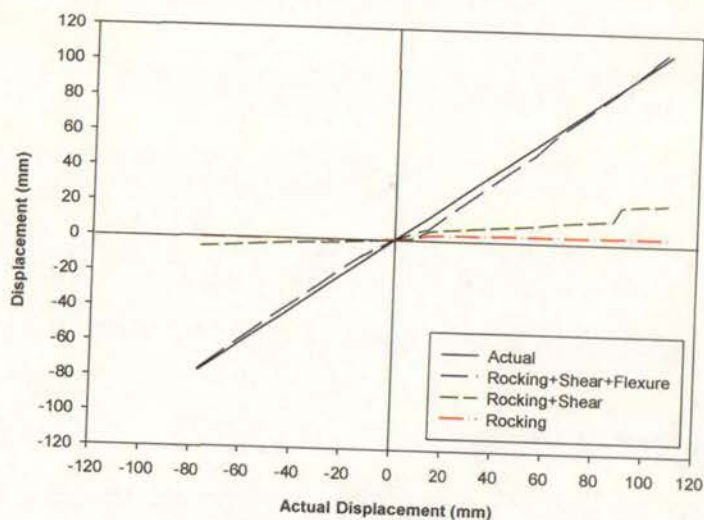


Figure C-80 Components of Displacement

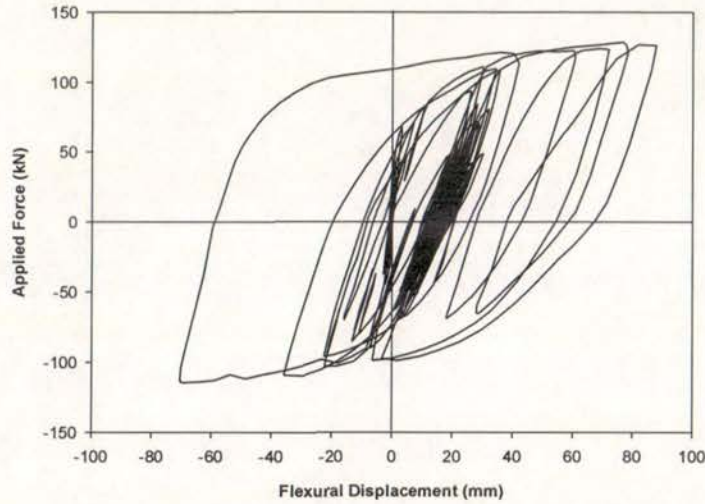


Figure C-81(a) Flexural Displacement Component

Figures C-81(a), C-81(b), and C-81(c) present the flexural, shear, and rocking displacement components for loading up to and including ductility 8. The shape of all three displacement components followed conventional behaviour.

### C.12.3 Energy Components

Figure C-82 illustrates the amount of energy dissipated through flexure and shear deformations and demonstrates that, as usual, the flexural deformations accounted for the vast majority of the total energy dissipated. The percentage of energy dissipated through shear deformation was comparable to results from acceleration histories B



Figure C-81(b) Shear Displacement Component

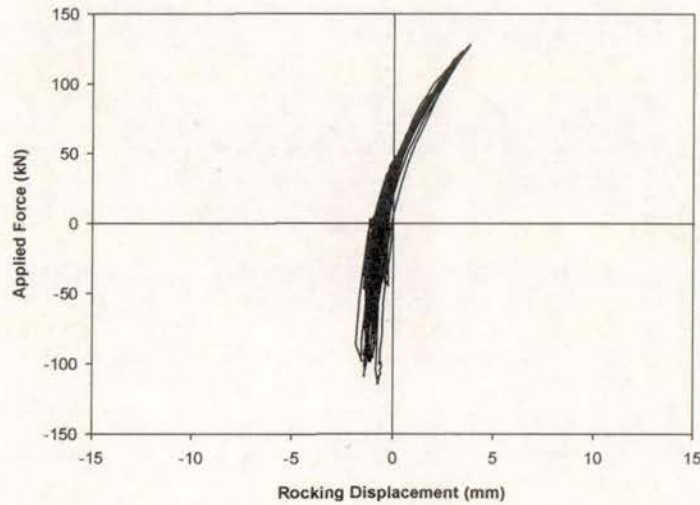


Figure C-81(c) Rocking Displacement Component

and C. Figure C-80 reveals that there was excellent agreement between the sum of the two components and the total amount of energy dissipated.

#### C.12.4 Moment–Curvature Response

Figures C-83(a) through C-83(c) detail the moment–curvature response for the three instrumentation panels during this test. The moment–curvature response from testing using acceleration history E followed the trends seen in the moment–curvature response from the New Zealand loading history, with poor correlation between the predicted and experimental yield plateau and little curvature demand in the third

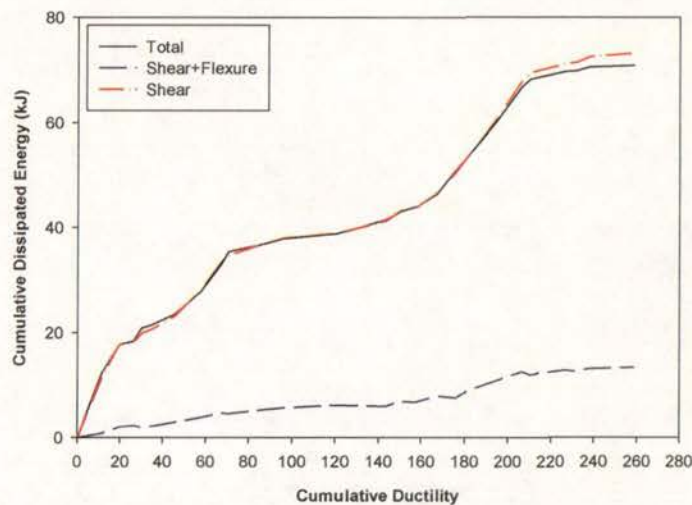


Figure C-82 Components of Energy Dissipation

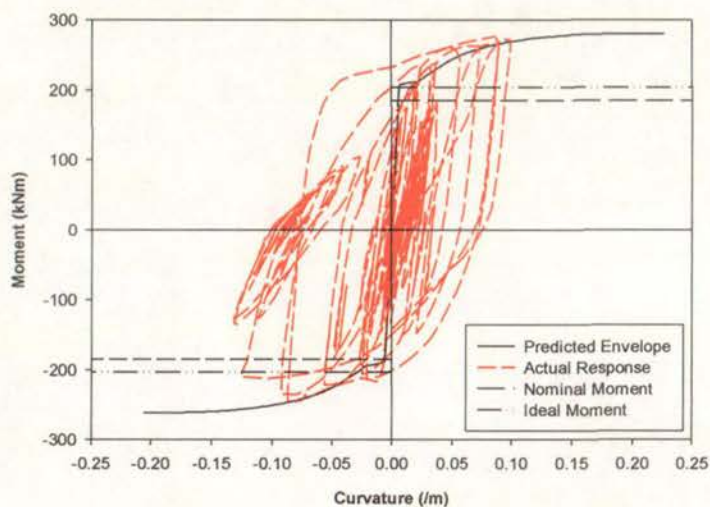


Figure C-83(a) Moment-Curvature Response (Panel 1)

panel.

#### C.12.5 Reinforcement Strains

The average strain in the bottom and top longitudinal reinforcement was plotted for each instrumentation panel, with Figures C-84(a) through C-84(c) detailing the reinforcement strains from panel 1, panel 2, and panel 3 respectively.

The reinforcement strains recorded in the first two instrumentation panels were slightly larger than the reinforced strains measured in acceleration histories B, C, or D. This was because this acceleration history had the largest displacements of the five

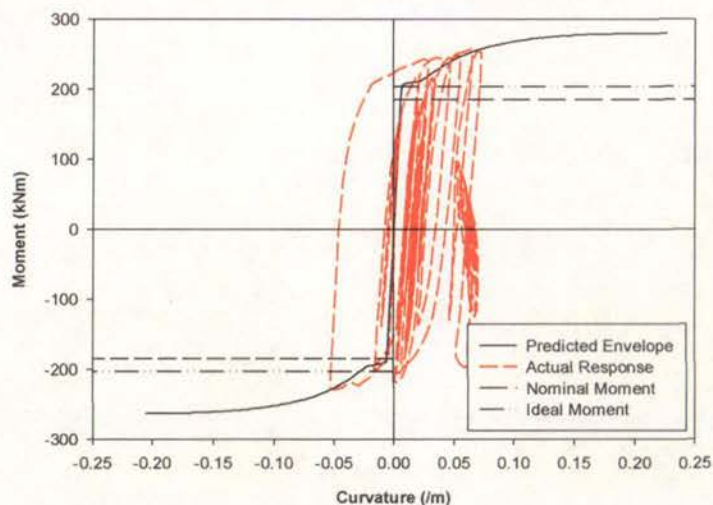


Figure C-83(b) Moment-Curvature Response (Panel 2)

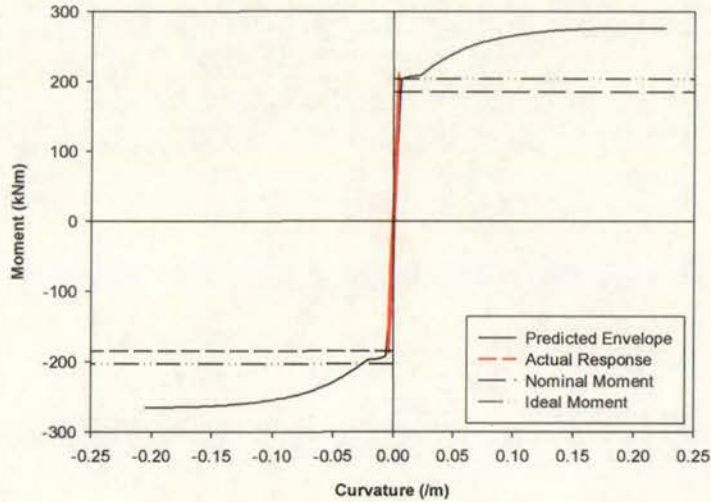


Figure C-83(c) Moment-Curvature Response (Panel 3)

acceleration histories. From Figure C-84(c), it was established that the longitudinal reinforcement in panel 3 did reach its yield strain.

### C.12.6 Beam Elongation

The horizontal elongation at the beam centreline was recorded for the duration of the test. Figure C-85 illustrates the horizontal elongation and reveals a maximum horizontal elongation of 37mm, which is equal to 6.17% of the total beam depth. This value of horizontal elongation was slightly larger than the elongation that occurred when testing using acceleration histories B or D, and again because this acceleration

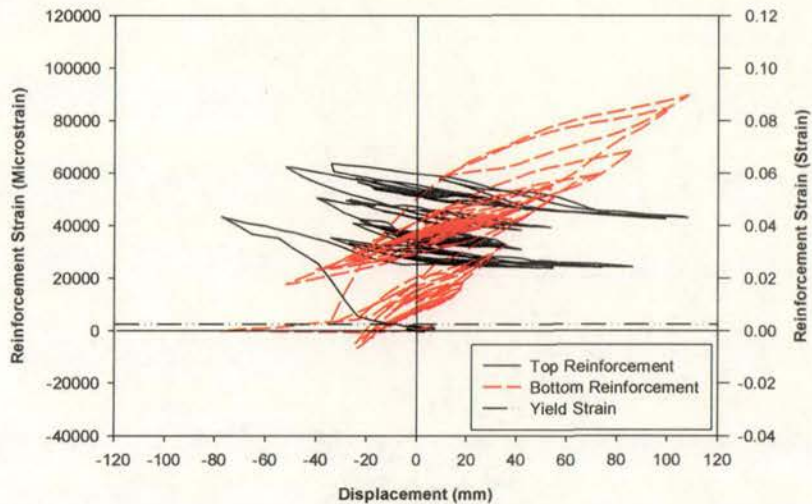


Figure C-84(a) Reinforcement Strains (Panel 1)

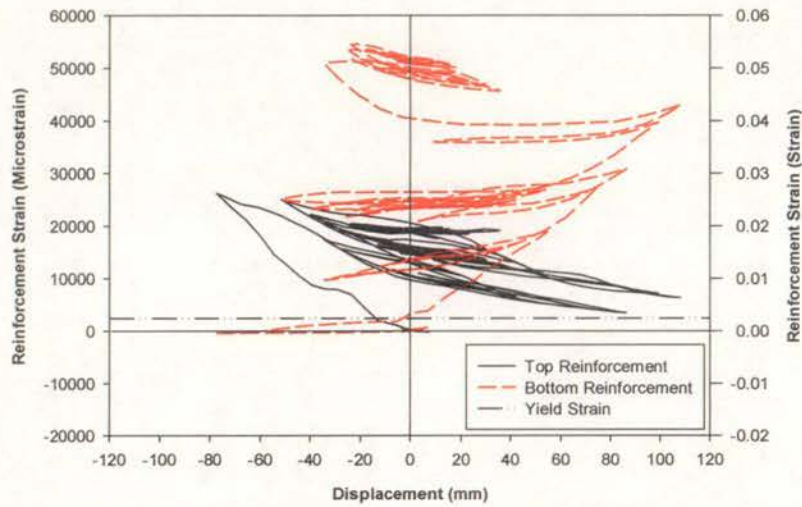


Figure C-84(b) Reinforcement Strains (Panel 2)

history applied the largest displacements of all the five acceleration histories.

### C.12.7 Summary of Test Results

Excellent agreement was obtained between the sum of the three displacement components and the actual displacement for the duration of the test.

Shear deformations accounted for a similar percentage of the total vertical displacement compared to that recorded during testing using acceleration histories B and C. All three displacement components followed conventional behaviour.

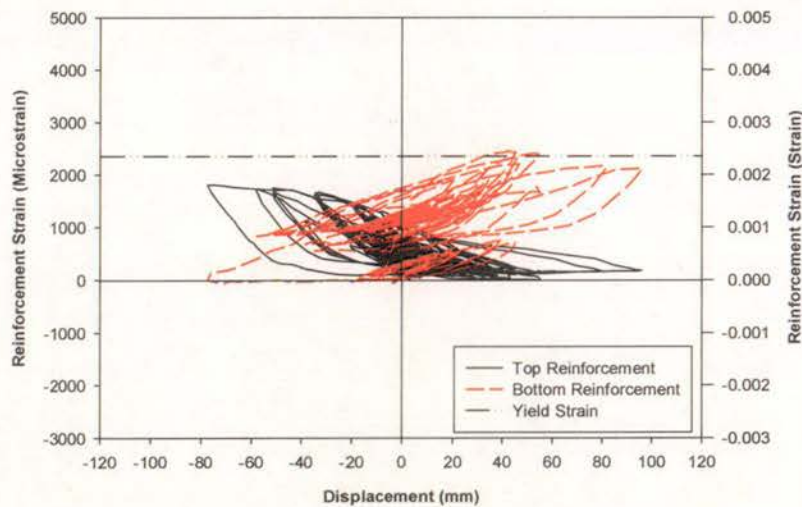


Figure C-84(c) Reinforcement Strains (Panel 3)

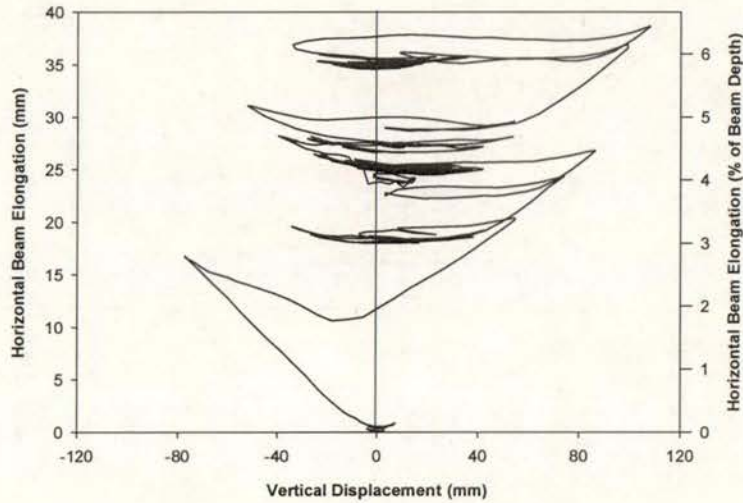


Figure C-85 Horizontal Beam Elongation

Poor correlation was observed between the predicted yield plateau and the actual yield plateau. However, the maximum strength of the beam was predicted accurately.

The reinforcement strains measured during this test were slightly higher than the strains recorded in acceleration histories B, C, or D. This was because this acceleration history applied the largest displacements of all the five acceleration histories. Yielding occurred in the third instrumentation panel.

A horizontal elongation equal to 6.17% of the total beam depth was recorded for the duration of the test. This is slightly higher than the elongation that occurred in acceleration histories B or D, again because this acceleration history applied the largest displacements of all the five acceleration histories.